Registration of Histology and Magnetic Resonance Imaging of the Brain

Jonas Pichat

A dissertation submitted in partial fulfillment

of the requirements for the degree of

Doctor of Philosophy

of

University College London.

Department of Medical Physics and Biomedical Engineering

University College London

January 12, 2018

I, Jonas Pichat, confirm that the work presented in this thesis is my own. Where information has been derived from other sources, I confirm that this has been indicated in the work.

Abstract

Combining histology and non-invasive imaging has been attracting the attention of the medical imaging community for a long time, due to its potential to correlate macroscopic information with the underlying microscopic properties of tissues.

Histology is an invasive procedure that disrupts the spatial arrangement of the tissue components but enables visualisation and characterisation at a cellular level. In contrast, macroscopic imaging allows non-invasive acquisition of volumetric information but does not provide any microscopic details.

Through the establishment of spatial correspondences obtained via image registration, it is possible to compare micro- and macroscopic information and to recover the original histological arrangement in three dimensions.

In this thesis, I present: (i) a survey of the literature relative to methods for histology reconstruction with and without the help of 3D medical imaging; (ii) a graph-theoretic method for histology volume reconstruction from sets of 2D sections, without external information; (iii) a method for multimodal 2D linear registration between histology and MRI based on partial matching of shape-informative boundaries.

Acknowledgements

My deepest gratitude goes first and foremost to Pr. Sébastien Ourselin, who gave me the opportunity to embark on this journey along with his trust, support and guidance until the end. I am also very thankful to my second (clinical) supervisor, Pr. Tarek Yousry, and my tertiary supervisors, Dr. Marc Modat and Dr. Juan Eugenio Iglesias for their patience, help and encouragements throughout the course of this thesis.

I would like to thank Pr. Olga Ciccarelli, Pr. Maria Thom, Dr. Steven Van de Pavert, Dr. Smriti Patodia and Mr. Marcello Moccia for providing us with imaging data and spending time going through them together. Thank you Smriti for letting me join the histological process, I learned a lot; and Marcello, for your communicative cheerfulness and kindness!

I am grateful to all my colleagues in TIG and CMIC (including all those who left in the middle and whom I hope I can meet again), who helped more than they could imagine just by being around, by asking me to hang out (sorry for saying no so often...) or by spending countless hours talking. I feel lucky having been part of this Centre and given the chance to share with several great researchers who were also great persons. I also feel lucky to be able and call some of them my friends.

In no specific order, special thanks to The Gang, the Lovers group, the Horn(se)y roaders, the best corner of TIG, Maria Z. (for, among other things, good times cycling to work) and the fussball table.

This thesis would not have finished without the support of my family. I will always remember the video call we had in the last weeks of the PhD (it was a Saturday morning of December at around 10am UK time), which ended up with you three standing behind the screen and cheering me up in a simple yet beautiful way—I just could not say a word and had to hang up...Thank you.

Last but not least, thanks to my badminton friends and teammates at UCL and Sobell. It was like a second family, always there to make you feel at home.

To my family and Hwanas

List of Publications

The present thesis develops works with first author contributions (underlined).

Peer-reviewed Journals

[J3] J. Pichat, J.E. Iglesias, S. Nousias, M. Moccia, S. Patodia, M. Thom, O. Ciccarelli, C. Bergeles, T. Yousry, S. Ourselin, M. Modat, Registration of Histology and MRI via Partial Matching of Shape-Informative Boundaries - *in preparation*

[J2] M. Moccia, S. van de Pavert, A. Eshaghi, J. Pichat, M. Yiannakas, S. Ourselin, Y. Wang, C. Wheeler-Kingshott, A. Thompson, F. Barkhof, O. Ciccarelli, Demyelination in the grey matter is the best correlate of magnetization transfer ratio in multiple sclerosis - *in preparation*

[J1] J. Pichat, J.E. Iglesias, T. Yousry, S. Ourselin, M. Modat, A Survey of Methods for 3D Histology Reconstruction. **MedIA** - *accepted*

Conferences

[C7] J. Pichat, J.E. Iglesias, S. Nousias, T. Yousry, S. Ourselin, M. Modat, Part-to-Whole Registration of Histology and MRI using Shape Elements. **ICCVW** (2017)

[C6] S. Nousias, F. Chadebecq, J. Pichat, P. Keane, S. Ourselin, and C. Bergeles, Corner-Based Geometric Calibration of Multi-Focus Plenoptic Cameras. **ICCV** (2017)

[C5] M. Moccia, S. van de Pavert, A. Eshaghi, J. Pichat, M. Modat, Y. Wang, A. Thompson, F. Barkhof, O. Ciccarelli, Pathological Correlates of Magnetization Transfer Ratio in Multiple Sclerosis. **ECTRIMS** (2017)

[C4] M. Moccia, S. van de Pavert, A. Eshaghi, J. Pichat, M. Modat, Y. Wang, A. Thompson, F. Barkhof, O. Ciccarelli, Association between CD20+ B-cells and age at death in multiple sclerosis. **ECTRIMS** (2017)

[C3] S. Patodia, M. Tachrount, J. Pichat, M. Modat, S. Ourselin, T. Yousry, S. Sisodiya, M. Thom, Delineating the Pre-Botzinger Nucleus in SUDEP. **69th Annual Meeting of the AES** (2015)

[C2] J. Pichat, M. Modat, T. Yousry, S. Ourselin, A Multipath Approach to Histology Volume Reconstruction. **ISBI** (2015)

[C1] C. Klemt, M. Modat., J. Pichat, M. J. Cardoso, J. Henckel, A. Hart, S. Ourselin, Automatic Assessment of Volume Asymmetries Applied to Hip Abductor Muscles in Patients with Hip Arthroplasty. **SPIE** (2015)

Contents

List of Figures

List of Tables

Chapter 1

Introduction

1.1 Overview

What is histology? Histology is concerned with the various methods of microscopic examination of a thin tissue section [2]. Cutting through a specimen reveals its internal topography and staining the sections permits the observation of differentiated complex structures. Then, the digitisation of histological sections (referred to as digital pathology) makes high-resolution microscope sections available for image computing and machine learning algorithms. These allow for example, for disease detection, characterisation and prediction so as to complement—and possibly replace, ultimately—the opinion of the pathologist [3], and constitute the field of histopathological image analysis [4]. It is most commonly performed *post mortem* but can also consist of a biopsy.

Difficulty in handling 2D images When willing to extend such examinations to the third dimension, one faces the following problem: starting from a series of two dimensional (2D) samples, how to regain information of the structure in three-dimensions (3D)? Volume slicing breaks the spatial relations between structures and creates discontinuities which hamper mental representations in 3D and thereby, a full understanding of the anatomy. In this respect, Gagnier *et al.* [5] illustrated the complexity in determining the progression of features into a volume, solely relying on a single face. In particular, they showed that participant's estimates were biased to assume that the surface continues straight back into the object. In addition, structures are independently altered due to the histology process itself (holes, tears, uneven staining, distortions etc.) as shown in Fig. 1.1 and detailed in §2.4. This may cause anatomically different structures to look similar in microscope slides and conversely, slicing may cause one same structure to have different views if not consistently cut. Other variations changes regard objects that may disappear or become highly salient from one

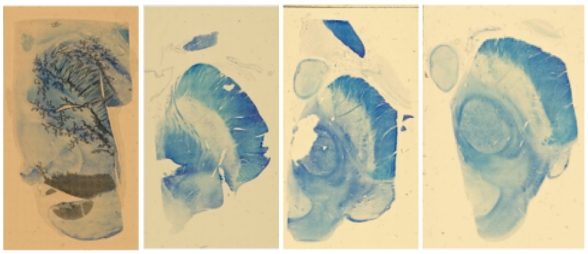

Figure 1.1: Artefacts related to the preparation of tissue sections (wax-embedded here). Those include (but are not limited to) intensity inhomogeneities, stain diffusion, tears, missing pieces, debris, air bubbles, various orientations and locations on glass slides, and spatial distortions.

section to another due to staining variability. Although humans can represent and mentally transform the shapes of objects [6, 7], this ability worsens when structures are interconnected within a dense and complicated environment or subject to complex transformations.

Giving body to visual understanding Reconstructing histology volumes from serial 2D sections seems natural in order to (re)gain knowledge about spatial environments in 3D, while accessing microscopic information about tissues. In this respect, the Swiss anatomist Wilhelm His Sr. (1831-1904) best explained that "just looking through sections does not enable one to build three-dimensional images in the mind and those who wish to grasp anatomical structures must actively engage in working through a reconstruction, reproducing the relationships they wish to understand" [8]. Histology reconstruction also represents an invaluable resource for (volume) quantification, as well as for registration with other modalities such as MRI, CT etc. (see §3.2).

When using histology alone, reconstruction algorithms aim to restore continuity and usually exploit the fact that the biological specimen's shape changes smoothly across sections. They provide a representation of structures and their environment in three dimensions, although one needs to bear in mind that the original shape is unattainable without prior knowledge. For illustration purposes, Malandain *et al.* [1] pointed out that if a banana is sliced, an ellipsoid will be reconstructed through pairwise alignment of adjacent slices, rather than the original fruit (Fig. 1.2). This is called the "banana effect" or "z-shift".

Digital histology reconstruction The most direct way of recovering volumes from sets of 2D serial histological sections is by optimising the spatial alignment of every pair of adjacent images using registration techniques. Composing the transformations from every slice to a reference slice completes the process—the reference slice is in general chosen for its high contrast, its small amount of artefacts, and preferably but not necessarily its

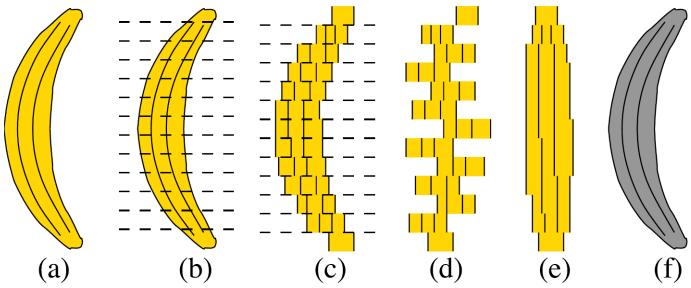

Figure 1.2: Illustrating the "banana effect". Image taken from [1].

location in the middle of the stack. A consequence is that any registration error impacts the final reconstruction by propagation throughout the stack due to the sequential nature of the process. Methods have therefore been developed to minimise these effects by looking at neighbourhoods rather than single slices in order to smooth those errors out (§3.1), or all of the images together via *e.g.*, groupwise registration; attention has also been directed toward preprocessing the images of tissue slices owing to their highly variable quality (§2.5).

Injecting volumetric structural information A remedy to the incorrectness of the histology reconstruction is the use of 3D medical images, such as magnetic resonance imaging (MRI). By providing structural ground truth (*structure* here is to be taken in the sense of a specimen's form or arrangement, which in most aspects can be considered as intact), they refine the space of solutions—although registration itself remains an ill-posed problem. Blockface photographs (*i.e.*, pictures of the tissue face taken prior to cutting) and needles can be used to reach better reconstructions. While the former provides images of the tissue free of cutting artefacts, the latter allows straightforward extraction and matching of landmarks in both medical imaging and histology. However, the set-up for blockface photographs is difficult and inconvenient (time, space etc.); the use of needles is also sparse in the literature for it may cause unwanted damage to the tissue.

Besides guiding reconstruction, 3D medical imaging constitutes an invaluable source for accurate, non-invasive study of biological structures and their functions. Relative to histology, Fischl [9] listed three advantages: the possibility of (i) imaging the exact same tissue with multiple contrasts (*e.g.*, T1 or T2 MRI, MTR, etc.)—although their counterparts have emerged in the field of histopathology with for example, multiplexed/multicolor immunohistochemistry and imaging mass spectroscopy; (ii) imaging large samples (*e.g.*, whole-brain or whole-hemisphere) with much less effort than for example, whole-brain or prostate whole-mount histology; (iii) preserving the geometry of the sample and avoiding

irreversible damage and distortions induced by processing, cutting, mounting and staining during the histological preparation.

Limits of medical imaging With respect to resolution, MR imaging is outperformed by histology ($< 1\mu m$). In addition, for many pathological disorders, there is still no no sequence acquisition that allows imaging to be a full substitute for histology. This is due to the poorly understood relationships between histological and magnetic properties of tissues. Directly predicting the imaging appearance of a histological signature is therefore extremely complex. Practically, this results in that different pathologies can share a common imaging phenotype [10]. For example, Filippi *et al.* [11] noted that in proton density, FLAIR and T2w MRI scans, Multiple Sclerosis (MS) lesions appeared as non-specific focal areas of signal increase and, therefore, resembled many other types of pathology. This makes it difficult to differentiate them with imaging only. Additionally, some cortical MS lesions can still be missed with conventional MRI sequences [12]. Direct comparisons with histology helps interpret images better and derive more information. They may also help in correcting or adjusting existing imaging protocols in order to optimally visualise pathological markers (*e.g.*, lesions in the grey matter of patients with MS).

Combining histology and medical imaging One of the many benefits of combining histology and medical imaging is to confirm non-invasive measures with baseline information on the actual properties of tissues [13]. By combining 3D medical imaging with digital pathology, it is possible to simultaneously obtain the rich non-invasive information of the former and the chemical and cellular information of the latter, which may allow for more complete characterisation and understanding of *e.g.*, diseases [14]. One can also derive more accurate segmentations of architectonic boundaries to be used in the creation of atlases [15, 16, 17, 18, 19] as well as brain mapping [20], by performing delineations on high-resolution tissue images. Note that a more realistic histology reconstruction is obtained when registered with clinical imaging, if a sufficient number of histological slices is available (this is discussed in §5.1). Such undertakings are intended to eventually bridge the gap between *in vivo* and *post mortem* studies.

The importance of comparing like with like Currently, direct overall visual comparison is considered acceptable to assess the correlation between histopathological findings and imaging observations. On that matter though, it was recently mentioned in the context of prostate cancer assessment that due to variations in imaging technologies, contouring

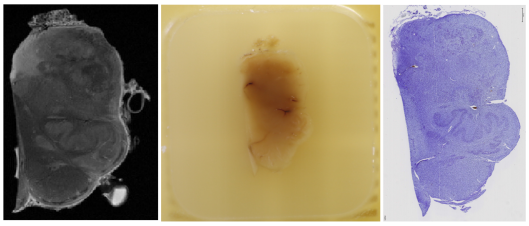

Figure 1.3: Modalities that may be involved in the registration process. From left to right, a screenshot of a T2w *ex vivo* slice ($0.1 \times 0.1 \times 0.4\text{mm}^3$) from human mesencephalon, a visually corresponding blockface photograph (tissue surrounded by wax) and a Nissl-stained histological section.

procedures and data analyses, available volume correlation studies had yielded conflicting results [21]. Such contradictions were explained by the worrying observation that nearly all prior attempts to define MRI/pathological relationships had relied on imprecise techniques such as manual registration, volume approximation, and 2D measurements. Following the same line of thought—two decades before—correlation was proved to be optimised when the alignment between data had first been carefully taken care of by use of a combination of linear and non-linear transformations [22]. In other words, ensuring the comparison of like with like is of utmost importance [3].

Multimodal image registration Multimodal image registration permits the automation of the alignment process and allows to redefine "visual closeness" as the optimisation of a certain matching criterion. It also accounts for the complex transformations that affect histological sections individually and grants higher reproducibility with less or no human effort. Careful use of registration techniques can establish more accurate correspondences between histology and volumetric medical imaging *i.e.*, produce histology reconstructions closer to reality, and contribute to more sound data analyses. To this end, it is not uncommon to use intermediate modalities (Fig. 1.3) in the process of relating *in vivo* to *post mortem*, so as to keep track on the deformations that the tissue undergoes during its changes of state.

1.2 Problems statements and solutions

1. There exists a vast amount of solutions to the problem of registering histology and medical imaging, should they stem from purely technical challenges or an effort to better understand a specific pathology via the application of one technique already established. Although the field is relatively old (about 30 years), it is still growing (mainly within the clinical scope of answering biological questions) but in some cases, surprisingly still relies on rather loose assumptions [21] (see also §3.2.1.1);

those include, but are not limited to, the constant spacing between consecutive histological slices, and the parallelism of cutting and acquisition planes respectively from histology and medical imaging. Such assumptions may have heavy consequences on subsequent statistical analyses. Add in the ill-posedness of the registration problem (two different solutions, each maximising a certain criterion, may be as *valid* as another and no ground truth is available to assess any of them), and over-simplification (though necessary in some cases) leads *de facto* to suboptimal solutions. Last but not least, these assumptions may also convey the wrong idea that *image registration* could be a solved problem.

One should also note that the the plurality of methods covered in the corpus of literature derive from the data at hands, whether one must deal with (i) a series of histology sections only, (ii) a series of histology sections and a medical image, (iii) one (or a few, sparse) histology section(s) and a medical image volume. Whereas the former two imply an actual histology reconstruction, the latter tackles the more general multimodal registration problem and cannot rely on the greater support that volumes offer for that matter. Other subcases may arise depending upon the study goals (like when building atlases) and the availability of the tissue.

Nota bene: it should be specified that the two methods I propose in the following fall respectively into the former (i) and latter (iii) cases.

Contributions

- By this survey of methods for histology reconstruction, first of its kind, I aim to identify sources of variability in approaches (from generating data to analysing them) and patterns of methodologies (with and without the help of medical imaging), highlight what seemed to be sound ways of formulating and solving the registration problem and put the field in perspective by highlighting difficulties that remain in preprocessing medical images, dealing with their various forms (resolution, missing or corrupted pieces of tissue...), defining and extracting meaningful information from them, and the need for cross-disciplinary knowledge to solve a biological question efficiently.

2. In some cases, one is only given a series of histological slices (with no other volumetric information). Specimen slicing, during tissue preparation, breaks the spatial

relations between structures. This creates discontinuities which hamper mental representations in 3D and thereby, a full understanding of the anatomy. In order to regain visual understanding of the structures in 3D and possibly allow for quantitative analyses, a smooth (or continuous) reconstructed volume is sought.

One bottleneck, and thus a limitation of the solution, should be noted: without the help of external information about the shape of the tissue prior to sectioning (*e.g.*, 3D medical imaging), the true, original arrangement is unattainable.

The method I develop for histology reconstruction was motivated by a paper from Yushkevich [23]: seeing the histology stack as a graph, each slice as a node, and a path (that connects two nodes) as a registration, reconstruction can be formulated as a shortest path problem, where *shortness* is evaluated in terms of images similarity. In other words, the goal is to find the path (*i.e.*, the sequence of pairwise transformations) that yields the *best* overall alignment in some sense.

This calls upon *comparability* in the sense that one path is favoured over another according to a certain measure; this is not taken into account in [23] but is a crucial consideration when separate images are involved in the computation of the graph edges weights. Comparability is the cornerstone of my approach.

Both methods consider several neighbours around each slice, and allow bypassing failures by skipping registration paths with lower weights (or lower similarity after registration), although it seems Yushkevich's method uses similarity as an absolute measure to do so in Dijkstra's algorithm. Note that failure is to be understood in a relative sense here, since there exist no absolute criterion that can tell whether a registration is actually successful—though there have been attempts [24].

Contributions

- I propose to explain every pairwise registration between adjacent sections as: (i) a regular direct transformation and, (ii) a set of indirect ones obtained through neighbouring registrations by transitivity; each path is associated with a weight (a similarity measure) computed after the floating image has been applied the (possibly composed) transformation associated with that path. The set of weights has, by design, a total ordering and the path that minimises the registration error between two adjacent sections can be identified (paths weights are

comparable with one another); once this is done for all pairs of slices, the shortest paths become the new direct paths and the graph gets updated dynamically until convergence (*i.e.*, all the shortest paths are the direct ones).

- The method relies on two parameters, η and ε, respectively responsible for the number of neighbouring slices taken into account in the shortest path search, and the maximum gap tolerated between two slices to be registered. I show that their tuning depends on the dataset at hands (especially its sparsity).

3. It is not uncommon for histopathological laboratories to receive specimens that are too large to be processed for histology at once. Consequently, they are cut into smaller blocks and processed individually. As for their registration with medical imaging—when no scan of each separate block is available—this necessitates either to record the arrangement of the blocks relatively to the whole specimen for initialisation, or manually align both images.

   My contribution lies in addressing the problem of locating and aligning a fragment of tissue in its whole (a medical image). This alignment is performed in 2D, with a visually corresponding MRI plane identified *a priori*. Although the proposed method does require manual interaction for the identification of an MRI slice, the rest of the matching is automated. It should be noted that potential for extending the method to the third dimension is shown (*i.e.*, the automation of the medical image plane selection); however this solution would not take into account the potential tilt induced by cutting the specimen, but would represent a trustful initialisation for other 2D-3D non-rigid registration methods. Letting aside the "partiality" of the problem—which in itself justifies the restriction to 2D—I find important to mention that such a choice was also made in view of the real data at hands: I was given large thick slices on the MRI side and a thin slab of consecutive sections on the histology side. This would make any attempt at 2D-3D (non-linear) registration very complicated without first taking care of the initial alignment of both modalities: even considering that it makes an angle with the MRI acquisition plane, one piece of histology spanned less than a voxel in the MRI.

   In view of the survey, I identified three features that my solution should have: (i) contrast-invariance: an MRI sequence is set to produce a given contrast image of the specimen, such as T2, T1, PD, etc. Equivalently, histology produces sections stained

with various dyes. Actually, even letting aside the fact that the histological process induces various alterations, the very contrasts of both modalities condition the presence or the absence of comparable content across images. (ii) Locality: although there exist local versions of intensity-based similarity measures, iconic methods are very sensitive to initialisation—which is even more cumbersome when only a fraction of tissue is available and is to be located within its whole in the image. Furthermore, in relation to the previous point, a one-to-one mapping between histology and MRI does not exist in general, since each modality exhibits its own structures. Finally, due to the deformations that the tissue goes through, the solution requires: (iii) the invariance to a certain class of transformations and I limited it to homographies: it seemed reasonable to incorporate more degrees of freedom than with affine transformations so as to take into account non-linear distortions that the tissue undergoes, while keeping their number relatively low in order to avoid overfitting.

The proposed solution is based on:

(i) a representation of images using pieces of their level lines (§5.2) *i.e.*, the boundaries of level sets, [25], which for some of them, coincide very well with objects boundaries; this representation was motivated by works from Monasse *et al.* in image processing [26] and grounds the shape recognition process that is necessary to multimodal alignment between histology and MRI. Level lines allow to reach contrast invariance and to consider several structural layers in the tissue (level lines coincide very well with objects boundaries)—as opposed to relying solely on its outer boundary.

(ii) a selection of shape-informative (or meaningful) level lines, based on length, contrast and irregularity (§5.3). From there, characteristic shape elements can be extracted locally along meaningful boundaries via their refined bitangents (§5.4).

(iii) a projective-invariant encoding of shape elements[1] (§5.5), so as to be robust to some non-linear deformations that tissues undergo during the histological process, and their comparison using the Fréchet distance; the minima correspond to matching pairs used for alignment. Outliers are robustly discarded using a

[1] Shape encoding relies on bitangents extracted along curves; their use in computer vision problems dates back to Lamdan, Rothwell and others in the late 1980s, early 1990s. Here, bitangents endpoints define pieces of level lines, the so-called *shape elements*, which are then be encoded.

threshold on the distance and RANdom SAmple Consensus.

Altogether, this allows matching shape elements regardless of the orientation of the tissue on glass slides. Registration is obtained as a result of shape recognition (§5.6).

Contributions

- I present a 2D linear geometric registration method which addresses the joint problem of multimodal registration between histology and an MRI plane, when only a fraction of tissue is available from histology.
- I propose an additional criterion for the selection of meaningful level lines based on the *temperature* (or complexity) of curves, which complements that of Desolneux *et al.* [27] based on contrast only. This contribution, tailored to the medical imaging application, is intended to detect first and foremost contrasted, irregular level lines (like the brain folding pattern) more useful to the shape recognition process so as to to make the method less compute-intensive and more robust to noise than curvature-based measures.
- I propose an efficient refinement of bitangents locations via ellipses fit around their end points and show improvement in the final alignment.
- I extend Rothwell's framework for object recognition by considering more peculiar shape elements using bitangents crossing the level lines; I propose to compare the resulting canonical curves (invariant to projections) via the Fréchet distance.
- I propose to fuse information from several MRI modalities by combining meaningful boundaries from each one of them in a single composite set used for comparison with histology. Similarly, the set of meaningful boundaries from histology is composed of those from each dye.
- I justify robustness of the approach to intensity bias—which commonly hampers medical image analysis—thanks to the locality and contrast-invariance requirement(s).
- I evaluate the performance of the proposed method, using BrainWeb T1 and T2w MRI contrasts, as well as a dataset composed of histology and MRI (in the context of multiple sclerosis—referred to as MS dataset in the following).

1.3 Thesis outline

Chapter 2 looks at the data—histology and medical imaging—through a historical lens and asks: how did we come to investigate the anatomy in such ways? This part of the thesis is intended to highlight the successive bottlenecks in the visualisation of the interior structures of the body, how those have been overcome across time and eventually led the anatomy to be presented the way it is today. I then detail two routine techniques for modern histopathology, list artefacts and present image processing methods developed to deal with them in digital pathology [J1].

Chapter 3 surveys about 30 years of literature on histology reconstruction with and without the help of medical imaging [J1], along with methods of validation and some applications. I also discuss what I believe is the most efficient way of dealing with the problem of multimodal registration between histology and medical imaging, and try to put the field into perspective.

Chapter 4 introduces a method for reference-free histology volume reconstruction from 2D serial sections [C2]. It is a graph-theoretic approach which respects comparability between paths. I also propose an original method for intensity standardisation that is not based on the arbitrary selection of a reference distribution.

Chapter 5 presents a multimodal registration method between histology and MRI [C7]. It was designed to solve the specific problem of locating and aligning a piece of tissue in histology, part of its whole in a medical image plane. The method is a 2D linear geometric approach to the registration problem, which relies on representing the images using their level lines so as to be robust to variations in contrast. Alignment is obtained as a byproduct of shape recognition, which is based on partial matching of shape-informative boundaries (a subset of *meaningful* level lines) [J3] in a projective-invariant manner. This approach may serve as initialisation for further refinement using 2D-3D nonlinear registration methods.

Chapter 6 summarises the key results and discussions of each chapter and concludes with some future works.

Chapter 2

Visualising the Anatomy

"Study the past if you would define the future."
Confucius

A glance at the history of anatomy—the study of the interior structures of the body—shows that its (re)presentation *i.e.*, the way it is brought to mind by description, took many forms before being the images one knows of and uses in digital pathology and clinical imaging.

In the following, we first detail three successive ways (each new at their time) to look at otherwise invisible objects, each of which redefined knowledge and problems, or marked as Latour [28] put it, "the end of an archaic and stable past" (Fig. 2.1a). Most importantly, they created entirely new scientific fields and triggered the progress of Science (Fig. 2.1b). As Martin Chalfie wrote in his Nobel lecture [29], "scientific inquiry starts with observation. The more one can see, the more one can investigate. Indeed, we often mark our progress in science by improvements in imaging". Altogether, those shifts contributed to the evolution of the intellectual and practical processes that led the anatomy to be visualised the way it is today. Then, I describe the two most common processes to generate histological data—as of today—(§2.3), the artefacts they each are associated with (§2.4) and the image processing methods developed to account for some of them (§2.5).

The first shift (§2.1.1) took place at the Renaissance and marked the collapse of Galen's predominance in the persons of Leonardo Da Vinci and Andreas Vesalius. It was embodied by incredibly detailed anatomical drawings, showing for the first time a symbiosis between artists and physicians with the common goal of exacting the human form.

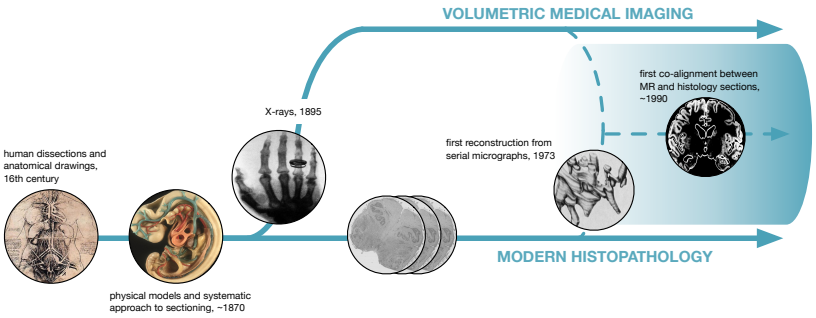

(a)

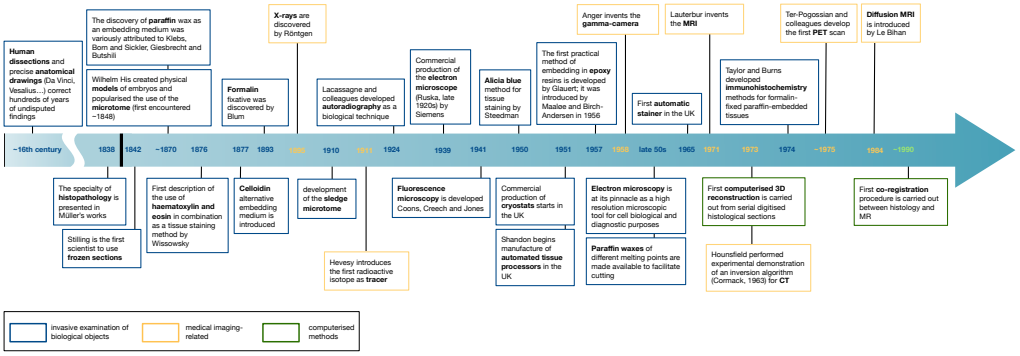

(b)

Figure 2.1: (2.1a) The three shifts in the history of anatomy visualisation and (2.1b) some of the main discoveries related to its development.

The second shift (§2.1.2) occurred in the late 19^{th} century, and showed another fruitful collaboration between anatomists and modellers: the creation of physical models introduced the concept of three-dimensional reconstruction so as to overcome the limitations of drawings in a dimensional scope. This, "far more than any mental construction, would give body to visual understanding again" [30] and laid the ground for modern histopathology techniques.

The third and last shift (§2.1.3) consisted of the advent of medical imaging, initiated by William Röntgen with the discovery of X-rays in 1895, which allowed to obtain pictorial information about interior structures of the body *in vivo*.

2.1 A brief history of anatomy

Although knowledge about the anatomy can be traced back to the Egyptians, as early as 1600 BC with the Edwin Smith Surgical Papyrus [31] and the Ebers Papyrus written in about 1550 BC [32]—they show that the heart, its vessels, liver, spleen, kidneys, hypothalamus, uterus and bladder had already been recognised—nomenclature, methods and applications

for its study all date back to the Greeks [33]. Most of them were gathered in the Hippocratic Corpus and show the beginnings of understanding of the function of certain organs like the kidneys.

The *comparative anatomy*, which is the study of similarities and differences in the anatomy of different species, was created by Aristotle around the 4^{th} century BC. Works by him and his contemporaries were based on animal dissections. First human dissections (on executed criminals) have been allowed under the Ptolemaic dynasty, later in the 4^{th} century (BC), and performed by Herophilus and Erasistratus. Incidentally, Herophilus was also accused of having dissected around 600 live criminals. Despite the charges, he is seen by many as the founder of anatomy as he discovered the nerves, distinguished them from the sinews [34] and proved Aristotle wrong: he showed that the brain was the centre of the nervous system while the latter believed that "the heart was the seat of the sensitive soul" [35].

The last major anatomist of ancient times, Aelius Galenus (or Galen, 2^{nd} century AD) also attacked Aristotle's theory and showed experimentally (through public dissections) that "all the nerves originated in the brain, either directly or by means of the spinal cord, which he [Aristotle] thought to be a conducting organ merely, not a centre" [35]. Thorndike added that "if Galen owed something to Herophilus, we owe much of our knowledge of the earlier physiologist to Galen". Indeed, Galen wrote more than 600 treatises covering anatomy, physiology and pathology. His writings remained undisputed and served as reference until the medieval times (when they were translated into Latin) but were shown to contain mistakes: Galen's experiments were mainly animal vivisections.

2.1.1 First shift: the anatomical drawings

It is at the Renaissance that the era of modern anatomical studies truly begins and this stems from a simple fact, Thorndike explains [35]: "the extant manuscripts of the Greek text are mostly of the fifteenth century and represent the enthusiasm of humanists who hopped by reviving the study of Galen in the original to get something new and better out of him than the schoolmen had".

It is also at the Renaissance that less restrictions were put on the dissection of cadavers, from which anatomical knowledge has greatly benefited. Some artists forged partnerships with physicians, who allowed them to attend procedures (highly restricted at the time) in exchange of anatomical drawings and illustrations (Fig. 2.2). Titian and Andreas Vesalius

Figure 2.2: *The Anatomy Lesson of Dr. Nicolaes Tulp* by Rembrandt (1632). In the painting, the physician Nicolaes Tulp shows seven surgeons (who paid commissions to be included in the painting) how the muscles of the arm are attached. The body was that of a criminal, Adriaen het Kint. Figure taken from Wikipedia.

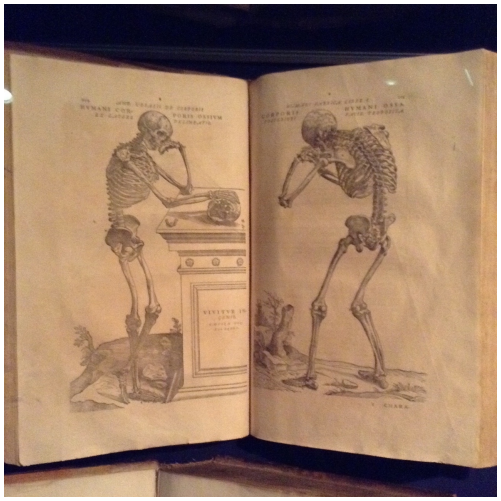

Figure 2.3: Copy of *De Humani Corporis Fabrica* from Andreas Vesalius (1543) at the Gutenberg museum in Mainz, Germany.

are one of the best-known example.

That time marks the moment when the representation of anatomy became inseparable from art. Incidentally, drawings were also more accessible than treatises in Latin and Greek—further details about the role of art in science can be found in [36].

Early modern anatomy is embodied by two figures: the Italian polymath Leonardo da Vinci (1452-1519) and the Flemish anatomist Andreas Vesalius (1514-1564), the latter being often referred to as the founder of modern anatomy (Fig. 2.3). They both promoted the dissection of human cadavers to learn about the human body, and proved several times Galen's assumption that animal and human anatomy were similar could not hold. They also provided the community with incredibly detailed anatomical drawings.

In this respect, Keele [37] observed that the anatomy could never have existed as a science without "adequate techniques for recording its observations", and he was referring to "those long, distasteful hours of adventurous dissection and patient drawing". Keele concluded by stating that Leonardo, or "the artist-anatomist who had created the new science" had thereby laid the ground for Vesalius' work [38]: Da Vinci had stimulated the fusion of art and science in anatomical representation.

Toga and Mazziotta [39] also acknowledged the contributions of Da Vinci, by being "the first who realised that a full understanding of anatomic structures could only be achieved through multiple views": Da Vinci knew how to present knowledge. In that sense, he created objects that were mobile but also immutable, presentable, readable and combinable with one another [40]; and as Latour wrote: "there is nothing you can dominate as easily as a flat surface".

According to Edgerton [41] however, the scientific revolution at the Renaissance owed more to the German theorist Albrecht Dürer (1471-1528), who introduced the rules of perspective, than to Da Vinci. These laws are still used in today's computer vision [42] and grant "translation without corruption": no matter from what distance and angle an object is seen, it is always possible to transfer it and to obtain the same object at a different size as seen from another position [40]. Linear perspective creates what Ivins [43] called *optical consistency*, for "the printed picture always presents a rational image based on the universal laws of geometry".

In some disciplines though, the 2D support of drawings was viewed as conceptually and practically limiting, and gave way to 3D physical representations. Quoting the Swiss anatomist Wilhelm His Sr. (1831-1904), Hopwood [8] wrote: "those who wished to grasp anatomical structure must actively engage in working through a reconstruction, reproducing the relationships they wished to understand. They must work not only with their brain and eyes but also with their hands. And they must not only draw but produce solid objects too".

2.1.2 Second shift: the physical models

Strictly speaking, wax models were first employed to teach anatomy early in the 14^{th} century. They were popularised by Alessandra Giliani of Persiceto [44]. Like in §2.1.1, such models were the result of a collaboration between anatomists and artists (modellers), who were usually hired to produce them for medical instruction.

The 19^{th} century appears to be historically the moment when modelling truly finds its

roots. This was within the field of embryology, where the need for building models emerged due to: (i) the fragility and short-lived conservation of specimen, which hindered the study of the developmental stages of embryos, and (ii) the limitation of drawings in a dimensional scope. This period is illustrated hereafter with the collaboration between Wilhelm His Sr. and the German modeller Adolf Ziegler (1820-1889), relying on the meticulous study from Pr. Hopwood [8].

As for (i), the histological practice was introduced in works from Johannes Peter Müller (1801-1858). He studied the cellular structure of tumours with the aid of a microscope after one of his colleagues, Theodor Schwann (1810-1882) [45] showed that the cell was the basic unit of structure in the animal body. Details on the preservation of specimen are given in §2.3.

As for (ii), Hopwood noted that models could achieve a "vividness and tangibility" that no flat picture could provide. Such models could also be used in making more accurate 3D drawings by appropriate shading of the elements[1].

Wilhelm His believed that only an investigation through 3D representations could help discover the causes of *form* (the morphogenesis). He was asking physiologically how one embryonic stage was transformed into the next. This mechanical approach to embryology (taken up from the mid 1880's) was the first main innovation credited to His, and the microtome (1870) was the second. The former constitutes the intellectual process and the latter is the practical aid: the tool that permitted the collection of sections and their use to build 3D wax models. This allowed making precise and systematic inspection of organism's interior structures easier.

Although cutting specimen had already been performed earlier (manually, using knives), it is the newly developed microtomes and the improvements in methods of specimen preparation that really contributed in making sectioning a routine process, more trustworthy and complete. Mechanical sectioning allowed for the visualisation of the internal topography of fixed specimens thanks to uninterrupted and precise series of slices. This laid invaluable foundations in modern histological practice.

[1]This was already mentioned by Galileo in a letter to Lodovico Cardi (also known as Cigoli) [46]: "The statue does not have its relief by virtue of being wide, long, and deep but by virtue of being light in some places and dark in others. And one should note as proof of this, that only two of its three dimensions are actually exposed to the eye: length and width. [...] We know of depth, not as a visual experience *per se* and absolutely but only by accident and in relation to light and darkness. And all this is present in painting no less than in sculpture. [...] But sculpture receives lightness and darkness from Nature herself whereas painting receives it from Art."

Figure 2.4: "Marilyn Monroe" by Park Changirl (2011), Korean Art Museum Association (`http://blog.naver.com/dkxmqkr`).

From there, Wilhelm His could use the set of sections for the object 3D reconstruction[2], because "just looking through sections did not enable one to build three-dimensional images in the mind. Rather, the preparation of the sections should be regarded as but the first step in an elaborate process of three-dimensional representation". This led to unequally detailed 3D wax models with the help of Ziegler, and Wilhelm His used them to give readers of the monographs what the plates of serial sections could not supply alone: physical images.

This is, I think, the first time 3D physical reconstruction from serial sections was explicitly promoted and used for better visualisation and understanding of the anatomy. Two problems however arise when making the transition from 2D to 3D representations:

(i) Models are difficult to produce [47] and reproduce, fragile, cumbersome and have limited mobility (an artistic illustration of a comparable effort is shown in Fig. 2.4). As a matter of fact, they make less immutable objects than drawings.

(ii) One often wants to use an object, has it been drawn or physically modelled. The points representing the structure thus take on a quantitative, not just descriptive, significance. Consequently, one would like not only to have large amounts of 3D data available in a systematic form, but in addition, to be able to use them in computations [48].

[2]"But sectioning [...] was necessary only because the smallness of the objects of interest made physical dissection impracticable, and yet they were too large and opaque for direct microscopical observation of their interiors. The methods of plastic reconstruction that he had developed would allow scientists to give body to visual understanding and so return in richer detail to the lost world of the pioneers" [8].

Since the early 1970s, computers have offered speed and facility to solve both these problems [49, 50, 51, 52]. They are now used at all stages of the 3D reconstruction, including data collection (digitised 2D micrographs), storage and analyses, as well as to create a visual representation of the reconstructed histological volume.

2.1.3 Third shift: the medical images

It all started in 1895 with the discovery of X-rays by Wilhelm Röntgen. This technique consisted of radiations piercing the tissues. Those revealed the different densities of tissues within the body (due to variable absorbance) on a photographic film or a fluorescent screen, thus creating an image. However, the 3D structure of the body is projected onto a 2D film and X-rays are unable to distinguish soft tissues.

Among major development in radiography, one can start with the use of radio-opaque contrast agents to help visualise organs and blood vessels. In particular, Cannon [53] used barium sulfate to study the intestines using Röntgen's X-rays. Then, in the late 1890's, Thomas Edison popularised fluoroscopy by discovering that the use of calcium tungstate produced brighter images than when using barium sulphate. In the early twentieth century, the Hungarian chemist Georg de Hevesy—considered as the father of nuclear medicine and awarded the Nobel Prize for Chemistry in 1943—first proposed the use of radioactive isotopes as tracers [54] to study chemical processes (*e.g.* the metabolism of animals).

The limits of X-rays were noted by Hounsfield in his Nobel lecture [55]: "[...] it is impossible to display within the framework of a two-dimensional X-ray picture all the information contained in the three-dimensional scene under view. Objects situated in depth *i.e.*, in the third dimension, superimpose, causing confusion to the viewer". Tomography was needed to retrieve the depth information. It consists of defining a planar slice of the body through which X-rays are passed only in directions that are contained within, and are parallel to, the plane of the slice. As such, no part of the body that is outside of the slice is interrogated by the X-ray beam, and this eliminates the problem of "depth scrambling" [56].

Computed tomography (CT) introduced a way of exploiting the huge amount of information contained in radiographic data so as to obtain a three-dimensional image of the human body while benefiting from "its enormously greater sensitivity" [57]. Volumetric medical imaging was born[3]. CT now provides anatomical and physiological information at

[3]Chronologically, Cormack proposed an inversion algorithm for computed tomography in 1963 and its

a macroscopic spatial resolution [58], hence giving a better insight into the pathogenesis of the body.

This was followed by the invention of positron-emission tomography (PET) in the mid-1970s with a first PET scan developed by [59]. PET imaging[4] is now particularly involved in studies of regional cerebral activation based on blood flow measurements. However, the risks due to radiation exposure in both PET and CT scans are non-negligible and have been discussed respectively in [60] and [61] respectively.

Around the same time, magnetic resonance imaging (MRI) was invented in 1971 by Lauterbur. It is now a routine clinical imaging device due to improvements in image quality and speed, new acquisition and reconstruction techniques, higher fields etc.

2.2 Trends and perspectives

According to Gore [10], macroscopic features of human anatomy have, to a great extent, been recorded and progress is now centred in the development, evolution, and function of those features. The goal of medical imaging could be less about improving image quality but rather to get a better understanding of what affects the signals used to construct images. Indeed, most modalities seem to be reaching practical limits on spatial resolution: the speed of acquisitions may increase but sensitivity for detecting pathologies is limited by radiation dose in *e.g.*, PET and CT or other safety requirements (like heating from absorbed RF energy).

Such considerations would help interpret images better and derive more information. Specifically, for each biological event associated with many pathological disorders, there is still no contrast mechanism that allows imaging to be a full substitute for histology: in many cases, multiple pathologies share a common imaging phenotype, making it impossible to differentiate them using imaging alone. By combining medical imaging with digital pathology, it should be possible to simultaneously obtain both the rich structural information of the former and the chemical or cellular information of the latter. This could allow, for example, for a more complete characterisation of disease.

---

experimental demonstration was done by Hounsfield in 1973. Cormack and Hounsfield shared the Nobel Prize in Physiology or Medicine in 1979. Oldendorf is also often cited for having published the first laboratory X-ray CT images in 1961.

[4] It is the invention of the γ-camera by Hal Anger in 1957 that truly marked the beginning of the era of nuclear medicine imaging: γ-cameras capture emitted radiation from internal radioisotopes.

2.3 From fresh tissue to digital pathology

A pathologist receiving fresh tissue has three options: keeping it fresh, stabilising it in a fixative, or freezing it. Biological tissue is too soft for direct sectioning (although a vibrating blade might work), so it is most commonly either embedded in a hardening material and sectioned using a microtome, or frozen and sectioned in a cryostat (a microtome inside a freezer). Sections are then mounted on glass slides and stained before being observed under the microscope by the histopathologist, and/or digitised using flatbed scanners [62] for image processing and analysis.

In the remaining of this chapter, I first describe the two most common processes to obtain sections, namely formalin-fixed paraffin-embedded (FFPE) sections (§2.3.1)—henceforth also referred to as paraffin sections—and frozen sections (§2.3.2). Further details can be found in [63]. Then, I briefly present several types of microscopy examinations and the process of digitisation (§2.3.3). Finally, I highlight the most common artefacts for both types of sections (§2.4) and the image processing methods developed to account for some of them (§2.5).

2.3.1 Paraffin sections

FFPE tissue sections with hematoxylin and eosin (H&E) stain are the gold standard [64] in histopathology: they provide with generic information in very little time and cost [65]. Their widespread use also relates to the familiarity histopathologists have with the method: the *artefact*[5] it produces at any stage during tissue handling and processing is recognisable and well-documented. In contrast, observing new patterns with other dyes requires time and training [63]. Knowledge of the steps relative to tissue preparation and diverse staining patterns is not only essential for diagnosis and risk assessment—and this is still an active area of research [67]—but also for all subsequent image analysis steps. In the following, I briefly describe the different stages of FFPE sections preparation.

Fixation It is the most important step when performing histological specimen preparation [68]. Fixation is critical for several reasons: (i) it prevents the tissue from autolysis; (ii) it keeps the tissue close to its living state, without loss of arrangement; (iii) it minimises changes in shape or volume in subsequent procedures and (iv) it yields clear staining of sec-

[5] *Artefact* is to be taken here in the sense that it refers to an *altered* state of the tissue and its structures (relatively to its living state) *i.e.*, the structures it exhibits are not naturally present in the living state of the tissue but are rather the product of a series of preparation steps (see also [66]). Throughout the rest of the thesis, the definition of artefact is narrowed down to (image) degradations.

tions. Formaldehydes, such as formalin—which is the most common of all—are routinely used for chemical fixation, such as in [69, 70, 71, 72, 73, 74]. Among others, glutaraldehydes may be used [75].

Tissue processing Since most fixatives are water-based and thus not miscible with wax, the tissue must be processed to enable impregnation. This process follows three steps. (i) *Dehydration*: it removes water by immersion in gradients of alcohol. (ii) *Clearing*: it replaces the dehydrating fluid with a wax solvent (the wax solvent has the effect of raising the refractive index of the tissue, making it appear clear, hence the name). Note that long-term clearing creates distortions. Xylene is routinely used for short schedules and blocks less than $4mm$-thick. Among others, toluene is also used and has similar properties. (iii) *Impregnation*: it replaces the clearing agent with the embedding medium.

Embedding The specimen infiltrated with wax is put in a mould covered with liquefied wax and topped with a cassette. The specimen should lay flat at the bottom of the mould as its orientation conditions the plane of sectioning (an important consideration when flatness is assumed for the comparison with clinical imaging). The ensemble then cools on a cold plate and makes a solid block for microtomy (blocks may also be stored at room temperature for decades, which forms an important archive in retrospective analyses). Paraffin was used for example, in [76, 77, 78, 79, 80]. Celloidin, more difficult to remove, was used in [81, 82, 83].

Cutting (or microtomy) It is performed with a microtome, to which the cassette with the wax-embedded tissue block is clamped. It begins with "trimming", which consists of removing the surplus of wax until a full section of tissue is available. It requires great care since tissue of diagnostic importance may be removed or the block surface damaged. Cutting is then processed at a certain thickness and the quality of the resulting sections depends upon several factors such as the knife angle, blade quality, speed of sectioning etc., as well as all the previous preparation steps. Thin sections ($1-20\mu m$) were cut in [84, 85, 86]. Thick sections ($> 20\mu m$) were cut in [87, 88, 89, 90].

Floating, drying The thin sections are picked up from the microtome and put in a flotation bath, filled with warm water in order to flatten. Then, they are collected on a glass slide and dried.

Staining, cover-slipping It is the process of colouring and differentiating certain structures in the tissue. H&E stain is the most common stain in histopathology laboratories. It was

used for instance in [91, 92, 93, 94, 95, 96, 97]. H&E method shows a wide range of normal and abnormal cell and tissue components and is easy to perform using either paraffin or frozen sections. Other popular stains include Cresyl violet (Nissl staining), as used in [98, 99, 100, 101, 102, 103], and methylene blue [104] for nervous tissue sections, silver and gold methods to demonstrate *e.g.*, cell processes in neurones, toluidine blue [105] to stain acidic components, Masson's trichrome [106] to stain connective tissue and Alcian blue [107] to stain certain types of mucin. If immunohistochemical staining is to be performed, it requires antigen retrieval (heat- or enzyme-enduced) due to loss of antigenicity during fixation [108]. Immunohistochemistry (IHC) was performed in [109, 110].

After the slice has been stained, it is cover-slipped: a smaller sheet of glass covers the tissue mounted on the glass slide. This creates even thickness for viewing and prevents the microscope lens from touching the tissue. The slide can then be observed under the microscope and/or digitised.

2.3.2 Frozen sections

Frozen sections are quicker to produce than paraffin sections but it is a very demanding process: good section quality (in terms of preservation of tissue morphology) is achieved through great care and expertise [111]. Although there are conflicting reports about how much freezing may degrade cell morphology and reduce the readability of histological specimens, rapid freezing is known for limiting ice crystal formation and minimising morphological damage. Among disadvantages, it is harder to make the tissue lay flat; frozen sections are also more difficult to cut than paraffin sections and inconvenient to store. The main advantages of using them are the shortcuts in the process (*e.g.*, no dehydration is needed), and their better preservation of antigens for immunohistochemistry. They were used in [112, 113, 13, 114, 115, 116, 117]. The different stages of frozen sections preparation consist of:

Cryo-protection/embedding The limiting factor involved in cryosectioning is the cutting consistency of the block and the freezing damages from ice crystals. Thus, the tissue may require cryoprotection to make it less brittle [118]. Cryoprotecting the tissue is not necessary and consists of fixation (formaldehyde), rinsing and infiltration in increasing series of sucrose solutions. The addition of sucrose provides a smoother cutting block and minimises freezing artefacts. It also happens that sections are prepared from fresh, rapid-frozen tissue but cutting can be incredibly hard without any fixation. Then, optimal cutting temperature

(OCT) compound is used to embed the tissue prior to frozen sectioning. OCT helps conduct heat away from the specimen during freezing, protects the tissue from drying during storage, and supports the tissue during sectioning.

Rapid freezing (or flash/snap freezing) Once embedded in a particular orientation *e.g.*, face-up, the tissue sample needs to be rapidly frozen to minimise freezing artefacts resulting from ice crystal formation as water freezes in the tissue [119]. One method is to use dry ice (-70° Celsius) on its own. It is simple and safe but creates freezing artefacts that break cell membranes. An alternative is the immersion of the sample in a freezing medium, like a mixture of dry ice and 2-methyl butane (isopentane), which achieves very rapid freezing. Note that direct freezing would cause the tissues or blocks to crack, which would make them very difficult to cut. Tissues with fat often produce poor quality sections since fat freezes at lower temperatures and thus remains too soft to cut; further decreasing temperature may weaken the sample and cause cracks. Tissues with substantial water content, such as the brain, often yield ice crystals during the freezing in the cryostat and result in *e.g.*, non-representative architecture of tumour growth or inflammatory infiltrate [120]. Snap freezing with liquid nitrogen is often employed to mitigate these artefacts. The frozen tissue can then be stored in a -80° Celsius freezer for future cutting.

Cutting This is similar to paraffin-embedded sections except it is performed in a cryostat. It also starts with trimming of the block. Frozen sections are usually cut between 3-10μm thick (5μm thick sections provide adequate morphology). Ultra-thin sections ($< 1\mu m$) were cut in [23] ($0.25\mu m$). Thin sections ($1 - 20\mu m$) were cut in [62, 121]. Thick sections ($> 20\mu m$) were cut in [115, 1].

Retrieving, drying Retrieving is the process of picking up the cut frozen section and putting it on a glass microscope slide. Tissue sections can be either picked up from the cryostat stage or from the block directly. From the time the tissue section touches a warm slide, it starts to develop a drying artefact. Air drying frozen section slides will however allow the sections to better adhere to the slide as complex staining procedures cause greater tendency for the tissue to come off the slide during staining.

Fixation Sections of fresh frozen tissue should be fixed immediately unless they are going to be stored for future study. A standard histology fixative: 4% neutral buffered formalin, is the most suitable fixative for frozen sections. Sections of fresh frozen tissue will rapidly dry if exposed to warm air, and this will result in cellular artefact.

Staining Slides prepared by frozen section technique can be successfully stained by many of the staining procedures used for routine paraffin embedded tissues. For example Nissl-stained sections were used in [23, 122, 62] and H&E stained sections were used in [121]. Frozen sections are usually preferred for immunohistochemical staining due preserved antigenicity. This a specific type of stain, in which a primary antibody is used to bind specifically to a particular protein for the purpose of detecting and measuring it. Then, a secondary antibody (which carries a colorimetric or fluorescent detection tag) is used to bind to the primary antibody and reveal its bounding location. IHC was performed in [123, 113, 124, 125].

2.3.3 Microscopy and digitisation

Major types of light (or optical) microscopy include brightfield [126], phase contrast, fluorescence [117] and confocal [127]. Electron microscopy encompasses transmission electron microscopy [128] and scanning electron microscopy, the latter being mainly used in the context of serial blockface imaging [129, 130]. The preparation of tissue specimens for light microscopy follows the steps from §2.3.1 and 2.3.2. The preparation of tissues for transmission electron microscopy is described in [131].

As for immunocytochemistry and immunohistochemistry [122], the reaction of antibody with antigen in can be examined and photographed with a fluorescence microscope. Histochemical and cytochemical procedures (based on *e.g.*, specific binding of a dye, a fluorescent dye-labelled antibody or enzymatic activity), can be used with both light microscopic and electron microscopic preparations. Light and electron microscopes produce high resolution micrographs (orders of magnitude of $0.1\mu m$ and $1nm$ respectively).

Autoradiography—or to be rigorous radioautography [132], can be observed with both light and transmission electron microscopes and reflects the rate of the energy consumption required to support cellular activity. It is quantified using tracers of glucose metabolism incorporated by living cells and tissues. They generate a labelled product allowing for example, to measure circulating glucose in the blood or radioactivity concentrations. The specimen is then killed and a sample is processed for histology and sectioned. Sections are placed against an X-ray film to produce autoradiographs. The exact 3D localisation of the radiation source is however unknown and thus requires the reconstruction of autoradiographic volumes [133]. Reconstruction is also a pre-requisite for comparison against other three-dimensional modalities such as functional imaging.

Although in the context of multimodal image registration, computer scientists usually

work with histological images at low resolution, similar to that of a clinical image—most high-resolution details in histology are biological noise for the purpose of registration—digital pathology should allow the histopathologist to scroll through any level of details of a "virtual" microscopic slide for its examination at any time and anywhere (*i.e.* not under a microscope), should it be on its own, against another histological section or a 3D medical image plane. This process of digitisation is fundamental [134] and brings together the fields of virtual microscopy, digital whole slide imaging and telepathology [135].

2.4 Artefacts

In histology, an artefact is the result of the alteration of a tissue from its living state, caused by the very process of dying and the histological preparation. Artefacts affect different structures from one same tissue section independently, and one *same* structure in adjacent tissue sections differently. Artefacts may compromise both image analysis for accurate diagnosis and image registration for precise alignment. One challenge is to be able to identify artefacts and not confuse them with normal tissue components or pathological changes. This means understanding the causes of such deteriorations as well as their expression in order to provide relevant corrections. Whether paraffin or frozen sections are used, some artefacts have similar characteristics despite having different causes. This makes some preprocessing methods applicable to both types of sections. An exhaustive list of artefacts encountered in paraffin sections, along with ways to minimise them is available in [136] and the most common ones are:

Loss of detail In paraffin sections, delayed fixation may cause poorly defined nuclei and imprecise cytoplasmic details. Improper draining of sections before drying may lead to out-of-focus areas, and imperfect dehydration before clearing, which leaves small water droplets in the tissue, may cause opaque areas. Similarly for frozen sections, drying (which starts as soon as the tissue is in contact with a warm glass slide) may blur nuclear details and cytoplasmic borders (due to the leakage of fluids from the cytoplasm), and a loss of contrast. Drying artefacts are described as cells melting and spreading on the slide by Peters [119].

Changes in morphology In paraffin sections, the use of an overheated forceps (beyond the melting point of wax) can cause local heat damage and changes in morphology of structures in the area surrounding the contact point. In frozen sections, drying may cause enlargement of cells and nuclei.

Uneven staining In paraffin sections, it may come from incomplete fixation of the specimen (which leads to zonal fixation), incomplete slide dewaxing (which results in slides containing patches of residual wax and produces unstained, or unevenly stained areas) and excessive heat in the slide drier. Approximate timing as well as different storage conditions also produce inconsistent results across sections. Poor quality formalin results in a "formalin pigment" formation in sections by reaction with haemoglobin, leading to unwanted colouration. As for frozen sections, issues may arise due to over-agitation of loosely adherent tissue in the staining solution.

Folds and wrinkles In paraffin sections, they may be due to poor fixation and/or processing, too large a clearance angle of the microtome, too thin sections, low temperature of the flotation bath (which may not allow sections to flatten properly) or mechanical damages (when attempting to remove a fold in the section with a brush). As for frozen sections, the tissue can fold, stretch or tear if one is too rough during retrieving.

Cracks and holes In paraffin sections, they may happen due to over-processing (which makes the tissue very brittle), under-processing (which makes the tissue poorly supported and therefore fragmented), flotation on a water bath that is too warm, prolonged drying at too high a temperature, too quick sectioning, insufficient clearance angle or a damaged cutting blade during microtomy. As for frozen sections, freezing blocks (instead of cooling them down) can make them crack during cutting. Another challenge is faced with large blocks of tissue, such as whole organs: liquid nitrogen will freeze faster and create a shell around the exterior of the tissue. Then, the organ is likely to crack when the interior expands due to slower freezing.

Contaminants In paraffin sections, this may happen when the water from the flotation bath is not replaced regularly, which favours contaminants that may end up on the slide under the section. Dust, organisms and other contaminants on the glass slide can also spoil otherwise good sections.

Compression and distortion In paraffin sections, they may be due to under-processing (which results in the shrinkage of the specimen); inappropriate size of the container compared to the size of the specimen (which means using an insufficient amount of fixative or squashing the specimen inside); rough handling; poor quality embedding wax (which produces blocks that are difficult to cut); suboptimal knife tilt angle during microtomy and wrong blade type; delay before cutting the final sections of a block (which makes the block

warmer); and overheated flotation bath and sections left too long in it (which cause over-expansion). It is also important to be aware that paraffin sections are unlikely to be of even thickness as the first couple of sections are the widest (due to the thermal expansion of the block during the first passes across the knife) and the least compressed; however as the block warms the sections get narrower and more compressed. As for frozen sections, compression and distortion will most likely result from ice crystal formation—the more water a tissue contains, the more chances artefacts will occur. As water freezes, the expansion of ice crystals compresses cellular tissues (compression artefacts) and distort histopathological correlations. They usually have the appearance of bubbles (ice crystals "bubbles" artefacts). The knife used in cryosectioning can also create cutting artefacts (shearing of the tissue).

In the end, artefacts are unavoidable but also surmountable as pathologists learn to read around them. However, it is very important to try to minimise their impact on subsequent steps, which heavily rely on the tissue quality: for example, sections with cracks and holes often have to be manually discarded because they cannot be registered. Artefacts hamper image computing methods by reducing comparability between supposedly similar structures within or across modalities. For this reason, preprocessing methods to account for their presence in images have been developed.

2.5 Preprocessing of digital pathology

Among the artefacts resulting from histological preparation, loss of detail and changes in morphology burden image analysis. Not much can be done about them as content is hardly retrievable from lost or corrupted information without any prior knowledge. When due to scanning, though (local poor focusing can cause blurred regions in images), loss of detail is surmountable but at the cost of time-consuming review by the scanner operator. In the context of whole slide imaging, Lopez *et al.* [137] automatically identified tiles that required additional focus points. Specifically, they compared the ability of several features in discriminating between blurred and sharp regions of images and showed that the Haralick contrasts and gradient-based features best performed at this task. Compression and distortion are usually taken care of by the process of registration. Regarding other artefacts such as: inhomogeneous intensity distributions within and across slices; folding and crumpling; cracks and holes, dedicated preprocessing methods are presented in the following paragraphs.

Inhomogeneous slices appearance Ideally, the absolute colour of a slide reveals the biological component that a pathologist wishes to retrieve. For example, in the case of H&E, the colour value quantifies the amount of nucleic acids (blue-purple) hematoxylin has bound to, and the amount of proteins (in pink) Eosin has bound to. However, for the reasons listed in §2.4—and/or because of the microscope and the camera used for imaging [138]—slides exhibit different colours. Improved feature classification, segmentation and visualisation require the reduction of these variations as well as some sort of standardisation of the imaging protocols [139]. This calls for transforming the appearance of a source image into that of a target image preferred by an expert.

In general, histology reconstruction methods use greyscale images for intensity standardisation (or the channel that provides the best contrast in an RGB image). Most techniques are based on histogram matching [140]. One representative method, used for example in [122] and [141], was proposed in [142]. Using Parzen windowing, continuous probability density functions from the discrete intensity histograms of two input slices were first computed—a Gaussian kernel was also used in [143] and [144]. Then, Malandain *et al.* estimated the optimal affine intensity transformation between them (though higher order polynomial fits may be used). This type of method can be applied in different ways and the reference slice is usually picked for its relative smooth intensity variation of staining and high-contrasted structures [145, 69]. In [98], the parameters of a global affine intensity transformation were optimised using white and grey matter masked images jointly. The central slice was taken as reference. In [99], histogram equalisation was used, in which case a flat histogram is implicitly used as reference for matching. Equalisation is however not robust because it is very sensitive to outliers (the extremal values of the intensity spectrum) [142].

Attempts at decreasing the bias introduced by selecting a single reference slice have been proposed: Li *et al.* [81] applied to each slice a transformation that was a weighted sum of transformations from that slice to a set of reference slices (experimentally, one slice every 30 slices). Weights were based on its distance to the corresponding references. Chakravarty *et al.* [146] used least trimmed square (LTS) to calculate the coefficients of two polynomials of order three that map the intensities of the current slice to the previous and the next one. The coefficients of the two polynomials were then averaged and applied to the single slice. Chakravarty extended this work in [102] by adding an extra step that accounted for local

variations: the same averaging process (though restricted to linear mapping) was applied to patches of every slice. This approach however depends on where it starts in the stack.

Should it be using a single, a set of, or an average reference distribution, normalisation always depends on the set of available histological slices. Hence, the purpose of standardising slices appearance is, in general, more to bring visual consistency and help with subsequent segmentation and classification tasks, than being representative of tissue behaviours relative to staining.

The idea of computing a standard histogram allows for a standardisation that is not "stack-specific". This was proposed in [147] within the context of clinical imaging, where a standard histogram was computed from a training dataset made of images coming from several acquisition protocols. A similar principle was used in [148]. The method developed in [149] followed the same effort, although standard values of each class of tissues had to be user-defined.

Within the field of histopathological image analysis, the importance of the consistency of *colour* has long been known and is an active research topic: computational methods, referred to as **colour normalisation**, have been developed to cope with inter-slice colour variations. Two ways of addressing the problem stand out: (i) *colour modification* methods represent the mathematical transformations applied to the source images to match the characteristics of a target image—they are similar to previously described intensity standardisation methods for grey-scale images. Colour modification was introduced by Shirley in [150], who proposed to match the colour distribution of one image to that of a reference image by use of a linear transform in Lab colour space (a more perceptual colour model than RGB) so as to match the means and standard deviations of each colour channel in the two images in that colour space. This was applied to histological data in [151]. In order to account for scanner-induced variations, [152] proposed to use a colour-calibration slide made in-house to derive a colour correction matrix. Bautista *et al.* [153] showed that it is possible to achieve consistent and accurate segmentations with simple classifiers by accounting for the staining conditions of the slides using dye amount tables. Within the (multi-modal) histology reconstruction literature, Braumann *et al.* [154] used them and linearly transformed the three RGB colour channels of every image to match the histogram statistics (*i.e.*, mean and standard deviation) of a manually selected reference slice. (ii) *Colour separation* (or deconvolution) methods, concerned with first extracting the main components

(*i.e.*, the stains) constituting the original image (relying on the manual delineation of regions of interest, non-negative matrix factorizations, plane fitting in the optical density domain or other colour models), then normalising them individually and finally recombining them, such as in [155, 156, 157, 158, 159, 160]. These methods apply to sections stained with more than one dye, mostly H&E stained images, and are still actively developed.

Folds They are defined as regions containing multiple layers of stained tissue. This results in regions with higher saturation and lower luminance. As such, Kothari *et al.* [161] used the difference between colour saturation and luminance to detect them. They developed a model that adaptively finds the difference-value range of tissue folds in order to account for the high variability of colour saturation and intensity in different slides. Bautista *et al.* [162] enhanced folds and limited the changes in hue by using the difference value between saturation and luminance as a shifting factor for pixel values. Palokangas *et al.* [163] used k-means clustering on HSI (Hue, Saturation, Intensity)-transformed images (although only saturation and intensity components were said to be discriminative enough). However, such clustering assumes that there are always folds in the images and the method relies on careful initialisation of cluster centres. Simple thresholds are said to be less effective because a tissue fold in a lightly stained image can look similar to *e.g.*, a tumour in a darkly stained image [161, 163]. Similarly to intensity/colour normalisation, fold detection and masking were shown to improve subsequent feature extraction and classification tasks.

The correction of folds may be one of the most difficult problem to solve here, mainly because of the interference of constituents caused by the overlap of different parts of the tissue. Although modelling of developable surfaces has been proposed in computer graphics [164], the reconstruction of unfolded tissue section is difficult as it supposes the separation of structures belonging to different overlapping bits of the tissue section—the number of folded layers is also unknown *a priori*.

Tears (or cracks) and holes Such artefacts are more frequently addressed than folds but their correction remains sparse. Cracks require, in general, manual delineation of the torn area [79] as it is challenging to automatically tell whether a piece of tissue is missing or if the tissue has effectively opened up without loss of material. Yang *et al.* [99] filled up the missing sections and missing parts and corrected folds using a procedure described in [165]. Choe *et al.* [114] proceeded with manual contouring of the torn area and filled it by repeating pixel values of the contour along the columns of that region. Such a process

however makes a strong assumption about the horizontality of tears. A similar protocol was followed in [166]. Breen *et al.* [167] used correspondences between landmarks to stitch the torn piece back: a first thin-plate splines (TPS) warping [168] was performed between histology and blockface photograph using manually defined sets of corresponding landmark points. Then, another set of landmarks was found at the borders of the torn piece of tissue in histology and in the intact corresponding piece of the blockface photo (both were overlaid to ease the process). Finally, a separate TPS warping was applied to register the torn piece of tissue back. Correspondences between sets of landmarks were found using the "live-wire" algorithm developed by [169, 170]. One could also approach the problem of tear correction as jigsaw puzzle solving [171, 172], although it has failed in [173] because these methods rely on borders and medical images usually have low signal and distortions at their boundaries. The tearing/cracking of thin sheets has been subject to extensive studies within the fields of statistical physics [174] or computer vision [175].

Masking In order to discard various contaminants in the background or edges of the glass slide, which could have an influence in subsequent registration steps, tissue is usually separated from the background. Thresholding is widely used [176, 1, 177, 178, 115, 179, 113] and it is usually complemented by mathematical morphology operations [142, 178, 115]. Dubois *et al.* [62] used iterative Gaussian smoothing of histograms for automatic threshold computation: following [180], they tracked the positions of modes in the scale-space and the two modes that remained across most scales were picked as those representing background and tissue. Region growing was then applied in the histogram using previously computed upper and lower bounds. Masking was preformed with mathematical morphology (successive erosions using *a priori* knowledge of the tissue surface) and the largest connected component was extracted. Yushkevich *et al.* [23] used active contour segmentation with region competition [181] followed by mathematical morphology to refine the masks: opening (which is less destructive than erosion alone but still removes isolated pixels) was performed and the largest connected component was kept as final mask. Level-sets were used with a dynamic speed function in [81], and in [182] (based on [183]). They incorporated higher level constraints obtained from prior knowledge and understanding of mouse brain anatomy. Palm *et al.* [115] used k-means clustering on the "a" channel, after transformation from RGB to CIELab colour space, to segment tissue in blockface photographs. This was followed by a hole-filling algorithm. Adler *et al.* [98] used Atropo [184], an n-class

Markov random field segmentation software package for tissue foreground segmentation. They used three labels: grey matter, white matter and background—grey matter and white matter labels were united into foreground tissue mask, from which the largest connected component was retained.

Vignetting (or shading) A common problem irrespective of the type of camera and method of microscope attachment is uneven illumination at the edges of the image [185]. In general, it occurs in most imaging sensors due to an uneven illumination of the scene being imaged. As a consequence, images are usually lighter near the optical centre and darker at image borders (*i.e.*, a shading artefact). This effect is particularly evident when stitching images into a mosaic in order to increase the field of view of the microscope to obtain *e.g.*, whole-slide images. Correction of uneven illumination in histological slices has borrowed ideas from intensity inhomogeneity correction in MRI [186, 187]. The correction of vignetting was addressed in [188, 189] and the interested reader may also refer to [190, 191]. In the (multi-modal) histology reconstruction literature, shading correction was performed as preprocessing in [71] using methods from [192]. Arganda-Carreras *et al.* [95] developed a background correction algorithm based on a phantom [193] that was used to correct the mosaic-like effect of the images caused by uneven illumination of the field of view of the microscope. Methods for compensation of such a light variability were also applied in [109], further described in [194]. Colour difference and optical degradation were accounted for in [195], by means of a Gaussian-like model and a wavelet-based image blending.

Stitching (or mosaicing) It is needed when the field of view of the classical microscope is too narrow to allow for the visualisation of the entire tissue. The section can either be physically cut into several pieces that are isolated in the image (see [196], or [96], who simulated it), or spatial tiles can be obtained by moving the microscope stage [109]. The latter protocol however introduces overlapping between adjacent fields of view. Overlap is recommended to account for field curvature-induced artefacts in the image and avoid loss of detail at the edges between images; in [197] 10% overlap in the translation step distance was included. Spatial rearrangement of the pieces relatively to each other is required in both situations to recover an image of the full tissue section for subsequent volume reconstruction or registration with other modalities. This is usually performed through image registration. In [109], stitching was performed by first positioning the tiles using landmark points, and then optimising a similarity measure in the parameter space of translations using n-step

search [198]. This method was implemented in GlueMRC [199]. In [195], mosaicing was solved by matching features detected in adjacent histological tiles. Those were extracted using wavelet-based edge correlation and pairs of corresponding features were then identified by maximisation of the normalised correlation coefficient. In [200], mosaicing of ssTEM images was addressed using previous work [201] and SIFT features.

There exist several softwares that automatically perform the task [202]: in ImageJ, the Stitching[6] plug-in [203]; Autostitch[7] [204]; MosaicJ[8] [205]; XuvTools[9] [206]; HistoStitcher and AutoStitcher[10] [196, 207]. Only a few studies, such as [208] using Autostitch, have been accounting for vignetting [202]. Piccinini *et al.* [202] developed MicroMos[11] and ensured their tiles had all been flat-field corrected prior to stitching them back together.

An automatic mosaic acquisition and processing system for multiphoton microscopy was described in [209], along with the importance of normalisation to avoid shading artefacts at the border of tiles. Methods that extend the tiles beyond their boundaries by propagating available structures were also developed in [210] and [173]. Stitching is extensively studied in the general computer vision literature [204].

[6] http://imagej.net/Image_Stitching
[7] http://www.autostitch.net/
[8] http://bigwww.epfl.ch/thevenaz/mosaicj/
[9] http://www.xuvtools.org/doku.php
[10] http://engineering.case.edu/centers/ccipd/content/software
[11] https://sourceforge.net/projects/micromos/

Chapter 3

Surveying Histology Reconstruction

3.1 3D histology reconstruction

Histology reconstruction methods aim to restore the loss of continuity due to volume slicing. They are based on the fact that the shape of a biological specimen changes smoothly across sections, but suffers from various artefacts that affect every section independently during its preparation. When using histology alone, reconstruction algorithms provide representations of structures and their environment in three dimensions—which helps with subsequent segmentation and classification tasks [237]—but one needs to bear in mind that

Table 3.1: Company/academic softwares and plugins for histology reconstruction from serial sections and their use in the literature.

softwares/plugins	institution	non-rigid warping	references	used in
TrakEM2 (ImageJ)	Uni of Zürich (CHE)	no	[211]	[212]
StackReg (ImageJ)	EPFL (CHE)	no	[213]	[214]
AutoAligner	Bitplane (CHE)	no	-	[215]
Voloom	TU München (DEU)	yes	[216]	[217]
BrainView	LIN (DEU)	yes	[218]	[62]
Free-D	INRA (FRA)	yes	[219]	[220]
BrainVISA	CEA I^2BM (FRA)	yes	[221]	[62]
AlignSlices (Amira)	FEI VSG (FRA)	no	-	[222, 223]
3DHISTECH	(HUN)	-	-	[224]
poSSum	Nencki Institute (POL)	yes	[225]	[225]
ImageRegistration (ImageJ)	NTUST (TWN)	yes	[126]	[126]
BioVis3D	(URY)	-	-	[226]
HistoloZee	UPenn (USA)	yes	[98]	[227]
Protomo	Florida SU (USA)	no	[228]	[229]
Reconstruct	Boston Uni (USA)	yes	[230]	[231]
IMOD	Uni of Colorado (USA)	yes	[232]	[233]
ImageJ	NIH (USA)	no	[234]	[91]
NIH Image	NIH (USA)	no	[235]	[236]

the original shape is unattainable without prior or external knowledge.

Reconstruction algorithms from serial histological slices rely on image registration and consist of optimising the spatial alignment of variously oriented 2D slices relative to each other, while being robust to artefacts following histological preparation. The most straightforward way is to register every slice with its direct neighbour and repeat the process with the following pairs, but this is not robust to errors. First efforts towards the reconstruction and visualisation of volumes from 2D sections relied on this technique and were initiated in the early 1970s [50, 51]. A list of company/academic softwares and plugins for histology reconstruction from serial sections is available in Table 3.1.

Registration is the process of bringing two images (one usually referred to as "reference, fixed or target" and the other as "floating, moving or source") into spatial alignment and deforming the floating image such that it looks like the reference image (for transformations others than rigid-body). The objective is to estimate the transformation that optimises an energy function. It is usually made of two terms, one referred to as the matching criterion (a distance measure, in a broad sense) and a regulariser, either implicit (by restricting the type of transformation) or explicit (e.g., deformation field filtering, penalty terms, etc.), which controls the transformation and prevents excessive or unrealistic deformations. This definition holds for the rest of the paper. Further details can be found in reviews about (medical) image registration [238, 239, 240, 241] and a report was recently presented in [242] to assess whether the goals of the field were met. A list of open-source toolkits for medical image registration is available in Table 3.2.

Histology reconstruction is obtained by the composition of every single pairwise transformation with respect to a certain reference. The quality of the resulting volume highly depends upon the choice of that reference slice. It is usually an arbitrary choice made by an expert, who selects a slice that exhibits little deformations, few artefacts and high contrast. Although the first slice [177, 243] is sometimes chosen as reference [70, 244], it may be preferable to select it around the centre of the stack [245, 246, 24]. This minimises the propagation of errors due to slight misalignments (let aside registration failures), which may produce skewed or helicoidal stacks. It seems that only Bagci *et al.* [148] proposed to automate the process of selecting the *best* reference slice by considering the information content in feature space.

Without any information about the true shape, volume reconstruction remains an ill-posed problem *i.e.*, although there exists a solution, it is not unique (and the *true* one is unknown); for example, changing the initial arrangement of slices relative to one another will lead to a different reconstruction. Whichever way it is addressed, the process tends to straighten up structures: a banana-like original volume, cut and reconstructed, will end up looking like an ellipsoid—hence its name, the "banana effect" or "z-shift" effect [1].

Some works tried to bypass registration failures through graph theoretic approaches [23, 98, 247], which formulate the reconstruction problem as a shortest path problem in order to identify the best sequence of transformations. Alternatively, most recent works commonly proceed by aligning every slice with a set of neighbouring slices (as opposed to considering only one neighbour) in order to smooth out potential errors and improve continuity [248, 249, 200, 216, 176].

I classify works aiming to reconstruct volumes based on the registration method they used. This yields two categories: registration using geometric features (§3.1.1) and registration using voxel comparison (§3.1.2). While the former may be fast (because it uses a subset rather than the whole image domain), the latter is more accurate but slower and requires careful initialisation as methods tend to settle in local optima.

3.1.1 Geometric methods (landmark-based)

Geometric methods aim to register two images by minimising a criterion that takes into account landmark information. The first step in geometric registration is to obtain points of interest (§3.1.1.1). Those are usually noticeable locations in the image, under the assumption that saliency at the image level is equivalent to relevant anatomical regions. After finding correspondences between landmarks, a smooth transformation is sought so that their alignment is respected (§3.1.1.2). Further details can be found in [241].

3.1.1.1 Detecting points of interest

Processing histological images is complex when it comes to using points of interest: the appearance of slices vary greatly and even adjacent sections expose *similar* rather than the *same* constituents. Consequently, their description should be flexible enough to grant matching, while peculiar enough to disambiguate between close potential candidates. Besides, the very task of locating reliable landmarks remains an open problem, and it is still

Table 3.2: List of open-source registration toolkits/softwares used for histology reconstruction (L and NL stand for linear and non-linear registrations respectively).

softwares/packages/plugins	institution	type of transformation(s)	references	used in
ANIMAL	McGill (CAN)	NL	[250, 251]	[102]
TurboReg (ImageJ)	EPFL (CHE)	L	[213]	[252]
UnwarpJ (ImageJ)	EPFL (CHE)	NL	[253]	[127]
MERIT (MeVisLab)	Fraunhofer MEVIS (DEU)	L/NL	[254]	[255]
bUnwarpJ (ImageJ)	UAM (ESP)	NL	[256]	[166]
Elastix	UMC Utrecht (NDL)	NL	[257]	[77, 113]
NiftyReg	UCL (UK)	L/NL	[258, 259]	[247]
VTK CISG	KCL (UK)	L/NL	[260]	[261]
AIR	USC (USA)	L/NL	[262, 263]	[264, 83]
ITK	NLM (USA)	L/NL	[265]	[266, 267]
ANTs	UPenn (USA)	NL	[268]	[98]
DRAMMS	UPenn (USA)	NL	[96]	[96]

an active area of research [241]. In this section, I use interchangeably the terms landmark, keypoint and point of interest. Points of interest fall into three categories: manually extracted landmarks, needle tracks, and automatically extracted landmarks.

Manual landmark selection It is usually carried out by experienced histopathologists and benefits from the rich details that high resolution histological images provide. The main advantage of manual selection is that it allows for accurate, consistent selection of anatomically relevant landmarks. The task is however very time-consuming and subject to inter- and intra-user variability, and was for example performed in [269]. In [270] contours of the autoradiographs were manually segmented, which is a special case of landmark extraction as points may be sampled along those contours or curves used as such for boundary matching.

Needle tracks Needles can either be inserted in the fresh tissue, or in the embedding medium by placing ink marks [271]. The marks can then be manually or automatically isolated, such as in [243] who identified centres of labelled needles tracks using Hough transform. Although the technique is known to be invasive, recent advances allow to minimise damages to the tissue [272]

Automatically extracted landmarks Within the context of histology, we identified three main types of features associated with automated methods to extract and describe them,

namely Fourier-based, blob-like and object-level features.

Fourier-based features Such features relate to edges extracted via harmonic analysis. Hsu [273] adapted a method introduced earlier in the context of mosaicing [195] to histology reconstruction, also based on [274]. The detection of edges was handled by wavelet transforms. The robustness to noise was achieved using edge correlation, as introduced in [275]. Reliability of feature points was increased by means of multiscale edge confirmation, which filtered out the noise since mostly features remain across multiple scales (unlike noise). The reader may also refer to Mallat's works for a thorough study of multiscale edge detection through wavelet theory [276]. The orientation of the feature point was determined through a line-fitting method rather than estimated using the result of the wavelet transform (which is sensitive to noise): it essentially considered a neighbourhood of a detected feature and estimated the orientation of the edge line passing through it and neighbouring edge points. Braumann *et al.* [154] used Fourier-Mellin invariant (FMI) descriptors of images [277]. They were obtained by Fourier-Mellin transform of the image in a polar coordinate system, which decoupled translation, rotation and scaling (respectively for rotation and scale invariance). Note that Ghorbel *et al.* [278] later showed that using instead the analytical Fourier-Mellin transform allows getting a complete set of similarity-invariant features.

Blob-like features The most popular blob detector in the computer vision literature is surely the Scale-invariant feature transform (SIFT). It is based on local extrema (or blob) detection [279]. The detector relies on difference of Gaussians (DoG), which is an approximation of the scale-normalised Laplacian of Gaussian (related to each other through the heat equation) and thus contains no directional information. Keypoints are local optima in the DoG scale space of the image. Candidate keypoints that are unstable i.e., low contrasted extrema or those lying on edges (since they are invariant to translations along their direction) are discarded. Location, scale and orientation (estimated as the main gradient orientation over a keypoint neighbourhood) are encoded in the descriptor of every keypoint. The interested reader may refer to [280] for an efficient encoding of that vector. An in-depth analysis of the SIFT method is available in [281].

It was used in [282] as well as in [200], based on previous work [201] for the registration of tiled serial TEM sections[1]. Colour deconvolution was used in [285] (see §2.5) to separate hematoxylin and eosin stain contributions from individual histopathological im-

[1] [283] developed plug-ins for ImageJ to extract SIFT and Multi-Scale Oriented Patches, MOPS [284] correspondences in two images: `http://imagej.net/Feature_Extraction`

ages. Eosinophilic structures were used as object-level features for image registration, from which points of interest were detected using DoG detector. This was reused in [126, 127].

Another popular feature detector and descriptor, SURF [286], was used in [287]. It is based on the determinant of the Hessian matrix operator and relies on integral images for fast computation. As far as SIFT is concerned, DoG is basically a Laplacian-based detector and the Laplacian operator is defined as the trace of the Hessian matrix. Using its determinant (instead of the trace) as it is the case with SURF, discourages the detection of elongated, ill-localised structures.

Binary Robust Invariant Scalable Keypoints, BRISK [288], were used in [289], based on the AGAST corner detector [290]. Note that an evaluation of binary feature descriptors performance can be found in [291].

Object-level (or high-level) features Another school of thought recommends the use of anatomical structures such as vessels, nuclei etc., [292]. The rationale is that traditional feature detection schemes generate a great amount that are regular in appearance, thereby making matching unrealistic. Such features are also described in [4]. For example, in [255], vessel-like structures were extracted in greyscale images using thresholding and mathematical morphology in every slice. The sets of structures were then refined using eccentricity, ellipticity and size criteria. In [293], specific regions in cochlear images were extracted using Otsu's thresholding, mathematical morphology and only the largest connected components was kept. In [294], colour segmentation followed by mathematical morphology allowed to segment significant structures such as blood vessels, other ductal structures or small voids within the tissue area for each stain type.

Other methods, although relying on that same type of features [295, 292, 95], address the matching step by comparing informative patches (also referred to as windows, blocks, boxes or tiles) centred around those keypoints. In other words, features are described by the intensities of pixels around them, which comes down to a block-matching strategy to infer correspondences. We thus detail the matching step for such approaches (referred to as tile-based methods) in §3.1.2. For the sake of completeness, in [295], relevant structures were extracted from the images based on colour and size. In [95], structures of interest were extracted by combining fast marching algorithm and level-sets. In [292], only tiles that have rich content i.e., which variance is above a certain threshold were considered.

Differently stained images One successful application of those high-level features has been the registration of differently stained histological sections, although the literature on that problem is relatively sparse [296, 106, 297]. It is a multimodal problem in that every section varies in appearance: images exhibit different colour distributions and different structures due to different staining. This is solved by identifying common structures and grouping them into comparable clusters. The problem thus becomes monomodal using labelled images or probability maps. In [296], every pixel was assigned a "segmentation vector" containing, for successive Gaussian smoothed versions of the image, its RGB value and the colour mean of a neighbourhood around the pixel. The clustering of the image into different numbered classes was based on [298], who selected the number of components that best modeled the distributions in order to represent the characteristics of the images adequately. A similar idea was proposed in [297] except that the segmentation vectors for each pixel, called "appearance feature vectors", also included information about texture. The clustering of the appearance feature vectors was carried out using a principal eigenvector binary tree clustering algorithm.

Contours One last type of approaches consists of using solely the tissue boundary (probably the highest-level feature), and the images thus simplify to curves. After extraction, those are used for contour matching. Extracted curves may also be sampled to perform point matching (those points are also referred to as nodes). Tissue edge points sampled along boundaries have the advantage of being less vulnerable to e.g., tearing—when sampled appropriately—from which intensity-based methods would suffer. However, their detection relies on accurate segmentations, which in turn may be affected by intensity inhomogeneities if for example a simple global threshold is to be used for all the slices.

In [299, 300, 301], tissue contours were obtained by thresholding. They were manually edited in [301], if necessary, in order to obtain satisfactory boundaries. Contours were then modeled using B-splines and the inverse chord length method [302] was used to estimate knot points that best described a given curve data. This method regulates their number based on the amount of shape variation a region subjected to (fewer knots when the variation is small). In [303], the locations of high confidence edges (including tissue boundaries) were extracted by thresholding edge images obtained from Canny edge detection [304]. In [305], the sharpest curvatures were extracted from the contours of the tissue, which yielded three feature points at consistent locations in every section. The tractability across slices

allowed for the computation of “trajectories”. In [306], contours were obtained using a 2D elastic physics-based deformable model. The model consisted of a set of nodes, initially distributed over a circle. In its fully deformable configuration, the model allowed each node to move independently, without affecting adjacent ones. In [307], two types of nodes were extracted with the aim of creating a mesh: the *object nodes* were automatically selected, ideally along the boundary of the structure i.e., with large gradient, and a minimum distance criterion to prevent them from being too close. The *background nodes* were sought in the background region with larger minimum distance. Delaunay triangulation from the obtained nodes provided a mesh with higher density over the domain of the tissue.

3.1.1.2 Correspondences and spatial transformations

Correspondences between landmarks may be straightforward, as it is the case when extracted manually (although labour intensive and time-consuming) or using segmented needle track holes. For example, in [269] landmarks (placed at identifiable locations along the tissue outer and inner boundaries) tracked across the slices had their trajectories computed through a fourth order polynomial fit. Note that polynomial transformations are usually advised to be computed using a low-degree polynomial due to noise and numerical instabilities [103].

Using needle tracks Holes from the tracks allow for the computation of a (linear) transformation by least-squares minimisation. In [243], a set of photographs of both anterior and posterior faces of every tissue sections was used. "Within-slice co-registration" was achieved by minimising the sum of squared distances between centres of labelled needles tracks for every pair of faces. Then, "between-slice co-registration” consisted of registering the posterior face of one section with the anterior face of the next using block-matching [245]. Other examples of use of fiducial markers include works from [308, 309]. Although they may increase the reliability of the registration process because their locations are easy to track in the images, needles also damage the tissues and introduce bias if the cutting plane is not orthogonal to the needles’ axes. This protocol was however improved in [93, 272].

Using automatically extracted features In contrast, automatically extracted features require a dedicated step that seeks for correct matching pairs in order to derive the correct transformation. Automatically discarding false matches is critical; otherwise the latter

methods would suffer from the same problems that hamper intensity correlation [303].

Using Fourier-based features In [273], an analytic robust point matching method was used for global registration. The alignment was refined using a feature-based modified Levenberg-Marquardt algorithm [310]. In [154], FMI descriptors between a reference and a target image were matched using a symmetric phase-only matched filtering [311]. The parameters of rigid transformations were derived from it.

Using blob-like features Matching pairs are usually found by minimising the Frobenius norm in the descriptor space. Random sample consensus, RANSAC [312] is then used to discard wrong correspondences and to solve for the transformation. In [282], it was assumed that serial section transmission electron microscopy (ssTEM) images were taken at the same scale, and suffered from minor deformation on the global scale, which made the scale-invariance requirement unnecessary. Only SIFT descriptors belonging to the same octave and scale of the DoG scale space thus needed to be compared against each other. To this end, Koshevoy *et al.* used an optimised *k*d-tree with a best-bin-first nearest neighbour search algorithm [313]. Wrong correspondences were filtered out using a criterion based on Euclidean distances, similar to that introduced in [274]. In [287], SURF descriptors were matched using a bi-directional brute-force matcher.

Solving for the transformation parameters was achieved using RANSAC in [282, 285, 126, 127, 287, 289]. It essentially estimates the set of feature points that behave consistently with respect to a linear transformation. Saalfeld *et al.* [201] estimated simultaneously the rigid arrangement of tiles within and across sections using SIFT features and RANSAC registration. The methods are available online[2]. It was extended in [200] by refining the alignment using intensity-based registration (a block-matching strategy detailed in §3.1.2). The combination of both strategies was used to initialise an elastic registration, for which each image was tessellated into a mesh of regular triangles. Like in [307], the system of equations representing the whole stack of slices was an elastic spring finite element model. The entire system stabilised when the sum of the forces of all springs was close to zero.

In [287], an extra-step consisted of computing a non-rigid transformation at multiple resolutions using feature pairs in adjacent sections to constrain control points of B-splines. At every iteration, the feature size decreased while the resolution of the grid of control

[2]Two stand-alone plugins were implemented: Elastic Montage, for mosaicing, and Elastic Stack Alignment, for the alignment of images from serially sectioned volumes. They are incorporated in the TrakEM2 software and available at `http://imagej.net/Elastic_Alignment_and_Montage`

points increased. No reference section was taken and all the images were deformed towards a minimum energy function. In [289], the non-rigid registration step consisted of the alignment of all BRISK feature pairs by least-squares deformations. This process was repeated if the pairs after transformation were not stable. The methodology was reused in [287] and incorporated into a multi-resolution framework.

Using high-level features The Euclidean distance in combination with other criteria, such as size, is also used to assess the similarity between pairs of object-level features. As such, in [255], all possible combinations of pairs in adjacent sections were tried. The transformation that gave the best similarity was kept. The matching cost took into account a distance range, within which matching pairs should lie, as well as the closeness in terms of object size (area). This was robust to cases where no valid correspondence was found. Pairwise non-rigid registrations [314] were performed and implemented as part of a software [254]. In [293], features were paired using the area only. Mismatches were identified using a distance-based criterion, similar to that presented in [282]. The linear transformation was derived from a matching graph, in which every node is a matching pair and is associated with a transformation. An edge exists between two nodes if the two transformations are *sufficiently* similar. The global transformation is the average of those constituting the maximal cyclic structure from the graph. It served as an initialisation for subsequent registration based on maximisation of mutual information and gradient information [315]. In [294] features were paired based on both size (area) and eccentricity. Mismatches were filtered out in a way similar to [293] and rigid transformation parameters were associated with every correct pair. The correct rigid transformation was then estimated through a voting scheme. Non-rigid registration was performed using second-order polynomials, which coefficients were calculated using correct feature pairs.

When registering differently stained histological sections Labelled classes must be matched to corresponding common structures in the images. In [296], a methodology partly based on [154] and reused in [316] was applied: after clustering the images into different numbered classes, class label adjustment was performed in cases where the assignment was not consistent. The problem of having more and/or different classes—because sections may exhibit different structures—was tackled by merging classes so as to have the same regions segmented in both images. Every labelled image pair was finally aligned by computing the displacement vector field using non-linear, non-parametric curvature-based registration. In

[297], the correspondence problem was solved by grouping clusters into three superclusters (called "content classes") in each image according to various partition schemes. The pair of partitions that maximised mutual information provided the optimal content classes in each image. These classes were then refined using spatial features. Then, each image was transformed into a multichanel probability map, where each channel corresponded to one content class. Block-matching registration was performed between pairs of probability maps for each channel independently. This provided a displacement field, from which a non-rigid transformation was estimated using a regularised least squares difference minimising method.

Using contours Curve matching was proposed in [301]. Contours from adjacent sections, modeled as B-splines, were matched by comparing their knot points. The major drawback associated with B-spline representations is the non-uniqueness of the set of control points, which hampers the comparison of curves. This was solved in [103] (see §3.2.1.2) using the intrinsic features of curves, which properties derived from the Frenet frames [317]. In [270], slices of autoradiographs were affinely registered by minimising displacement of manually segmented contours (using sum of squared differences, SSD) by analysis of point-to-point disparities in two images: a boundary point in one section differs from its corresponding point in the adjacent section by a disparity vector. In [318], Curvature Scale Space [319] was used to represent shape (the tissue boundary) at various scales and register whole-slide images of histological sections.

When sets of points sampled along the boundary of the tissues are to be matched, one popular method is the Iterative Closest Point (ICP) method [320]. In [300], ICP was used to register every histological slice with its corresponding blockface photograph. Points were uniformly distributed along every smoothed boundary of the tissue by excluding high curvatures using a rolling-ball filter. Shojaii *et al.* argued that "high-curvature boundaries might lead ICP to converge to local minima and deteriorate its robustness". Deformable registration was then performed using thin-plate spline (TPS). In [303], the affine transformation parameters and the one-to-one correspondences between two sets of edge points in adjacent sections were simultaneously optimised. This method is referred to as robust point matching. In [306], correspondences between contour nodes of adjacent slices were found using an affinity matrix. Corresponding nodes between adjacent slices were couples which relative distance was lower than a certain threshold. False matching were filtered out

by global affinities, which ensured that correct correspondences also exist in slices further away. Translation and rotation parameters were computed by minimising the mean square error between pairs of matching nodes. In [269], the offsets of every landmark to a smooth curve representing the trajectory of that landmark across slices were used to compute a sparse displacement field for every slice; the vector fields were then densified [321]. Every image was finally deformed such that its landmarks lied on the trajectories, and every following slice was then registered to it. A similar strategy was followed earlier by [305], where three edge points in every slice were used as control points of three non-uniform rational B-spline curves (trajectories).

3.1.2 Iconic methods (intensity-based)

Histology reconstruction can also be achieved by means of intensity-based registration. The main difference with the geometric methods described in §3.1.1, is that—as their name suggests—iconic methods are based on voxel intensities instead of features. This means the distance-optimisation framework (where the distance can be a similarity measure) is applied to the entire image domain. In that sense, they can potentially be better at estimating a dense deformation field (feature-based methods require interpolation) which makes them less accurate when the set of landmarks is sparse. However, their efficacy comes at a computational cost.

Linear transformations Some authors have relied on linear registrations to address that task. Andreasen *et al.* [322] optimised the parameters of every rigid transformation by minimising a weighted SSD between the intensities of two adjacent slices. Weights were defined as the ratios of intensities of both images. More recently, methods more robust to intensity variations across slices have been proposed. Block-matching, developed by Ourselin *et al.* [323] was used in [62, 245]; it consisted of (i) finding correspondences between blocks of two images by maximisation of a certain similarity criterion within an exploration neighbourhood, and (ii), using the resulting displacement field, filtering out mismatches via least trimmed squares (LTS) [324] in order to compute a robust, global rigid transformation between the two images. Nikou *et al.* [176] defined a local energy function that was optimised sequentially in order to bring into rigid alignment every unvisited slice with a group of neighbouring slices. They used M-estimators as cost functions, which aimed to reduce the effect of outliers in the regression process by replacing the square function of

the residual in the standard least square minimisation by the German-McClure ρ-function. Dubois *et al.* [62] jointly reconstructed histological and autoradiographic volumes by first stacking sections using their centres of mass, and registering pairs of adjacent sections for each stack using block-matching. The histological volume was then used as a reference for the refinement of the reconstructed autoradiographic volume (2D-2D registration between autoradiographs and histology), due to the fact that inner anatomical structures of the brain are more visible in histology.

Non-linear transformations Other authors employed non-linear transformations [325] for reconstruction. Such methods must however be initialised with a linear registration (or with manual alignment, or image centres alignment). One should note that initialisation is a non-trivial and non-negligible step, and this statement holds for §3.2 too. Incidentally, non-linearly deforming slices has been criticised in [177] and [62]; in particular, Lee *et al.* stated that they preferred to preserve the shape of the tissue rather than arbitrarily and possibly wrongly compensate for distortions. Since no external information about the shape of the tissue is available, bias may be introduced by choosing one slice as the reference shape.

In [24] smoothness of the reconstructed volume was ensured in three steps: the volume was initially reconstructed using pairwise rigid registrations. Next, boundaries of interesting structures were extracted (by thresholding) in every 2D section and smoothed using a min-max curvature flow constrained to 2D (out-of-plane)—and using a mean curvature flow in [326]. This provided a sparse displacement field computed over pixels along the initial boundary of the extracted surface, then extrapolated to the entire slices. Smoothness was also used as a criterion for histology reconstruction in [144], where the refined alignment of the stack was a solution of the heat diffusion equation. The algorithm alternated between the updates of slices' transformations and their neighbours' transformations until convergence. Finally, accumulated transformations updates were applied to each slice. The same purpose was followed in [327], where the reconstruction of a stack of histological slices was formulated as an iterative Gauss-Seidel update scheme applied to images, using by definition two adjacent slices (above and below) and modified to also include information from the image itself [145]—thereby, they also showed that a small neighbourhood is sufficient to restore smoothness. That scheme allowed for smoothing high-frequency perturbations more than lower frequencies associated with the progression of anatomical structures along

the stack (as it is assumed to vary slowly enough by nature of the histological process). A similar strategy was followed earlier in [244], using iterated conditional modes [328] for the optimisation of a global energy function that quantified similarity between slices.

In [329], deformations were represented by independent single valued functions in horizontal and vertical directions: they considered that every 2D warp can be decomposed into 1D piecewise linear deformations with elastic constraint in x and y. The minimisation of the error function for registration was achieved by means of an extension of the dynamic time warping in 1D [330] to 2D problems.

In [331], slices were first rigidly registered using principal axis transformation, and then performed multi-scale non-linear registration with a regularisation based on elastic potentials. The system of Navier-Lamé equations was linearised by means of a non-linear Gauss-Seidel iteration method and approximated by finite differences. This was extended in [332] by replacing the SSD similarity measure in the variational formulation with a weighted combination of two derivative-based (respectively gradient and Laplacian of the image) SSD measures. The error function was thereby less sensitive to intensity inhomogeneities.

In [154], non-rigid registration on rigidly pre-aligned slices were performed in two steps. First, they used polynomial warping on luminance-transformed images: correspondences between control points of adjacent slices were used to estimate the polynomial coefficients through the minimisation of a least-square error. This provided a sparse displacement field. Then, a curvature-based registration [321] was performed on staining-based tumour probability maps. Such maps reduced artefacts around the tumour and thus eased the registration. Braumann *et al.* also suggested to skip the intermediate polynomial registration as improved performance is expected using a multi-grid scheme for the curvature-based registration.

In [246], a method that computed a global non-linear transformation by elastically interpolating between linear transforms defined on pairs of sub-images (hence the name of "piecewise affine registration") was developed. These sub-images represented geometrically, and often anatomically, coherent components. They were automatically extracted through clustering of an initial displacement field [323] computed between the images to be registered.

In [216], the problem of optimising transformation parameters for every slice relative

to, simultaneously, a reference image and the two neighbouring sections, was formulated as Markov random fields (MRF). The MRF energy is composed of unary potentials, which account for the registration to the reference images and pairwise potentials, which encode the registration to neighbouring slices and the regularisation of the displacement field. This formulation served as basis for the deformation field model in [333].

In [334] an initial affine registration followed by non-rigid registration, were performed both by maximisation of the NMI. The latter transformation was modelled as a cubic B-spline free-form deformation [335].

In [336], the reconstruction was initialised by registering slices affinely using a variant of principal axes transformation (PAT, [337]). They adopted the stochastic interpretation of PAT presented in [314] (p.45), in which the images are represented as Gaussian density functions. The problem was formulated as the estimation of a density that best fits a set of reference densities in the sense that the Kullback-Leibler distance is minimised. Due to the lack of robustness of Gaussian distributions to perturbations, such as tears, wrinkles, torn out pieces, artefacts etc., Schmitt *et al.* used Cauchy density functions instead, on which robust PAT relies. Standard PAT was used in [338]. This was followed by two partial optimisations of the SSD with respect to the shear first, and then to rotation, shearing and translation. Finally, elastic deformation was performed, similar to that used in [200].

The only work, to the best of our knowledge, explicitly addressing the problem of histology reconstruction with missing slices was found in [145] and dealt with by interpolating them. Images adjacent to a missing slice were non-rigidly registered using the variational approach of the problem defined in [339]. The interpolated deformation field, which is a fraction of the resulting deformation field depending on the gap between the two registered images, is applied to the template image to approximate the missing intermediate slice.

Tile-based approaches introduced in §3.1.1.1 use patches of the image as features and are therefore similar to block-matching when establishing correspondences. In [292], the translation and rotation parameters relating a block with its corresponding block (within a sufficiently large area in the adjacent slice, referred to as the search or exploration neighbourhood) were found by maximisation of normalised cross-correlation. This provided a sparse displacement field and a second-order polynomial transformation was computed, which coefficients were obtained using least squares. In [295], the method was explicitely based

on block-matching [323]. In [95], a shape-based rigid registration method was proposed. After an initial rigid-body registration between adjacent sections, correspondences between structures of interest were sought for by means of bounding boxes around them. Overlapping boxes in adjacent sections were assigned the same group label. Two bounding boxes overlapping in the same section were grouped into a supergroup. Remaining ungrouped structures were assigned the number of the closest group/supergroup in the adjacent section. Registration of every grouped structures was performed using the phase correlation method. Correction of remaining misalignments was achieved by elastic registration using B-splines in a multiresolution framework. In [340], meaningful tiles (called "subimages") that satisfied a variance criterion were also kept. Their centres were used as control points for TPS registration. TPS was preferred for its physical properties but Auer *et al.* outline that it highly depends on the control points, as opposed to e.g., B-spline interpolation.

3.2 Histology reconstruction using medical images

This section presents pipelines that aim to improve histology reconstructions with the help of 3D medical images. As mentioned earlier, this supposes the access to a suitable set of histological slices. By suitable we mean that a sufficient number of sections with an appropriate spacing between them (relative to the MRI slices thickness) is available. Hence the slight abuse of language made in the section (and the chapter) title in cases where only a single or too few histological slices are available: the purpose is no longer histology reconstruction but the correspondence problem remains the same and calls for 2D-2D or 2D-3D registration techniques. Since those techniques are not limited to single-section studies—and could well be applied to a group of sections [92], we also describe them in the following.

Combining histology and medical imaging dates back to the late 1980s. Early attempts include works by Sze *et al.* [341], who aimed to provide histological explanation for high intensities detected routinely in MR, and Nesbit *et al.* [342], who studied the pathogenesis of multiple sclerosis using MR, computed tomography (CT) and a biopsy.

The process of combination benefits from the heterogeneity and multiple resolutions of the images. In the end, it serves to increase the specificity of medical imaging analysis with baseline information about the actual properties of the underlying biological tissues [13]: since medical imaging provides only indirect information, it is essential to show that resultant findings correlate with pathological findings.

Multi-modal works treat their different images as separate entities: the terms (co-)registration, (co-)alignment, matching, mapping or warping are used interchangeably in the covered literature. They all provide additional, combined information in the form of overlays for diagnostics, treatments, quantification etc. The term "fusion" is also commonly used but it should be distinguished from "data fusion" in the sense of creating a single composite image from different sources via numerical fusion operators, extensively reviewed in [343] and more recently in [344] for medical images.

This section is structured according to the modalities involved in the registration process: (i) registration of histology with *ex* and/or *in vivo* 3D medical imaging (§3.2.1). This includes cases where *ex vivo* is used as an intermediate modality; (ii) registration of histology with *ex* and/or *in vivo* 3D medical imaging using blockface photographs as an intermediate modality (§3.2.2). This also includes cases where both blockface photographs and *ex vivo* are used as intermediate modalities.

3.2.1 Histology $\leftrightarrow$ 3D medical imaging

Multi-modal registration between histological slices and 3D medical imaging can be addressed in three ways (Fig. 3.1):

- *Slice-based approaches* (§3.2.1.1 and 3.2.1.2) They consider every histological slice as an individual object. Those may be preferred over volume-based approaches in cases where e.g., the histological dataset is too sparse or has too few slices. The alignment between histology and medical imaging is then carried out using either (i) slice-to-volume (2D-3D) registration or (ii) slice-to-slice (2D-2D) registration, which is a simplification of the former point and requires careful identification of the "corresponding" plane in the medical image volume.

- *Volume-based approaches* (§3.2.1.3) They consider the set of histological slices as a whole and therefore rely on an initial histological volume. The main goal of initial reconstruction is to correct for the various orientations that the tissues may have across slices (when mounted on glass slides) in order to facilitate subsequent registration with 3D medical imaging. It provides better "support"—as opposed to simply stacking slices—and aids the optimisation of the similarity measure. More complex initialisations have also been developed, which intended to be more robust to registration failures. Both the alignment and the reconstruction are then refined in various ways.

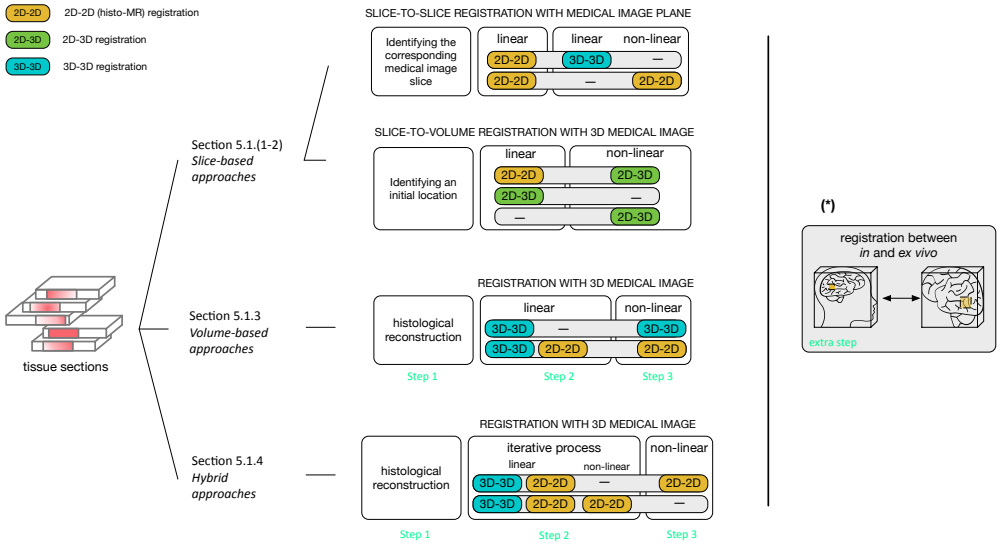

Figure 3.1: Strategies to register histology with volumetric medical imaging (*ex* or *in vivo* alone). The three main approaches (slice-based, volume-based and iterative) are presented. (*) In cases where *ex vivo* imaging is used as an intermediate modality, correspondences between *ex vivo* and histology are achieved through steps 2 and 3, and the mapping between histology and *in vivo* is completed via registration between *ex* and *in vivo* scans (extra step).

- *Hybrid approaches* (§3.2.1.4) They also rely on initial histology reconstructions and alternate between volume- and slice-based approaches so as to get the best out of the two worlds: a more accurate histology reconstruction for a refined alignment with clinical imaging and *vice versa*. They repeat until the reconstruction has converged.

3.2.1.1 Slice-to-slice approaches (2D-2D)

These methods assume that the cutting planes of histological slices and the acquisition planes of the 3D medical image are parallel and that there always exists a histological section that has a counterpart in the set of MR slices. The problem therefore simplifies to a 2D-2D registration between every histological slice and its corresponding slice in the 3D medical image.

Visual selection Slice correspondences can be achieved visually [345, 346, 89], in which case an expert radiologist is most commonly asked to identify the MRI slice corresponding to a histological slice on the basis of anatomical landmarks. Chappelow *et al.* [346] took advantage of all the data to drive image registration using a multivariate formulation of mutual information, while Mazaheri *et al.* [89] performed rigid alignment of the images' centres of mass, followed by 2D affine registration and finally 2D non-rigid registration using free-form deformations (FFD) [347]. Li *et al.* [348] used TPS transformation to

register the *in vivo* MR plane with its visually corresponding histological slice. It was a smooth registration based on specified corresponding landmarks. The optimal number of landmarks was evaluated as a minimiser of the non-rigid registration error. Gangolli *et al.* [345] manually extracted landmarks at visually matching locations along the tissue edges, within and at the boundary between grey and white matter. Then, a forward non-linear moving least squares transformation [349] was applied to register the histological section with the MRI slice.

Automatic selection Automated selection of corresponding slices can be achieved via the optimisation of a similarity measure between each histological slice and every slice of the 3D medical image. This assumes that the maximum similarity is obtained when *actual* corresponding slices are compared. However, Xiao *et al.* [350] showed that both visual and automated approaches failed to reliably determine slice correspondences mostly due to the alteration of the tissue during the histology preparation *i.e.*, direct comparison of images from different modalities is a non-trivial task which is prone to errors. Rather, they proposed to compare the set of histological slices with all possible subsets of equal number of *in vivo* MR slices using mutual information. These subsets were ranked based on cumulated similarity. A group of top-ranked MRI subsets was retained and their lists of correspondences were averaged. The final list was used for 2D affine registrations between slices from both modalities followed by 3D affine registration.

In the clinical literature, slice-to-slice approaches seem to be favoured for the visual control they allow. However, in most of the works the problem is only partly stated and adressed [351, 352, 353]. In [354], linear registrations between *ex vivo* MR slices and histological images was performed and these were then visually matched to the closest (*in vivo*) 3T MR slice. In [355] and [356] histological sections were manually matched to their corresponding MR planes using the marked locations with the fiducials in the MR images, the ink markings in the histological sections, and gross morphological features. In [357], the histological sections that were morphologically close to the $T_{1\rho}$ mapping image were visually identified, and only those were stained. In [358], the tissue sections of the largest cut surface of the tumour was compared side-by-side with MR imaging.

State of the art data analyses therefore rely on two rather loose assumptions:

(i) The sampling during histology is consistent and can coincide with that of the MRI.

However, it is for example well-known that thermal expansion of the tissue when a new block face is exposed during microtomy causes uneven thickness of histological sections. Otherwise, one counts on interpolation whereby, depending on resolution, new and uncertain content is created.

(ii) The histological cutting planes are parallel to each other and to the MRI acquisition plane. One counter-argument directly follows from (i); another, from the fact that it is very difficult to ensure that the specimen lies perfectly flat at the bottom of the cassette during histology processing (this is especially true when tissue is the frozen).

As a result, apparatus have been developed to help cutting the specimen at the *same* interval and orientation as the MR images, as proposed by [359, 360] in the context of prostatectomy, or by means of 3D-printed brain holders [361, 362] but their use is not so common. The error made when selecting the *closest* MR slice was considered in [363], and the consequences of differences in sampling were noted in [364] in the specific case of vascular trees from the femoral trochlea. By disregarding such approximations, one needs to be aware that wrong correspondences are very likely to be established and this directly affects, for example, statistical analyses. Similarly, these challenges were described in [365] and numerous erroneous assumptions made during the process of alignment were listed in the case of prostate cancer. In some cases when the medical image has low (axial) resolution and the histological dataset is sparse or limited to a few consecutive slices, or when the contrast/quality of histological slices is poor, one should acknowledge the fact that visual selection of corresponding slices, manual alignment of images, manual selection of landmarks or manual initialisation remains the safest and quickest way to address multimodal registration.

In some cases when the medical image has low resolution (thick slices) and the histological dataset is sparse or limited to a few consecutive slices, or when the contrast/quality of histological slices is poor, one should however acknowledge the fact that visual selection of corresponding slices, manual alignment of images, manual selection of landmarks or manual initialisation remains the safest and quickest way to address multimodal registration.

3.2.1.2 Slice-to-volume approaches (2D-3D)

Slice-to-volume approaches extend methods presented in §3.2.1.1 by acknowledging that nothing ensures that the cutting plane of histological slices is parallel to the 3D medical

image acquisition plane. Likewise, there is no guarantee that the histological slices are parallel to each other. This means that structures belonging to a tissue slice may extend over several 3D medical image slices, or in other words, a histological slice may lie obliquely in the medical image volume. This in turn suggests that the corresponding 3D medical image slice can only be found through a slice-to-volume (2D-3D) registration. Reviews on slice-to-volume registration can be found in [366] and [367].

Landmark-based In [368], a histological section was rigidly registered with a μCT volume using a density-driven RANSAC for plane fitting [369] and relied on SURF keypoints detected in both histological and each μCT slices. The resulting 3D point cloud had an increased density of matches at the correct location of the histology section, and this was used as a criterion to filter out incorrect pairs. The random sampling of RANSAC plane fitting was thereby biased towards those points that were close to the μCT plane of interest. The alignment between the interpolated plane and histology was further refined using 2D Demon registration tool[3] [370]. In [93], well-arranged strand-shaped fiducial markers were utilised. They allowed for the determination of the location and orientation of each section. First, a 2D-3D affine transformation that mapped a fiducial histological slice to its corresponding points on the MR image was found by minimisation of the residuals. Then, a 2D-2D affine transformation mapping each histology slice to its counterpart in the MR was computed using spatial information from all fiducial markers. Finally, the fiducial correspondences were refined using a local optimisation and one last affine transformation was computed using the affine transformation from the previous step as initialisation. Using non-anatomical fiducials was argued to provide robustness to variations in the appearance of the prostate on MR and histology images. In [103] registration was approached as a contour matching problem and the multimodal registration problem thereby becomes monomodal. The contour curves were described by means of sets of affine invariants constructed from the sequence of area patches bounded by the contour and the line connecting two consecutive inflections. The affine transformation was estimated from matching vertices using the least square error estimation method.

Intensity-based Nir *et al.* [92] aimed to find the poses of all the histological slices such that the transformed segmented histology slices optimally matched the corresponding re-sliced images of the 3D medical image. They made use of particle filtering to model pose un-

[3]Code is available on MathWorks File Exchange.

certainty, where each particle represents a combination of histological slices in various 3D poses, and derived optimal affine registration parameters in a Bayesian approach. The admissible space of 3D poses was constrained such that the transformed slices do not intersect. In [88], geometric transformations that combined a rigid alignment with a 3D deformation field parametrised by various classes of spline functions, various similarity measures, different optimisation algorithms and different optimisation strategies were proposed and compared. In [371], polynomial transformations were used to warp an initial *in vivo* MRI slice that produced minimum error (when compared with all the histological slices). The parameters of a low-order polynomial transformation between the MRI slice and the histological section were optimised by minimisation of the SSD and the correlation coefficient. This method was reused in [372, 90]. In [82], a non-linear registration method was proposed to align histological brain sections with a volumetric brain atlas. They started with an image to planar surface matching, during which sections were linearly matched with an oblique slice automatically extracted from the atlas. An image-to-curved surface matching was then performed, during which each section was matched with its corresponding image overlaid on a curved-surface within the atlas. Specifically, a PDE-based registration technique was developed that was driven by a local NMI similarity.

3.2.1.3 Volume-based approaches (3D-3D)

The main drawback of slice-based (2D-3D) approaches is their sensitivity to initialisation as the landscape of cost functions is very complex and this conditions the convergence behaviour. Other challenges involve the cost function selection and the optimisation strategy [88]. The information from a single histological slice is used alone and its content may be hard to handle by itself (see §2.3 and 2.5) in a multi-modal registration problem: the performance of slice-to-volume registration shows greater dependence on the input images than 3D-3D registration [88]. Considering histological slices altogether i.e., the histological dataset as a whole, allows overcoming such issue. Volume-based approaches follow Procedure 1.

Initial histology reconstruction (Step 1) can be achieved in several ways and the reader is referred to §3.1 for a more complete list of methods dedicated to that purpose. Simple stacking by alignment of centres of mass was used in [179]. The most common way however consists of serial pairwise linear registrations and provides roughly aligned though satisfac-

Procedure 1 Volume-based approaches (3D-3D)

Input: M, *ex* **or** *in vivo* 3D MRI and $\{H_i\}$, a set of 2D histological slices.
Output: histological volume H^f aligned with M.
1: $H^0 \leftarrow$ Reconstruct histological volume from $\{H_i\}$ ▷ Step 1
2: $H^1 \leftarrow$ Linearly register M and H ▷ Step 2
3: $H^f \leftarrow$ Non-linearly register M and H^1 ▷ opt. Step 3

tory enough initial volumes [373, 1, 81, 96, 143, 77, 99, 113]. In particular, in [143], every slice was registered with its successor starting from the bottom of the stack and repeated the process starting from the top of the resultant stack. In contrast, in [113], the process started from the middle of the stack (the most central slice with minimum artefacts was manually picked) and registrations between pairs of adjacent slices after aligning the centres of mass of masked images were performed. Maximisation of mutual information was used in [96], and block-matching in [1] and [99]. Initial reconstruction may also be achieved by use of fiduciary rods, such as in [121], for which the Euclidean distance between corresponding segmented holes from pairs of adjacent slices was minimised.

Other reconstruction methods consider neighbourhoods around slices (as opposed to a single adjacent slice) in order to improve the consistency of the resulting volume. In [102], every slice was registered with both its successor and its predecessor and applied the average transformation to the original slice so that the transformed slices match both their neighbours simultaneously. A similar strategy was used by Rusu *et al.* [249]. In [23], the size of the neighbouring was extended up to five slices away. A weighted graph was built, with slices as vertices, edges symbolised registrations, and weights were given by an information- and distance-based measure. The shortest path from every vertex in the graph to a specific reference slice was found using Dijkstra's algorithm, and incidentally favoured slices that registered well (hence bypassing those that registered poorly). The concatenation of rigid transformations yielded a reconstructed histological volume. Such reconstruction method was reused in [98] with different edge weights. Later, however,manual histology reconstructions using HistoloZee were used in [227] and [374]. While much more labor-intensive, it was found that manual reconstructions led to better histology reconstructions especially when slices were torn or poorly stained.

Multimodal alignment Once an initial histological volume is available, a coarse, linear alignment of the geometries of both medical image and histological volumes is performed

(Step 2), which may then be refined by non-linear registration (Step 3). This can be achieved using standard inter-modality registration techniques implemented in packages such as AIR [262] followed by Diffeomap (LDDMM) [375] in [143], landmark-based registration followed by ANIMAL [376] in [102], or maximisation of mutual information [377] followed by free-form deformations [347] and a pyramidal approach with gradually increasing number of control points in [373]. Only global linear registration was performed in [113].

Variations A variation of Procedure 1 consists of complementing Step 2 with the registration of every slice from the globally aligned histological volume with its 2D counterpart in the medical image volume. Such variation is the cornerstone of hybrid approaches described in §3.2.1.4. In [81], the centres of mass of each histological slice were aligned with their corresponding *in vivo* MR plane (although this is not a registration *per se*) after 3D rigid registration between both volumes. This was refined by 3D non-rigid registration using the adaptive bases algorithm (ABA) [378]. In [23], each histological slice of the 3D aligned histological volume was deformed towards the average of its immediate neighbours (predecessor and successor) and the corresponding MR slice. Some of their methods have been included in the framework developed by [225][4]. In [121], only linear registration between every histological slice and its 2D counterpart in the MR was performed.

Matching *in vivo* imaging *Ex vivo* correspondences can be further carried to *in vivo* space by an extra registration between both image volumes. Given the registration between histology and *ex vivo*, concatenating transformations relates histology and *in vivo* medical imaging. As such, in [77] 3D linear (rigid, affine) and elastic registration were performed between histological and *ex vivo* MR volumes, followed by 3D rigid, affine and elastic registration between *ex vivo* and *in vivo* MR volumes. All registrations were performed using Elastix [257]. Affine registration between the reconstructed histological and *ex vivo* volumes was also performed using Elastix in [249]. *Ex vivo* and *in vivo* medical images were affinely registered, yielding linear alignment between histology and *in vivo*. Finally, non-rigid registration between histological and *in vivo* volumes refined the alignment of both modalities using free-form deformations in a multiscale setting.

[4] `http://www.3dbar.org/wiki/barPosSupp`. The source code is available for download at `https://github.com/pmajka/poSSum`.

3.2.1.4 Hybrid methods

We call hybrid methods those similar to Procedure 1 except both the serial arrangement of the histological volume (its reconstruction) and its alignment relative to the medical image volume are jointly refined (Procedure 2). Both processes hence benefit from each other as changing one affects the other. Initial histology reconstructions (Step 1) follow methods presented in §3.2.1.3.

Procedure 2 Hybrid methods

Input: M, *ex* **or** *in vivo* 3D MRI and $\{H_i\}$, a set of 2D histological slices
Parameter: N, number of iterations after convergence
Output: histological volume H^f aligned with M

$H^0 \leftarrow$ Reconstruct histological volume from $\{H_i\}$ ▷ Step 1
$k = 0$
repeat ▷ Step 2
    Linearly register H^k and M
    for all slices **do**
        $H_i^k \leftarrow$ Linearly register H_i^k and M_i
    end for
    $H^{k+1} \leftarrow \{H_i^k\}$
    $k = k + 1$
until convergence
$H^f \leftarrow$ Non-linearly register H^N and M ▷ opt. Step 3

Step 2 consists of iterating over two registrations: (i) a 3D-3D registration, which updates the global alignment between the current estimate of the histological volume and the 3D medical image, and (ii) 2D-2D registrations, which affect the serial arrangement of slices relative to each other by aligning them with their (current) corresponding slice in the medical image volume used. This in turn provides a new histological volume which is used at the next iteration. This process is repeated until convergence. In general, linear registrations are used in the iterative process to avoid creating wrong correspondences through non-rigid registration. In particular, block-matching was used in [1], the ANTs toolkit with NMI was used in [98] and maximisation of MI was used in [99]. The latter addressed the specific case of separate pieces of tissue by using 2D piecewise local registration. They also addressed the challenging case of automatically initialising the location of a tissue block that is a subvolume of the tissue MR. Yang *et al.* identified the locations of the first and last slices of the histological block in the MR as those maximising NMI after 2D rigid registrations.

Once the iterative process has converged, a final step may consist of a non-rigid reg-

istration to refine the matching (Step 3). The 2D diffeomorphic registration in [98] was similar to that introduced in [23], while cubic B-spline parametrisation for 3D non-rigid registration and the normalised correlation coefficient was used as a similarity measure in [99].

Variations A variation of Step 2 was proposed in [96]. They iterated over: (i) a 3D affine registration between the current histological and MR volumes, by maximisation of the correlation coefficient and (ii) a 2D rigid registration between every histological slice and the central histological slice. Subsequent steps jointly addressed the segmentation and the refinement of the registration of prostate cancer images and also consisted of an iterative process.

Another variation was proposed by Goubran *et al.* in [179], who embedded the non-rigid registration of Step 3 in the iterative process of Step 2. The pipeline thus consisted of iterating over: (i) a 3D rigid registration of the current estimate between the current histological volume with the MR, (ii) 2D rigid registrations between every histological slice and its currently corresponding MR plane, and (iii) 2D non-rigid registrations between every histological slice and its currently corresponding MR plane using free-form deformations.

Matching *in vivo* imaging Correspondences between histology and *ex vivo* can be further carried to *in vivo* space similarly to §3.2.1.3. In [379], the *ex vivo* MR was first translated to match the *in vivo* MR space in order to facilitate the placement of landmarks in subsequent steps. Then, 3D linear (rigid+scaling) landmark-based registration was performed between *in vivo* and *ex vivo* MRs using manually picked landmarks. This was refined by 3D non-rigid registration between both 3D MRIs using landmark-based registration and a symmetric implementation of FFD, respectively for hippocampal and neocortical specimen.

3.2.2 Histology $\leftrightarrow$ 3D medical imaging using blockface photographs

Blockface photographs provide structural information of the tissue face prior to cutting and therefore allow correcting for subsequent tissue deformations (mainly induced by cutting, floating and mounting). In theory, they should be inherently aligned by virtue of the set-up: it consists of a camera on a tripod—or mounted on the microtome itself—oriented towards the face of the tissue block secured on the microtome, and which imaging plane is parallel to the block face. Though, it is common to affinely register them with each

other in order to account for small displacements [104, 122, 110] but this not robust to perspective distortions (the camera imaging plane is never and can not remain truly parallel to the block face). Eiben *et al.* [380] considered that each time the microtome cuts a section out of the tissue block, its face lies in a slightly different plane (due to small mechanical imprecisions or due to the expansion of the tissue when a new face is exposed). This leads to a perspective error, which may hinder the consistency of the reconstructed volume. Their method provided a way to correct for scaling variations and displacements of the sample that may occur from one acquisition to the next. However, they did not take into account the camera motion (as small as it may be). Breen *et al.* [79] assessed the camera lens for image distortion by ensuring that lines from manually selected points (including edges of the image) remained straight. They also ensured those lines were not blurred in any region of the image. Casero *et al.* [144] corrected the perspective error of the blockface photograph acquisition by computing a projective transformation using manually extracted landmarks. "Scratched" photographs (which occur when using a poor quality knife blade during microtomy) were also taken care of: images were first rotated to make the scratches horizontal/vertical using the wax block sides; then, the image rows/columns intensities were scaled so that their median values equalled the wax median value.

We identified three main types of pipelines that relate histology to volumetric medical imaging according to how they exploit blockface (BF) photographs as an intermediate modality (Fig. 3.2), namely for histology reconstruction or for alignment with medical imaging (§3.2.2.1: resp. BF for histoRec, and BF for MedIm alignment) and for both (§3.2.2.2: BF^2).

3.2.2.1 Single use of blockface photographs

These pipelines follow Procedure 3.

Procedure 3 BF for histoRec

Input: M, *ex* **or** *in vivo* 3D MRI, $\{H_i\}$, a set of 2D histological slices, $B = \{B_i\}$, a set of 2D blockface photographs.
Output: histological volume H aligned with M

1: **for all** slices **do** ▷ Step 1
2: $H_i^0 \leftarrow$ Register H_i and B_i
3: **end for**
4: $H^0 \leftarrow \{H_i^0\}$
5: $H^1 \leftarrow$ Register H^0 and M ▷ Step 2
6: $H^f \leftarrow$ Non-linearly register H^1 and M ▷ opt. Step 3

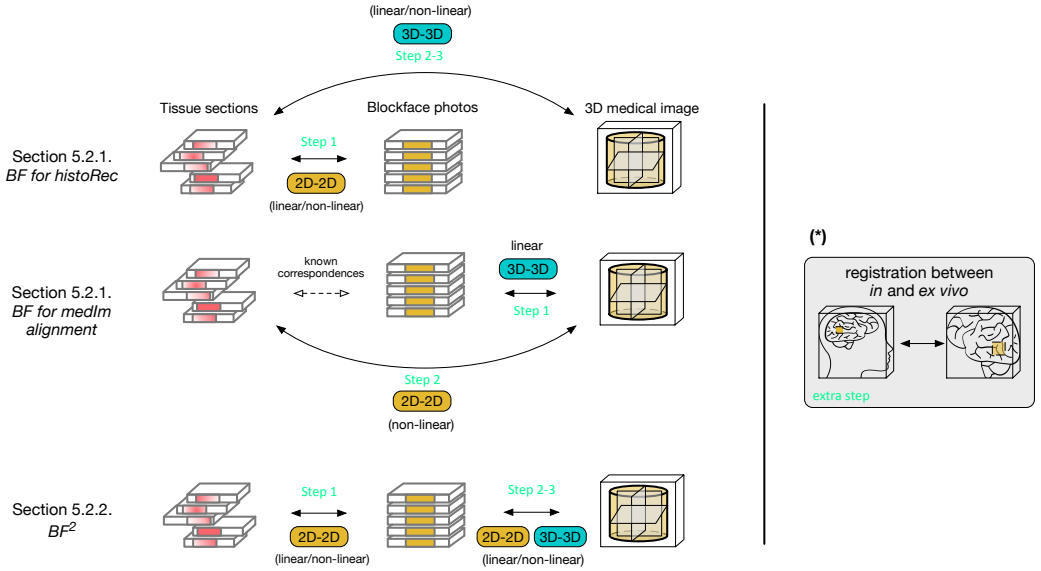

Figure 3.2: Strategies to register histology with volumetric medical images using blockface photographs as intermediate modality; (*) see Fig. 3.1.

As per Step 1, Alegro *et al.* [141] affinely registered each histological image with its corresponding blockface photograph by optimisation of mutual information, as defined by Mattes *et al.* [381]. Schormann and Zilles [73] first reconstructed the blockface volume by least square minimisation between corresponding pairs of landmarks in adjacent photographs [80] and then registered each histological section with its corresponding blockface photographs using an extension of principal axes theory generalised to affine transformations (in order to be able to account for shearing artefacts introduced during the tissue preparation). Johnson *et al.* [101] used 2D moments-based rigid alignment for some brains, then refined using AIR software. For other brains, the method by Thevenaz *et al.* [213] was used between corresponding images with manual refinement. This protocol was reused in [382].

As per Step 2, Alegro *et al.* [141] used symmetric diffeomorphic 3D registration, SyN [383] to align the reconstructed histological and the MRI volumes. In [101], the reconstructed histological was first linearly aligned with MR volumes using a quaternion transform followed by an affine transform. Then, the alignment was refined using a multi-resolution diffeomorphic registration algorithm [383]. In [73], a 3D affine registration between the histological and the MR volume was first performed, followed by a 2D non-linear registration between every histological sections and its corresponding MR plane using a 3D

elastic full-multigrid technique [384] restricted to 2D [385]. It was initialised with a 2D linear registration driven by the analysis of Rayleigh-Bessel statistics, which describe the probability density of local non-linear deformations in histological sections [80].

Variations A variation of Step 2 consists of considering slices instead of volumes: in the method developed by Burgel *et al.* [71], after reconstructing the histological volume, every histological slice was warped to its corresponding *ex vivo* MR plane, based on the methodology developed in [386, 80].

A variation of Procedure 3, BF for MedIm alignment, was proposed in [17] and relied on the registration between the blockface volume and the 3D medical image. Then, using the direct, known 2D correspondences between histology and blockface, every histological slice was registered with its corresponding MR plane.

3.2.2.2 Dual use of blockface photographs

Such works use blockface photographs for both histology reconstruction and matching with 3D medical images. They are to be the most frequent way to address the problem and follow Procedure 4.

Procedure 4 BF^2

Input: M, *ex* **or** *in vivo* 3D MRI, $\{H_i\}$, a set of 2D histological slices, $B = \{B_i\}$, a set of 2D blockface photographs.
Output: histological volume H^f aligned with M

1: **for all** slices **do** ▷ Step 1
2: $H_i^0 \leftarrow$ Register H_i and B_i
3: **end for**
4: $H^0 \leftarrow \{H_i^0\}$
5: Register B and M ▷ Step 2
6: Non-linearly register B and M ▷ opt. Step 3

Linear transformations The choice of aligning every histological slice to its corresponding blockface photograph (Step 1) using linear registration (as opposed to non-linear) may stem from the poor content that the unstained tissue face exhibits. Blockface photographs provide little structural information apart from the tissue borders (higher contrast with the surrounding embedding medium), which could lead to erroneous deformations of the inside of the tissue. Linearly registering every pair of corresponding images may suffice to restore a globally consistent arrangement of histological slices, which will be refined locally when matched with the medical image volume. Lebenberg *et al.* [125] rigidly aligned every histological section with its corresponding blockface photograph; every autoradiograph

(see "Cerebral function" in §3.3 for a brief definition of autoradiography) was then rigidly registered with its histological slice counterpart, both using block-matching [323]. This was reused in [387]. Yelnik *et al.* [122] first reconstructed the blockface volumes using iterative closest point [320] *i.e.*, by registering every photograph to its immediate neighbour (binary images of segmented rivets) and then performed 2D rigid registration between every histological section and its cryo-blockface counterpart. In order to refine the histological volume, 3D regions of interest centred around the basal ganglia were extracted using Yav++ software [388] in both histological and blockface volumes and 2D hierarchical registration (rigid, homothetic and affine) was performed between corresponding 2D images. Dauguet *et al.* [178] aligned every histological section with its corresponding blockface photograph using a "hemi-rigid" method, which accounted for the independent spreading of the hemispheres on the glass slides.

Non-linear transformations Other authors have chosen to refine Step 1 with a non-rigid registration. For example, in [114], 2D linear followed by 2D non-linear registrations were performed between light micrographs and corresponding blockface photographs using respectively maximisation of MI and ABA [378]. Breen *et al.* [79] performed 2D non-rigid registration between a histological section and its corresponding blockface photograph using TPS and corresponding landmarks: interior ink fiducials and anatomical landmarks, such as blood vessels, and corresponding points along the external tissue boundary using "live-wire" semi-automated algorithm [169, 170]. TPS was also used in [97] with 7 control points; six control points were used in [389] and [390]. In [110] 2D rigid, followed by 2D non-rigid FFD-based registrations [347] were performed.

As per Steps 2 and 3—consisting of registering blockface and medical imaging—pipelines start with 3D linear registration [110]. In [178] 3D rigid registration between the blockface volume and the *in vivo* T1 MRI was performed by maximisation of mutual information, as defined by Viola and Wells [391]. 3D non-rigid registration between the blockface volume and the MRI was performed using free form deformations [347], similarly to what Groen *et al.* proposed [110], and the composition of the two previous transformations was applied to the "hemi-rigid" transformed histological volume. The same sequence was applied by Lebenberg *et al.* [125]. Choe *et al.* [114] also described a similar strategy apart

from the last step of the non-rigid registration between blockface and *ex vivo* T2w MR volumes, for which they made use of ABA. The composition of the transformations between blockface and the medical image volume, and between histology and blockface volume was applied to the T2w image in order to resample it in the histological space. The 3D non-rigid registration between blockface and *ex vivo* MR volumes was performed using TPS with 6 control points in [97]; 18 control points were used in [389] and [390].

Other applications of Procedure 4—without the non-rigid refinement of Step 3—include [122], who performed 3D rigid registration between blockface and *ex vivo* T1w MR volumes one hemisphere at a time [392]. The alignment was refined by a 3D hierarchical registration between 3D regions of interest centred around the basal ganglia and propagated to the full volumes. In [79], 3D linear (rigid+scaling) registration between the blockface volume (stack of 3*mm*-thick slice faces) and the MR volume was performed, for which the centres of the needle paths were manually segmented. The global transformation was optimised using the iterative closest point algorithm [320]. Non-rigid refinement was not performed and the method was validated in [393].

Variations A variation of Procedure 4 was proposed in [182] and consists, as in §3.2.2.1, of considering slices instead of volumes. After reconstructing the histological volume (Step 1), 2D non-registration was performed between every blockface photograph and the corresponding *in vivo* MR planes. Registrations were based on moving landmarks sampled on curves generated from the contours of corresponding anatomical features. Once landmarks locations were optimised for matching through minimisation of a cost function based on the local curvature of the curves and limited to small displacements, TPS interpolation [168] for point-based registration was performed.

Matching *in vivo* imaging *Ex vivo* correspondences can be further carried to *in vivo* space through an extra registration between *ex* and *in vivo* medical image volumes in order to relate histology to *in vivo* imaging. As such, in [110] the *ex vivo* μCT and the *in vivo* CTA were rigidly (point-based) registered using manually selected landmarks (e.g., calcium spots, lumen, bifurcation position are clearly visible in both medical imaging modalities). In [97], 3D non-rigid registration between the *ex vivo* and *in vivo* MRs was performed using 3D TPS with 14 control points, and it was used as an initialisation for a last non-rigid

registration between *in vivo* volume and the blockface image by optimising the position of 7 control points and using mutual information as the objective function. Piert *et al.* [389] reused the methodology presented in [390]: the *ex vivo* MR and *in vivo* T2 MR volumes were non-rigidly registered using TPS with 7 control points. The T2 MRI was chosen as the reference space. Additionally, *in vivo* T2 and CT volumes were non-rigidly registered using TPS with 7 control points and PET and CT volumes were rigidly registered.

3.3 Validation methods

We hereafter detail the ways authors have validated the accuracy and the precision of image registration, as defined in [238], in the context of mono- or multimodal histology reconstruction (with or without medical imaging).

Visual assessment It may be the most intuitive way of validating the registration accuracy but must be carried out by experts and does not provide with any quantitative measure. In the case of histology volume reconstruction, criteria used to tell whether registrations are successful encompass improved representations of small structures (subcortical nuclei, cortical areas) and smooth inner and outer borders [331]. Wirtz *et al.* used three classes of neuroanatomical structures that are recognisable after registration when examining whole rat brains: subcortical nuclei, ventricles, certain cerebral and cerebellar cytoarchitectonic layers. Smoothness was explicitly used a criterion for reconstruction in [24]. In [329] the reconstructed volume was compared to real histology sections from the Paxino's Atlas [394] at similar sagittal and horizontal locations.

Visual assessment can also be used when comparing one method against others (assuming that the same data have been used). Gaffling *et al.* [269] compared the reconstruction against that obtained through standard non-registration scheme (without landmarks) using histological data from [329] and artificial data. In [329], the reconstruction was compared against that obtained from the method described in [307].

In the case of multi-modal alignment, visual assessment can be performed by (i) cross-section comparison. In [1], two synchronised 3D viewers were used to display the two volumes in the same geometry. This allowed showing same cross-sections (axial, sagittal and coronal) as well as a cursor at corresponding positions. In [77], the alignment between 3D *in vivo* T2 and histological volumes was qualitatively evaluated by two observers using visual inspection with a moving quadrant view; or by (ii) superposition of adjacent sections [81, 114]. In [178], the external and internal borders of the MRI brain—extracted using

Deriche filter [395]—registered onto the blockface volume were superimposed. A similar visualisation can be used to assess the quality of the histology reconstruction [125, 1, 243].

Landmark-based validation It is the most widespread method, used for example in [92, 93, 396, 94, 99, 96]. It consists of computing the Euclidean norm between corresponding tie points extracted in two images (also referred to as target registration error, TRE). This measure might not be not appropriate for the validation of histology reconstruction from 2D sections only [329]: a minimum distance does not mean the true shape has been recovered. It is however very relevant in the case of multi-modal registration. Those landmarks can be:

- *needle tracks*, such as in [243, 393, 397].
- *manually identified anatomical landmarks*, that are visually tractable across modalities. The anterior commissure, the pillars of fornix, perivascular spaces and optic chiasm were used by Kim *et al.* [371]. Automatically extracted sulcal lines of maximal depth (sulcal fundi or sulcal bottom lines) were used by Osechinskiy *et al.* [88]; the extraction procedure is described in [398]. The urethra, nodules, scars (from previous biopsies), calcifications, and "other general distinguished anatomical features" were considered by Nir *et al.* [92] with the help of a radiologist. Landmark points were extracted manually by Goubran *et al.* [179, 379] to compute the TRE. Boundary curves were manually drawn by Adler *et al.* [98] to compute the boundary displacement error. When such landmarks are used for registration, reliability of their locations is usually assessed by looking at intra- and inter-user variability. For example, Gangolli *et al.* [345] evaluated the former by asking a user to perform landmark selection twice, five days apart, and comparing registered voxels shifts. The latter was assessed by asking two different users to perform the previous procedure. In addition, artificial perturbation of an established set of landmarks in histology was performed in order to test the robustness of the registration method to such changes.
- *anatomical artefacts*. Singh *et al.* [90] used the centroids of manually segmented lesions to evaluate and validate the registration accuracy. Alic *et al.* [77] identified characteristic features in the tumour and its contour.
- *Ink marks* made on the fresh tissue, such as in [79].

Measures of overlap They rely on regions of interest (RoIs) manually delineated by an expert in two images. The Dice score or the Jaccard index are two measures that can be computed to quantify the amount of overlap between the two regions [81, 141, 83, 399, 75].

Specifically, Lebenberg *et al.* [125] manually delineated the hippocampus, cortex, and striatum, as well as the corpus callosum and substantia nigra, to compare different reconstructed histological volumes. The hippocampus was also manually delineated in every histological atlas in [115]. In [89], the whole prostate, the peripheral zone, and the transition zone were outlined by an experienced radiologist in MR and histology images. In [92], the segmentations in the registered histological slices were compared with the corresponding manual segmentations in the re-sliced images of the MR volume of the prostate. The Dice score was shown to be a reliable indicator of registration accuracy only for small and localised RoIs (which approximate point landmarks) in several locations in the image space [400].

Texture-based methods Grey-level co-occurrence matrices (GLCM) were presented in [401] and were used to assess the alignment quality of the histology reconstruction [75, 24]. Such matrices were computed by calculating how often the pair made of a pixel of interest with a certain intensity and its immediate neighbour in the direction going across slices (orthogonal to the cutting plane) occurs. Cifor *et al.* [24] computed GLCMs in the neighbourhood around the boundaries of the tissue rather than the whole volume in order to quantify the smoothness of the reconstruction.

Artificial perturbation of a ground truth Artificially perturbing a ground truth allows having access to the original alignment, against which the resulting alignment is compared. It is done by taking a volumetric image which original alignment is known (e.g., a 3D medical image) and applying random, smooth transformations to each of its slice independently (as well as e.g., including artefacts that simulate holes/tears, ignoring some slices etc.). The error made after reconstruction is then computed [24, 176, 329, 154, 225, 148]. Synthetic datasets (e.g., phantom models) were used in [255, 96, 95]. Comparison against manually realigned stack (by an expert physician researcher) can also be performed [244, 110]. Robustness to holes and tears was tested by Cifor *et al.* [24], and the effect of missing sections was assessed in Arganda-Carreras *et al.* [95]. Both were addressed by Nikou *et al.* [176].

3.4 Applications

We underline three main areas of applications within which the covered literature falls into: (i) examining structures with respect to their environment in 3D (§3.4.1) with or without the help of 3D medical imaging; (ii) the correlation of data (§3.4.2), which benefits from the access to the underlying microbiology to improve the characterisation/discrimination of signals in non-invasive imaging; and (iii) the creation of digital atlases (§3.4.3), which

allows for easy 2D and 3D visualisations as well as quantitative measures of anatomy when independent data from different subjects are included.

3.4.1 Examining functions and relationships in 3D

This section includes works for histology reconstruction with or without the help of 3D medical imaging.

Mice brains were reconstructed in [269, 327] and [333]. Nissl-stained cryosections of an adult mouse brain, available from [329], were used in [269]. Other organs, such as rat liver tissue were studied in [255], who proposed a registration method for the reconstruction of histological whole slide images that exhibit vessel structures. Human liver tissues were studied in [106] and [402]. In [70], the 3D configuration of extravascular matrix patterns in archival human uveal melanoma tissue was described. Mice lungs [249] and heart [107, 403] were also studied.

Tumours The 3D structure of tumoural invasion fronts of carcinoma of the uterine cervix was investigated by Braumann *et al.* [154] in order to understand their architectural-functional relationship, while Wentzensen *et al.* [316] analysed the spatial organisation of a cervical cancer.

Vasculature Xu *et al.* [295] studied the microvascular structure of the mouse hind-limb. Due to the 3D rearrangement of the microvessel networks during pathology, a reconstruction was critical in understanding the dysfunction of organs during disease. The 3D vascular network from immunostained sections of the human spleen was reconstructed by Ulrich *et al.* [289].

Cerebral function is dependant on neurological organisation and metabolic activity [404]. Autoradiography allows looking in great details at, among others, the cerebral metabolic rate of glucose utilisation in response to physiologic activation of the visual, auditory, somatosensory, and motor systems, and in pathologic conditions. Rat brains are often studied [405, 406, 270, 407, 408, 409, 176, 177, 62]. The auditory activation of visual cortical areas was studied in the blind mole rat by Bronchti *et al.* [409]. Lee *et al.* [177] studied the cerebral glucose metabolism in the rat cortical deafness model using 3D voxel-based statistical analysis of autoradiographic data. They observed a significant decrease in the glucose metabolism in the bilateral auditory cortices. Dubois *et al.* [62] combined histology and autoradiography to study interhemespheric differences through voxel-wise statistical analyses. Hess *et al.* [399] studied the metabolism and function of gerbil brains. Autoradio-

graphic volumes from 2-DG autoradiographs of primates were reconstructed using 3D MRI [303, 1].

3.4.2 Characterising 3D medical imaging signals

Neurological diseases A 3D mapping of pathological changes throughout the brain for Creutzfeld-Jacob disease was developed by Colchester *et al.* [243]. Goubran *et al.* [179, 379] identified and delineated lesions in MRI in order to improve the surgical treatment of epilepsy. Lockwood *et al.* [124] investigated specific semi-quantitative 3T MRI parameters in order to understand whether they are associated with particular histological features. The study was performed on temporal lobe specimens in epilepsy surgery patients whose conventional MRI scan appeared normal.

Stroke Li *et al.* [348] correlated signal changes observed in T1-weighted images acquired during brain ischemia in small animal models to molecular features obtained from histology. A similar effort was followed by Stille *et al.* [113], who registered "abnormal" images from a rat model of stroke with 3D *in vivo* T2w MR images to study neurobiological correlates of the variations in MRI signal intensities.

Cancer Histopathologic examination can be related to *in vivo*—or *ex vivo* [93], MR imaging with the aim of improving prostate cancer detection rate [92, 94, 77, 346, 84, 350, 89, 96, 85]. Le Nobin *et al.* [91] compared prostate tumour boundaries on MRI to those in histology in order to define an optimal treatment margin for achieving complete tumour destruction during image guided focal ablation. Edwards *et al.* [410] used histology to identify the tumour boundaries in oral cancer patients with better accuracy in order to enable precise PET-guided resection. Jiang *et al.* [87] combined *in vivo* MRI/MRSI, *ex vivo* brightfield/fluorescence microscopic imaging, and histology to study human breast cancer. Seeley *et al.* [123] studied secondary breast cancer in the bone using diffusion weighted MRI, Matrix-Assisted Laser Desorption/Ionisation Imaging Mass Spectrometry and histology in order to observe changes caused by tumour cells in the bone at the protein level. Studies from Mertzanidou *et al.* [411, 248] investigated the mapping between histology and 3D whole specimen imaging along with whole mastectomy volume reconstruction from radiographs. Breen *et al.* [79] correlated *in vivo* MR thermal lesion images with histological tissue damage in rabbit thighs. Humm *et al.* [121] developed a stereotactic fiduciary marker system for hypopharyngeal tumour xenografts in rodents to co-register MRI, PET, histology, autoradiography, and measurements from physiologic probes.

Vascular lesions can be seen in human MRI but are only detected reliably in histology. Singh *et al.* [90] registered lesions microscopical features with their corresponding locations in the *in vivo* MR images in order to understand better their MRI signatures. Coombs *et al.* [412] correlated MR signal characteristics with carotid atherosclerosis plaque components in order to optimise protocols for future clinical carotid MRI. Groen *et al.* [110] studied the relationship between biomechanical parameters and atherosclerotic tissue components in the carotid using histology, *in vivo* CT angiography and *ex vivo* MRI and CT imaging.

3.4.3 Combined MRI-histology atlases

Atlases provide detailed segmentations and classifications of certain regions and subregions in a common anatomical reference framework. They stem from the need for accurate maps of architectonic areas with reference to MRI images. The main rationale is to help understanding the localisation of functional activity in different regions [413] but they are also of great importance in segmentation [414] or can be used to improve preoperative planning [415] and post-operative follow-up.

There exist three types of atlases:

- *MRI-based atlases* [416, 417]. They are useful for measuring volumes and analysing large morphological features but suffer from imprecise delineations due to low resolutions.
- *Histology-based atlases* [329]. Most of them derive from rodent brains but are limited: it was reported in [418] that distortions during tissue preparation and the lack of structural ground-truth in 3D make it hard to extract spatial cues or to derive quantitative group variations. In [104], a high-resolution 3D reconstruction of blockface-imaged Methylene blue perfused primate brain tissue was proposed as the basis for detailed stereotaxic anatomical atlases. The use of blockface images bypasses the tedious correction and alignment of histological sections without external information.
- *Combined MRI and histology atlases* [419]. They combine accurate anatomical delineations in histology for propagation in the 3D medical image, with ground truth 3D shape for improved histology reconstructions. We emphasize the last type of atlases as it involves multimodal image registration.

Human studies The creation of a brain atlas of the human basal ganglia based on histological images and MR images was investigated by Ourselin *et al.* [420]. Other brain atlases of the basal ganglia and the thalamus derived were then proposed by Chakravarty *et al.* [102],

Yelnik *et al.* [122], and Bardinet *et al.* [421] based on immunohistochemical and MRI data.

Animal studies Johnson *et al.* [422, 101] presented an atlas of the C57BL/6 mouse brain based on MRI and conventional Nissl histology. Lebenberg *et al.* [125] derived an MRI-based 3D digital atlas from C57Bi/6J mouse brain, which was matched with 3D reconstructed post-mortem data in order to evaluate morphology and functions of mouse brain structures in the context of Alzheimer's disease. Mailly *et al.* [100] reported a procedure for the construction of a 3D digital model of the primate and rodent basal ganglia. Yushkevich *et al.* [23] used an average MRI of 30 *in vivo* scans of 10 mice in order to build a 3D reference histological atlas of the mouse brain from Nissl-stained sections. Ali *et al.* [103] combined histological sections of rat brain with a 3D brain atlas in order to contribute to brain mapping efforts. Gefen *et al.* [82] followed the same path by aligning Nissl-stained histological sections with a volumetric mouse brain atlas for the segmentation of hippocampal complex. dauguet *et al.* [178] proposed a pipeline for the reconstruction of a histological volume from whole baboon brain Nissl-stained sections using *in vivo* MRI. Amunts *et al.* [17] created an ultrahigh-resolution 3D model of a human brain at nearly cellular resolution of 20 micrometers.

Finally, histology-MRI atlases have also been used by Burton *et al.* [86], who combined MRI and Trichrome-stained histological sections in order to construct histo-anatomically detailed models of cardiac 3D structure and function at a high resolution.

3.5 Discussion and perspectives

This section covers three topics: (i) some methodological comments on pipelines (§3.5.1), their differences, advantages and drawbacks; (ii) some of the remaining challenges (§3.5.2); and (iii) concluding remarks on the importance of cross-disciplinary knowledge in solving the biological question associated with histology-MRI registration (§3.5.3).

3.5.1 Methodological comments

On hybrid pipelines We discuss three points: (i) the methodology *per se*, (ii) the usefulness of complex initial 3D histology reconstructions when medical images are available and (iii) the types of datasets and what to do with them.

(i) Volume-based approaches (§3.2.1.3) rely on a single round of registration between histology and medical image volumes. In that respect, changing the input (another reconstructed histology volume) results in a different global alignment and thereby estab-

lishes different correspondences between both modalities. On the contrary, hybrid pipelines (§3.2.1.4) rely on the principle that global alignment between both volumes is optimal only when the arrangement of histological sections relative to each other (the 3D histology reconstruction) is itself optimal, and *vice versa*. In other words, one conditions the performance of the other. This strategy offers a robust way to achieve accurate reconstructions and we highlight two representative works from Adler *et al.* [98] and Goubran *et al.* [179]:

- Goubran *et al.* relied on an iterative process that consisted of both (3D and 2D) linear and (2D) non-linear registrations between histology and medical imaging. However, there is no preliminary guarantee that a histological section and its "corresponding" (resampled) MRI plane at some iteration are actual counterparts to each other. In fact, unless the histology stack has first been well initialised (with a linear transformation that brings it to the MRI space), there is a risk of biasing both its final reconstruction and the global alignment with medical imaging by non-linearly transforming histology when registering it with the wrong (resampled) MRI plane.
- On the contrary, Adler *et al.* performed 2D non-rigid registrations between histology and medical imaging only after the same type of iterative process (though consisting exclusively of linear registrations) had converged.

(ii) In view of Figure 9 from the work by Adler *et al.* [98], the gain from complex methods (compared to pairwise registrations or simple stacking) for initial histology volumes when medical images are available is also unclear in general. Furthermore, whereas consistency and accuracy of the initial reconstruction would matter in the case of volume-based approaches, hybrid pipelines allow to relax that constraint as they account for it by design. Manual reconstructions using open-source softwares represent another attractive solution [227, 374].

(iii) It goes without saying that volume-based and hybrid approaches (§3.2.1.3 and 3.2.1.4) as well as pipelines described in §3.2.2 all manipulate volumes *i.e.*, assume that a suitable set of histological sections is available. Yet, it happens that one only has access to a single or a few (either sparse, or thin and consecutive) sections, which naturally points towards slice-based approaches (§3.2.1.1 and 3.2.1.2) and no longer aims for histology reconstruction—the correspondence problem solved by multimodal registration remains the same. Now it should be highlighted that every approach that has been described here is driven by the data, which is to be generated in relation to the study and its goals;

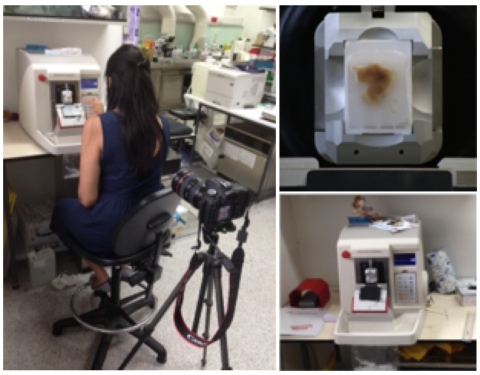

Figure 3.3: Working with blockface photographs. Left: camera fixed on a tripod, standing behind the histopathologist collecting tissue sections from an automated microtome (bottom right). Top right: one blockface photograph is shown.

among the parameters that matter for registration, one should consider the number of and spacing between histological sections relative to the medical image resolution. For example:

- Thick MRI slices relative to a thin slab of several consecutive histology sections (spanning less than one MRI voxel in z) could either call for 2D-3D or 2D-2D registration techniques in order to establish correspondences; sources of error could come from the identification of the (visually) corresponding MRI plane (the initialisation in the former technique) and from the fact that they rely on interpolation (resampling the medical image volume is more or less effective/meaningful depending upon its resolution).
- A sparse histological dataset, in the sense that its sections exhibit large morphological changes and therefore break the smoothness assumption, may also require to consider them individually (and echoes the previous point).

On the use of intermediate modalities Mapping histology with medical imaging is challenging due to the alteration of the tissue between the starting (*in* or *ex vivo*) and the end (histological images) points of its handling. Not using any proxy may complicate the path to a plausible solution.

Similarly to longitudinal image analysis, the more snapshots during tissue preparation, the easier it is to track and correct deformations between *in vivo* imaging and sectioned histology (of the same specimen). This is where blockface photographs are of great value (Fig. 3.3). Using in addition fixed *ex vivo* medical images allows accounting for the non-uniform shrinkage that happens when extracting the sample. Besides, the main rationale for also using fresh *ex vivo* scans may be the study of the influence of fixation on tissues

magnetic properties (see §3.5.3). The right balance should however be found when using intermediate modalities as this not only calls for more resources (time, space, study goals etc.), but also impacts the accuracy of the histology reconstruction: (i) none [98]; (ii) *ex vivo* medical images [179]; (iii) fresh + fixed *ex vivo* and blockface photographs [84].

Another advantage of intermediate modalities lies in that they offer additional levels of resolutions between that of *in vivo* imaging and histology. This naturally results in pyramidal schemes, in which the optimisation of the transformation parameters is less likely to get trapped in local optima.

3.5.2 Remaining challenges in histology reconstruction

Preprocessing Tears and folds may be the most challenging artefacts to account for and frequently result in discarding the damaged section. The correction of tears requires to ascertain that no tissue material has been lost. Assuming this is possible to tell automatically, the problem is to recover in-plane continuity between separated structures. The problem of tears can be extended to purposeful cuts when for example, whole mount histology is to be studied and the tissue slice needs to be cut into several pieces. Mosaicing/stitching is extensively studied in the general computer vision literature [204] and may also be approached as Jigsaw puzzle solving [423, 424]. So far, detection of folds has relied on rather simplistic assumptions about the colour brightness properties of an image and could benefit from the addition of geometrical considerations. It is challenging to know how many layers a single fold is made of. Assuming it is possible to know that number, the correction of a fold still requires the separation of structures belonging to each of the layers that compose it. It also necessitates the rearrangement of the entire piece of tissue according to its configuration prior to folding (i.e., unfolding), which may be approximated from adjacent sections.

Other fields are involved in similar problems and give potential to exciting parallels. They include computational geometry [425] and computer vision with e.g., the simulation and visualisation of realistic tearing and cracking of thin sheets [175]; material science with e.g., the study of mechanical instabilities of certain materials during compression [426, 427]; statistical physics with e.g., the modelling of folding of thin sheets [428, 429]; or even geology with e.g. the study of orogeny [430]. As a matter of fact, extensive information about the nature of tissue distortions during microtomy was already given in [431].

Image analysis The extraction and manipulation of meaningful information from histology and medical images is a very complicated task. Thus, attention has been directed towards

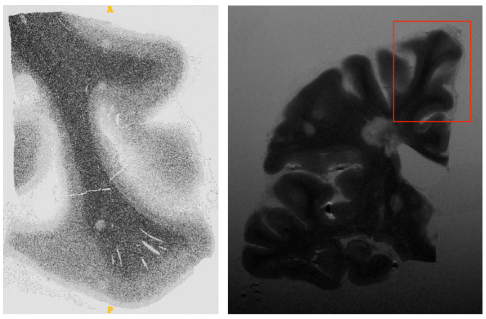

Figure 3.4: Part-to-whole registration. One T2 slice from a slab of a whole brain is shown in the image on the right. It was then cut into blocks, each of which was put in separate cassettes and processed for histology. A GFAP-stained section from one of these blocks (delineated in red) is shown in the image on the left.

simplifying them, that is classically, using the *shape* and the *edges*.

Such simplification is not trivial [432] and it cannot be achieved by only looking at intensity changes [433]: many unwanted edges are produced in the process, and not only texture and noise are responsible for it (e.g., tears and cuts in histological images). The reduction of images to their main features thus relies on smoothing, which has become a commonplace to separate "true edges" from noise. However, the type of smoothing in multi-scale approaches—how to actually build a scale space [434]?—remains an important matter to guarantee reliable and tractable detections.

In the monomodal case, feature-based based methods were successfully applied to the registration of histological slices but investigations such as the study of factors that influence keypoint stability in scale space [435], or the derivation of criteria for detectors comparison [436] may be of great benefit to the field: in general, little details are given about the consistency and reliability of detections. Besides, a common drawback in their use for histopathological image analysis is the large amount of features that may be generated; this is due to the rich content of images, which can quickly turn into "biological noise".

In the multimodal case, histology and medical imaging have, by nature, their own contrast and there does not always exist a mapping between their constituents—incidentally, the latter is one reason why intensity-based methods tend to get trapped in local optima. As a matter of fact, classical feature description methods, such as SIFT [279], will also fail to match features [437] especially due to non-linear local intensity mappings (letting aside the lack of counterpart, which could be handled with suitable descriptions).

Alternative methods are necessary and rethinking descriptions may be required [438]. Note that manual extraction of anatomical landmarks in histology and medical imaging still

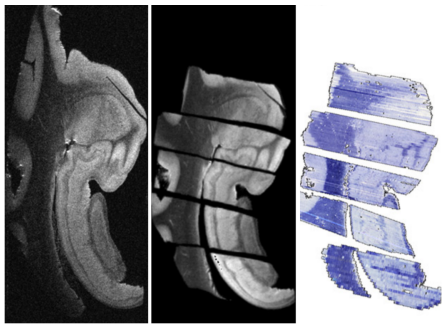

Figure 3.5: The block of tissue (left) being too thick for histology processing, was cut into sub-blocks, re-scanned (middle) and individually processed. (Right) reconstructed and rearranged Nissl-stained histological sub-blocks. Image reproduced with permission from [98].

remains a safe way to establish correspondences [345].

Lastly, shape—as defined by Attneave [439], can become a valuable asset (see Fig. 3.4), and multimodal registration may be obtained as a result of shape recognition (see Chapter 5).

Gutierrez *et al.* [440] tackled the aforementioned limitations about description in a multimodal setting by learning correspondences between context-aware Haar-like features from intravascular ultrasound and histology, and inferring displacements by means of a regression forest. Such approach naturally brings the promising tracks related to convolutional neural networks [441] in the medical domain. The alignment problem could directly benefit from the computational power of such methods for learning correspondences between two different modalities. For example, a method for real-time 2D-3D registration of tools images with 3D CT was developed by Miao *et al.* [442]. A survey on deep learning in medical image analysis was recently proposed by Litjens *et al.* [443].

Part-to-whole It is not uncommon for histopathology laboratories to receive tissue samples that are (p1) too wide (Fig. 3.4) or (p2) too thick (Fig. 3.5) to be processed as they are. The sample is therefore cut into separate sub-blocks, each of which is processed individually. If no scan of each sub-block is available, one has to keep track on which part of the sample each sub-block corresponds to and use that knowledge to initialise the registration of histological slices with the clinical image, or manually align them. As for problem (p2), attempts at using similarity measures have been made to initialise registrations, but those are ambiguous and rely on absolute measures rather than relative ones [99]. On that matter, it was shown that direct comparison of images from different modalities is non-trivial, and fails to reliably determine slice correspondences [350]. No automatic method to address

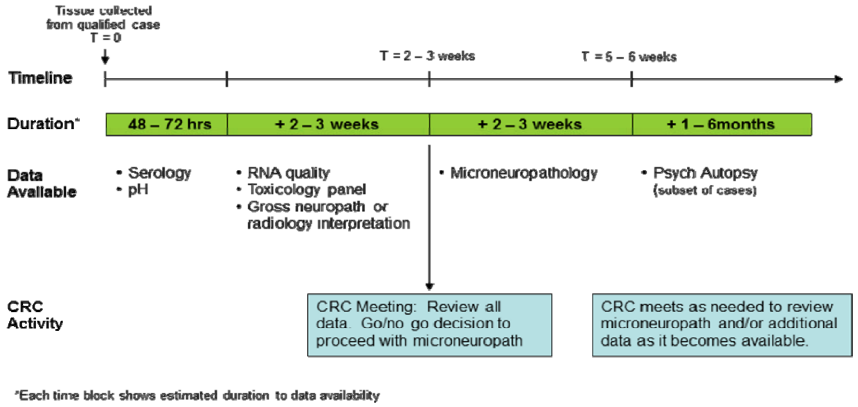

Figure 3.6: Example of a timeline for histology/medical imaging studies. Image taken from [18]

(p1) has been proposed in the literature yet (see Chapter 5).

Fusion It seems that the first true attempt at drawing mutual enrichment from separate modalities (mass spectrometry and microscopy) has been made by Van de Plas *et al.* [444]. This seems reasonable to think that one goal of combining information could also be to actually do so through fusion (as opposed to only overlay images), and thereby for example, increase the spatial resolution as well as augment the informative power of 3D medical imaging.

3.5.3 Concluding remarks

The problem of histology reconstruction using medical imaging involves at least four experts: a histopathologist, a physicist, a computer scientist and a physician in order to answer a single biological question. Interdisciplinary collaborations are essential and communication on the object to be delivered/handled at every stage, time constraints and resources is critical (what? how? when?). This allows avoiding compromises, thinking backward and instead appropriately (re)defining a problem [445]. For the sake of illustration, such a timeline is presented in Figure 2 of the Supplementary Methods 1 from the work by Hawrylycz *et al.* [18] (see Fig. 3.6). Cross-field awareness is crucial as data analyses rely on the assumption that the object remains similar enough through time and stages to be reliably compared across modalities. Improvements are consistently being made to minimise alterations of tissue and towards understanding the causes and effects of such variations.

Ex vivo MRI is commonly applied in neuroscience for a better understanding of the contrast mechanisms of disease-induced tissue changes. Its use supposes that the tissue has been preserved (fixed/frozen). As a matter of fact, the effect of time and storage conditions

on the magnetic properties of *post mortem* tissue is important for correct interpretation of *in vivo* clinical results based upon *ex vivo* measurements.

According to Fischer *et al.* [446] and more recently to Kaye *et al.* [447], quick deep freezing is a satisfactory method of storage for tissue samples (e.g. brain, heart) which does not affect T1 or T2 significantly. However, this method is not applicable to liver and muscle tissues [448].

In contrast, chemical fixation (aldehydes, and commonly formalin) causes reduction in tissue T1 and increase in T2 relaxation times for human tissue [448], as well as a significant decrease of mean water diffusivity in e.g. nervous tissue. Little is known about how fixative solutions alter the tissue microstructures responsible for its MRI properties: while some effects may be reversible, others may be irreversible [449, 450]. Conducting such investigations may require the imaging of the fresh specimen (fixative-free) as well as examinations of the effects of different fixation protocols [450].

Lastly, detailing data acquisition protocols goes beyond the scope of this review but it still seems relevant to stress out the importance of generating standard data. As far as image registration is concerned, it is simply a tool designed to achieve accurate and reproducible correspondences between separate images. However, improving it becomes vain if similar attention is not also directed towards ensuring consistent, quality input data within and across institutions [451, 452, 453]. Standardising protocols is not easy and immediate, and although the importance of such undertaking is acknowledged by many, so is the amount of work that remains to be done. Furthermore, since quantitative measurements are to be extracted from those images and interpreted by clinicians/physicians, a comparable amount awaits computational imaging scientists dealing with such variations [3].

Chapter 4

A Graph-theoretic Approach to Histology Volume Reconstruction

4.1 Introduction

4.1.1 Overview

Specimen slicing, during tissue preparation, breaks the spatial relations between structures. This creates discontinuities which hamper mental representations in 3D and thereby, a full understanding of the anatomy. In order to regain visual understanding of the structures in 3D and possibly allow for quantitative (volumetric) analyses, a smooth (or continuous) reconstructed volume is sought.

One bottleneck, and thus a limitation of any solution, should be noted: without the help of external information about the shape of the tissue prior to sectioning (*e.g.*, 3D medical imaging), the true, original arrangement is unattainable. In the present chapter, I am only given a series of histological slices.

Reconstruction algorithms rely on image registration for the spatial alignment of slices, and aim to be robust to artefacts following histological preparation. The most straightforward way is to register every slice with its direct neighbour and repeat the process with the following pairs. The reconstruction is obtained by the composition of every transformation with respect to a certain reference slice. However this is not robust to misalignments and registration failures.

As a remedy, methods that use several neighbouring slices—as opposed to a single one—have been considered. Some register every slice with some of its neighbours above and below, and average the transformations in order to smooth out errors locally [102]. Others consider those same neighbourhoods and find the transformation parameters that

optimise a local energy function sequentially (composed of *e.g.*, a similarity measure) [248, 176]. In both cases, the neighbourhood information acts as regularisation. Further details about reconstruction methods from serial histological sections can be found in §3.1.

Here, the problem is approached from a graph-theoretic perspective. In the following, I highlight what seems to be a limitation of Yushkevich's work [23], which led to the adjusted design I propose.

4.1.2 Problem formulation

Following the formalism of Yushkevich, the histological stack is represented as a graph, where each node is a histological section, an edge represents a linear registration between two images (resp. nodes) and edge weights are measures of similarity between two images after alignment (hence they are referred to as *distances* and use the letter d). The goal is to find the sequence of linear transformations (referred to as a *path* in the following) that provides the best alignment of all sections *i.e.,* a smooth reconstructed volume.

Yushkevich's method works as follows: after registering every slice i to not only its immediate neighbour but also to slices further away, j, weights, are assigned to every such edges. Then, the shortest path is found using Dijkstra's algorithm.

By definition, Dijkstra's algorithm finds the path which *sum* of weights (or cost) is the smallest. This presupposes that paths are comparable with each other or more formally, that they have a total ordering.

In [23], weights are based on the product of two distances: between $d_1(i,j) = \big(1 + \mathrm{MI}(i,j)\big)$ (which is not a metric) and $d_2(i,j) = |i-j|(1+\varepsilon)^{|i-j|}$; in [98], between the information-based metric $d_3(i,j) = \big(1 - \mathrm{NMI}(i,j)\big)$, with NMI normalised between $[0,1]$—it is equivalent to the distance $d(i,j) = \big(2 - \mathrm{NMI}(i,j)\big)$ with NMI normalised between $[1,2]$, which is a metric [454] *i.e.*, it satisfies the requirements (R1) positivity, (R2) non-negativity, (R3) symmetry and (R4) the triangle inequality—and $d_4(i,j) = (1+\varepsilon)^{|i-j|}$. For both, $\varepsilon \in \mathbb{N}^*$ is a parameter that refers to the number of slices allowed to be "jumped over". The case $\varepsilon = 0$ thus refers to (direct) pairwise transformations between adjacent slices propagated to the entire stack.

As far as Dijkstra's algorithm [455] is concerned, although comparability between edges is guaranteed by use of d_3 alone (since (R4) grants a binary relation between weights), the source of the problem is instances where weights violate the triangle inequality. In order to satisfy that inequality, it seems mandatory to ensure that $d_3 d_4$ is a metric; we show that

this is not the case.

First we can note that d_4 alone is not a metric because it does not satisfy (R4): considering 3 adjacent slices i, j, k with $j = i + 1$ and $k = j + 1$, then $d_4(i,k) = (1+\varepsilon)^2$ and $d_4(i,j) + d_4(j,k) = 2(1+\varepsilon)$ (equality holds for $\varepsilon = 1$).

Now, we can also show that $d_3(i,j)d_4(i,j)$ fails to satisfy (R4) $\forall i, j$ and $\forall \varepsilon \in \mathbb{N}^*$. Considering the same consecutive three slices i, j, k, with $\varepsilon = 1$ and $\mathrm{NMI}(i,k) = \frac{1}{4}$, $\mathrm{NMI}(i,j) = \frac{1}{4}$, $\mathrm{NMI}(j,k) = \frac{3}{4}$ (after registration).

Thus we have on one side:

$$d_3(i,k)d_4(i,k) = \big(1 - \mathrm{NMI}(i,k)\big)(1+\varepsilon)^2 = 3, \tag{4.1}$$

and on the other side:

$$d_3(i,j)d_4(i,j) + d_3(j,k)d_4(j,k) = (1+\varepsilon)\big(2 - \mathrm{NMI}(i,j) - \mathrm{NMI}(j,k)\big) = 2. \tag{4.2}$$

In practice, the set $\{d_3 d_4\}$ takes values that highly depend on the histological dataset, but it seems possible that the triangle inequality is violated. This makes the decisions taken by Dijkstra's algorithm (*i.e.*, the shortest path and thereby the chosen sequence of transformations) difficult to assess and explain since there exists no binary relation between such weights: considering four slices i, j, k, l, $\mathrm{NMI}(i,j)$ and $\mathrm{NMI}(k,l)$ are incomparable. As a result, the reconstructed volume is itself difficult to assess.

Note that even assuming that the weights are expressed using the information-theoretic metric only, d_3, then the inequality $w(i,k) \leq w(i,j) + w(j,k)$ would hold $\forall i, j, k$ in that order. In other words, the path that skips slices would always be favoured. This questions the meaningfulness of such a shortest-path algorithm when applied to a registration problem (histology reconstruction). In the case of [23] and [98], though, alternative paths may have been chosen on occasions where the inequality is violated.

I propose an adjustment to the shortest path search in a graph where weights are based on similarity after registration: comparability between the different paths (*i.e.,* sequence of transformations) is ensured by computing distances on the same two images (in terms of information content). Let us consider the three registrations mentioned earlier between slices i, j and k providing us with the transformations $T_{i\leftarrow j}$, $T_{k\leftarrow j}$ and $T_{i\leftarrow k}$. The set $\Big\{ d(i, j \circ T_{i\leftarrow j}),\, d(i, j \circ T_{k\leftarrow j} \circ T_{i\leftarrow k}) \Big\}$ has a total ordering because each weight quantifies

the similarity between the same two slices i and j—the difference being that the floating image is transformed using two different transformations, each of which corresponds to a different path. As a consequence, the "shortest" path can be picked as the one inducing the highest similarity between a pair of images.

Contributions

- I introduce a graph-theoretic method that aims to bypass erratic pairwise linear registrations when reconstructing a volume from 2D histology slices. Unlike previous approaches, the proposed method relaxes the constraint of choosing a reference slice. The main novelty lies in ensuring *comparability* between the weights by design. Indeed, it seems that Yushkevich's original method [23] uses non-comparable weights to skip sections that register poorly (*i.e.*, connected by edges with lower weights) via Dijkstra's algorithm. Instead, I propose to compute a set of weights that has a total ordering for each pair of images subjected to different transformations, thereby asserting the existence of a shorter path and a "best" reconstruction. Although reconstruction is achieved via linear registrations, the resulting alignment may be used as initialisation for further refinement (and improved structural smoothness) using non-linear transformations. I chose not to carry on with this step: although no information about slice thickness was available, the morphology did change from one slice to the next. I preferred to preserve the shape of the tissue rather than arbitrarily and possibly wrongly compensate for distortions.

- One last difference with [23] and [98] is that the use of Dijkstra's algorithm effectively skips slices that register poorly, meaning that those will not be part of the final reconstruction. On the contrary, the present method aims to keep them all, although selecting the "best" (or shortest) path does not guarantee that a registration failure has been corrected.

The key idea is based upon the simple observation described in Fig. 4.1, where the transitive relation on the set N of n slices (or nodes) s is defined as: $\forall\, s_i, s_{i+1}, s_l \in N$ with $l \neq \{i, i+1\} : \left(s_{i+1} R s_l \wedge s_l R s_i\right) \Rightarrow s_{i+1} R s_i$, where s_l is an intermediate neighbouring slice, the binary relation R is equivalent to a linear registration in our case and $\wedge$ is the logical conjunction. This relation can be extended to any number of intermediate slices. In practice,

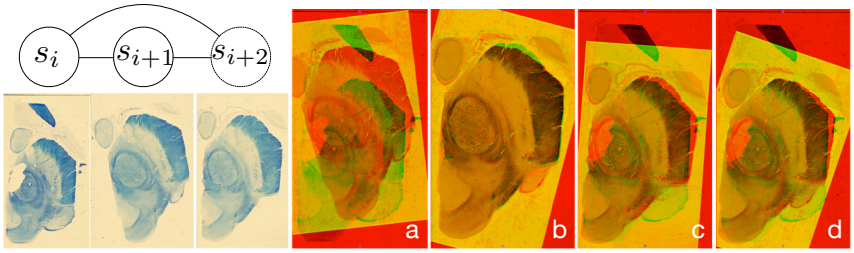

Figure 4.1: Illustration of the pairwise rigid registration specificity among three consecutive histology slices s_i, s_{i+1} and s_{i+2}. The registration of slices s_{i+1} and s_i fails (a), whereas the two neighbouring registrations of slices s_{i+1} and s_{i+2}, and of slices s_{i+2} and s_i work (b)-(c). The right-most panel shows that composing two intermediate good transformations $T_{s_{i+2} \leftarrow s_{i+1}}$ and $T_{s_i \leftarrow s_{i+2}}$ results in a better alignment of slices s_{i+1} and s_i (d).

this means that instead of relying on a single transformation between adjacent slices, every transformation is expressed 1) directly and 2) indirectly as the composition of two (or more) transformations using neighbouring slices. For every pair of adjacent slices (s_i, s_{i+1}), one thus aims at finding the transformation (should it be a composition of intermediate transformations), or path, that minimises the dissimilarity. The process is iterated until convergence to guarantee the recovery of a reconstructed histological volume with continuous structures.

4.2 Preprocessing

4.2.1 Intensity standardisation

Inconsistencies in the staining process may exhibit large differences in the appearance of slices. In order to standardise their texture, an optimal cumulative distribution function (CDF) matching algorithm [456] is used. It makes use of the advantageous property that a CDF is a monotonically non-decreasing function, as opposed to histogram matching which involves distributions with complex non-linear behaviours. In effect, every value from the target distribution is mapped to its nearest value in the source distribution (Fig. 4.2a). Similarly to the registration problem, a reference histogram is required, to which every other histogram is matched, or as in [142] the normalisation between each pair of adjacent slices is propagated along the stack, which goes back to implicitly taking the first histogram as reference. This means the intensity-compensated stack changes with the choice of the reference slice. To bypass the non-uniqueness of the solution, a groupwise approach was chosen (Fig. 4.2b). The CDFs c of the images of slices are derived from their histograms, and the mean CDF $\widetilde{c}$ is computed using least trimmed squares (LTS), which consists of minimising: $\widetilde{c} = \arg\min_{c} \sum_{i=1}^{h} \left(r^2\right)_{i:n}$, where $(r^2)_{1:n} \leq \ldots \leq (r^2)_{h:n}$ are the ordered squared residuals, $r_i = \sum(c_i - c)$. LTS regression consists of finding the subset of $h < n$ CDFs (n being the

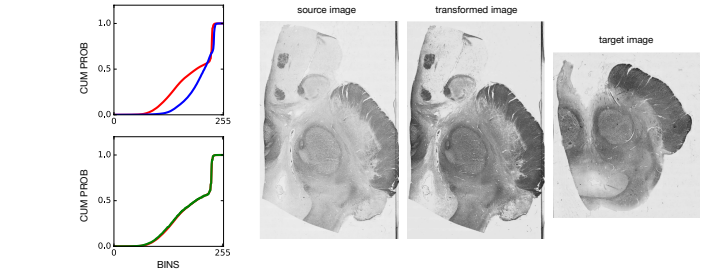

(a)

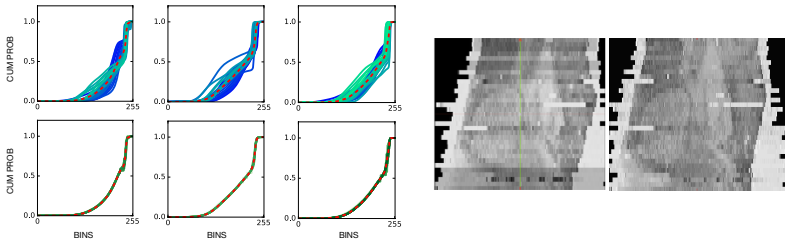

(b)

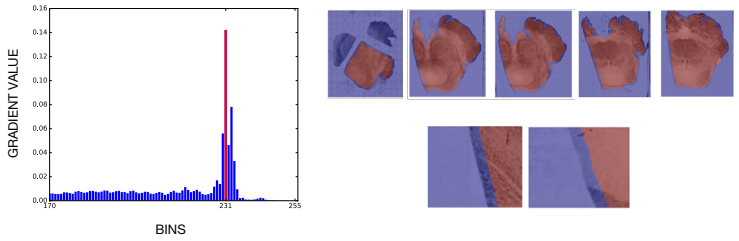

(c)

Figure 4.2: Normalising intensities using optimal cumulative distributions function (CDF) matching algorithm. (4.2a) Source (blue), target (red) CDFs and transformed (green) CDFs are shown. The next panel shows the source image transformed according to the target's intensity distribution. (4.2b) The CDFs of all the histological sections (blue) that compose three datasets (one for each column) are transformed CDFs (green) to match an unbiased average CDF (red) and the resulting correction is shown next to it. The threshold used for masking is computed for every image using its CDF and refers to the bin associated with the largest gradient value. (4.2c) Mathematical morphology is then applied to fill masks and crop tissue edges.

total number of CDFs) whose least squares produces the smallest sum of squared residuals. The number of inliers was set to $h = \lfloor n/2 \rfloor$, assuming that the outliers constitute less than 70% of the CDFs; this is a rough initial guess reflecting the data quality: looking at the data, it seemed reasonable to consider that around 30% of the slices had a severe intensity bias. This way, the bias from these outliers was decreased. Every CDF is then matched to the estimated mean CDF, $\widetilde{c}$.

4.2.2 Masking

Every slice has its tissue masked in order to drive the registration process using relevant information only. This is solved as a two-class problem, where the large contribution of the background (high) intensities can be identified in the matched CDFs, $c_i^{'}$ (*i.e.*, largest slope). The threshold is therefore set as the bin where the derivative of $c_i^{'}$ is maximum. Note that problems may occur when the background is not the dominant region in the image but no such situation was encountered here. Besides, it seemed robust to noise since no smoothing of any kind was applied to images prior to computing their masks. Erosion (the size of the structuring element depends on the resolution of images) is then applied to the binary image so that the edges of the tissue block are not taken into account (Fig. 4.2c). This, in addition to the fact that largest connected component is kept as the final mask, is to prevent unwanted boundaries due to tearing from impacting the registration.

4.3 Shortest path optimisation

The method finds the shortest paths in a dynamic graph. By dynamic graph, one denotes the graph $G = (N,A)$ subject to a sequence of updates. A, is the set of arcs and each arc represents a rigid registration between two connected nodes. A depends on two parameters, η and ε, being respectively: the number of neighbouring slices taken into account in the shortest path search, and the maximum gap tolerated between two slices to be registered. The cost function to optimise is expressed as:

$$\sum_{1\leq i\leq n-1} \min_{T_{s_i\leftarrow s_{i+1}}} d\left(s_i, s_{i+1}\circ T_{s_i\leftarrow s_{i+1}}\right), \tag{4.3}$$

where d is the dissimilarity and $T_{s_i\leftarrow s_{i+1}}$, an element of the special Euclidean group $\mathrm{SE}(2)$, is the rigid transformation that minimises d. G is static between two updates and I aim at shortening the arcs (s_i, s_{i+1}).

4.3.1 Generating the graph G

For a given pair (s_i, s_{i+1}), let K be the total number of paths that connect, directly and indirectly, s_{i+1} to s_i. A path $p_{i,k}$, $k \leq K$, exists if it meets three conditions:

(i) $p_{i,k}$ is a directed[1] acyclic graph (since, by composition of the transformations associated with each edge, a cycle would be equivalent to applying an identity transforma-

[1]The directionality constraint can be dropped here since we use transformations that are inverse of each other when two nodes are swapped (see §4.3.2). Therefore a sufficient condition is that $p_{i,k}$ is a tree.

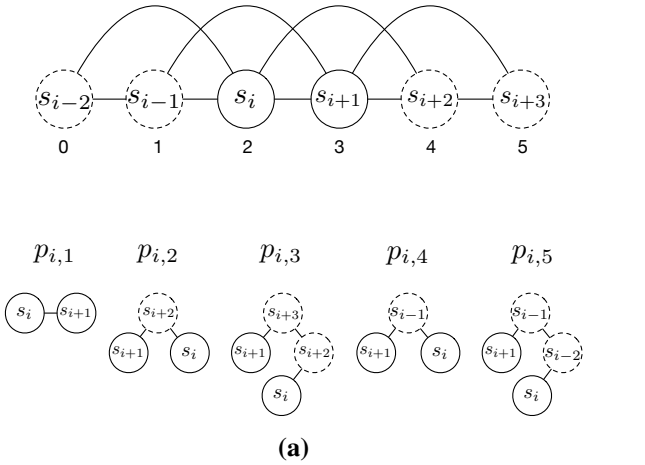

(a)

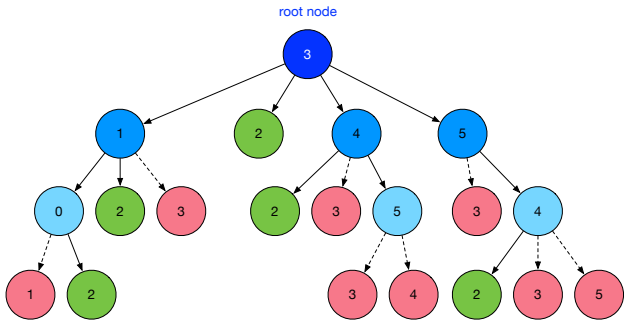

(b)

Figure 4.3: The subgraph and the set of paths associated with a pair of adjacent slices (s_i, s_{i+1}) are presented in (4.3a) ($\eta = 2$ and $\varepsilon = 1$). In practice, the set of paths is obtained from searching a subgraph according to the three rules listed in §4.3.1 using Breadth-first search (4.3b). The exploration starts from a root node (dark blue) and consists here of three levels of neighbours. Red nodes correspond to cases where not all three conditions are respected. This example considers 6 slices numbered from 0 to 5 and it is the pair $(2,3)$ that is looked at. Once the list of paths is available, the path $p_{i,k}$ ($1 \leq k \leq 5$ here) with the minimum cost is identified and the arc (s_i, s_{i+1}) is updated accordingly.

tion).

(ii) every arc of the path $p_{i,k}$ involves only nodes which indexes are within the range $[i-\eta; i+1+\eta]$,

(iii) if j is the index of the current node, a successor is within the range $j \pm (\varepsilon + 1)$.

This inspection is done using a breadth-first search (Fig. 4.3b)—other algorithms for searching trees may be used but were not considered here. Thus, the arc set of G, $A(G)$ is the union of the arc sets of all the subgraphs associated with pairs (s_i, s_{i+1}) and paths $p_{i,k}$ (Fig. 4.3a). The transformation $T^{(k)}_{s_i \leftarrow s_{i+1}}$ associated with the pair (s_i, s_{i+1}) and path $p_{i,k}$ is defined as the

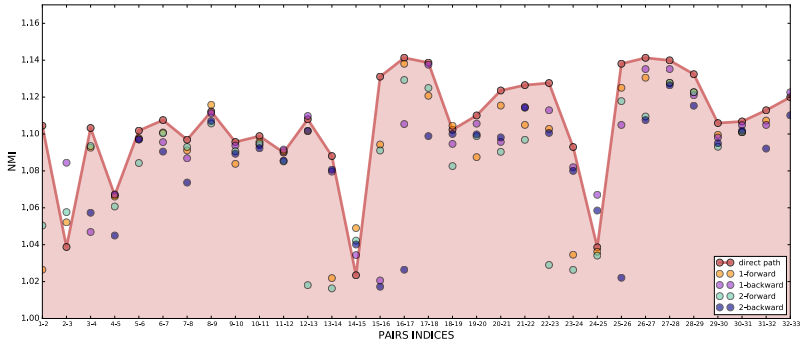

Figure 4.4: The costs of each path for every pair of adjacent slices, *i.e* using direct registration (p_1: red) and four indirect registrations (p_2: orange; p_3: cyan; p_4: magenta; p_5: blue) are ranked at every iteration. The figure shows the second iteration of our approach. The registration illustrated in Fig. 4.1 for the pair $(14, 15)$ can be further improved and we can see that the direct path (whichever transformation(s) it was made of at the previous iteration) would be replaced by the transformation obtained through p_2 at the next iteration. On the other hand, it seems to have settled already for most of the other pairs.

composition of the transformations of every arc in the arc set of $p_{i,k}$.

4.3.2 Registrations

The rigid registrations[2] are done using the block-matching strategy described in [323]. Prior to any registration, we use the masks obtained in §4.2.2 and align the centres of mass of the two binary images. The reason for this is that the size of the search neighbourhood for a given block may not be large enough in cases where the tissue does not lie in the middle of the glass slide (see Tile-based approaches in §3.1.2 for more details). Aligning the centres of images may therefore not suffice—and lead the optimisation to get stuck in a local optimum—as locations of the tissues may vary substantially from one slice to the other. Rather, aligning the axes of inertia through, for example, the principal axis transformation, could be considered knowing that block matching does not capture large rotations; however this means presupposing that the tissue shape does not approximate a circle.

The transformations are symmetric [259], making the graph G undirected. The computation of the transformations is done once for all before the shortest path search, and the list is given by the arc set $A(G)$.

[2] `http://sourceforge.net/projects/niftyreg/`

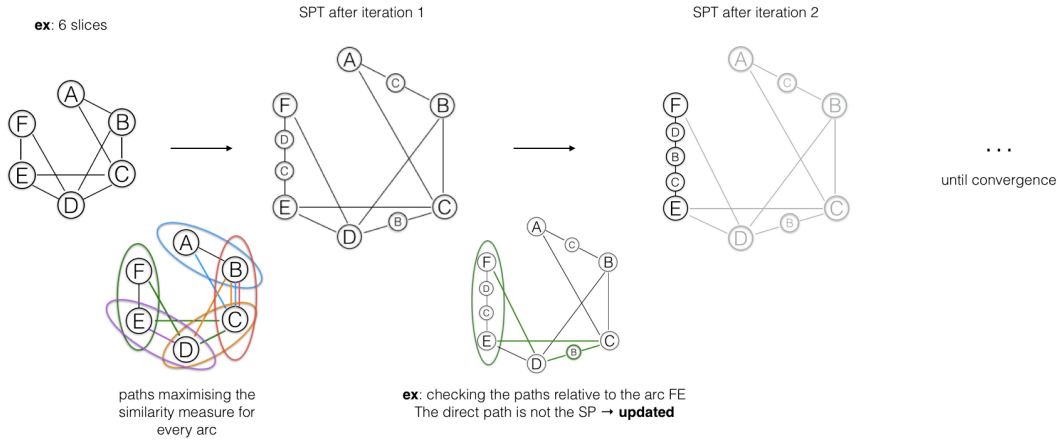

Figure 4.5: Updates of a graph made of 6 slices. The first step consists of computing all the pairwise transformations between connected nodes (according to Fig 4.3a). Then, considering the pair (E,F), the set of (di)similarities is computed according to eq. (4.4). In this illustration, the transformation $T_{F\leftarrow E}^{\{E,C,D,F\}} = T_{C\leftarrow E} \circ T_{D\leftarrow C} \circ T_{F\leftarrow D}$, associated with the path $\{E,C,D,F\}$ gives the lowest cost *i.e.,* the highest similarity $d\big(E, F \circ T_{F\leftarrow E}^{(E,C,D,F)}\big)$ between E and F. The same principle is applied to all pairs of adjacent sections in parallel. A new iteration starts when the direct links between all pairs of adjacent sections have been updated with their "best transformation" according to eq. (4.5). The process repeats until convergence (when all direct links are the best paths).

4.3.3 Updates and convergence

G is broken up into smaller overlapping subgraphs. One iteration is complete when all the arcs (s_i, s_{i+1}) of G have been shortened. An illustration is given in Fig. 4.5.

For every subgraph associated with a pair (s_i, s_{i+1}), the set of dissimilarities:

$$D_i = \{d(s_i, s_{i+1} \circ T_{s_i\leftarrow s_{i+1}}^{(k)} | 1 \leq k \leq K\}, \tag{4.4}$$

where $k = 1$ refers to the path connecting directly s_{i+1} to s_i, is computed and has a total ordering (Fig. 4.4). The arc (s_i, s_{i+1}) at the next iteration is associated with the new transformation:

$$T_{s_i\leftarrow s_{i+1}}^{(1)} \leftarrow \underset{T_{s_i\leftarrow s_{i+1}}}{\arg\min} D_i. \tag{4.5}$$

The convergence is reached when all the $p_{i,1}$ (direct links between every s_{i+1} and s_i) are the shortest links. Several similarity measures can be used since intensities have been standardised and the problem is monomodal; normalised cross correlation (NCC), local NCC and Normalised mutual information (NMI) were considered here.

An extra step consists of doing another pass through the method described, using the sequence of "best" pairwise transformations as an initialisation for the registrations to come.

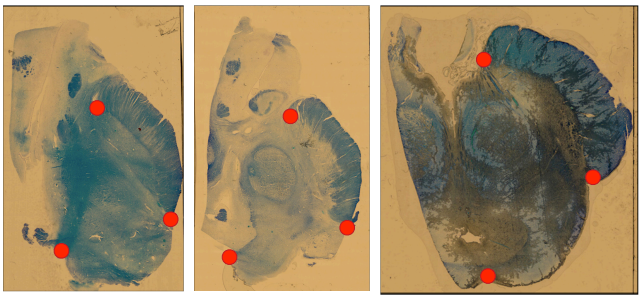

Figure 4.6: Illustrating the landmarks chosen for the first dataset. Three slices are displayed, respectively bottom, middle and top of the stack

By definition of an ill-posed problem, changing the initial conditions changes the outcome; it is thereby proposed that using the newly aligned sections (in the second pass) rather than the original, supposedly worse alignment (in the first pass), will allow for improved reconstruction (if the optimisation got trapped in a local optima at some point for example).

The volume is finally reconstructed by applying the final sequence of "best" transformations to the corresponding slices. The choice of the reference slice only impacts the resolution of the space in which every image is resampled.

4.4 Results and validation

4.4.1 Data

The protocol for the generation of histological data was not made available. Likewise, no information was available on the MRI protocols used for validation. As a result, error measures are given in pixels since the resolution of images was unknown.

4.4.2 Results on real data

The method was applied to three datasets of respectively 33, 25 and 28 histological slices. In the registration step: percentage of blocks used in the optimisation scheme: 70%; number of levels used to generate the pyramids in the coarse-to-fine approach: 5; maximum number of iterations in the LTS to perform per level: 50; standard deviation (in voxels) of the Gaussian kernel used to smooth the pair of images to be registered: 5 (3 in the second pass). The multi-path approach took between 4 and 8 iterations to converge (including the second pass). In the following, target registration errors were computed using three landmarks identified at the base, top and right of the tissue in every section of each dataset (as shown in Fig.4.6); for each slice, mean registration errors (mean RE) were calculated by averaging the distances (in pixels) between its landmarks and the corresponding ones in

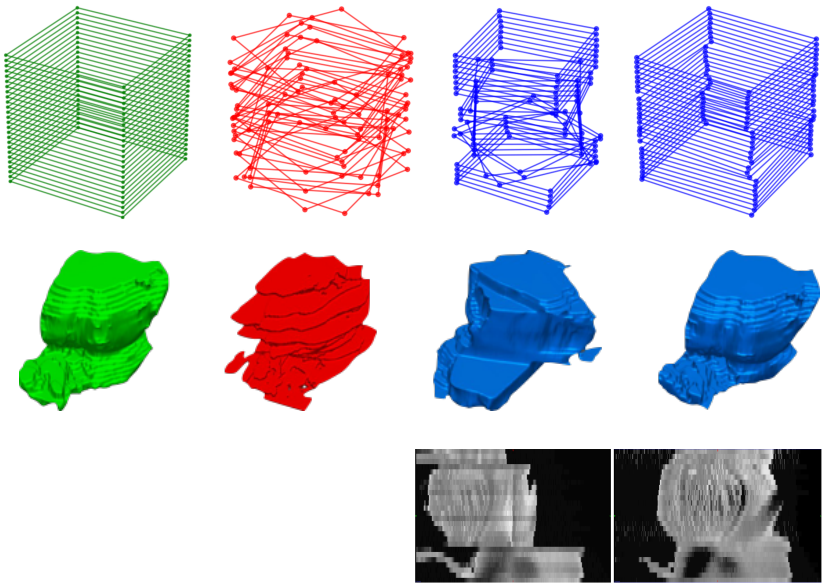

(a) Validation. Corrupted set of slices (red), taken from a sliced 3D MR ground truth image (green) and reconstructions using pairwise registration between adjacent slices (blue, left) and using our method (blue, right). The bottom panel shows the corresponding MR volumes in coronal views.

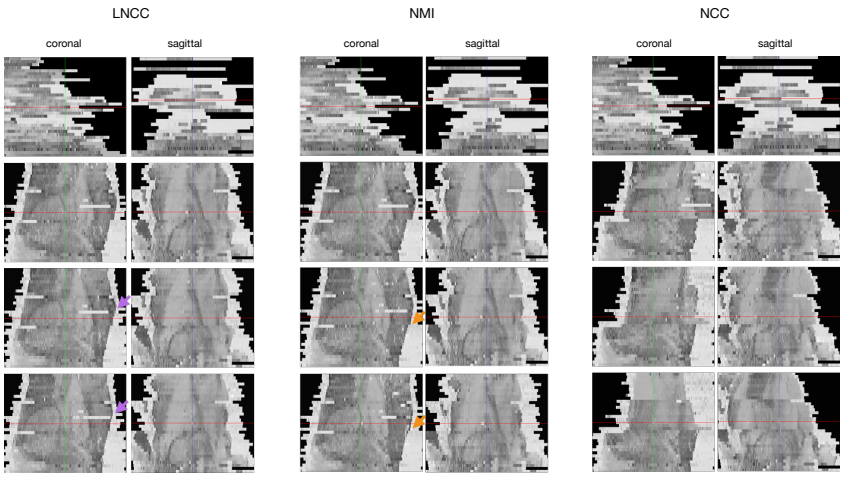

(b) Results. **First row**: reconstruction with an initialisation using image centres, and no graph (*i.e.*, simple pairwise registrations between adjacent slices). **Second row**: reconstruction with initialisation using image centres, our graph theoretic approach and no reinitialisation. **Third row**: results with initialisation using image CoGs, our graph theoretic approach and no reinitialisation. **Fourth row**: results with an initialisation using image CoGs, our graph theoretic approach and reinitialisation. Each column displays results using a different similarity measure to evaluate the costs of each path.

Figure 4.7: Validation and results

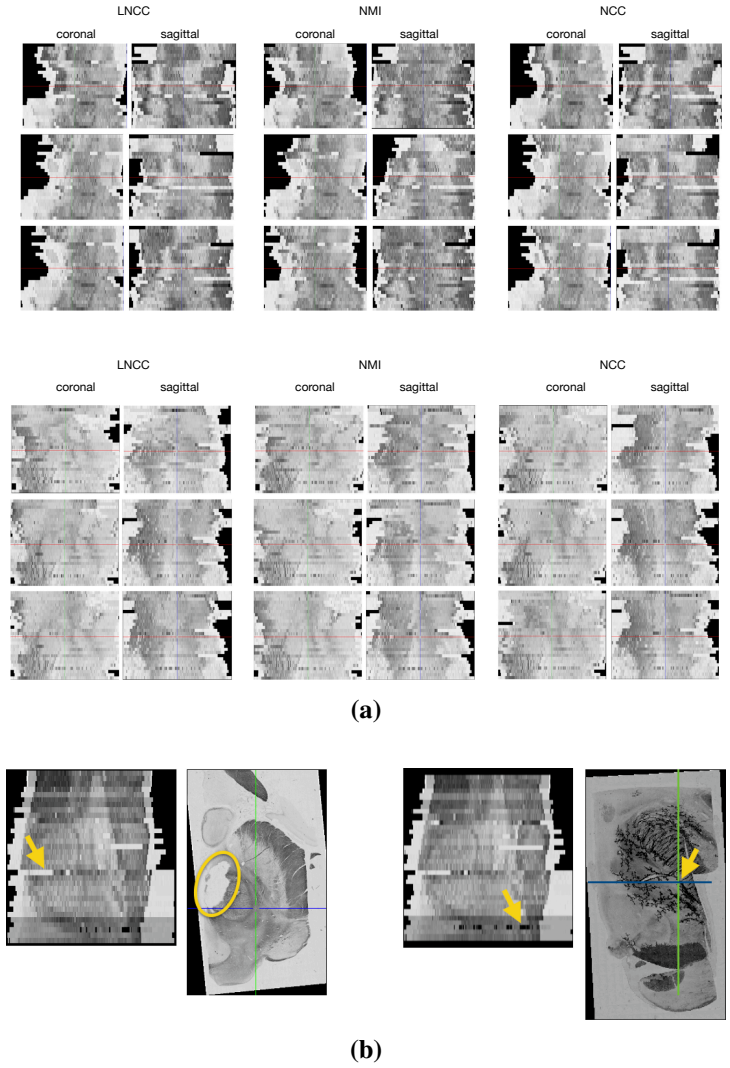

Figure 4.8: Results. (4.8a) Results for 2 other datasets. Settings (by row) correspond to those presented in second, third and fourth rows of Fig. 4.7b. (4.8b) Deteriorations or corruption of individual sections due to *e.g.,* tearing or staining (intensity variations are also visible, prior to standardisation).

the slice below. Intra-rater variability was accounted for by repeating the process five times. Inter-rater variability was not assessed.

In order to choose η and ε, ranges of values were considered: $\eta = [1,2,3,4]$ and $\varepsilon = [0,1,2,3]$ for each dataset reconstruction.

After reconstruction of the first dataset using NMI as a similarity measure, the couple $(\eta = 2, \varepsilon = 1)$ gave the lowest RE among all couples (η, ε): mean RE= 2.0pix $\pm$0.4 (max= 3.1pix). Qualitative results are shown in the last row of the NMI column in Fig. 4.7b. Using LNCC, the same couple $(\eta = 2, \varepsilon = 1)$ was picked, reaching a very comparable mean RE= 2.9pix $\pm$0.8 (max= 3.9pix). Using NCC however, all couples failed to reach as low

a mean RE, though $(\eta = 2, \varepsilon = 2)$ was selected: mean RE= 6.1pix $\pm$1.7 (max= 47.9pix). This is due to two main failures visible in the last column of Fig. 4.7b.

Looking at Fig. 4.7b (see arrows in the last row), one can tell that increased smoothness is reached in the last settings of the method. Besides, local normalised correlation coefficient and normalised mutual information perform similarly (visually) whereas normalised correlation coefficient fails to reconstruct the histological volume. This tells that NCC was less discriminative in the choice of paths since the registration method was a fixed parameter in the method.

The reconstruction accuracy of the last two datasets using the proposed method (last rows of each panel of Fig. 4.8a) is more difficult to assess visually, although smoothness does seem to improve when reinitialisation is performed (last row of each panel). Major failures that could not be corrected happened using NCC and LNCC with any couple (η, ε) for the second dataset, and with NCC and LNCC for the third dataset (misalignments occurred using NMI); this is confirmed by the relatively low "max RE" using NMI (and observed in the last row of the NMI column, bottom panel of Fig. 4.8a).

After reconstruction the second and third datasets using NMI as a similarity measure, the couples $(\eta = 2, \varepsilon = 1)$, and $(\eta = 2, \varepsilon = 2)$ gave the lowest mean REs: mean RE= 4.2pix $\pm$2.5 (max= 7.1pix) and mean RE= 3.6pix $\pm$1.8 (max= 5.6pix) respectively. Using LNCC, the same couples $(\eta = 2, \varepsilon = 1)$, and $(\eta = 2, \varepsilon = 2)$ were chosen with similar mean REs: mean TRE= 4.5 $\pm$2.7 (max= 18.1pix) and mean RE= 3.8pix $\pm$1.8 (max= 2.6pix) respectively. Finally, for NCC, couples $(\eta = 2, \varepsilon = 1)$ and $(\eta = 3, \varepsilon = 2)$ were picked, reaching mean RE= 5.2pix $\pm$2.5 (max= 27.9pix) and mean RE= 4.6 $\pm$1.8 (max= 32.6pix) respectively; one can observe those failures in the last row of the NCC column in both panels of Fig. 4.8a (incidentally, both failures happen at the top of the stacks). The relatively low mean TRE despite the large failure along the stack (max RE) however shows that most of slices register well (though the method still fails to reconstruct the stack perfectly).

Lack of (visual) continuity in some areas may come from the large thickness of slices (which as a matter of fact also hampers not only direct pairwise registrations, but also indirect ones when slices further above or below are considered in the multi-path strategy), especially in the case of the second dataset (top panel of Fig. 4.8a). Note that darker pixels in sections arise due to staining, and missing pieces are clearly visible (Fig. 4.8b).

4.4.3 Validation on MR datasets

In order to validate the efficiency of the proposed method, two MR volumes were sampled to create a sequence of 2D slices perfectly aligned: MR1, with 26 slices and MR2 with 29 slices. These volumes were used as our ground truths to compute target registration error (TRE). The resolution of 2D slices was 512×512pix. Every 2D slice was corrupted with random rotations ranging from [-50;50] (in degrees) with uniform distribution. This range proved sufficient considering it could potentially cover cases where two adjacent slices are more than 90° rotated relative to each there. Note that corrupting with translations was not needed, since images were masked and their centres of mass were aligned. Several levels of Gaussian noise were added to images ($\sigma_{noise} = 0.05, 0.1, 0.5$). For each set of MR slices, and each level of noise, 1000 such volumes were produced.

As per the choice of the parameters η and ε, each of the 1000 volumes from MR1 and MR2 were reconstructed ($\sigma_{noise} = 0.05$) using the proposed method with different values of $\eta = [1,2,3,4]$ and $\varepsilon = [0,1,2,3]$. The minimum average TREs were reached with the couples $(\eta = 2, \varepsilon = 2)$ $(\eta = 3, \varepsilon = 3)$ respectively: mean TRE=2.3pix $\pm$1.2 (max= 3.6pix) and mean TRE=2.6pix$\pm$1.7 (max= 4.7pix). Note that errors were computed using the corners of MR images, less prone to errors that picking landmarks though magnifying the effect of misalignments. These couples were used to assess the difference in the TRE distributions for both datasets using the proposed method and direct pairwise reconstruction.

As per MR1, for noise level $\sigma_{noise} = 0.05$, there was a significant difference between the two distributions (Kolmogorov-Smirnov test, $p < 0.01$); although still significant, it raised to $p < 0.05$ for both noise levels $\sigma_{noise} = 0.1$ and $\sigma_{noise} = 0.5$.

As per MR2, for noise level $\sigma_{noise} = 0.05$, there was a significant difference between the two distributions ($p < 0.01$); however no significant differences were found for noise levels $\sigma_{noise} = 0.1$ ($p < 0.1$) and $\sigma_{noise} = 0.5$ ($p = 0.13$).

For the sake of illustration, Fig. 4.7a shows one repetition with noise level $\sigma_{noise} = 0.05$ for MR1: the volume exhibited two major failures after direct pairwise reconstruction, which were corrected using the proposed method. On the other hand, MR2 was unique in that the pairwise reconstruction was inducing a spiral movement of the stack for lower values of η and ε (and $\sigma_{noise} = 0.05$). This is illustrated in Fig. 4.9 $(\eta = 2, \varepsilon = 1)$, where the error accumulates (almost linearly—that would be the case for a helicoid). By taking into account registrations involving pairs of non-adjacent slices (further ahead, *i.e.*, with $\eta = 3$),

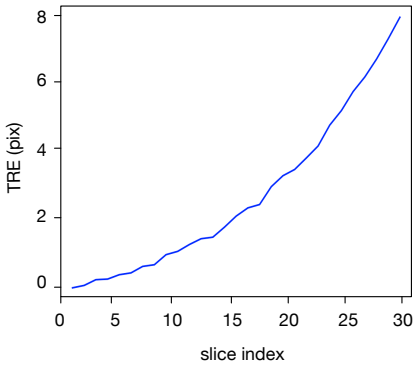

Figure 4.9: Illustrating the spiral effect when reconstructing MR2 using $(\eta = 2, \varepsilon = 1)$.

and allowing for further jumps ($\eta = 3$), the latter effect was constrained and the TRE was reduced to the previously given value. Setting the values of the couple (η, ε) highly depends on the dataset at hands, and especially the thickness of slices.

4.5 Discussion

General comments The method proposed here allowed explaining correspondences between adjacent slices in different ways. The criterion that was used for the ranking of the paths was a similarity measure computed after registration between every pair of slices. More advanced criteria may be needed to quantify registration failures: although it seemed to provide "visually satisfying" reconstructions with LNCC and NMI (at least in the case of the first dataset), NCC was apparently unable to capture the right sequence of paths. In other words, it could be that updating the graph according to a certain path (chosen with NCC) at a certain iteration has aligned slices in a configuration that will then make the registration between two slices fail whatever the path. Among possible improvements, one could think for example of using grey-level co-occurrence matrices, as Cifor *et al.* [24] did in the context of smoothness quantification, to spatially compare the textures of registered adjacent slices (considering intensities have been standardised).

Like with direct pairwise reconstruction methods, the success of that method depends on the quality of sections and "how well" they are placed on the glass slides since it relies on intensity-based registrations. Its main advantage can however be illustrated as follows: knowing that in general direct pairwise registration methods (using block-matching) are unlikely to account for rotations larger than 90 degrees, let us consider that case, where two adjacent sections, a and b are 90-degree rotated relative to each other. If a third slice, c (immediately) following b is 45-degree rotated relative to a, registration between these two

is less likely to converge to a wrong optimum. Similarly, a second intermediate registration between c and b eventually connects a with b. An alternative to that limitation would be to consider geometric (landmark-based) registration methods.

Lastly, the reader is referred to §3.5.1 for a discussion about the usefulness of such reconstruction as an initialisation for multi-modal registration with medical imaging.

Intensity standardisation Variations in the colour and intensity of e.g. H&E-stained histological slides can potentially hamper the effectiveness of quantitative image analysis. Standardisation of histopathological images to reduce the effect of these variations is necessary. However, most methods developed in the field of computer-based histology reconstruction rely on histogram matching and thus do not address the full dimension of the problem. Those methods, like the one presented in this chapter, focus on transforming image intensity profiles solely based on pixel greyscale values, without caring about the properties of the underlying tissue. Although it is true that they ease subsequent segmentation/classification tasks and grant visual convenience, normalisation methods would be a lot more relevant to any subsequent pixel-based analysis if they took into account, for example, the variations in absorbance of staining compounds, *i.e.*, if they actually addressed the problem of retrieving the biological component of a pixel value [155] (see **colour normalisation methods** in §2.5). By extension, statistical analyses performed across modalities, for example to compare histology with medical imaging, must rely on standard signals. Medical images require careful handling too (various preprocessing methods exist including bias field correction, motion, aliasing artefacts and magnetic susceptibility artefacts correction, etc.) and understanding the magnetic properties of tissues is still an active area of research.

Registrations As in [177], it is chosen to preserve the shape of the tissue at this step rather than arbitrarily and possibly wrongly compensating for distortions via non-linear registrations. Thus, the number of degrees of freedom was restricted to 3, as no external information about the true shape was used here. The number of rigid registrations is $\sum_{j=0}^{\varepsilon} N-(j+1)$, making the method have a linear time complexity (although all the registrations were performed in parallel). The previous number does not depend upon η because redundant registrations are discarded and the transformations are symmetric (only the inverse of a computed transformation is taken when needed). η and ε should be chosen according to the spacing between slices, and the "speed" at which structures change across slices. Indeed, large η and ε will not allow explaining correspondences better if it involves looking too far away in

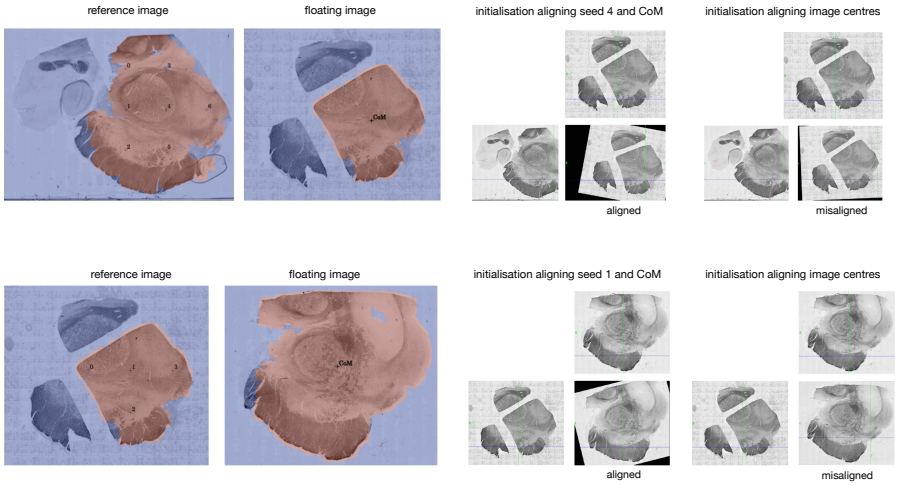

Figure 4.10: Pairwise linear registration involving a torn piece of tissue. Masked tissue is displayed in red (background is blue). Note that the best seed roughly corresponds to the centre of mass (CoM) of the largest connected component (in the torn piece) and improves registration compared to initialising with the images' centres. In this illustration, two sections above and below a torn piece of tissue are considered to assess the effect of tearing.

the stack and this will only increase the number of registrations to compute.

Dealing with artefacts The present framework is proposing alternative ways to reach alignment despite various degradations, rather than addressing the correction of any of them specifically. Robustness to degradations is actually largely dependant upon the registration method itself. But involving slices with slightly different features, positions and orientations that are potentially more conducive to reaching global optimum is most likely helping the process.

The method showed robustness to tissues torn into several pieces when the largest connected component was used to drive the registration of the entire image (Fig. 4.2c and 4.10). One may also want to consider each connected component as an independent tissue element, and then fuse them back into a unique image after separate alignments, as inspired from [246].

Future works may involve more complex image correction techniques able to differentiate between cases where tissue is missing or just torn open, also discussed in §3.5.2.

Chapter 5

Registration of Histology and MRI via Partial Matching of Shape-Informative Boundaries

5.1 Introduction

5.1.1 Overview

Image registration between histology and magnetic resonance imaging (MRI) is a challenging task due to differences in structural content and contrast.

Too thick and wide specimens cannot be processed all at once and must be cut into smaller pieces. This dramatically increases the complexity of the problem, since each piece should be individually and manually pre-aligned.

According to the survey of Chapter 3, it seems that no automatic method can reliably locate such piece of tissue within its respective whole in the MRI slice, and align it without any prior information.

The problem being multimodal and fractional by nature (in the sense that only a *fraction* of tissue is to be registered with its whole in the medical image), it seems natural to formulate a solution that involves contrast- and geometric-invariance, as well as locality. Following those requirements, the proposed solution is based on:

(i) a representation of images using pieces of their level lines (§5.2) *i.e.*, the boundaries of level sets, which for some of them, coincide very well with objects boundaries. It allows to reach contrast invariance and to consider several structural layers in the tissue (level lines coincide very well with objects boundaries)—as opposed to relying solely on its outer boundary. This representation grounds the shape recognition

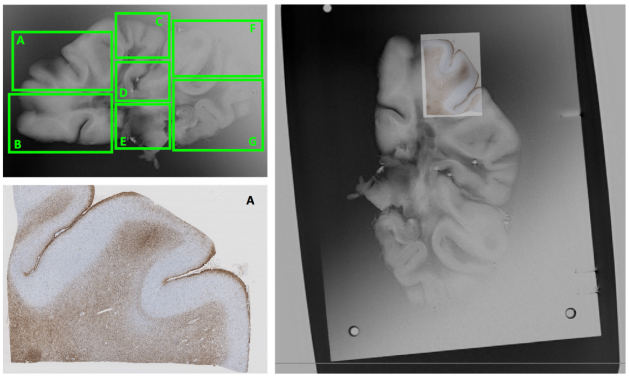

Figure 5.1: Given a histological slice (bottom left) part of a whole specimen, our method aims to automatically spot where it was taken from in the clinical image and align it (right). The result should agree with the areas delineated prior to cutting (top left) to avoid any manual intervention.

process which is necessary to multimodal alignment between histology and MRI.

(ii) a selection of shape-informative (or meaningful) level lines, based on length, contrast and irregularity (§5.3). From there, characteristic shape elements can be extracted locally along meaningful boundaries via their refined bitangents (§5.4).

(iii) a projective-invariant encoding of shape elements[1] (§5.5), so as to be robust to some non-linear deformations that tissues undergo during the histological process, and their comparison using the Fréchet distance; the minima correspond to matching pairs used for alignment. Outliers are robustly discarded using a threshold on the distance and RANdom SAmple Consensus.

Altogether, this allows matching shape elements regardless of the orientation of the tissue on glass slides. Registration is obtained as a result of shape recognition (§5.6).

5.1.2 Problem formulation

The problem to be addressed in this chapter is: locating and registering an object, part of a whole, within that whole.

The objects are a digitised histology section, sampled from a whole specimen that was imaged using conventional clinical imaging—MRI (see Fig. 5.1). An MR plane, manually picked for its partial similarity to the piece of histology is considered in the following.

[1] Shape encoding relies on bitangents—which use in computer vision problems is established since Lamdan, Rothwell...in the end of 1980s and the 1990s—extracted along a curve. Their endpoints define pieces of level lines, the shape elements, which can then be encoded.

Most of the observations, properties and choices described in the following overlap with the ones presented in §3.5.2 and Chapter 3 as a whole.

Given that problem, one wants the solution to have the following properties:

(i) *invariant to homographies*: as seen in the previous chapters, the tissue may suffer distortions such as non-uniform shrinking, shearing and other non-linear deformations during histological processing, microtomy or flotation; tissue pieces also lie at variable locations/orientations on glass slides and reflexions can occur when the tissue is picked from the microtome stage and placed onto the flotation bath.

(ii) *invariant to contrast*: an MRI sequence is set to produce a given contrast image of the specimen, such as T2-weighted (T2w), T1, PD, etc. Equivalently, histology produces sections stained with various dyes. Actually, even letting aside the fact that the histological process induces various alterations such as folding, holes, cracks, contaminants etc. (and thereby creates unique features) [457], the very contrasts of both modalities condition the presence or the absence of comparable content across images. In other words, a one-to-one mapping between histology and MRI is not (and rather far from being) guaranteed.

(iii) *local*: histopathology laboratories can receive tissue samples that are: (p1) too wide or (p2) too thick, to be processed as they are. The sample is therefore cut into separate sub-blocks, each of which is processed individually for histology. Unless additional scans of sub-blocks are acquired, one must record which part of the sample each sub-block corresponds to and use that information to initialise the registration of histological slices with the clinical image, or manually align them. As for (p2), attempts at using intensity-based similarity measures have been made to initialise registrations, but those are ambiguous and rely on absolute measures rather than relative ones [99]. On that matter, it was shown in [350] that direct comparison of images from different modalities is non-trivial, and fails to reliably determine whole slices correspondences. Lastly, the state of the art seems to lack an automatic method to address (p1) (see Fig. 3.4). This is the problem I address here.

Unfortunately, the third requirement almost instantly rules out iconic registration methods: although intensity-based similarity measures have been designed to be robust to intensity changes—including local versions of them—the fractional nature of the problem and the peculiar contents of each modality make a trustful and efficient exploration of the cost

function landscape over the entire image domains very unlikely. In other words, unless the part is correctly initialised in its whole, it will not converge to the *right* solution—the problem being ill-posed, rightness can be defined (and assessed) as a minimal target registration error (TRE) using manually picked landmarks for example.

This essentially leaves geometric methods (*i.e.*, using landmarks). Such approaches however rely on the assumption that there exists a set of characteristic landmarks that is consistent across modalities *i.e.*, which serves the purpose of correspondence; and this is an equally complex task: not only extracting reliable points is difficult [241], but their description is also very challenging (the purpose of multimodal imaging being to combine images of different nature). More specifically, local intensity mappings are non-linear and conventional images may exhibit different structures [458]—the latter being a reason why intensity-based methods tend to settle in local optima. Hence, classical feature description methods, such as SIFT [279] or SURF [286], respectively used by Saalfeld *et al.* [200] and Lobachev *et al.*[287] to register histological sections together, will also likely fail to match features in a multimodal setting [437]. Incidentally, manual extraction of landmarks may remain the safest way [345].

Note that although geometric methods can be used for more complex transformations than rigid and affine (if the sets of points are large enough and well-distributed), intensity-based methods would likely perform better at such task for they use the entire image domain (contrary to features, which would likely be concentrated along contrasted boundaries).

The additional use of non-linear registration is often a source of discussions in the literature [459, 62]. On the one hand, these transformations can provide a better overlay and grant richer quantitative analyses. On the other hand, there is no preliminary guarantee that the two objects to be deformed are counterparts to each other. By using such transformations, one thus takes the risk of creating wrong correspondences—as in overfitting the wrong target image.

Apparatus have been designed to help cutting the specimen at the *same* interval and orientation as the MRI slices, like in the context of prostatectomy [360], or using 3D-printed brain holders in [361], but their use is not so common yet.

In general, the solution to the registration problem is conditioned by the nature of the histological dataset, if:

(i) It has only few sections that do not cover several MR planes and thus does not consti-

tute a histological volume *per se* (histological sections can also be too sparse). Then, the safest way is picking corresponding slices by visual similarity. However, there have been attempts at solving the registration problem via 2D-2D and 2D-3D approaches. Those rely on different kinds of assumptions presented earlier in §3.2.1.1 and §3.2.1.2.

(ii) It has a sufficient number of sections which span the MRI volume. Then, in view of §3.5.2, registration pipelines like those of Adler *et al.* [98] and Goubran *et al.* [179] can be developed and have proved efficient: both made use of intensity-based registrations but full slices (in-plane) were considered and the specimen, otherwise too thick for histology, had to be cut. While Adler *et al.* fall into (p2) but relied on additional scans of each sub-block, Goubran *et al.* used only one slice of each 4.4 mm-thick sub-block and covered the whole extent of the scanned specimen (and therefore do not strictly address a "part-to-whole problem"). In such pipelines, the serial arrangement of the histological stack and its alignment with the MRI volume are jointly refined via 2D-2D and 3D-3D registrations. Both processes hence benefit from each other as changing one affects the other. This robust initialisation of histology within the MRI volume grants safer use of subsequent non-linear transformations [98].

In the present situation, the original histological dataset consists of a few consecutive slices—the resulting slab being about one order of magnitude thinner than one MRI voxel. At this stage, only 2D-2D or 2D-3D approaches could be considered. In addition, the low resolution of the MR images along z cause the anatomy of the brain to change substantially from one plane to the next; this makes any attempt for interpolation delicate, and the selected approach is thus chosen to be 2D-2D (with a manual selection of the MRI plane that visually looks the most similar to histology). Finally, the problem is fractional; in view of the aforementioned limitations of intensity-based registration methods with respect to initialisation, a geometric approach is chosen and the review of related works is restricted to those.

5.1.3 Related work

One possible strategy to align histology and medical imaging is to simplify the images into their contours, so as to come down to a monomodal registration problem and use the shape information provided by the external boundaries.

Ali *et al.* [103] used contours from both histology and slices from a rat brain atlas, extracted via thresholding and represented using B-splines. Note that edges obtained via edge detectors are not curves but rather sets of points with an orientation, which have to be connected afterwards. They also require different thresholds since contrast is not absolute, are sensitive to noise and rely on multi-scale theory. Then, Ali *et al.* described curves by means of sets of affine invariants constructed from the sequence of area patches bounded by the contour and the line connecting two consecutive inflections. Another solution proposed by Trahearn *et al.* [318] made use of Curvature Scale Space [319] for the registration of whole-slide images of histological sections in order to represent shape (the tissue outer boundary) at various scales.

Davatzikos *et al.* [460] used curvature maps at different scales to match boundaries of full brain MRI extracted via an active contour algorithm. The main weaknesses of active contours are the number of parameters and the sensitivity to initialisation.

An alternative to using a single contour of objects was proposed by Caselles *et al.* [25] within the general field of image analysis, and it grounds the representation of images used throughout this chapter: they observed that level lines provide a complete, contrast-invariant representation of images. Furthermore, level lines fit the boundaries of structures and sub-structures of objects very well. Then, given two images, the problem becomes to retrieve all the level lines that are common to both images; this is however feasible only if curves have been appropriately simplified (smoothed) [433] (p.95). Smooth pieces of level lines (the *shape elements* [461]) can be encoded to represent shape locally in *e.g.*, an affine-invariant manner [462, 463]. The comparison of the resulting canonical curves then permits to identify portions of level lines common to two images.

Contributions

- I present a 2D linear geometric registration method which addresses the joint problem of multimodal registration between histology and an MRI plane, when only a fraction of tissue is available from histology.

- I propose an additional criterion for the selection of meaningful level lines based on the *temperature* (or complexity) of curves, which complements that of Desolneux *et al.* [27] based on contrast only. This contribution, tailored to the medical imaging application, is intended to detect first and foremost contrasted, irregular level lines (like the brain folding pattern) more useful to the shape recognition process so as to

to make the method less compute-intensive and more robust to noise than curvature-based measures.

- I propose an efficient refinement of bitangents locations via ellipses fit around their end points and show improvement in the final alignment.

- I extend Rothwell's framework for object recognition by considering more peculiar shape elements using bitangents crossing the level lines; I propose to compare the resulting canonical curves (invariant to projections) via the Fréchet distance.

- I propose to fuse information from several MRI modalities by combining meaningful boundaries from each one of them in a single set used for comparison with histology. Similarly, the set of meaningful boundaries from histology is composed of those from each dye (11).

- I justify robustness of the approach to intensity bias—which commonly hampers medical image analysis—thanks to the locality and contrast-invariance requirement(s).

- I evaluate the performance of the proposed method, using BrainWeb T1 and T2w MRI contrasts, as well as a dataset composed of histology and MRI (in the context of multiple sclerosis—referred to as MS dataset in the following).

5.2 Preprocessing

Two standard preprocessing steps were used: first, smoothing, in order to simplify the image, preserve the shape of the tissue, remove unnecessary details and obtain smooth level lines (Fig. 5.2a); then, intensity correction, in order to account for inhomogeneities of the field in MR images or illumination in histology.

Smoothing is based on Affine Morphological Scale Space (AMSS) [464]. It is governed by the partial differential equation: $\frac{\partial u}{\partial t} = |Du|\text{curv}(u)^{1/3}$ where u is the image, $|Du|$ is its gradient, $\text{curv}(u)$ is the curvature of the level line and t is a scale parameter. The sequence of updates necessary to its computation follows that presented by Mondelli and Ciomaga [465] (equations of §2.3). Whereas linear smoothing (*e.g.*, with a Gaussian kernel) is related to the heat equation (and therefore tends to blur an image as scale increases), AMSS is asymptotically related to morphological operators. Indeed, as noted previously

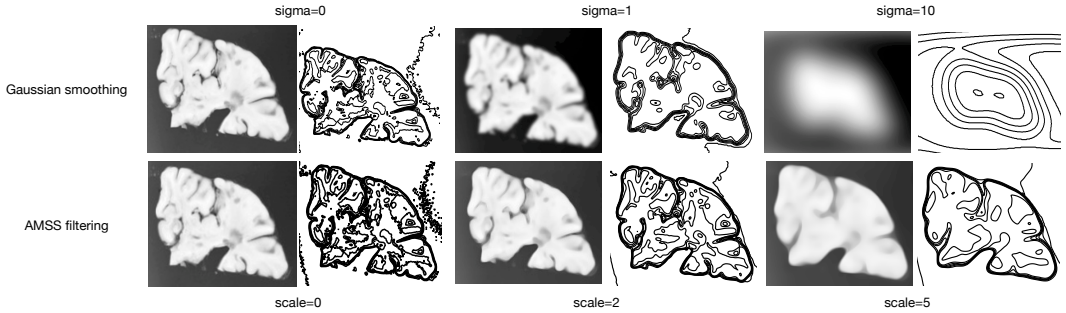

(a)

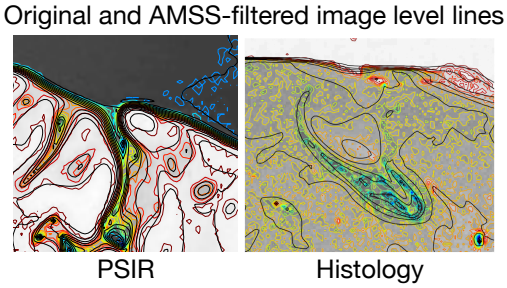

(b)

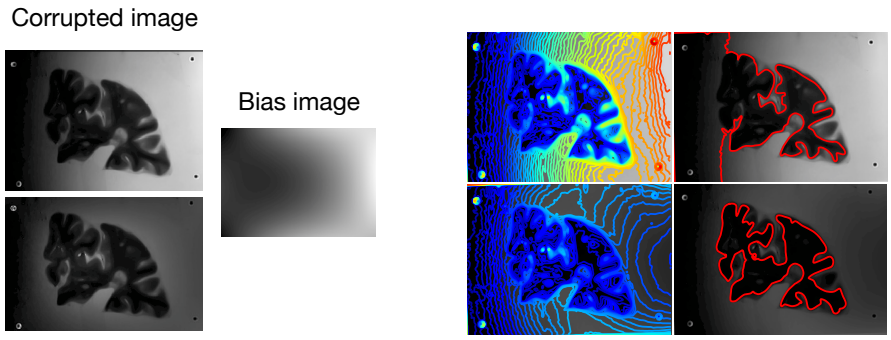

(c) **(d)**

Figure 5.2: Smoothing and bias correction. (5.2a) Gaussian smoothing at large scales breaks the topology of level lines (1/16th of all levels are displayed) and does not preserve the object's shape (it actually creates content). (5.2b) Level lines (multiple of 16) prior (in colour) and posterior to AMSS filtering (scale 2). (5.2c) Corrupted and bias corrected images of a T2 image of a human brain, along with the estimated bias (Legendre polynomials of order 2). (5.2d) The effect on level lines of corrupted and corrected images is shown.

[463, 466], smoothing an image is equivalent to smoothing its level lines directly via the alternate application of erosions and dilations. This yields an image for which homogeneous regions are smoothed and the tissue boundaries are enhanced, hence the choice (Fig. 5.2b).

Image intensity correction (Fig. 5.2c) relies on surface fitting [467]: the low-frequency bias of an image can be estimated using an adequate basis of smooth and orthogonal polynomial functions. It then comes down to solving the least square problem $A\mathbf{c} = \mathbf{b}$, where $\mathbf{b} \in \mathbb{R}^N$ is the vector of all the pixels values, and $\mathbf{c}$ the coefficients of one linear combination of basis functions. $A \in \mathbb{R}^{N\times(n+1)(m+1)}$ is the matrix of the system: its k-th row is the vectorised outer product $\Phi(x_k) \otimes \Phi(y_k)$ with $\Phi(x_k) = [P_0(x_k), P_1(x_k), \ldots, P_m(x_k)]^T$ and $\Phi(y_k) = [P_0(y_k), P_1(y_k), \ldots, P_n(y_k)]$ for pixel $k \leq N$. $P_i(.)$ denotes a certain 1D polynomial of degree i. Degrees m and n are usually taken small so as not to overfit the image intensities. The left inverse of A (it is full rank) gives the bias image, and correction is straightforward. The effect bias correction has on level lines is illustrated in Fig. 5.2d and discussed in the following. Note that N3 bias correction was also tried but reached similar results visually.

5.3 Selection of meaningful boundaries

In the following, a level line of an image u is a Jordan curve (a plane closed curve with no self-intersection) contained in the boundary of a level set λ, $\{x, u(x) \leq \lambda\}$. Note that in practice, not all level lines are Jordan curves because closedness is not always guaranteed. Meaningful boundaries of an image are the level lines that are long enough, contrasted enough and complex enough. The detection relies on two geometric events; E_1: "a strong contrast, c along a level line of an image"; E_2: "a high temperature, T along a level line of an image". The notion of temperature relates to the definition of the entropy of a plane curve, which quantifies its behaviour: it is a positive measure that increases with complexity and is null for a straight segment. Considering both contrast and complexity allows to increase the number of false alarms (NFA) of regular (*i.e*, cold) high-contrasted level lines (like the skull or the tissue/background boundary in some cases) and detect first and foremost long, lesser contrasted though convoluted (*i.e.*, hot) boundaries (like the white/grey matter boundary or other tissue inner boundaries), more useful to the shape recognition process. Note that which boundary is most contrasted depends on the MR sequence; this is the reason why I fuse meaningful boundaries from several sequences.

The main rationale of this section is to prune the complete set of level lines—which contains thousands of curves (Fig. 5.6a), and only keep a subset of shape-informative

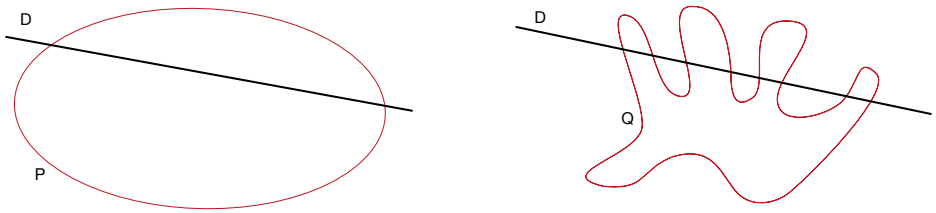

Figure 5.3: The more irregular (or complex, convoluted, chaotic,...) a curve, the larger the possible number of intersections with a line. The curve P would have at most 2 intersections with a random line D of the plane, whereas the curve Q would have at most 8 intersections with it.

boundaries for computational efficiency.

5.3.1 Temperature of level lines

The main idea behind this section is that the irregularity of a curve is seen as the number of its intersections with random straight lines of the plane: one can picture (see Fig.5.3) the fact that the more irregular (or complex, convoluted, chaotic,...) a curve, the larger the possible number of intersections with a line. Conversely, a closed convex curve will have at most 2 such intersections.

In the following, a level line, $\mathcal{L}$ is a plane rectifiable curve of length L. The irregularity of level lines is expressed by their thermodynamic temperature, based on a definition of the entropy, H of curves introduced by DuPain and Mendès France [468]:

$$\mathsf{H}(\mathcal{L}) \stackrel{\text{def}}{=} -\sum_{k=1}^{\infty} p_k(\mathcal{L}) \log p_k(\mathcal{L}), \tag{5.1}$$

where $p_k(\mathcal{L})$ is the probability that a straight line D intersects $\mathcal{L}$ in k points.

5.3.1.1 Entropy of plane curves and integral geometry

The estimation of p_k in (5.1) essentially relies on Morgan Crofton's (1826-1915) result in integral geometry which states that the expected value of x, where x is the number of intersections of a random line with a plane curve, (so the average number of their intersections) is proportional to the length of that curve.

Let $D(p,\varphi) = \{D : 0 \leq \varphi \leq 2\pi, \mathsf{p} \geq 0\}$ be the set of lines cutting $\mathcal{L}$ in exactly k points, where φ is the angle that the direction perpendicular to D makes with a fixed direction and p, its distance from an origin O (Fig. 5.4).

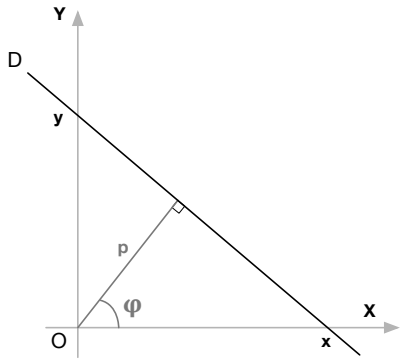

Figure 5.4: One-to-one correspondence between the points (p, φ) of the (p, φ)-plane and the straight lines of the plane.

Hugo Steinhaus rewrote Crofton's result as [469]:

$$\sum_{k=1}^{\infty} k\, m_k = 2L, \tag{5.2}$$

where m_k denotes the measure of $D(\mathsf{p}, \varphi)$ (see (3.5) in [470] and Appendix A.1), which is defined by the integral, over the set D, of the differential form:

$$\mathrm{d}D = \mathrm{d}\mathsf{p} \wedge \mathrm{d}\varphi \tag{5.3}$$

Thus one has:

$$m_k(D; D \cap \mathcal{L} = k) \stackrel{\text{def}}{=} \int_{Card(D\cap\mathcal{L})=k} \mathrm{d}D. \tag{5.4}$$

The left-hand side of Eq. (5.2) can be rewritten as: $\sum_{k=1}^{\infty} k \int_{Card(D\cap\mathcal{L})=k} \mathrm{d}D$ and by the dominated convergence theorem, one therefore has the equivalent equality:

$$\int n_D \, \mathrm{d}D = 2L, \tag{5.5}$$

where the integral extends over all the lines of the plane and $n_D = Card(D \cap \mathcal{L})$, n_D being 0 for the lines D which do not intersect $\mathcal{L}$ (see Appendix A.2 for the proof).

One also has, for the convex hull Ω of $\mathcal{L}$ of perimeter $\mathsf{P}(\Omega)$ (see Appendix A.2 for details), the equality:

$$\int_{D\cap\Omega\neq\emptyset} \mathrm{d}D = \sum_{k=1}^{\infty} m_k = \mathsf{P}(\Omega). \tag{5.6}$$

Now let:

$$p_k = \frac{m_k}{\sum_{j=1}^{\infty} m_j} = \frac{m_k}{\mathsf{P}(\Omega)}. \tag{5.7}$$

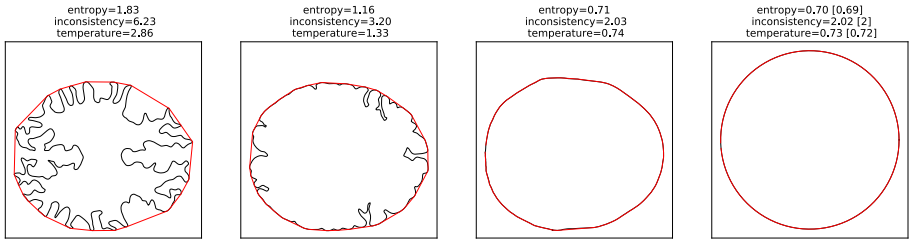

Figure 5.5: Curves of decreasing complexity are shown from left to right. It shows a highly irregular level line (black) and its convex hull (red), which corresponds to the white/grey matter boundary; a level line which delimitates grey matter and CSF; a level line that follows the skull; a circle. For each of those curves, the entropy (5.11), the inconstancy (5.12) [471] and the temperature (5.17) [468] are given and behave as expected: these measures decrease as the curves become more regular, and reach their minimum for a closed convex curve (the example of a circle is taken). The numbers in square brackets are the analytical values.

The distribution that maximises H in (5.1) for a given ratio ${}^{L}/_{\mathsf{P}(\Omega)}$, subject to $\sum p_k = 1$ and $\sum k\ p_k = {}^{2L}/_{\mathsf{P}(\Omega)}$, is a Boltzmann distribution [468]. This can be verified using the method of Lagrange multipliers (see Appendix B for the proof), which yields:

$$p_k = (e^{\beta} - 1)e^{-\beta k}, \tag{5.8}$$

with

$$\beta = \log\Big(\frac{{}^{2L}/_{\mathsf{P}(\Omega)}}{{}^{2L}/_{\mathsf{P}(\Omega)} - 1}\Big). \tag{5.9}$$

The entropy corresponding to the distribution of probabilities (5.8) is therefore:

$$\begin{aligned} \mathsf{H} &= -(e^{\beta} - 1)\log(e^{\beta} - 1)\sum_{k=1}^{\infty} e^{-\beta k} + (e^{\beta} - 1)\,\beta \sum_{k=1}^{\infty} k\, e^{-\beta k} \\ &= -\log(e^{\beta} - 1) + \beta \frac{e^{\beta}}{(e^{\beta} - 1)}. \end{aligned} \tag{5.10}$$

Taking a step back, the original definition of the entropy of a curve given by Mendès France is:

$$\log\ \overline{n}_D, \tag{5.11}$$

where $\overline{n}_D$ is the average number of intersections of a random straight line D with a given plane curve $\mathcal{L}$ which, as seen previously, equals:

$$\overline{n}_D = {}^{2L}/_{\mathsf{P}(\Omega)}. \tag{5.12}$$

One can verify that a closed convex curve has an entropy of $\log 2$. Allouche *et al.* [471]

call $\overline{n}_D$ the *inconstancy* (which minimum value is 2 for a closed convex curve) and (5.11) then reads: "the entropy is the logarithm of the inconstancy". Interestingly, they make the parallel with psychophysics and the Weber-Fechner law, which states that "sensation is proportional to the logarithm of excitation" [472].

Mendès France then proposes the alternative definition (5.1), which is used here, closer to information theory. Using (5.9) and (5.11), (5.10) becomes:

$$\mathsf{H}(\mathcal{L}) = \log\left(\frac{2L}{\mathsf{P}(\Omega)}\right) + \frac{\beta}{(e^{\beta}-1)}. \tag{5.13}$$

In view of Fig. 5.24, one can see that these two definitions of entropy yield similar histograms, since the two quantities are proportional.

5.3.1.2 Thermodynamics and irregularity

A Boltzmann distribution, $\mathcal{F}$ in statistical mechanics is expressed in the form:

$$\mathcal{F}(\mathrm{E}) \propto e^{-E/\mathsf{kT}}, \tag{5.14}$$

where E is a state energy, k is the Boltzmann constant, and T is the temperature of the system. By analogy, the present system is a level line $\mathcal{L}$, in the state energy $k = Card(D \cap \mathcal{L})$ "at a certain time D" i.e., $\mathcal{L}$ has k intersections with a certain straight line of the plane D; and T is the temperature of $\mathcal{L}$.

Intuitively, one can see the macrostate of $\mathcal{L}$ as the average number of its intersections with random straight lines D. Microscopically though, every straight line "interacts" with $\mathcal{L}$ in a certain way, and corresponds to a microstate of the system's energy $E_k \equiv k = Card(D \cap \mathcal{L})$.

Now the statistical expression of the first law of thermodynamics gives, considering a finite number of microstates, M:

$$U = \langle E \rangle = \sum_{k=1}^{M} p_k E_k, \tag{5.15}$$

which defines the internal energy of the macrostate as the average over all M microstates of the system's energy. In other words, the macroscopic thermodynamic properties of $\mathcal{L}$ are related to the partition function that sums the energies of all its microstates. Using (5.8), (5.15) is thus equivalent to:

$$\overline{n}_D = (e^{\beta} - 1) \sum_{k=1}^{M} k e^{-\beta k} = \frac{2L}{\mathsf{P}(\Omega)}, \tag{5.16}$$

where it is assumed that the maximum number of intersections between D and $\mathcal{L}$ is finite. From there, β can be interpreted as $^1/_{\mathsf{kT}}$, which finally yields the definition of temperature of a plane rectifiable curve $\mathcal{L}$ (setting $k = 2$):

$$\mathsf{T}(\mathcal{L}) \stackrel{\text{def}}{=} \frac{1}{2} \left(\log \left(\frac{^{2L}/_{\mathsf{P}(\Omega)}}{^{2L}/_{\mathsf{P}(\Omega)} - 1} \right) \right)^{-1}. \tag{5.17}$$

Eq. (5.17) assigns a temperature of 0 to straight segments (for which $\mathsf{P}(\Omega) = 2L$), and the more complex the curve, the higher its temperature (see Fig. 5.6c). This behaviour holds for other measures of irregularity (see Fig. 5.5). As for closed curves, the minimum temperature is achieved for convex curves and equals $^1/_{2\log 2}$ (since $L \geq \mathsf{P}(\Omega)$, $\forall \mathcal{L}$).

One can also note that the approximation of T around $y = 0$, where $y = {}^1/_x$ and x is a given ratio $^L/_{\mathsf{P}(\Omega)}$, is $y + \mathcal{O}(y^2)$. This means that the temperature of a curve increases linearly with the ratio $^L/_{\mathsf{P}(\Omega)}$ "at infinity" (in our case, for a very long curve packed into its convex hull, say $L = 5\,\mathsf{P}(\Omega)$, then $\mathsf{T} \approx 5$ for example).

5.3.2 *A contrario* detection using contrast and temperature

The method is based on the *a contrario* detection theory introduced by Desolneux *et al.* [474]. It formalises the Helmholtz principle, according to which an event is "meaningful" when the expectation of its occurrences is *very small* in a random image: in the present case, a geometric event that jointly considers length, contrast and irregularity of level lines becomes relevant if it rarely occurs by chance. This allows for the selection of a subset of meaningful level lines. We assume in the following that contrast and irregularity are independent.

5.3.2.1 Contrasted boundaries

Let $x_1, x_2, \ldots, x_l$ be one sampling of a level line, $\mathcal{L}$ of Euclidean length, L[2]. As defined by Caselles and Monasse [476], the x_i are the intersections of $\mathcal{L}$ with the Qedgels (the segments joining two adjacent pixels centres) of an image u. Taking a subset of those points (*e.g.*, every other point, as suggested by Tepper *et al.* [475]) ensures statistical independence

[2]Note that in the original paper of Desolneux, the length of $\mathcal{L}$ was approximated by the number of its sampled points, l—see the definition of the number of false alarms (NFA). However, a better approximation is possible by considering the actual distances between all its points. Adjustments were therefore made in the formulas. Incidentally, it came to my attention that this had already been noted by Tepper *et al.* in [475].

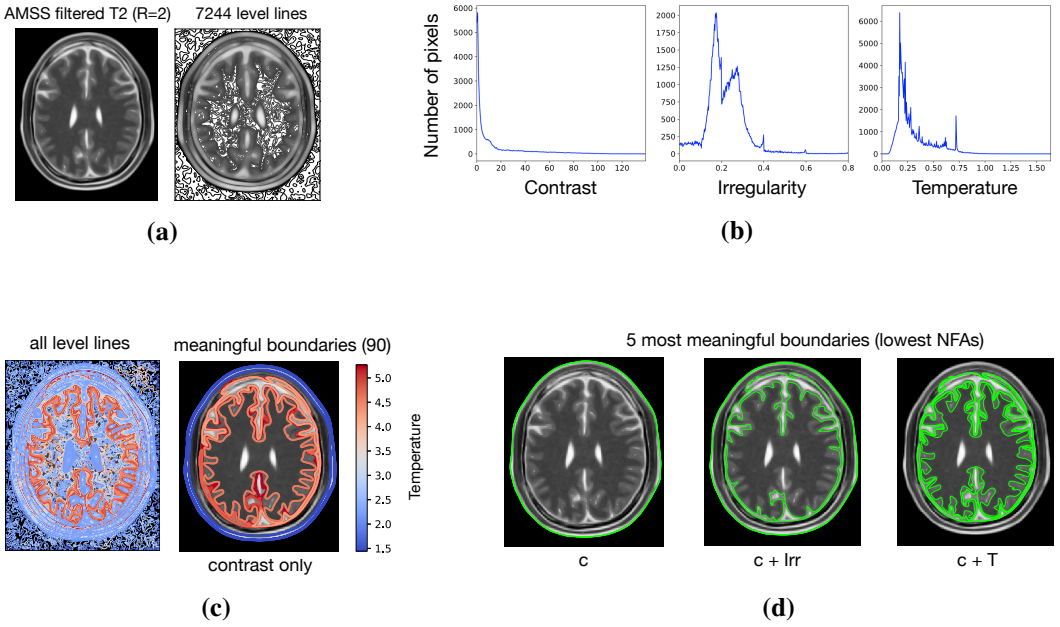

Figure 5.6: Extraction of meaningful level lines based on length, contrast and irregularity. (5.6a) AMSS-smoothed T2 image is composed of 7244 level lines. (5.6b) Histograms of contrast, irregularity and temperature in the T2 image at scale $l_0 = 10$ (for irregularity and temperature). The 90 most meaningful level lines (lowest NFAs), using contrast only, are shown in (5.6c)—colours represent their global temperatures according to eq. (5.17). (5.6d) The 5 most meaningful level lines (in green) using contrast only [27], both contrast and an adaptation of regularity [473] into irregularity (c+Irr), and both contrast and temperature (c+T).

of the gradient values almost everywhere, under the assumption that pixel values of u are independent. Hence the contrasts, c_i at each of these points (defined here as the l_1-norm of the gradient, $D(u)$ of an image u: $c_i = |D(u)|(x_i)$) are independent almost everywhere. Desolneux *et al.* [27] introduce the geometric event E_1: "for all $1 \leq i \leq l$, $c(x_i) \geq \mu$" *i.e.*, each point of $\mathcal{L}$ has a contrast larger than μ. It is only required that a random gradient value is associated with each of the point x_i of $\mathcal{L}$. These l independent random variables have the same distributions $P(|D(u)|(x_i) \geq \mu) = \mathcal{H}_c(\mu)$:

$$\mathcal{H}_c(\mu) \stackrel{\text{def}}{=} \frac{Card(\{x \in u : |D(u)|(x) \geq \mu\})}{M}, \tag{5.18}$$

where M is the total number of pixels where $|D(u)|(x) > 0$ (a dequantisation of the norm of the gradient—to avoid null gradients—is obtained by Gaussian smoothing of u with a standard deviation of 0.5). The number of false alarms (NFA) is then defined as:

$$\text{NFA}_c(\mathcal{L}) \stackrel{\text{def}}{=} N \times \mathcal{H}_c\left(\min_{x \in \mathcal{L}} |D(u)|(x)\right)^{L/2}, \tag{5.19}$$

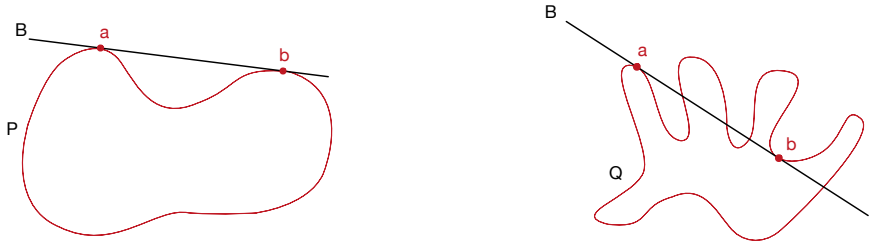

Figure 5.7: The shape elements of P and Q are respectively defined as $P\restriction[a,b]$ (resp. $Q\restriction[a,b]$). B is a bitangent of both curves, *i.e.* a line of the plane that is tangent to a curve in 2 points, and a and b are the 2 points of "bitangency".

where N is the number of level lines in the image. For each level line, the estimation of $\mathcal{H}_c$ is deduced from the image histograms, as illustrated in Fig. 5.6b. A level line is called *meaningful* when $\mathrm{NFA}_c(\mathcal{L}) \leq \varepsilon$.

5.3.2.2 Hot boundaries

The local temperature of level lines relies on a local definition of (5.17), which is obtained by considering the arcs, A_i of lengths L_0 centred at every $x_i \in \mathcal{L}$, and the chords, C_i joining the two endpoints of A_i. Let ω_i be the convex hull of A_i, and setting $\gamma = {}^{2L_0}/_{\mathsf{P}(\omega_i)}$, the local temperature at $x_i \in \mathcal{L}$ is:

$$\mathsf{T}_{L_0}(x_i) \stackrel{\text{def}}{=} \frac{1}{2}\left(\log\left(\frac{\gamma}{\gamma-1}\right)\right)^{-1}. \tag{5.20}$$

Similarly to §5.3.2.1, the temperatures at each point of $\mathcal{L}$ are independent random variables. A second geometric event is now considered, E_2: "for all $1 \leq i \leq l$, $\mathsf{T}_{L_0}(x_i) \geq t$". For the sake of clarity, the scale subscript L_0 in the definition of the local temperature is dropped in the rest of the chapter, but use definition (5.20). It is only required that a random temperature value is associated with each of the point x_i of $\mathcal{L}$. These l independent random variables have the same distributions $P(\mathsf{T}(x_i) \geq t) = \mathcal{H}_\mathsf{T}(t)$:

$$\mathcal{H}_\mathsf{T}(t) \stackrel{\text{def}}{=} \frac{Card(\{x \in u : \mathsf{T}(x) \geq t\})}{M'}, \tag{5.21}$$

which is the probability for a point on any level line to have a temperature larger than t, M' being the total number of pixels where the temperature is evaluated (only level lines of length greater than L_0 are considered).

The NFA (5.19) thus becomes:

$$\mathrm{NFA}_{c\mathsf{T}}(\mathcal{L}) \stackrel{\text{def}}{=} N \times \mathcal{H}_c\left(\min_{x\in\mathcal{L}}|D(u)|(x)\right)^{L/2} \times \mathcal{H}_\mathsf{T}\left(\min_{x\in\mathcal{L}}\mathsf{T}(x)\right)^{L/2L_0}. \tag{5.22}$$

A boundary is meaningful when $\mathrm{NFA}_{c\mathsf{T}}(\mathcal{L}) \leq \varepsilon$, where ε is an *a priori* fixed expectation of false alarms; it is taken equal to 1 in the rest of the chapter. The resulting five most meaningful boundaries (smallest NFAs) are shown in Fig. 5.6d and compared qualitatively with those detected using contrast only, and contrast + irregularity. Irregularity is defined as "Irr = 1 − regularity", using the quantity given in [473] (i.e., the smaller Irr, the more regular the arc) to make it comparable with temperature.

Definition (5.22) conveys the following desirable properties: (i) a contrasted, irregular curve will be detected; (ii) an irregular, non-contrasted curve will not be detected; (iii) a regular curve will not be detected. The extraction of meaningful level lines in the MS dataset (histology and MRI) using contrast + irregularity is illustrated in Figs. 5.8 and 5.9.

5.4 Finding bitangents

Shape elements are extracted by means of bitangents of level lines (Fig. 5.7). Bitangents are identified via the tangent space (§5.4.1) and each one is refined using two ellipses fitted in the neighbourhood of estimated bitangent points (§5.4.2.1). Since two ellipses have at most four bitangents (§5.4.2.2), one needs to be singled out which corresponds to the refined bitangent of the level line (§5.4.2.3).

In the following, a *bitangent point* is one of the two points where a bitangent is in contact with the level line. The *length* of a bitangent is defined as the number of inflections of the portion of level line that it covers. As a result, a *short* bitangent refers to a bitangent that covers portions with exactly two inflections and a *long* one, more than two.

5.4.1 Dual curve

Let $\mathcal{L}$ be a level line. Duality is defined as the polarity that sends any point to a line and *vice versa*. The image of a point with parameter $t = t_0$ is the line:

$$ux(t_0) + vy(t_0) + 1 = 0. \tag{5.23}$$

If the parameter t covers the whole range of definition, the resulting set of straight lines is the envelope of $\mathcal{L}$: the dual $\mathcal{L}^*$ of $\mathcal{L}$ is the set of its tangent lines. A parametrisation of $\mathcal{L}^*$ in homogeneous coordinates can be obtained from (5.23) by differentiation w.r.t the parameter t and elimination. This yields $u = \frac{-\dot{y}(t)}{\dot{x}(t)y(t)-\dot{y}(t)x(t)}$ and $v = \frac{\dot{x}(t)}{\dot{x}(t)y(t)-\dot{y}(t)x(t)}$ with $x, y \neq 0$ (dot notation is used for differentiation).

Dual curves feature the following properties: an inflection of $\mathcal{L}$ maps onto a cusp of

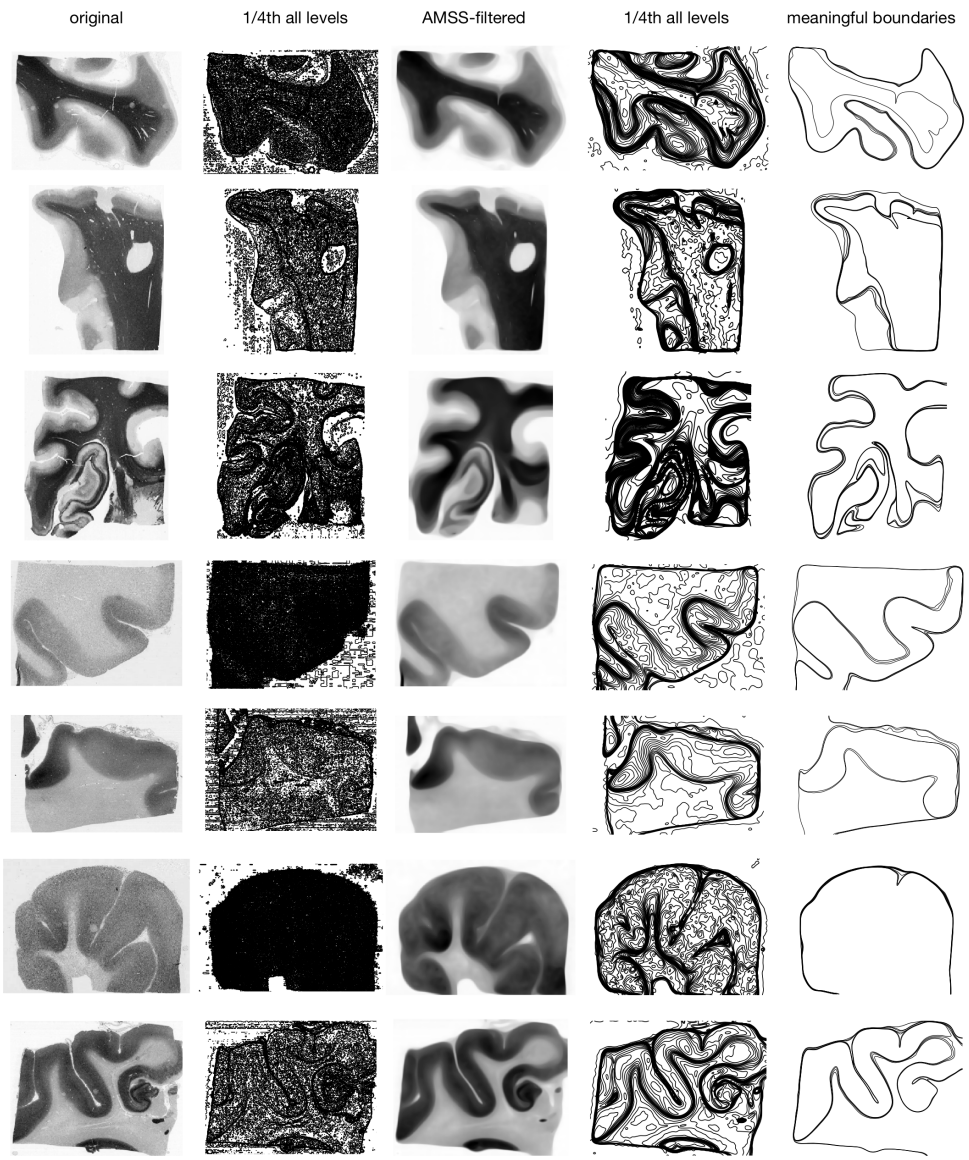

Figure 5.8: *A contrario* detection of meaningful boundaries using contrast and temperature ($c + \mathsf{T}$). Only the 5 level lines with lowest NFAs (5.22) are shown in the last column (and those are the curves used in the rest of the method). Original images and their level lines (1/4th of the levels 0-255 are displayed for clarity) as well as AMSS-filtered (scale 4) images and their level lines (1/4th of the levels) are shown in columns 1 to 4 respectively. Interestingly, one can note that the tears in pieces of rows 2 and 3 disappear after smoothing. In effect, images are greatly simplified: fewer level lines are observed in homogeneous regions of the tissue, while those following well the boundaries were preserved and are smoother (column 4). Besides, the tissue of row 2 exhibits a case where a highly contrasted though regular level line (the ellipse) is not selected (see last column). Finally, the tissue of row 6 illustrates a limiting case where no shape element can be extracted and used for recognition (curves are almost convex).

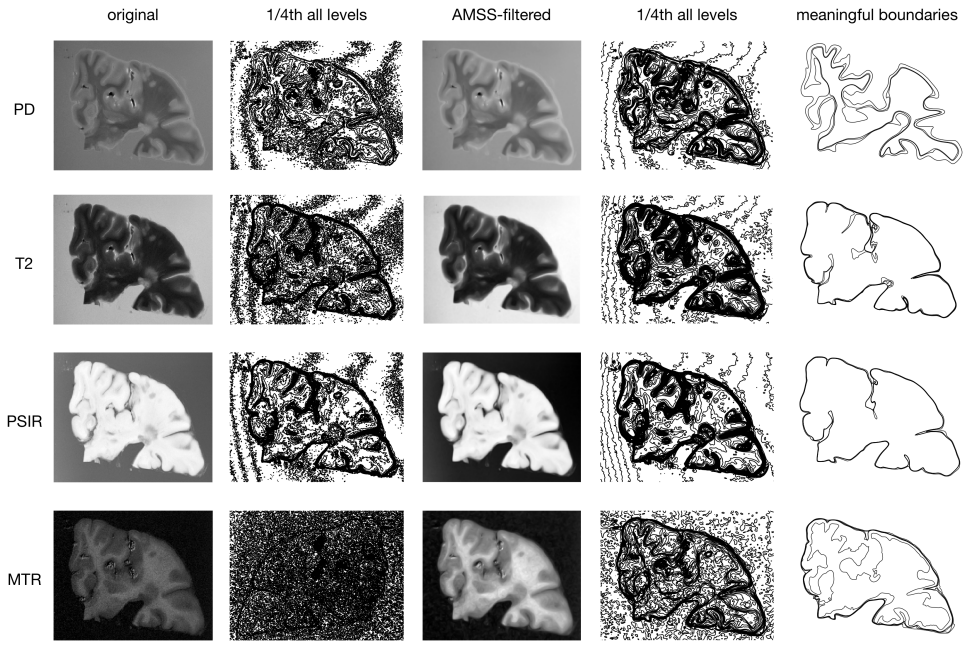

Figure 5.9: *A contrario* detection of meaningful boundaries using contrast and temperature ($c+\mathrm{T}$) for 5 different MRI modalities (rows 1 to 5): PD, T2w, PSIR and MTR from the MS dataset. Only the 5 level lines with lowest NFAs (5.22) are shown in the last column (and those are the curves used in the rest of the method).

the dual, and two points sharing a common tangent map onto a double point of the dual curve. More generally, a set of n points sharing a common tangent line maps onto a point of multiplicity n of the dual curve (see Fig. 5.10a). Finding the bitangents of $\mathcal{L}$ is therefore equivalent to finding self-intersections of the polygonal curve $\mathcal{L}^*$. To that end, the Bentley-Ottmann algorithm [477, 478] was used, which is a line sweep algorithm that reports all intersections among line segments in the plane (Fig. 5.10).

5.4.2 Refining bitangents locations

The refinement of bitangents is preferable: since the slopes of tangents vary substantially in portions of high curvature, the lengths of segments of the dual curve increase on portions where a self-intersection may happen. The evaluation of that double point thus degrades, which directly affects the estimation of bitangent points.

5.4.2.1 Ellipse fitting

In order to cope with bitangent errors, their locations are refined by fitting ellipses [479] around estimated bitangent points. This allows skipping the rotation part prior to the quadratic fitting in [480]. Beforehand, bitangents lying on almost straight edges of the level lines are removed by looking at the residual of a line fit on the portions bounded by

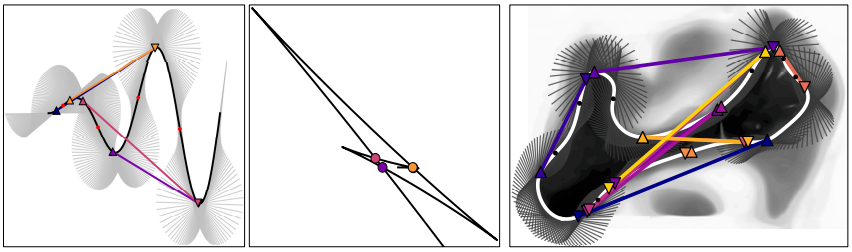

(a)

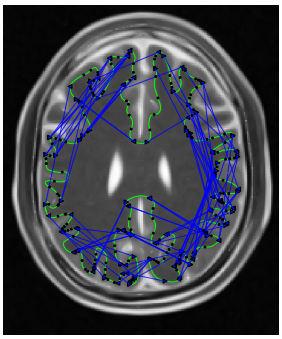

(b)

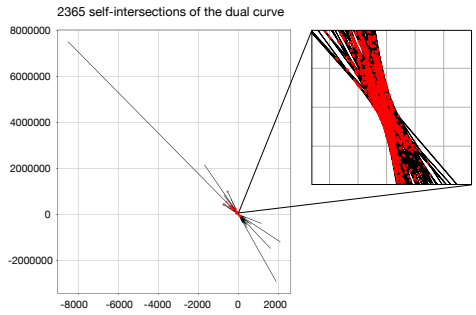

(c)

Figure 5.10: (5.10a) Left: the function $x \mapsto x\sin(x)$ for all $x \in [0, 4\pi]$, and the set of its tangents (in grey) are shown. Inflection points are shown with red dots (black dots in the right picture) and bitangents are coloured lines. Middle: the dual curve: its 4 crossing points correspond to the 4 coloured bitangents on the left. Right: bitangents (11 in total) of one level line (in white) from a histological slice (after §5.4.1). (5.10b) 76 bitangents (in blue) covering portions of a meaningful level line (in green) of a T2w MRI plane from BrainWeb—the portions have between 20 and 23 inflections (black dots). These bitangents correspond to a subset of self-intersections of the dual curve (red dots) in (5.10c), which in total amounts to 2365 bitangents.

the two bitangent points. This is intended to avoid the degenerate case of fitting an ellipse to a nearly straight line.

Let F be a general conic. It is defined as the set of points such that:

$$F(\mathbf{a}, \mathbf{x}) = \mathbf{a}.\mathbf{x} = ax^2 + by^2 + cxy + dx + ey + f = 0, \tag{5.24}$$

where $\mathbf{a} = [a\ b\ c\ d\ e\ f]^T$ and $\mathbf{x} = [x^2\ y^2\ xy\ x\ y\ 1]^T$.

The least squares problem to solve here is the minimisation of the distance $d = ||D\mathbf{a}||^2$, where D is the *design* matrix, made of the N points to be fitted: $D = [\mathbf{x}_1\ \mathbf{x}_2\ \ldots\ \mathbf{x}_N]^T$. In other words, fitting a conic to N points comes down to minimising $\sum_i^N \mathbf{a}^T D_i^T D_i \mathbf{a} = \mathbf{a}^T S \mathbf{a}$, where $S = D^T D$ is the *scatter* matrix.

In addition, since the conic F is to be an ellipse, the parameters must satisfy the equality

constraint $4ac - b^2 = 1$. This can be rewritten in matrix form as $\mathbf{a}^T C \mathbf{a} = 1$, where C is called the *constraint* matrix:

$$C = \begin{bmatrix} 0 & 0 & 2 & 0 & 0 & 0 \\ 0 & -1 & 0 & 0 & 0 & 0 \\ 2 & 0 & 0 & 0 & 0 & 0 \\ 0 & 0 & 0 & 0 & 0 & 0 \\ 0 & 0 & 0 & 0 & 0 & 0 \\ 0 & 0 & 0 & 0 & 0 & 0 \end{bmatrix}. \tag{5.25}$$

Solving the now constrained minimisation problem:

$$\begin{aligned} &\text{minimise } \mathbf{a}^T S \mathbf{a} \\ &\text{s.t. } \mathbf{a}^T C \mathbf{a} = 1, \end{aligned} \tag{5.26}$$

is done by the method of Lagrange multipliers; introducing the Lagrangian function $\mathscr{L}$ with Lagrangian multipliers λ:

$$\mathscr{L}(\mathbf{a}, \lambda) = \mathbf{a}^T S \mathbf{a} - \lambda (\mathbf{a}^T C \mathbf{a} - 1). \tag{5.27}$$

Differentiating (5.27) w.r.t $\mathbf{a}$ (differentiating w.r.t λ gives the constraint) and equating to zero yields the generalised eigenvalue problem (GEP):

$$S\mathbf{a} = \lambda C \mathbf{a}. \tag{5.28}$$

The ellipse coefficients, $\mathbf{a}$ are the elements of the eigenvector that corresponds to the only positive eigenvalue. Although the impact of S being nearly singular and C being singular on the stability of the eigenvalues computation is discussed by Halir and Flusser [481], no problem was encountered in the experiments.

5.4.2.2 Bitangents of ellipses

The main goal of this section is to compute the bitangents of two ellipses efficiently. This is achieved by transforming a system of two polynomial equations into a polynomial eigenvalue problem (PEP), and for further performance, into a generalised eigenvalue problem (GEP). The problem of finding a compact basis of monomials during the conversion of the equations to a PEP was recently addressed in [482], but Heikkila's solution was not used here.

Let us consider two ellipses, $E_1(\mathbf{a_1}, \mathbf{x})$ and $E_2(\mathbf{a_2}, \mathbf{x})$ defined by bivariate quadratic polynomials, like in (5.24). The tangent line, T: $y = ux + v$ to say E_1, is the line that intersects E_1 at exactly one point. By substitution, one gets a degree 2 polynomial in x, which has a single root if and only if its discriminant, $\Delta(\alpha_1, \mathbf{u}) = 0$. When considering the tangent

to both ellipses, this gives a system of $n = 2$ polynomial equations in unknowns u, v:

$$(s1): \begin{cases} \alpha_{11}u^2 + \alpha_{12}v^2 + \alpha_{13}uv + \alpha_{14}u + \alpha_{15}v + \alpha_{16} = 0 \\ \alpha_{21}u^2 + \alpha_{22}v^2 + \alpha_{23}uv + \alpha_{24}u + \alpha_{25}v + \alpha_{26} = 0, \end{cases} \tag{5.29}$$

with $\alpha_{i1} = e_i^2 - 4c_i f_i$, $\alpha_{i2} = b_i^2 - 4a_i c_i$, $\alpha_{i3} = 4c_i d_i - 2b_i d_i$, $\alpha_{i4} = 2d_i e_i - 2b_i f_i$, $\alpha_{i5} = 2b_i d_i - 4a_i e_i$, and $\alpha_{i6} = d_i^2 - 4a_i f_i$, $i = \{1,2\}$.

To start with, u is hidden in the coefficient field; $(s1)$ becomes a system of two equations $f_1(u,v)$ and $f_2(u,v)$ in one variable v and coefficients from $\mathbb{R}[u]$ i.e. $f_1, f_2 \in (\mathbb{R}[u])[v]$. The degrees of these two equations are $d_1 = d_2 = 2$.

Homogenising $(s1)$ using a new variable w gives $(s2)$, a system of two homogeneous polynomial equations $F_1(v,w)$ and $F_2(v,w)$ in two unknowns v, w:

$$(s2): \begin{cases} \alpha_{11}u^2 + \alpha_{12}v^2 + \alpha_{13}uv + \alpha_{14}uw + \alpha_{15}vw + \alpha_{16}w^2 = 0 \\ \alpha_{21}u^2 + \alpha_{22}v^2 + \alpha_{23}uv + \alpha_{24}uw + \alpha_{25}vw + \alpha_{26}w^2 = 0, \end{cases} \tag{5.30}$$

The total degree $d = \sum_{i=1}^{n}(d_i - 1) + 1$ equals 3. This gives the set $\mathcal{S}$ of $\binom{n+d-1}{d} = 4$ possible monomials $\omega^{\delta} = v^{\delta_2} w^{\delta_3}$ in variables v, w of total degree d i.e., such that $|\delta| = \sum_{i=2}^{3} \delta_i = 3$: $\mathcal{S} = \{v^3, v^2 w, v w^2, w^3\}$. The set $\mathcal{S}$ can be partitioned into two subsets according to a modified Macaulay-based method [483]:

$$\begin{aligned} \mathcal{S}_1 &= \{\omega^{\delta} : |\delta| = 3, v^{d_1} | \omega^{\delta}\}, \\ \mathcal{S}_2 &= \{\omega^{\delta} : |\delta| = 3, w^{d_2} | \omega^{\delta}\}. \end{aligned} \tag{5.31}$$

In other words, $\mathcal{S}_1$ (resp. $\mathcal{S}_2$) is the set of monomials of total degree 3 that can be divided by v^2 (resp. w^2). This gives $\mathcal{S}_1 = \{v^3, v^2 w\}$ and $\mathcal{S}_2 = \{v w^2, w^3\}$, from which the extended set of four polynomial equations: $vF_1 = 0$, $wF_1 = 0$, $vF_2 = 0$ and $wF_2 = 0$ can be derived.

After dehomogenisation (by setting $w = 1$), the extended system can be rewritten as a polynomial eigenvalue problem (PEP):

$$\mathsf{C}(u)\mathbf{v} = 0, \tag{5.32}$$

where $\mathbf{v} = [v^3\ v^2\ v\ 1]^T$ and:

$$\mathsf{C}(u) = \begin{bmatrix} \alpha_{12} & \alpha_{13}u+\alpha_{15} & \alpha_{11}u^2+\alpha_{14}u+\alpha_{16} & 0 \\ 0 & \alpha_{12} & \alpha_{13}u+\alpha_{15} & \alpha_{11}u^2+\alpha_{14}u+\alpha_{16} \\ \alpha_{22} & \alpha_{23}u+\alpha_{25} & \alpha_{21}u^2+\alpha_{24}u+\alpha_{26} & 0 \\ 0 & \alpha_{22} & \alpha_{23}u+\alpha_{25} & \alpha_{21}u^2+\alpha_{24}u+\alpha_{26} \end{bmatrix}. \tag{5.33}$$

Non-trivial solutions to (5.32) are the roots of $\det(\mathsf{C})$, which gives up to four real solutions for u.

For each one of them, for example u_1, the corresponding singular value decomposition has the form: $\mathsf{C}(u_1) = \mathsf{UHV}^T$, where the solution vector $[\mathsf{v}_1\ \mathsf{v}_2\ \mathsf{v}_3\ \mathsf{v}_4]^T$ is the column of V that corresponds to the smallest singular value. The particular solution v_1 associated with u_1 is *e.g.* $\frac{\mathsf{v}_3}{\mathsf{v}_4}$, meaning that one bitangent is parametrised by T_1: $y = u_1 x + v_1$.

For the sake of completeness, the PEP (5.32) can be further transformed into a GEP by first rewriting it as:

$$\left(\underbrace{\begin{bmatrix} 0 & 0 & \alpha_{11} & 0 \\ 0 & 0 & 0 & \alpha_{11} \\ 0 & 0 & \alpha_{21} & 0 \\ 0 & 0 & 0 & \alpha_{21} \end{bmatrix}}_{\mathsf{C}_2} u^2 + \underbrace{\begin{bmatrix} 0 & \alpha_{13} & \alpha_{14} & 0 \\ 0 & 0 & \alpha_{13} & \alpha_{14} \\ 0 & \alpha_{23} & \alpha_{24} & 0 \\ 0 & 0 & \alpha_{23} & \alpha_{24} \end{bmatrix}}_{\mathsf{C}_1} u + \underbrace{\begin{bmatrix} \alpha_{12} & \alpha_{15} & \alpha_{16} & 0 \\ 0 & \alpha_{12} & \alpha_{15} & \alpha_{16} \\ \alpha_{22} & \alpha_{25} & \alpha_{26} & 0 \\ 0 & \alpha_{22} & \alpha_{25} & \alpha_{26} \end{bmatrix}}_{\mathsf{C}_0} \right) \mathbf{v} = 0, \tag{5.34}$$

which is equivalent to the GEP:

$$\mathsf{A}\mathbf{y} = u\mathsf{B}\mathbf{y}, \tag{5.35}$$

with $\mathsf{A} = \begin{bmatrix} 0_4 & I_4 \\ -\mathsf{C}_0 & -\mathsf{C}_1 \end{bmatrix}$ and $\mathsf{B} = \begin{bmatrix} I_4 & 0_4 \\ 0_4 & \mathsf{C}_2 \end{bmatrix}$, 0_4 and I_4 being the $[4 \times 4]$ zero and identity matrices, and $\mathbf{y} = \begin{bmatrix} \mathbf{v} \\ u\mathbf{v} \end{bmatrix} = [\mathsf{y}_1\ \mathsf{y}_2\ \ldots\ \mathsf{y}_8]^T$. A particular solution v_1 is *e.g.*, the quotient $\frac{\mathsf{y}_3}{\mathsf{y}_4}$ (or equivalently $\sqrt[3]{\frac{\mathsf{y}_1}{\mathsf{y}_4}}$) from the eigenvector associated with eigenvalue u_1.

Note that the resolution of (5.35) is two orders of magnitude faster compared to (5.32) using linear algebra packages.

Lastly, when the two ellipses E_1 and E_2 intersect in two points, two out of the four eigenvalues obtained for u are complex. These correspond to the two internal bitangents: in that case, ellipses have only two external bitangents associated with the other two real eigenvalues. It is also worth noting that, when they exist, internal bitangents are associated with the extremal (real) eigenvalues.

5.4.2.3 Selecting one bitangent

In this section, the only bitangent of E_1 and E_2 that is also a bitangent of $\mathcal{L}$ (Fig. 5.11a Right)—referred to as the *usable* bitangent is identified.

Let us consider: (i) bitangents directed from E_1 to E_2, (ii) E_1 is oriented anticlockwise

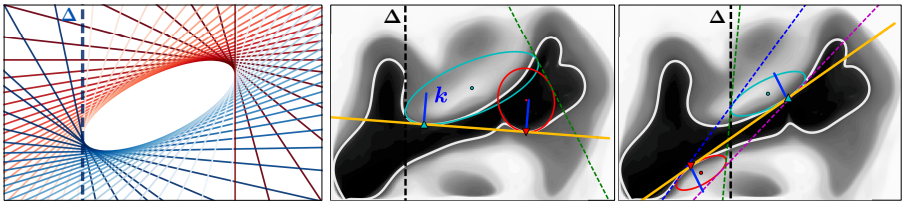

(a)

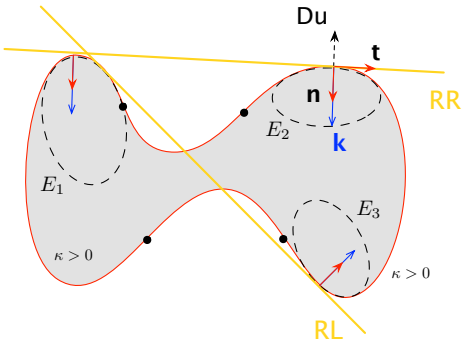

(b)

Figure 5.11: (5.11a) Left: ordering of bitangents. Middle/right: Refinement of bitangents through ellipse fitting (E_1 is in cyan and E_2 in red). The curvature vectors are shown in blue, bitangent points are shown with triangles, and bitangents with coloured dashed lines. Selected refined bitangents are shown in yellow (usable bitangent types: middle, *LL*; right, *RL*). (5.11b) The curvature vector, k (in blue) is used to discriminate between cases. Inflection points are shown with black dots and bitangents (along with their respective types), in yellow.

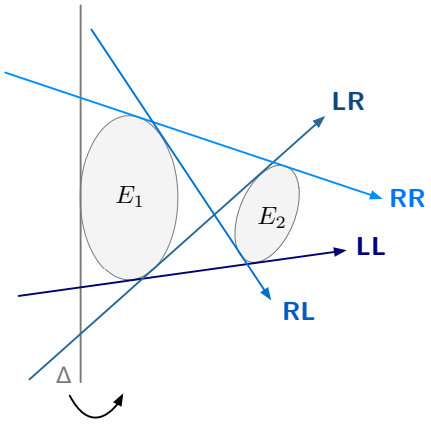

(a)

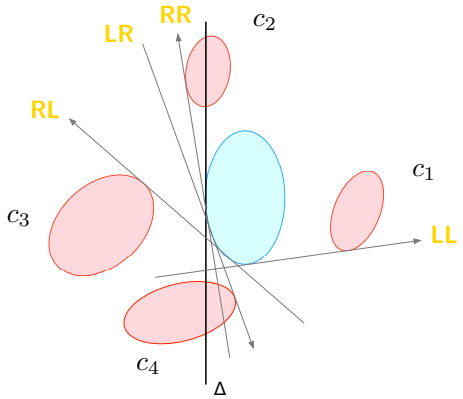

(b)

Figure 5.12: (5.12a) Cyclic order of bitangents. As the left-most tangent of E_1 (Δ) rotates positively around E_1, bitangents of both ellipses are successively of types *LL*, *LR*, *RL*, *RR*. (5.12b) The 4 possible configurations in which E_2 (red) falls relative to E_1 (blue) lead the first bitangent of both ellipses to be of type *LL*, *RR*, *RL* and *LR* in cases (c1), (c2), (c3) and (c4) respectively. The types of the other 3 bitangents in each case can be deduced from that information using the previous cyclic order.

(or positively) and (iii) Δ is its left-most vertical tangent. Bitangents of E_1 can be cyclically ordered by considering independently the tangents below (in blue in Fig. 5.11a Left), and above (in red) it, and sorting them by decreasing y-intercept with the ellipse's left-most tangent, Δ. This holds for cases where an ellipse lies above (resp. below) all of the bitangents. Lemma 1 in [484] states that the resulting cyclic order of the bitangent directions is $\mathcal{C}$: $[LL, LR, RL, RR]$ (L and R stand for left and right and refer to the locations of an ellipse relative to a bitangent). Indeed, looking at Fig. 5.12a, as Δ rotates anticlockwise around E_1, bitangents are successively of types *LL*, *LR*, *RL* and finally *RR*.

Four possible cases arise (Fig. 5.12b): (c1) E_2 stands to the right of E_1, (c2) is above E_1 intersecting Δ, (c3) is to the left of E_1, and (c4) is below E_1 intersecting Δ. For each case, the first bitangent encountered starting from Δ, anticlockwise, has type *LL*, *RR*, *RL* and *LR* respectively; the next up to three bitangents for each case have their types deduced from the positive cyclic order $\mathcal{C}$.

Now in order to select the usable bitangent, one has to rely on the geometry of the level line $\mathcal{L}$. Let us define the unit curvature vector k, at every point along $\mathcal{L}$ as the vector pointing toward the centre of the osculating circle: $k = \kappa n = \langle k_x, k_y \rangle$, where κ is the scalar curvature and n is the normal (it is colinear to the gradient of the image along $\mathcal{L}$ and directed toward the inside of the clockwise-oriented closed curve here). The orientation of k allows differentiating otherwise ambiguous situations; for example, two pairs of ellipses (E_1, E_2) and (E_1, E_3), all of them fitting portions with same curvature and satisfying the configuration of case (c1), can be associated with a different type of usable bitangent, *RR* and *RL* respectively (see Fig. 5.11b). This happens when k_1 and k_3 have opposite sense, while k_1 and k_2 have the same. In the following, positiveness is defined for (c1) and (c3) as $k_y > 0$ and as $k_x > 0$ for (c2) and (c4), and is denoted with the superscript $(+)$.

From there, four patterns can be defined: (p1) $(k_1^{(+)}, k_2^{(+)})$, (p2) $(k_1^{(+)}, k_2^{(-)})$, (p3) $(k_1^{(-)}, k_2^{(+)})$ and (p4) $(k_1^{(-)}, k_2^{(-)})$. In cases (c1) and (c2), they correspond to the usable bitangent type *LL*, *LR*, *RL*, *RR* respectively. Conversely, in cases (c3) and (c4), they correspond to the type *RR*, *RL*, *LR*, *LL* respectively. Since there is a one to one correspondence between the four bitangents and the four types, it only requires identifying one of four patterns (p) and one of four cases (c) to pick the usable bitangent parameters.

The mapping is also extended to intersecting ellipses (Fig. 5.11a Right) by observing that the cyclic order of bitangents is of the form $[T_e, T_i, T_i, T_e]$ (subscripts e and i stand for

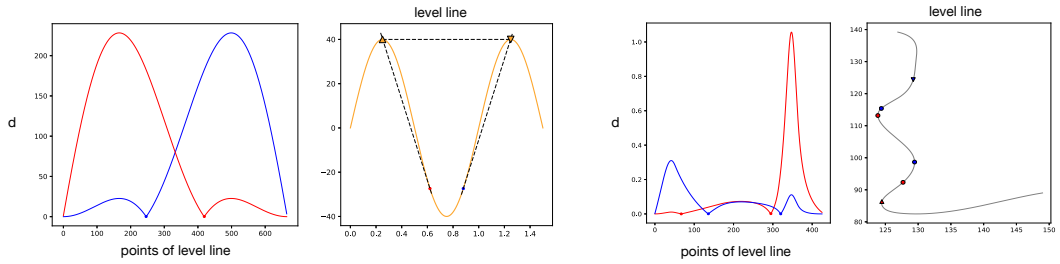

(a) **(b)**

Figure 5.13: Level line frames. (5.13a) Cast points of a portion of level line bounded by two bitangent points b_1 and b_2 (resp. upper and lower yellow triangles) are identified as the points at which the tangents of the curve intersect it as close as possible to b_1 and b_2 (resp. red and blue dots). That distance, d is shown on the left and its absolute minimum corresponds to a cast point. (5.13b) In the case of a more complex portion of level line (right) i.e., with more than 2 inflections, several such points (red/blue dots) exist for each bitangent point (resp. red/blue triangles) and thus correspond to local minima of d (left).

external and internal). Since only external bitangents exist in the case where E_1 and E_2 intersect in two points (§5.4.2.2), one is left with the cyclic order $[T_e, \_, \_, T_e]$.

Bitangent points are straightforward to obtain for E_1 and E_2 by substitution of the tangent equation in the ellipses equations. Finally, the point of $\mathcal{L}$ that is the closest to an ellipse bitangent point is selected. Note that once all bitangents are refined, some bitangent points may collapse to similar locations. In order to reduce ineffective redundancy, only one bitangent out of those that have their end points close to each other is kept.

5.5 Projective shape representation

A set of refined bitangents is now available. Let us consider one bitangent and its endpoints b_1 and b_2. In order to encode the shape of a portion of (oriented) level line $\mathcal{L}_r = \mathcal{L}\restriction[b_1, b_2]$ (assuming b_1 comes before b_2) in a projective invariant manner (as opposed to affine invariant [462], used in [463]), two more points are required: the cast points $c_.$. The four points b_1, c_1, c_2, b_2, invariant under projective transformation, form the vertices of a polygon—the level line frame $\mathcal{F}_l$—and are mapped onto the unit square vertices, $\mathcal{F}_c$ (the canonical frame) [480]. The resulting projection is applied to $\mathcal{L}_r$ and provides a *canonical* curve that can be used for shape comparison and matching.

A cast point c_1 (resp. c_2) is defined as the contact point of the tangent to $\mathcal{L}_r$ that intersects the level line at b_1 (resp. b_2). In practice, cast points are the points where the function, f:

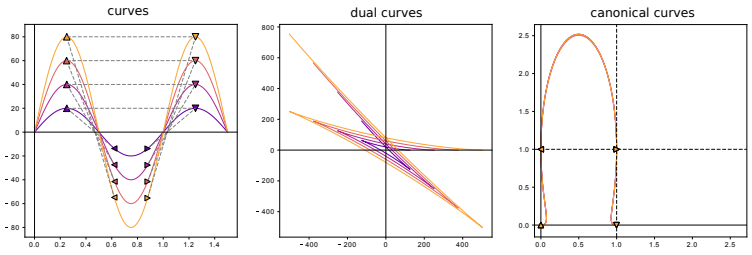

Figure 5.14: Illustrating the (projective-invariant) encoding of curves. A sine function is non-uniformly scaled into several other sine functions. Using the projective transformation that maps the vertices of their frames (bitangent points—upper/lower triangles—and cast points—left/right triangles) onto the vertices of the unit square (the canonical frame), the curves are granted, as expected in that case, similar signatures. This holds for other transformations as long as they belong to the class of homographies, and this grants comparability between different shape elements.

$$f\Big(T,(x_{b_\cdot},y_{b_\cdot})\Big)=\frac{|ux_{b_\cdot}+vy_{b_\cdot}+w|}{\sqrt{u^2+v^2}}, \tag{5.36}$$

that evaluates the distance from the bitangent point $b_\cdot(x_{b_\cdot},y_{b_\cdot})$ to the tangents of the level line, $T:=ux+vy+w=0$ for all $(x,y)\in\mathcal{L}\restriction]b_1,b_2[$, is (locally) minimum.

Although there is a unique minimum corresponding to $c_\cdot$ for each bitangent point $b_\cdot$ when a portion of level line has only two inflections (see Fig. 5.13a), there exist several such points when $\mathcal{L}_r$ has more inflections (see Fig. 5.13b).

It thus becomes critical to ensure that a candidate frame $\mathcal{F}_l$ forms a convex polygon so as to get an acceptable projection of $\mathcal{L}_r$ to the canonical frame. In the case of short bitangents, the construction of $\mathcal{F}_l$ is straightforward as only two cast points exist. As for long bitangents, a single portion of curve may be associated with several canonical curves, each of which depends on the frame configuration. As noted in by Rothwell [480], it is preferable to pick those making a wide angle between the bitangent and the cast tangents, as well as those having the cast points as far from one another as possible: unbalanced frames may give distorted canonical curves. This holds for bitangents crossing the level line. It is also worth mentioning that this step drastically prunes the set of bitangents that can lead to satisfying frames.

5.5.1 Canonical curves

The goal is here to determine the 2D homography matrix such that $\mathbf{x_i}=\rho\mathsf{T}\mathbf{X_i}$ [42], where $\mathbf{X_i}=[X_i\ Y_i\ 1]^T$ is the i-th point in F_l (which no 3 are colinear) in homogeneous coordinates, $\mathbf{x_i}=[x_i\ y_i\ 1]^T$ is the i-th vertex of the unit square defined by $(0,0,1)$, $(0,1,1)$, $(1,1,1)$ and

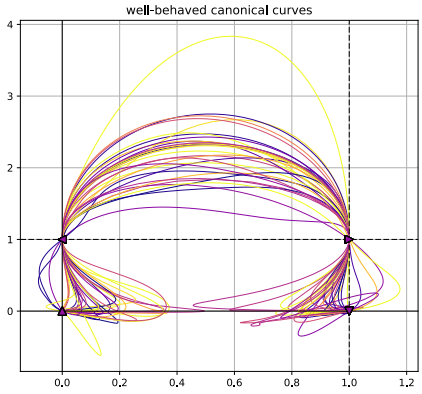

Figure 5.15: Illustrating the transformation of all the shape elements with 3 inflections (along one meaningful level line of a T2w MR image) into canonical curves (MS dataset).

$(1,0,1)$, T is a $[3\times 3]$ matrix of the transformation parameters with $\mathsf{T}_{33}=1$ and ρ is a non-zero scalar that gives by elimination 8 equations linear in the parameters. Rewriting in matrix form, one gets $\mathsf{A}\mathbf{p}=0$ where A, is the concatenation of equations:

$$\mathsf{A}_i = \begin{bmatrix} X_i & Y_i & 1 & 0 & 0 & 0 & -X_i x_i & -Y_i x_i & -x_i \\ 0 & 0 & 0 & X_i & Y_i & 1 & -X_i y_i & -Y_i y_i & -y_i \end{bmatrix} \tag{5.37}$$

from 4 correspondences and $\mathbf{p}=[\mathsf{T}_{11}\ \mathsf{T}_{12}\ \ldots\ \mathsf{T}_{32}\ 1]^T$. Like in §5.4.2.2, after obtaining the SVD of A, the unit singular vector corresponding to the smallest singular value is the solution $\mathbf{p}$ that is sought for.

A normalisation step, or preconditioning, is recommended for it forces the entries of A to have similar magnitude. Further details can be found in the book from Hartley and Zisserman [42] (p.108) and §4 of [485]. In practice, points of F_l and F_c are independently (i) translated so that their centroid is at the origin and (ii) scaled so that the average distance from the origin is equal to $\sqrt{2}$; this gives two similarity transformations S_1 and S_2. The homography is obtained as described above using normalised point correspondences. Finally, the projective transformation that transforms portions of level lines into canonical curves is ${\mathsf{S}_1}^{-1}\mathsf{T}\mathsf{S}_2$ (denormalisation); an illustration is given in Fig. 5.15.

5.5.2 Comparing polygonal curves

Contrary to Rothwell *et al.* [486], who relied on rays extended from an origin $(1/2,0)$ in $\mathcal{F}_c$ and designed a feature vector made of all the distances from every intersection point with the canonical curve to the origin, canonical curves are compared by means of the Fréchet distance (Fig. 5.16c). The rationale is that the bitangents that cross level lines are also taken

into account. This means that the resulting canonical curves may cross the base of $\mathcal{F}_c$ (the x-axis) one or several times with more or less complex convolutions, making the use of rays impractical.

There are (at least) two common ways of defining the similarity between polygonal curves: the Hausdorff distance [487] and the Fréchet distance [488]. The latter has the advantage that it takes into account the ordering of the points along the curves, thereby capturing curves structure better.

Let P and Q be two polygonal curves in $\mathbb{R}^2$ *i.e.*, two continuous functions $[0,m] \to \mathbb{R}^2$ (resp. $[0,n]$) such that for each $i \in \{1,2,\ldots,m\}$ (resp. $j \in \{1,2,\ldots,n\}$), the restriction of P (resp. Q) to the interval $[i-1,i]$ (resp. $[j-1,j]$) is affine; in other words, they form chains of line segments.

The Fréchet distance between P and Q is defined as:

$$d_{\mathcal{F}}(\mathsf{P},\mathsf{Q}) \stackrel{\text{def}}{=} \inf_{\alpha,\beta} \max_{t\in[0,1]} \Big\{ d_p\big(\mathsf{P}(\alpha(t)),\mathsf{Q}(\alpha(t))\big) \Big\}, \tag{5.38}$$

where α (resp. β) is a monotone reparametrisation of $[0,m]$ (resp. $[0,n]$) *i.e.*, a continuous non-decreasing function $\alpha : [0,1] \to [0,m]$ with $\alpha(0) = 0$ and $\alpha(1) = m$, and $d_p(x_1,x_2)$ is the distance between x_1 and x_2 under the L_p norm ($p = 2$ here and $d(.,.)$ denotes the Euclidean distance).

The Fréchet distance if often explained using the *leash* metaphor [489]: "a man walks on one curve, his dog walks on the other curve. Man and dog are connected by a leash. Both can vary their speeds, but they may not walk backwards. The Fréchet distance is the length of the shortest leash so that man and dog can walk from the beginning to the end of the respective curves".

For the sake of speed however, the discrete Fréchet distance (see Table 1 of [490]) was used, which is an approximation of the continuous Fréchet distance: it only uses the curves vertices for measurements. In that case, both the dog and its handler can only stop at vertices of P and Q and at any step, each of them can either stay at their current vertex or jump to the next one. The discrete Fréchet distance is defined as the minimal leash necessary at these discrete moments.

Let $\langle p_1, p_2, \ldots, p_m \rangle$ and $\langle q_1, q_2, \ldots, q_n \rangle$ be the two sequences of vertices of P and Q. A

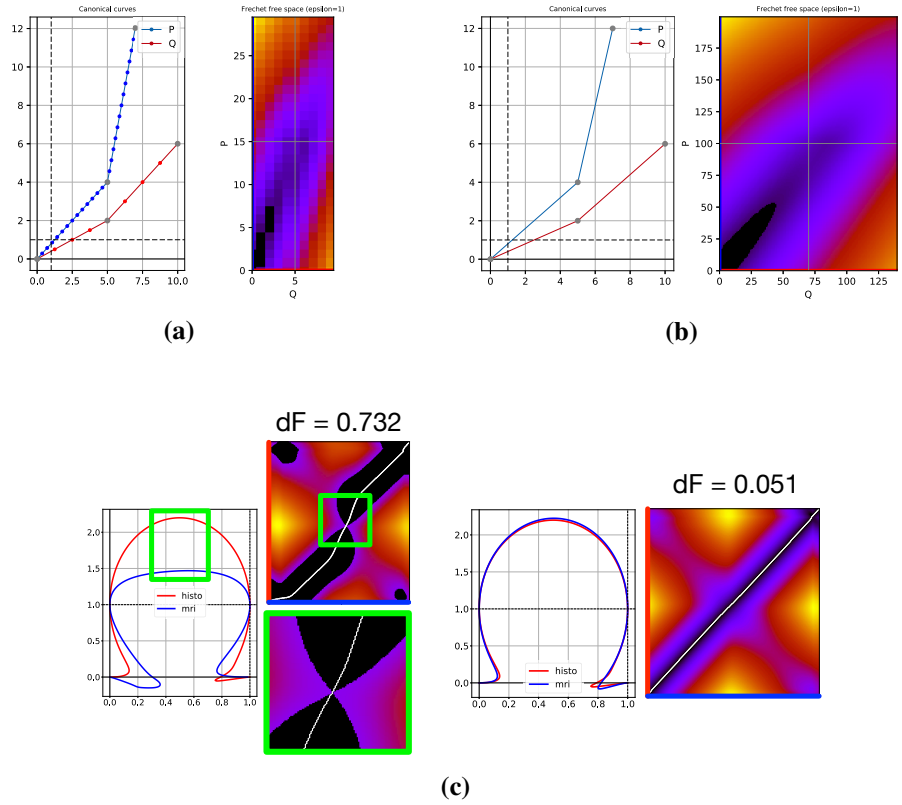

Figure 5.16: Comparison of canonical curves and free space diagrams. Distance between two polygonal curves, P and Q made of two segments each (each segment has (5.16a) $|\mathsf{P}|$ =15 points and $|\mathsf{Q}|$ =5 points; and (5.16b) $|\mathsf{P}|$ =100 points and $|\mathsf{Q}|$ =70 points. Boundaries of cells in the Fréchet free space (grey lines) correspond to each segment endpoints. The free space (*i.e*, d<1) is shown as dark pixels. (5.16c) For two shape elements from histology (red) and MRI (blue), the Fréchet distance, $\delta_{\mathcal{F}}$ is computed between their canonical curves and the associated free space diagrams with Fréchet paths (white line) are shown—only endpoints of segments are used. The reachable free space corresponds to region in black (d$\leq \delta = \delta_{\mathcal{F}}$ here, which is the smallest δ that allows reaching the top right corner starting from the origin).

traversal β of P and Q is a sequence of pairs $(p,q) \in \mathsf{P} \times \mathsf{Q}$ such that:

(i) the traversal β begins with the pair (p_1,q_1) and ends with (p_m,q_n),

(ii) the pair (p_i,q_j) can only be followed by (p_{i+1},q_j), (p_i,q_{j+1}) or (p_{i+1},q_{j+1}).

In other words, β is an order-preserving complete correspondence between P and Q. The discrete Fréchet is defined as:

$$\delta_{\mathcal{F}} \stackrel{\text{def}}{=} \min_{\beta} \max_{(p,q)\in\beta} d(p,q), \tag{5.39}$$

where β ranges over all order-preserving complete correspondences.

Note that another interesting way of looking at it is by considering *free space diagrams*.

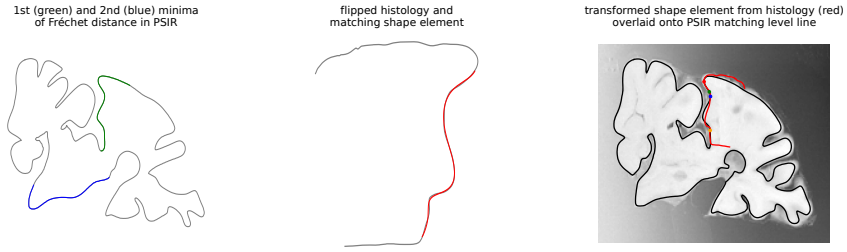

Figure 5.17: Comparing shape elements from a flipped histological slice and a medical image. One shape element from histology (in red in the middle) is compared to several shape elements in the MR (only two are shown on the left). The minimum Fréchet distance is obtained for the green element; the second minimum corresponds to the comparison with the blue element (mismatch). However, one can note that up to a projective transformation, the blue and red elements do match well too. The affine transform computed from the 4 pairs of matching points is applied to the whole level line from histology (red), overlaid on the medical image and one of its meaningful level lines (black).

The free space diagram is the grid $G = [0,m] \times [0,n]$, made of mn cells. In each cell, the distance function $d(\mathsf{P}(x), \mathsf{Q}(y))$ is defined for one segment of P against another of Q (Fig. 5.16a and 5.16b). The free space is defined as the set of points (x,y) for which $d \leq \delta$, a distance parameter—this leads to the notion of reachable free space, which allows tracking local similarity between two curves [491]. The computation of the Fréchet distance thus becomes a shortest path problem through the free space diagram (Fig. 5.16c). It is defined as the minimum δ that allows reaching (m,n) from $(0,0)$ (the Fréchet path) crossing cells $[i,i+1] \times [j,j+1]$ by a straight segment.

5.6 Matching and registration

By cross-comparisons between histology and MRI, one obtains a measure of shape similarity (§5.5.2). Because each level line is associated with many canonical curves (one for each shape element), matches are found when the Fréchet distance is minimum and below a certain threshold. Correspondences between $\mathcal{F}_l$ in histology and MRI can then be used to compute an affine transformation (same principle as in §5.5.1 with only three points—each providing two equations—and $\mathbf{p} = [T_{11}\ T_{12}\ \ldots\ T_{23}\ 0\ 0\ 1]^T$). In order to minimise the global alignment error, the points must be well-arranged in images *i.e.*, the frames should be as wide as possible, hence the advantage of using long bitangents (Fig. 5.17). When considering several level lines in both modalities, each canonical curve of each level line from histology returns at most one matching canonical curve for each level line in the MRI. False matches are filtered out using random sample consensus (RANSAC) [312] and a global

similarity transformation is computed. RANSAC allows for robust estimation of parameters from a subset of inliers (matching frames) even when many outliers may be present in the complete dataset.

5.7 Results and discussion

In the following, *confusing* (as opposed to *meaningful*) level lines refer to those not providing relevant information about the tissue shape.

5.7.1 Data

5.7.1.1 Multiple sclerosis (MS dataset)

Protocol - *post mortem* MRI

Right coronal hemi-slices of sixteen brains of people with MS and four controls with no known neurological condition were collected. Note that only limited brain tissue was available as parts of those hemi-slices were shared with other research groups. For each case, a 10-15mm thick slice was taken, corresponding to the same anatomical region (*i.e.*, the second slice posterior to the mammillary bodies).

Unfixed tissue was submerged in PBS and put in an MRI-compatible holder made of Plexiglas and scanned using a 3T Philips Achieva system. MRI sequence parameters were the following:

- PD/T2w (TE=12/80ms, TR=4000ms, resolution=$0.25 \times 0.25 \times 2\text{mm}^3$, FoV=$160 \times 160 \times 16\text{mm}^3$)
- MTR (TE=5.5/12.7ms, TR=37ms, resolution=$0.25 \times 0.25 \times 2\text{mm}^3$, FoV=$160 \times 160 \times 60\text{mm}^3$)
- PSIR (TE=13ms, TR=7000ms, resolution=$0.25 \times 0.25 \times 2\text{mm}^3$, FoV=$160 \times 160 \times 16\text{mm}^3$)

To account for effects of temperature tissue was submerged in PBS at room temperature, and temperature measurements were taken before and after scanning. After MRI, the tissue was fixed through submersion in a 10% buffered formaldehyde solution for a minimum of seven days.

Protocol - histology

For seven cases, the 10-15mm thick slice was subdivided into cassette blocks, ensuring that thalamic grey matter and hippocampal structures were not dissected and would be kept intact. Record was kept of where the cassette blocks were sampled from, which provided a

ground truth arrangement used for validation (see Fig. 5.1).

The cassette blocks were paraffin-embedded and sectioned at $5\mu m$. Then, 11 adjacent consecutive sections were stained using the following 11 markers (with targets into brackets):

- H&E (Nuclei, cytoplasm and extracellular proteins)
- NF200 (Neurofilament, 200kDa)
- SMI94 (myelin basic protein)
- CD68 (macrophages/microglia)
- CD20 (B lymphocytes)
- CD3 (T lymphocytes)
- CD8 (MHC class 1 - cytotoxic T lymphocytes)
- GFAP (astrocytes)
- IBA1 (microglia/macrophages)
- VDAC1 (mitochondria)
- COX4 (mitochondria electron transport chain)

At this point, it is worth noting that because the resulting histological stack was about $50\mu m$-thick—compared to a $2mm$-thick slice from MRI—2D-3D registration methods were not practicable. Data were then digitised by the Division of Pathology and images are transferred to servers of NMR research group. In the following, three cases are considered, for the other cases provided histological data that were too difficult to handle with the proposed method.

Evaluation overview

For each case, the medical image plane that looked the most similar to the associated histological cassettes was visually identified by an experienced clinician.

The method was evaluated on seven pieces of tissue (shown in Fig. 5.8), altogether covering three different cases (subjects). The reason why so little data was used here is that most pieces of tissue could not even be located by eye onto the selected medical image plane; only referring to the marked locations of the cassettes prior to cutting allowed so. Additionally, little structural detail and convexity of layers in many pieces of tissue made the proposed method fail.

The ground truth arrangement mentioned in the histological protocol consisted of reporting the cassettes locations onto the selected slice of a medical image in order to keep

track on which part of the sample the tissue piece was cut from. Note that the corners of the green boxes in Fig. 5.1 are not used for assessment of the registration accuracy. Those are purely informative, and serve the purpose of telling qualitatively whether histology has been located correctly or not. Rather, target registration error (TRE) is computed between the corners of the histology image registered onto the MRI slice using the proposed method, with the corners of the same image manually registered.

5.7.1.2 Brainweb

T1 and T2w images were used from the simulated MRI volumes for normal brains. The slice thickness was 1mm, noise level was 3% and the level of intensity non-uniformity was 20%. Images were 181$\times$217 (pix): affine morphological scale space smoothing allowed keeping good structural details while reducing computations due to large images.

Evaluation overview

Briefly (details are given in §5.7.2), the goal was to crop a subimage from one modality's plane to try and see whether, after corruption, it could be located and aligned with the other modality's (full) image. Since both medical image volumes are registered, ground truth alignment is available (a patch cropped from one modality's plane has its counterpart in the other). Further experiments were carried out and are described in the following section.

5.7.2 Experiments and results

Experiments on images alignment

MS dataset

(E1) investigated 2 questions: (i) What is the impact of confusing level lines as well as their number, on the matching and the alignment? and (ii) can level lines be used as they are, without any form of prior knowledge about the tissue boundaries in images? Note that level lines were computed at quantised levels 0 to 255 by steps of 1 and only those multiple of 16, 12, 8 and 4 were used in histology and MR images. This allowed to cover a good spectrum of image quantisation, from coarse (1 every 16) to fine (1 every 4).

One expects that the sparser the set of level lines, the less informative about the actual tissue shape they can be (since information is lost when quantisation is coarse). This indeed translates in higher numbers of false than true matches when using between 1/16th and 1/8th of all available level lines (except for pieces 1 and 3 when using 1/8th). When sufficient information comes in (1/4th), recognition becomes more suc-

cessful: despite finding more false than true matches for piece 2, RANSAC was able to return the correct transformation—most of the false matches being isolated and spread across the MR image domain in that case. Here, I define the "correct" transformation qualitatively, in the sense that—using this transformation—the piece was placed correctly according to the ground truth arrangement. Quantitative results are given later. In contrary, RANSAC was unable to deal with false matches for pieces 5 and 6, those being related to ambiguities (shape elements were small and confusing). Results are reported in the left bar chart of Fig. 5.18.

(E2) investigated the question: how robust is the matching/alignment when injecting confusing information into a subset of meaningful level lines? As such, one meaningful level line was selected among all those obtained in §5.3.2. In addition, an increasing number of adjacent levels were considered, from ± 5 to ± 20 (quantisation in the image was taken equal to 1). For example, if the level line at level 180 is meaningful, 10 additional level lines at levels $[175;185]$ are considered (resp. 40 at levels $[160;200]$). the number of neighbouring level lines was increased from ± 5 to ± 20 around a meaningful one. One can observe that the more localised around relevant information the level lines are, the higher the ratio true/false matches and the more trustful the set of correspondences fed to RANSAC. This is where redundancy is very valuable. However, as one adds levels, more confusing elements come into play (see the increase in false matches). Due to the complexity of the information and the sinuosity of the shape, it is believed that starting from a meaningful subset of level lines is an important consideration. Results are reported in the right bar chart of Fig. 5.18. The parameters used in RANSAC were as follow: the minimum number of points to fit a model to was 3; the maximum distance for a data point to be classified as inlier was found through experiment. Such a threshold can be identified once the number of inliers starts plateauing as the distance increases. Here, it was taken equal to 4.

(E3) investigated the question: to which extent does the refinement of bitangents matter in the alignment? It is discussed in the paragraph "**Alignment results**" (MS dataset), where target registration errors are reported in Table 5.1. This experiment relied on the sets of five most meaningful level lines from a histological slice and a visually corresponding MR plane. The set of meaningful level lines from medical images combined those of PD, T2w and MTR (five lowest NFAs of each modality).

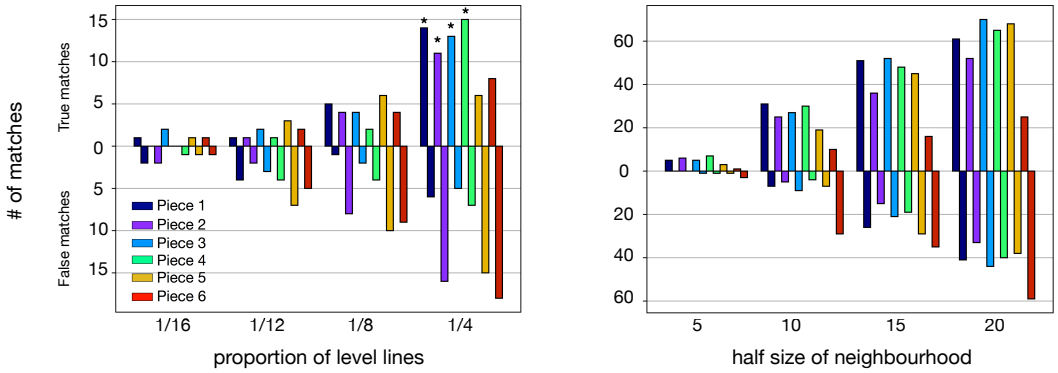

Figure 5.18: Recognition results w/o meaningful boundary selection. Left: (E1) joint effects of sparsity and confusedness on the recognition of shape elements between histology and MRI for six pieces of tissue, along with the ability of RANSAC to provide the correct transformation (*). Right: (E2) effects of redundancy/confusedness starting from a set of meaningful boundaries. Numbers of true/false matches (different opacity) are reported for each piece (different colours) in both experiments. RANSAC is successful five out of six times in (E2).

(E4) examined the evolution of the number of true and false matches when comparing shape elements of increasing complexity (ranges of inflections) from one piece of histology (with sufficiently complex content) and from a visually corresponding MR plane. The sets of meaningful level lines were similar to those of (E3). Results are presented in Fig. 5.19a with four intervals of increasing numbers of inflections. Although the number of true matches could be expected to increase with complexity (while the number of false matches would decrease, as observed), I noted in the case presented here that the more complex the shape elements, the fewer true matches also were (but the better the ratio TM/FM). This can be explained by the fact that fewer shape elements of large complexity are present in the image.

(E5) investigated the evolution of the minimum Fréchet distance over all the cross-comparisons between shape elements from histology and five MR planes (two slices above and below the visually corresponding plane). Changes in orientation were not considered here because of the coarse resolution of MR (out of plane): slices were 2*mm*-thick so the morphology changed substantially from one slice to the next; this did not allow for reliable up- or resampling. The sets of meaningful level lines were the same as those in (E3). A fixed range of inflections was chosen for each piece, such that peculiar shape elements were extracted. Results are reported in Fig. 5.20a. However, the figure is to be taken carefully, since nothing ensures that the minimum Fréchet distance corresponds to true matches. The only information that the figure

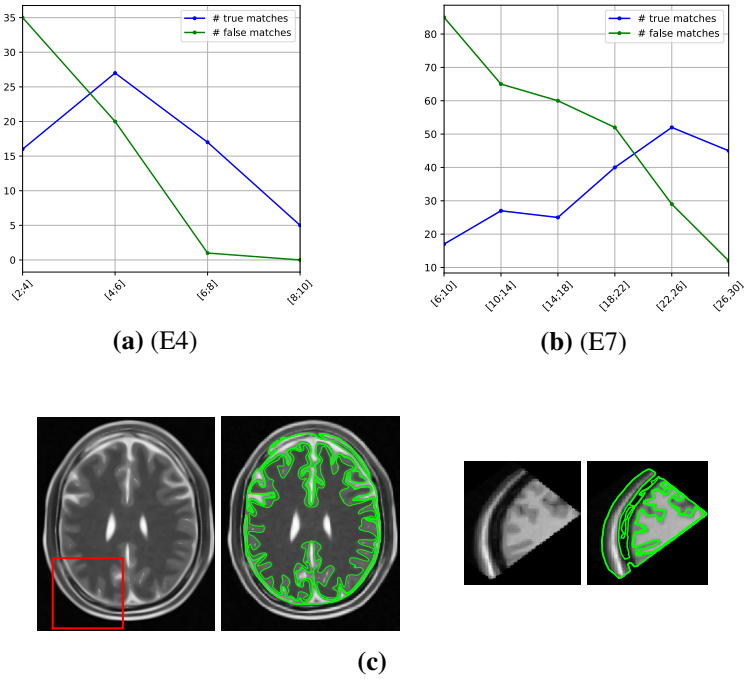

(a) (E4) **(b)** (E7)

(c)

Figure 5.19: Evolution of the number of true (TM) and false (FM) matches when comparing shape elements of increasing complexity (ranges of inflections) (5.19a) from histology and a visually corresponding MR plane; (5.19b) from a (randomly corrupted and flipped) T1 patch and the corresponding T2w MR plane (5.19c); the five most meaningful level lines are displayed for each modality, along which shape elements of increasing complexity are extracted and compared. The thresholds on the Fréchet distance are 0.07 in (5.19a) and 0.03 in (5.19b).

provides is that among all the shape elements in histology, there was one, which canonical curve has such a minimum distance from a canonical curve associated with a shape element extracted from the composite set of meaningful boundaries in the medical images. This is especially true when comparing images that do not, even visually, correspond (like when looking 4*mm* below the visually corresponding plane); as a result, the Fréchet distance increased. That being said, it also served as a sanity check: one verifies that an appropriate threshold on the Fréchet distance ($\delta_{\mathcal{F}}^{t}$) was chosen such that there is no match in the medical image planes adjacent to the visually corresponding one. One can finally note that piece 6 was slightly ambiguous as the adjacent planes had close minimum values (see Fig. 5.20a).

BrainWeb

(E6) investigated the same question as (E3). It is discussed in the paragraph "**Alignment results**" (BrainWeb), where target registration errors are reported in Table 5.2. The experiment relied on the sets of five most meaningful level lines for each modality.

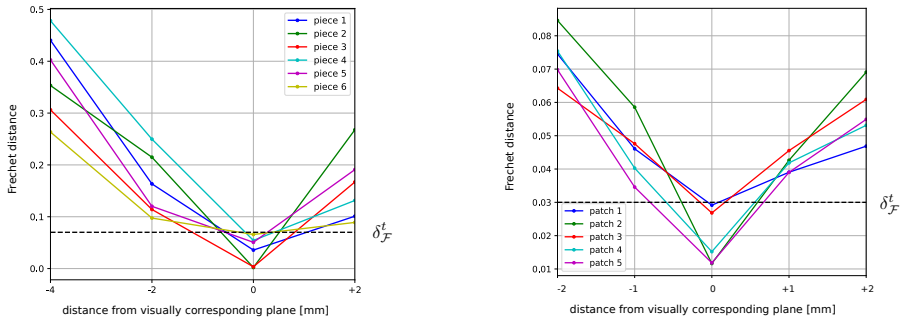

(a) (E5) **(b)** (E8)

Figure 5.20: Evolution of the minimum Fréchet distance over all the cross-comparisons between: (5.20a) all the shape elements from histology and each of four consecutives MR planes (1 slice above and 2 slices below the visually corresponding plane *i.e.*, within the range [-4mm;+2mm]). The threshold on the Fréchet distance used for matching is denoted $\delta^t_{\mathcal{F}}$ and equals 0.07; (5.20b) all the shape elements from five (corrupted) T1 patches and each of five consecutives T2w MRI planes (2 above and 2 below the central plane, which is the corresponding plane). Slices are 1*mm*-thick. The threshold on the Fréchet distance is 0.03. A fixed number of inflections was chosen in each case in order to ensure the extraction and the comparison of characteristic shape elements.

(E7) investigated the same question as (E4). It considered shape elements from one T1 patch and from the corresponding T2w MR plane, along the five most meaningful boundaries in each image. Results are reported in Fig. 5.19b. A conclusion similar to that of (E4) can be drawn: confusion arises when shape elements to be matched are too small (with too few inflections) and the ratio TM/FM improves as complexity grows. The larger number of inflections required in order to get satisfying ratios TM/FM—compared to (E4)—can be explained by the fact that the level lines were more complex and convoluted. Hence the requirement of using more inflections in order to get sufficiently long and characteristic shape elements. Incidentally, the interval [2;6] is not presented in Fig. 5.19b because there were too many false matches.

(E8) investigated the same question as (E5), except that the shape elements from five T1 patches were compared with those of the visually corresponding T2w MR plane and two adjacent slices above and below it—here too, the five most meaningful level lines in each image were considered. Each patch was randomly taken within a fixed T1 plane (such that it included some brain), had a random size (width between 50 and 100 pixels) and was finally applied a random projective transformation (8 degrees of freedom: 2 scale, 2 rotation, 2 translation and 2 lines at infinity). The slice thickness of 1*mm* could potentially be reduced by considering affine invariant curve signatures (projective invariance might be too "tolerant" in terms of the deformations that are

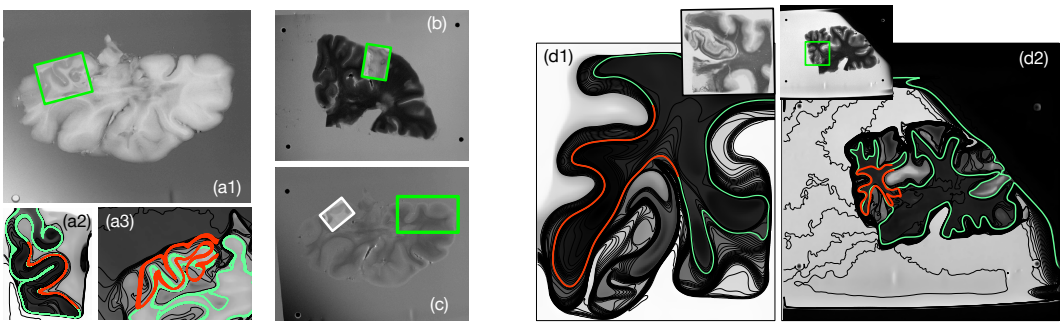

Figure 5.21: Alignment results (w/o meaningful boundary selection). (a1)-(b) Successes and (c) failure (the right location is highlighted with a green box) of the approach for pieces 1, 5 and 6, using PSIR, T2 and PD images respectively. (a2) One matching shape element (orange), part of a level line (green) in piece 1. (a3) Level lines of histology (orange) transformed according to §5.6, overlaid onto a PSIR image (level lines matching those from histology are displayed in green, others are left black). (d1) One matching shape element (orange) part of a level line in histology (green) and (d2) the affine-transformed level line of (d1) (orange) overlaid onto a T2 image (the level line matching that of histology is displayed in green, others are left black).

allowed, but this was not investigated here), but such data was not available at the time of the experiments. Results are reported in Fig. 5.20b and the observations made in (E5) seem to hold.

Alignment results

MS dataset

- *Without meaningful boundary selection.* Qualitative alignment results are shown in Fig. 5.21 for 4 pieces, considering neighbourhoods of ± 10 level lines. Overall, 5 pieces were matched and aligned correctly and two incorrectly. As for piece 6, no shape element was discriminative enough to be correctly matched with an MRI portion of level line without any ambiguity (Fig. 5.21c), as only relatively short bitangents could be extracted. As for piece 7, this is due to the fact that the piece of tissue is close to convex (and thus was not incorporated in the experiments and results). As a result, a few or no bitangents could be extracted from that histological image and no match was therefore available.

  The main requirements of the approach are twofold and relate to the *length* of the bitangents and the threshold on the Fréchet distance. As stressed out earlier, short bitangents convey little and ambiguous information about shape. This results in false matches especially because of the sinuosity of the MRI level lines (particularly in the brain), and the projective-invariant signature of shape elements (which may tolerate too wide a range of deformations). As a matter of fact, the approach was constrained

to using long bitangents so as to use peculiar shape element: in practice, those covering portions of a level line with more than 6 inflections were used. This number was picked after examination of the shape elements: curves with 6 inflections were complex enough to be matched without ambiguity. If a histological image happened to have informative portions with more than two inflections but less than 6—as it was the case for piece 5—then the longest bitangents were used (4 and 5 inflections in that case). An upper bound was also set (10 inflections) in order to speed up the matching process (quicker is always better, and the method tends to be rather long due to all the cross-comparisons: it took up to 15min without meaningful boundary selection; up to 7min using only the ten most meaningful boundaries. The improvement is not linear with the number of level lines, since most of those in the background tend to have less complex shape elements; this however depends on the smoothing scale) and avoid aberrant comparisons with bitangents covering the whole MR image; that range was applied to both MRI and histology. The rationale for considering such a range is also that it is not guaranteed that two level lines have the exact same number of inflections on corresponding portions across modalities, but their smoothness ensures those numbers are close. Long bitangents produce characteristic canonical curves (furthermore associated with wide frames) and allow for lower thresholds on the Fréchet distance while discarding false matches better.

- *With meaningful boundary selection.* Target registration errors are presented in Table. 5.1. The five most meaningful level lines (Fig. 5.8) were used for the extraction and matching of shape elements. This number was picked as a trade-off between redundancy and locality (by locality, I mean the concentration of level lines around a meaningful boundary of the tissue; one does prefer sharp edges, *i.e.,* close level lines, in order to guarantee more accurate alignments). One first observation, although significance has not showed due to the lack of data, is the improvement in terms of TRE when bitangents are refined (§5.4.2): not only does it allow for quality shape elements (level line frames are built better and more consistently)—and thereby for meaningful comparisons between canonical curves across modalities (see also (v) in §5.7.3), but also more accurate transformations can be estimated using such pairs of matching points with RANSAC. The consistency of some TREs despite bitangent refinement can be explained by the fact that the refinement step in §5.4.1 has left bi-

Table 5.1: (E3) Target registration errors (in pixels) between the 4 image corners of the 6 pieces of tissue manually aligned, and those of the same pieces registered using the present method, with and without bitangent refinement (w. and w/o BR) and using the 5 most meaningful level lines of each modality.

	1		2		3		4		5		6	
	w/ BR	w/o BR	w/ BR	w/o BR	w/ BR	w/o BR	w/ BR	w/o BR	w/ BR	w/o BR	w/ BR	w/o BR
TRE	2.52	2.68	2.33	2.01	1.90	1.92	2.06	2.71	3.56	3.64	143.4	55.7

tangents where they already were (and thus takes into account similar shape elements for recognition): this is the case when a level line does not have too strong a curvature locally. Overall, the "right" location (defined qualitatively from the ground truth arrangement) was found for five pieces of histology out of six (considering piece 7 is excluded because of its convexity) within the medical image plane (all TREs are lower than about 4pix), should it be with or without refinement. In the case of piece 6, the restriction of sets of level lines to meaningful boundaries did not help, and this shows that the approach fails when there is shape ambiguity (*i.e.*, too short bitangents)—incidentally visual assessment was also tricky; on a side note the lower TRE without bitangent refinement (piece 6) does not mean the approach worked better; it just shows that other wrong shape elements were matched (which happened to be closer to the *right* location). Slightly higher TREs ($\geq$ 3pix, for piece 5) arise when some frame points are not well spread across the tissue (*e.g.*, when shape elements are relatively flat or small) and since the corners of aligned images are used as landmarks, those may be more affected by misalignments. Another observation relates to the fact that tissue boundaries are blurry, making several parallel level lines refer to the same edge (see also (iii) in §5.7.5); blurriness does affect the accuracy of the alignment, but their low number mitigates this effect (in general only 2 or 3 follow the same edge, the others following different tissue boundaries); in addition, AMSS filtering allows to keep boundaries clear enough at coarse scales while getting rid of spurious details. Lastly, one must recall that the visually corresponding MR plane (2*mm*-thick slice) is not the actual slice that matches histology. Hence, the transformation obtained by the present method does not derive from actual correspondences, and manual alignment cannot, strictly speaking, be considered as ground truth.

BrainWeb

- *With meaningful boundary selection*. Target registration errors are reported in Table 5.2; the errors were computed using the corners of registered T1 patches using

Table 5.2: (E6) Mean target registration errors (in pixels) between the 4 image corners of 5 manually aligned T1 patches, and those of the same patches (initially corrupted) registered with a corresponding T2w MRI plane using the present method, with and without bitangent refinement (w/ and w/o BR) and using the 5 most meaningful level lines of each modality. 100 transformations, which parameters were drawn from normal distributions, were applied to each patch. High significance of the bitangent refinement is denoted by (**) for $p < 0.01$, while significance is denoted by (*) for $p < 0.05$ and was assessed by a paired t-test.

	1 (**)		2 (**)		3		4 (**)		5 (*)	
	w/ BR	w/o BR	w/ BR	w/o BR	w/ BR	w/o BR	w/ BR	w/o BR	w/ BR	w/o BR
TRE	2.44 ±1.21	3.21 ±1.62	2.09 ± 1.01	3.33 ± 1.9	5.65 ±2.81	5.76 ±2.75	2.16 ±1.15	3.45 ±1.67	4.18 ±2.02	4.89 ±2.39

the present method (with bitangent refinement), and those of the same patches (before corruption) manually aligned with the corresponding T2w plane. Overall, the right location was identified for all patches. Although the patches were largely distorted in some cases (compared to what would happen in reality—see second patch in Fig. 5.22), the method successfully matched elements and registered images. The refinement of bitangents significantly improve registration accuracy for 4 patches out of 5. This was assessed by means of a paired t-test. I chose to apply 100 projective transformations to each patch, which parameters were drawn from normal distributions. An additional observation could be that the method proved robust to artificial shape elements arising from cropping: indeed, cropping creates rectilinear boundaries at the edge of the patch, which level lines follow. Those portions being straight, though, even if a bitangent connects the brain folding pattern through a patch edge, the resulting shape element will be too peculiar to match any other shape element of the T2w full slice. Lastly, larger TREs were usually encountered for larger patches (since, like in the previous paragraph, the corners of images are used as landmarks). Another reason for such errors is the distribution and flatness of useful shape elements within the patches: if those concentrate at the bottom of the patch—see second patch in Fig. 5.22—, the estimation of the transformation can be erroneous and misalignments have more effect on the opposite corners of the patch. Qualitative alignment results are illustrated in Fig. 5.22 for 2 patches; although rotation seems to have been recovered well in the first case, the scale parameter along y seemed lesser than the actual one. In the second case, the rotation/shear parameters were not estimated accurately enough, causing the top of the image (especially the ventricles) to not be registered precisely (and some perspective to remain).

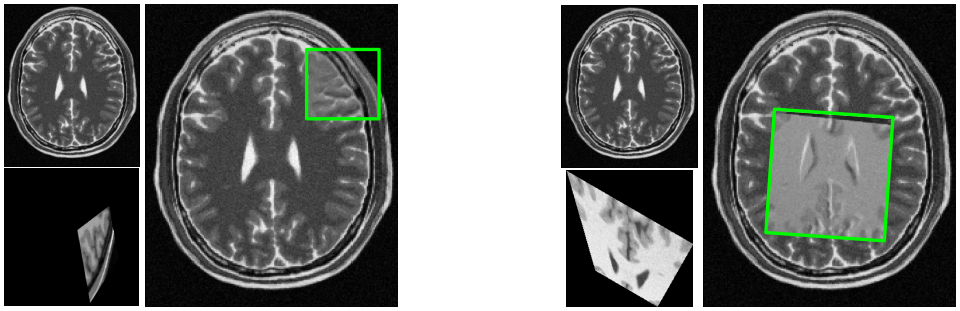

Figure 5.22: Alignment results (w/ meaningful boundary selection): illustrating 2 randomly corrupted (projective transform) patches of a T1 image to be registered with a corresponding T2w full slice. Registered patches are overlaid (opacity of 0.5) on the T2w image in the right panels.

5.7.3 Methodological comments

Several points that were not addressed in the experiments are discussed here.

(i) The effect of bias and its correction, on the coincidence of level lines with object boundaries. In a biased image, level lines "break" and do not follow the full length of the tissue boundaries; this results in curves that partially coincide with the tissue edges and go through the background in some other parts. In our case, it can be observed that the stronger the bias, the shorter the bitangents should be in order to avoid considering erroneous shape elements. In theory, the method should still reasonably work in the presence of a moderate bias in the image, since it is local (Fig. 5.23). Nevertheless, experiments were performed on bias corrected images so as to ensure long bitangents could be trustfully extracted. Further tests would be required to assess the exact effect of bias on the extraction of shape elements, their matching and the final accuracy of the registration.

(ii) The effects (and importance) of each geometric event on the selection of meaningful level lines. Since the exponent in the contrast term is greater than the exponent in the regularity term ($L > {}^{L}/_{L_0}$), contrast dominates the detections in general, and the temperature rather reinforces the criterion: the five most meaningful level lines are, in general the same, should one consider contrast or contrast+temperature *e.g.*, in the case of histology. In practice, the extra-event of irregularity benefits detections only for some specific images; several cases appear: (a) one wants to extract small convoluted structures in an image; then those should be highly contrasted and the contrast event will be sufficient for useful detections. This works well, for example, with pieces of tissue in histology stained with appropriate dyes. (b) One wants to ex-

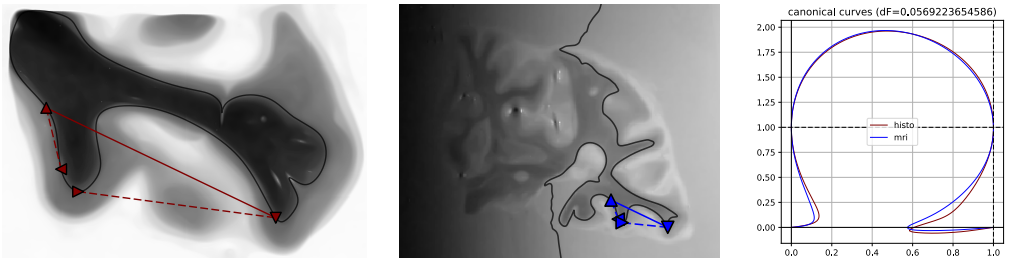

Figure 5.23: Illustrating the advantageous property of locality in the method by displaying two matching shape elements from histology and MRI despite a bias.

tract less contrasted complex structures; then those should be long and the irregularity extra-event will cause the NFA of highly contrasted long level lines to increase, while the NFA of less contrasted (preferably longer) but more complex ones will decrease. This works well, for example, with MRI scans of the full brain (Fig. 5.6).

This however needs to be put in perspective, as images also exhibit many uninteresting irregular level lines. This is why image simplification is first needed, during which an appropriate denoising (see §5.2) that smooths homogeneous regions and preserves the shape then allows keeping only the most informative boundaries.

With regard to other complexity measures (Fig. 5.24), it seems that the behaviour of the irregularity measure adapted from [473] is noisy for moderately complex curves; the repartition function becomes quite steep within that range, and thereby induces a risk for the NFA to be incorrectly balanced by that geometric event. In practice, this means moderately complex curves may be missed, unless their contrast is very high. An alternative is discussed in the first point of §5.7.5.

(iii) The method proved robust to "artificial edges" due to cutting. Although most registration methods are robust to such degradations, this is not trivial in shape recognition, since there is no definition of a tear (see also §3.5.2). Those can however be characterised as mostly rectilinear and therefore provide no or few informative bitangents (covering portions of the level line with little inflections). In addition, tissue cracks lead to large dissimilarities locally (when a bitangent covers a portion of level line that follows a tear): the associated shape element is discarded via the low threshold on the Fréchet distance. Because of the blurriness of edges, other adjacent (locally parallel) level lines that do not follow the tear, bound the tissue edges to its full extent; although less accurate, those can still be used for registration.

(iv) An invaluable advantage of the method is the possibility to combine meaningful level

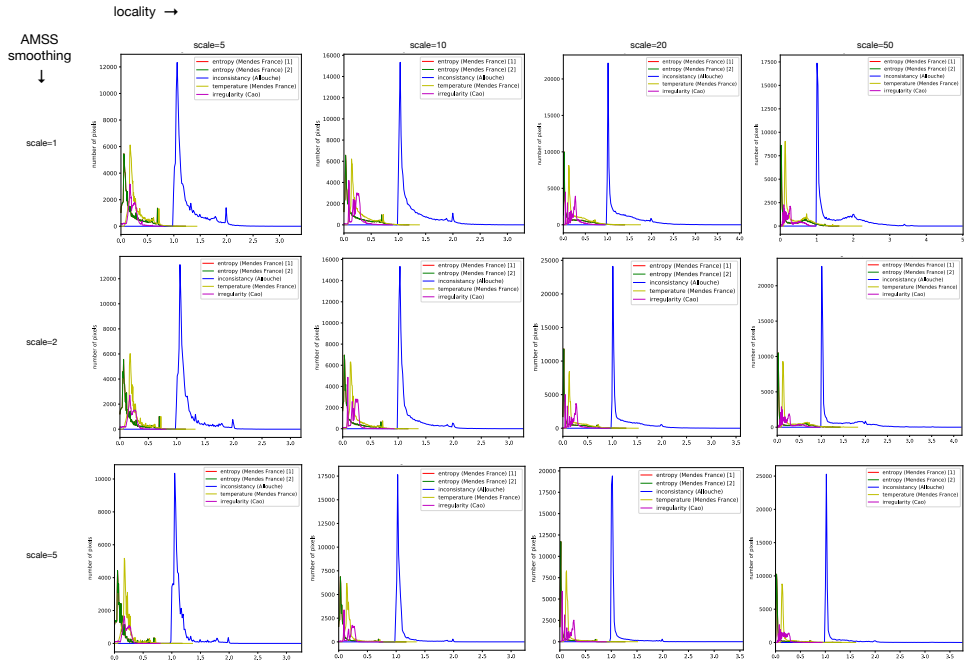

(a)

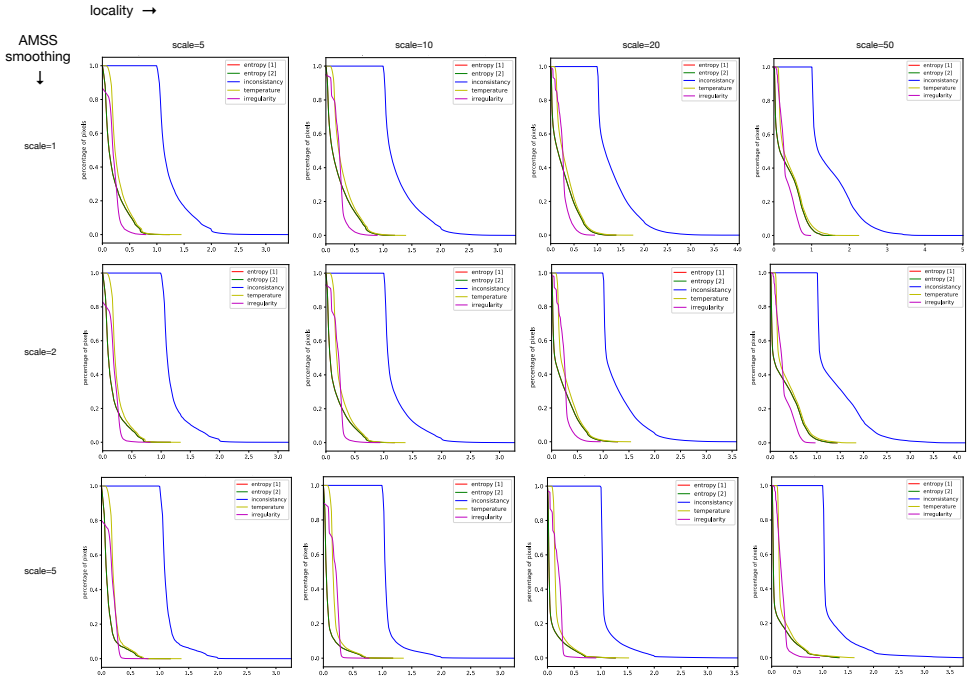

(b)

Figure 5.24: (5.24a) Histograms and (5.24b) repartition functions of the local complexity along level lines in a T2w scan of the brain, at various scales (locality) and for several levels of image smoothing (AMSS). The local measures of complexity considered here are definitions (5.11) [1] and (5.13) [2] of the entropy of plane curves, the inconstancy (5.12), the irregularity adapted from [473], and the temperature (5.20).

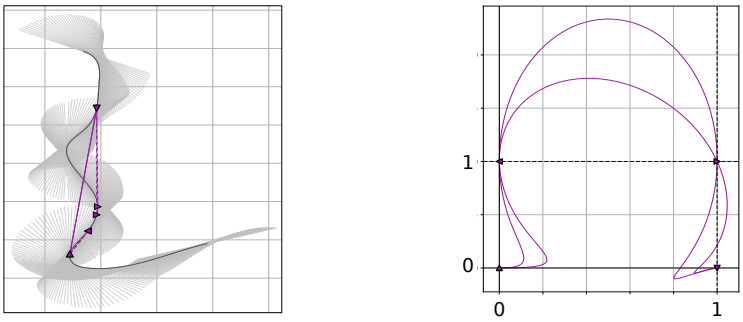

Figure 5.25: A portion of level line, $\mathcal{L}$ from histology is presented on the left, along with one of its bitangent. Up and down triangles symbolise the two bitangent points (resp. b_1 and b_2); left and right triangles symbolise the associated two cast points (resp. c_1 and c_2). In this illustration, the same frame is used twice, except c_2 is shifted along the level line in one case, so as to see the effect on the resulting canonical curves, on the left.

lines from several MRI modalities, which in effect is equivalent to fusing information (as defined in §3.2). The same thing is possible on the histological side, by grouping meaningful boundaries from each of all 11 dyes into a single set. Indeed, different shape-informative boundaries derive from different contrasts. Merging them into a single composite set is useful for recognition and matching for it gets more robust to the various layers that may be revealed by different dies in histology and different contrasts in MRI. Note that without any dye, the tissue is hardly differentiable from its background, some dyes stain the whole tissue uniformly (this was the case for most of the dyes used in the MS dataset)—while they do provide microscopic information, those are less useful for registration purposes—and others finally expose internal boundaries of the tissue very well. Likewise, while some MRI contrasts (like PSIR) hardly provide any structural information of the inner tissue, others like PD or MTR give valuable extra-information.

(v) The risks of building imbalanced frames (Fig. 5.25): even qualitatively, one understands the importance of carefully designing (level line) frames for meaningful comparisons between shape elements transformed in the canonical frame; indeed, the estimation of cast points directly derives from the accuracy of the placement of bitangent points (this is also a reason why a threshold on the Fréchet distance is required, as no two shape elements ever perfectly match across modalities). Conversely, one could also think of designing a canonical frame that is less sensitive to the closedness of the cast points (especially in the case of smaller bitangents). This stems from the fact that a small portion $\mathcal{L}\restriction[c_1,c_2]$ is more affected by the projective transformation than

a larger portion $\mathcal{L}\lceil[c_2, b_2]$, which biases the Fréchet distance during cross-modality comparisons. Overall, erroneous locations of the (level line) frame points result in the estimation of a projective transformation that provide more unique and less similar canonical curves. This observation could actually represent in itself a criticism to using projective invariance, as opposed to affine-invariance which tolerates less deformations but would require other kinds of frames.

As pointed out earlier, more than one frame may exist for long bitangent and it is critical to pick those that do not create pathological curves. This leads to one drawback of the method: although using long bitangents increases the robustness to false matches, it also increases the complexity of the algorithm as it creates many more possible frame configurations for a single bitangent (hence the importance of limiting the set of level lines to only those that are truly meaningful, and that of choosing frames that are wide and well distributed). Other canonical frames could be designed in order to reduce the risk of imbalance, and this could be added to Future work (§5.7.5).

(vi) An obvious limitation of the method is its restriction to 2D-2D registration (although comparisons with adjacent MR planes were carried out—see (E5) and (E8) in §5.7.2). This choice was made in view of the data available, for which the large MRI slice thickness did not allow for any kind of interpolation in order to densify the volume. As a consequence, it appeared safer to focus on 2D linear registration between a histological slice and a visually corresponding plane. Further refinement can then be thought of, including intensity-based linear and non-linear registration.

5.7.4 Conclusion

This chapter addressed the registration of a piece of tissue from histology and its whole in a medical image plane, regardless of the orientation of the piece of tissue on the glass slide (flips, rotations). The solution is geometric and jointly tackled the fractional and multimodal nature of the problem by relying on a local and contrast-invariant representation of the images that uses pieces of level lines (referred to as shape elements). The set of all level lines was limited to meaningful boundaries for computational efficiency and robustness. The shape elements were identified via the extraction of bitangents of the resulting level lines and efficiently refined using ellipses (a single bitangent was retained according to the local geometry of the level line). The elements were encoded in a projective-invariant manner so as to be robust to distortions happening during the histological process, and provided

canonical curves. The proposed framework took advantage of long shape elements, which are more discriminative but for which the corresponding bitangents may cross the level line, and found matches by comparison of the associated canonical curves across modalities using the Fréchet distance. Matching shape elements were fed into RANSAC and a unique similarity transform was computed; registration was thereby obtained as a byproduct of shape recognition. The method was validated on simulated and real data and showed good accuracy with an improvement when caring about refining bitangents.

5.7.5 Future work

Several tracks could be further investigated:

Selection of meaningful boundaries

(i) Other measures of curve complexity, on the basis of the concepts introduced by Mendès France [468] relative to thermodynamics and integral geometry. In particular, the "volume" V and "pressure" P of a curve were defined by assimilating them, respectively, to the length and the inverse of the perimeter of the convex hull of that curve. Plugging those quantities back into (5.17) gives the following relation between T and PV:

$$PV \stackrel{\text{def}}{=} \frac{1}{2}\,\frac{e^{2\mathsf{T}}}{e^{2\mathsf{T}}-1} \tag{5.40}$$

Intuitively, PV should describe how compressed (or closed on itself) a curve is *i.e.*, how it occupies the space within its convex hull (hence the interesting notions of pressure and volume). For the sake of illustration, one can picture the situation of Fig. 5.26, where one curve fills its hull, while the other folds on itself and remains close to its boundary (the reader should ignore the fact that those two curves clearly have different lengths). From there, it is possible to imagine another C-like level line, which two ends nearly meet, with a folding pattern similar to that shown in the right panel and having the same length as the curve in the left panel.

Now, the problem with eq. (5.17)—and therefore with (5.40)—is that two plane curves will have the same temperature (and thus the same PV values) as long as they have the same lengths and their convex hulls have the same perimeters. Definition (5.40) should thus (and remains to) be modified such that it can reflect the various ways a curve can fold, and how "flattened" or squeezed (and oppositely loose) it may look.

Ultimately, one could differentiate better between level lines following the actual

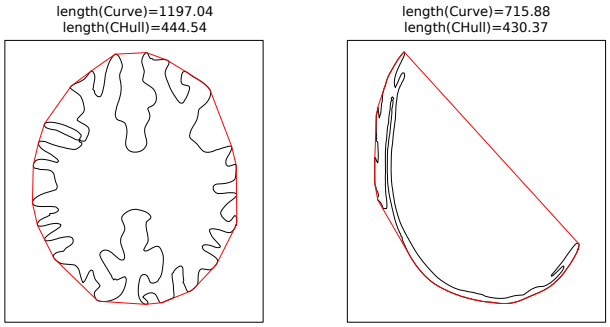

Figure 5.26: Illustrating two ways a curve can occupy the space within its convex hull.

brain folding pattern, and others, nearing the skull and more regular globally but *e.g.*, following vessels along the way or any high intensity blob causing the level line to "loop on itself".

(ii) The definition of the number of false alarms [27] (as recently discussed and extended by Tepper *et al.* [475]) and more specifically its sensitivity to the proposed joint contributions of the two geometric events: contrast and irregularity (the NFA is in general dominated by the contrast event, but one could try to weight them better).

(iii) The maximal meaningful boundaries. Due to sampling and interpolation, images are blurry and there is a (thin) transition layer around objects boundaries. This causes several "parallel" level lines to be selected as meaningful for one same object boundary (see Figs. 5.8 and 5.9). It may be useful to eliminate some of them to avoid redundancy (*i.e.*, unnecessary extra-computation) and misalignments. On the other hand, such redundancy could equally increase the number of true matches and false matches—depending on the peculiarity of the shape elements under comparison. Identifying maximal boundaries requires computing the tree of shape of an image (strictly speaking, it is, in that case, the tree of meaningful level lines that is needed), which is based on the inclusion principle of closed level lines (they are Jordan curves) [492].

Matching shape elements

(iv) The shortcut Fréchet distance [493]. The use of Fréchet distance is in itself a limitation of the method, since any deterioration of a level line locally will lead to large distance, and therefore the rejection of the corresponding shape element: a level line in histology may be globally close in terms of its shape to part of another in MRI but because of a tear that it follows, the distance between the associated canonical

curves will be large. However, this supposes a clear definition of what a tear is in histological images, which is far from trivial. Ideally, although this may not represent a significant improvement in terms of matching and alignment accuracy, investigating other measures of similarity between (canonical) curves should enrich the description of the problem by using such deteriorations (as opposed to discarding them).

The method as a whole

(v) The extension to 3D. This requires: (a) considering isosurfaces (as opposed to isolines or level lines) of images, (b) quantifying the irregularity of isosurfaces (*i.e.*, again via their intersections with random straight lines or planes...), (c) extending the dual theorem to 3D by describing surfaces as a family of tangent planes *i.e.*, computing the tangential surface—which represents the exact tangent planes to a surface—in order to identify bitangent planes of an isosurface, (d) refining bitangent planes using ellipsoids, (e) studying tangent planes of 2 ellipsoids, (f) defining and computing canonical surfaces, (g) quantifying similarity using distances between surfaces, like the continuous Procrustes distance in [494].

Chapter 6

Conclusions

Chapter 2 presented the evolution of the practical and intellectual process that led the anatomy to be presented and available in its current form, namely, via digital histology (or serial histological sections) and volumetric medical imaging. It also described today's techniques to generate FFPE and frozen sections, the artefacts they each are associated with, and the image processing methods developed to account for them (along with some remaining challenges, such as the correction of folds). The main objective of this chapter was to look at the data through a historical lens and observe that one has always tried to see more (or visualise better) in order to understand better. As Martin Chalfie said: "scientific inquiry starts with observation. The more one can see, the more one can investigate. Indeed, we often mark our progress in science by improvements in imaging".

Chapter 3 surveyed the literature on histology reconstruction with and without the help of external information, such as volumetric medical imaging or other intermediate modalities like blockface photographs. I also detailed the generation of such data, the artefacts associated with their preparation, and the preprocessing methods developed to deal with some of those degradations. Finally, I described common methods to validate registration/reconstruction pipelines and some applications. The discussion of the survey started with highlighting the advantages of *hybrid* pipelines (when the histological dataset is sufficient) over slice-based (their accuracy highly depends on the initialisation) and volume-based (they rely on a single round of 3D registration between histology and medical image volumes) approaches for histology reconstruction. In essence, hybrid pipelines rely on the principle that global alignment between both volumes is optimal only when the arrangement of histological sections relative to each other (the 3D histology reconstruction) is itself optimal, and *vice versa*. In other words, one conditions the performance of the other. This

strategy offers a robust way to achieve accurate reconstructions. Then, I presented some remaining challenges in image preprocessing: among others, one can think of the correction of folds, which remains an open problem as it requires knowing how many layers a single fold is made of. Assuming it is possible to know that number, the correction of a fold still requires the separation of structures belonging to each of the layers that compose it. It also necessitates the rearrangement of the entire piece of tissue according to its configuration prior to folding (*i.e.*, unfolding). I discussed the use of intermediate modalities, which depends on the very goals of the study, but should take into account requirements related to image registration in order to guarantee sufficient accuracy in the multimodal mapping (differences in contrast, content, resolution...). Indeed those proxy represent invaluable resources to keep track on tissue deformations along the histological process but may require additional set-ups and scheduling. I finally highlighted the importance of image analysis in histopathology owing to their richness in structural content. This was followed by some unaddressed problems and possible ways to investigate them. In particular, the latter led to the shape-based method presented in Chapter 5. I also thought it was relevant to stress out the two following points: (i) Cross-field awareness in histology reconstruction is crucial as data analyses rely on the assumption that the tissue remains similar enough through time and stages to be reliably compared across modalities. Improvements are consistently being made to minimise alterations of tissue and towards understanding the causes and effects of such variations. (ii) This brings us to second point, about the importance of understanding data: as far as image registration is concerned, it is simply a tool designed to achieve accurate and reproducible correspondences between separate images. However, improving it becomes vain if similar attention is not also directed towards ensuring consistent, quality input data within and across institutions. Standardising protocols is not easy and immediate, and although the importance of such undertaking is acknowledged by many, so is the amount of work that remains to be done. Furthermore, since quantitative measurements are to be extracted from those images and interpreted by clinicians/physicians, a comparable amount awaits computational imaging scientists dealing with such variations

Chapter 4 presented a method for histology reconstruction from serial sections, and an unbiased intensity standardisation method via a groupwise approach. With respect to the latter point, the biological component of the standardisation—as described in the colour normalisation methods of §2.5—was not addressed and remains an interesting extension

if *e.g.*, the optical properties of tissues are available. As for the former point, a graph-theoretic approach was introduced, which ensured comparability between the graph edges. I proposed to explain every pairwise registration between adjacent sections as: (i) a regular direct transformation and, (ii) a set of indirect ones obtained through neighbouring registrations by transitivity; each path is associated with a weight (a similarity measure) computed after the floating image has been applied the (possibly composed) transformation associated with that path. The set of weights has therefore, by design, a total ordering and the path that minimises the registration error between two adjacent sections can be identified (paths weights are comparable with one another); once this is done for all pairs of slices, the shortest paths become the new direct paths and the graph gets updated dynamically until convergence (*i.e.*, all the shortest paths are the direct ones). The proposed framework is intends to offer alternative ways to reach alignment despite various degradations, rather than addressing the correction of any of them specifically. Robustness to degradations is actually largely dependant upon the registration method itself. But involving slices with slightly different features, positions and orientations that are potentially more conducive to reaching global optimum helps the process. Although limited data (and information about them) were available, I showed that the method performed significantly better than direct pairwise reconstructions. Improvements to the method could be made by automating the selection of its two parameters, which are critical to guarantee good reconstructions and highly depend on the thickness of histological sections.

Chapter 5 introduced a method for multimodal registration between a piece of tissue from histology and its whole in an MRI based on shape recognition. It relied on representing images using their level lines. Such a formulation allowed for a contrast, projective invariant description of shape elements, and matching regardless of the orientation of the piece of tissue on the glass slide (flips, rotations). Additionally, the complete set of level lines was restricted to meaningful boundaries based on the *a contrario* detection model enriched with a geometric event relative to curve irregularity. A computationally efficient refinement of bitangents using ellipses was also introduced (and proved to significantly ameliorate alignments), from which a single bitangent was retained according to the local geometry of the level line. All this however, is to be related with the complexity of medical images; successful alignments require characteristic shape elements. I proposed to obtain them by considering bitangents that could as well cross the level lines and by preferring

long bitangents (those covering portions of level lines with many inflections): indeed, they produce characteristic canonical curves (furthermore associated with wide frames) and allow for lower thresholds on the Fréchet distance while discarding false matches better. I also propose to use meaningful level lines from several MRI protocols (those were aligned by default) so as to perform actual fusion and enrich shape representation. Likewise, meaningful level lines from several histological dyes were considered all at once (considering all slices have been registered together): some dyes stain the whole tissue uniformly (this was the case for most of the dyes used in the MS dataset)—while they do provide microscopic information, those are less useful for registration purposes—and others finally expose internal boundaries of the tissue very well. This allows going far beyond using a single contour for curve matching. Finally, I justified robustness of the approach to intensity bias—which commonly hampers medical image analysis—owing to the locality and contrast-invariance requirement(s). Indeed, shape elements characterise portions of the tissue; considering the bias is not too strong, level lines are not affected locally by intensity variations. However, experiments were performed on bias corrected images so as to ensure long bitangents could be trustfully extracted. Further tests would be required to assess the exact effect of bias on the extraction of shape elements, their matching and the final accuracy of the registration. Improvements to the methods could consist of improving the selection of meaningful boundaries, by adjusting the geometrical event related to the complexity of curves; or consist of trying to use the shortcut Fréchet distance to get estimates of the similarity between canonical curves that are robust to tears. One last possible improvement could be that the extension of the full method to three dimensions, though this comes with complicated requirements: irregularty of isosurfaces, an extension of the dual theorem to 3D by describing surfaces as a family of tangent planes, the refinement of bitangent planes using ellipsoids, the study of tangent planes of 2 ellipsoids, the quantification of similarity using distances between surfaces, etc...

Appendix A

Length, Shape and Area

In this Appendix[1], we start with expressing densities for sets of straight lines with different parametrisations (§A.1); then (§A.2), we go through the proof of eq. (5.5): the measure, $m(D)$ of the set of straight lines, D that intersect a rectifiable curve $\mathcal{C}$ of finite length L is $2L$ (see Fig. 5.4 for the original parametrisation of a given line). It follows that the measure of the set of lines that intersect a convex curve is the length of that curve, as introduced in eq. (5.6).

Definition 1. [470] *The measure of a set of lines $D(\mathsf{p},\varphi)$ is defined by the integral, over the set, of the differential form*

$$dD = d\mathsf{p} \wedge d\varphi, \tag{A.1}$$

where dD is called the density for the set of straight lines D.

A.1 Density for different line parametrisations

Let D be determined by its intercepts x and y on the coordinate axis (Fig. 5.4). Thus one has the relations:

$$\mathsf{p} = \frac{xy}{(x^2+y^2)^{3/2}} \text{ and } \varphi = \arctan\left(\frac{x}{y}\right), \tag{A.2}$$

and the partial derivatives: $\frac{\partial \mathsf{p}}{\partial x} = \frac{y^3}{(x^2+y^2)^{3/2}}$, $\frac{\partial \mathsf{p}}{\partial y} = \frac{x^3}{(x^2+y^2)^{3/2}}$, $\frac{\partial \varphi}{\partial x} = \frac{y}{(x^2+y^2)}$ and $\frac{\partial \varphi}{\partial y} = \frac{-x}{(x^2+y^2)}$.

Let us call ϕ the map $(x,y) \mapsto (\mathsf{p},\varphi)$ and one wants to pass from one set of coordinates to the other.

[1] The title is borrowed from H. Steinhaus' paper [469].

First, one needs the differential of ϕ, ϕ_* (or pushforward) at x and y, which can be obtained by the chain rule:

$$\phi_*\Big(\frac{\partial}{\partial x}\Big) = \frac{\partial \mathsf{p}}{\partial x}\frac{\partial}{\partial \mathsf{p}} + \frac{\partial \varphi}{\partial x}\frac{\partial}{\partial \varphi} = \frac{y^3}{(x^2+y^2)^{3/2}}\frac{\partial}{\partial \mathsf{p}} + \frac{y}{(x^2+y^2)}\frac{\partial}{\partial \varphi}, \tag{A.3}$$

and similarly:

$$\phi_*\Big(\frac{\partial}{\partial y}\Big) = \frac{x^3}{(x^2+y^2)^{3/2}}\frac{\partial}{\partial \mathsf{p}} - \frac{x}{(x^2+y^2)}\frac{\partial}{\partial \varphi}. \tag{A.4}$$

In order to get the pullback of the differential form $d\mathsf{p}\wedge d\varphi$, it must be evaluated on the previous pushforwards (A.3) and (A.4):

$$\begin{aligned}
&(d\mathsf{p}\wedge d\varphi)(\phi_*\partial_x, \phi_*\partial_y) = (d\mathsf{p}\wedge d\varphi)\Big(\frac{y^3}{(x^2+y^2)^{3/2}}\partial_{\mathsf{p}} + \frac{y}{(x^2+y^2)}\partial_\varphi,\\
&\frac{x^3}{(x^2+y^2)^{3/2}}\partial_{\mathsf{p}} - \frac{x}{(x^2+y^2)}\partial_\varphi\Big)\\
&= \frac{-xy^3}{(x^2+y^2)^{5/2}}(d\mathsf{p}\wedge d\varphi)(\partial_{\mathsf{p}}, \partial_\varphi) - \frac{x^3y}{(x^2+y^2)^{5/2}}(d\mathsf{p}\wedge d\varphi)(\partial_{\mathsf{p}}, \partial_\varphi)\\
&= \frac{-xy}{(x^2+y^2)^{3/2}},
\end{aligned} \tag{A.5}$$

by bilinearity and skew-symmetry of forms. Additionally, it is recalled that $(d\mathsf{p}\wedge d\varphi)(\partial_{\mathsf{p}}, \partial_\varphi) = 1$ and that $(d\mathsf{p}\wedge d\varphi)(\partial_{\mathsf{p}}, \partial_{\mathsf{p}}) = 0$.

Thus, one finally gets:

$$dD = \phi^*(d\mathsf{p}\wedge d\varphi) = \frac{xy}{(x^2+y^2)^{3/2}}dx\wedge dy, \tag{A.6}$$

since the density is taken at absolute value [470]. Note that the Jacobian of ϕ at x is the matrix representation of the differential of ϕ. Hence a similar result could have been obtained by simply differentiating (A.2) w.r.t. x and y and taking the outerproduct of the coordinate vectors.

If D is parametrised using the coefficients u, v of its equation: $ux+vy+c=0$ (c is a constant), one has: $x = {}^{-1}/_{u}$ and $y = {}^{-1}/_{v}$.

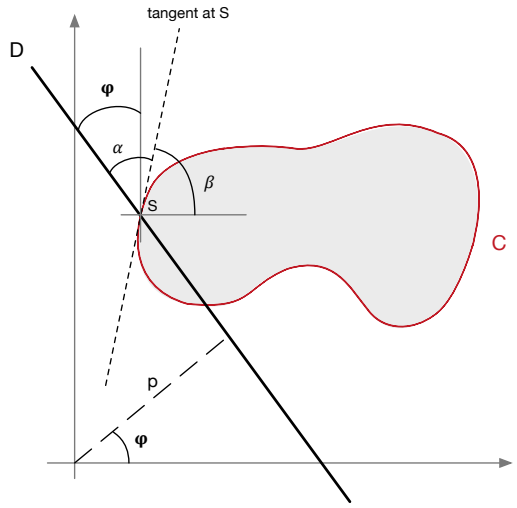

Figure A.1: Intersection of a straight line D with a given closed curve $\mathcal{C}$.

Considering the map $\psi:(u,v)\mapsto(x,y)$ one gets in a similar fashion:

$$\psi^*(dx\wedge dy)=\frac{1}{u^2v^2}du\wedge dv, \tag{A.7}$$

and finally, using (A.6):

$$dD=\frac{1}{(u^2+v^2)^{3/2}}du\wedge dv. \tag{A.8}$$

A.2 Measure and density for straight lines

Proof. Let D intersect a given closed plane curve, $\mathcal{C}$ of finite length, L at $S(x,y)$ (Fig. A.1). The angle that D makes with the tangent at that point is denoted α, and β is the angle that the tangent makes with the x-axis. One therefore has the relationship between angles:

$$\begin{aligned}&\beta+(\alpha-\varphi)={}^{\pi}/_{2}\\&\text{i.e. }\varphi=\beta+\alpha-{}^{\pi}/_{2}.\end{aligned} \tag{A.9}$$

Because $S\in D$, one has:

$$x\cos\varphi+y\sin\varphi-p=0. \tag{A.10}$$

Thus:

$$d\mathsf{p}=\cos\varphi\,dx+\sin\varphi\,dy+(x\sin\varphi-y\cos\varphi)d\varphi. \tag{A.11}$$

One also has, using the tangent at S: ${}^{dy}/_{dx} = \tan\beta$, i.e. ${}^{dy}/_{ds} = \sin\beta$ and ${}^{dx}/_{ds} = \cos\beta$, s being the arc length in the parametric equation of $\mathcal{C}$: $x = x(s)$ and $y = y(s)$.

In (A.11), this yields:

$$\begin{aligned} d\mathsf{p} &= \cos\varphi\cos\beta\, ds + \sin\varphi\sin\beta\, ds - (x\sin\varphi - y\cos\varphi)d\varphi \\ &= \cos(\varphi-\beta)ds - (x\sin\varphi - y\cos\varphi)d\varphi. \end{aligned} \tag{A.12}$$

The angle β being a function of s only, one has using (A.9):

$$d\varphi = d\alpha + \beta'(s)ds. \tag{A.13}$$

Using (A.12) and (A.13), the density dD yields:

$$\begin{aligned} d\mathsf{p}\wedge d\varphi &= \cos(\alpha - {}^{\pi}/_{2})\, ds \wedge \left(d\alpha + \beta'(s)ds\right) \\ &= \sin\alpha\, ds\wedge d\alpha. \end{aligned} \tag{A.14}$$

This result is taken at absolute value, since the density is positive.

Now using Def. 1 in order to get the measure of the set of straight lines, D, one takes the integral, over the set of lines, of the differential forms in (A.14). The domain $\omega = [0,L]\times[0,2\pi]$ is restricted to $[0,L]\times[0,\pi]$ since the same lines are found for $\alpha\in[\pi,2\pi]$ (and would therefore be counted twice). It is also recalled $\Omega = [0,+\infty[\times[0,\pi]$.

By integration of the right-hand side of (A.14), one gets:

$$\int_0^L ds\int_0^\pi |\sin\alpha|\, d\alpha = 2L. \tag{A.15}$$

Similarly, the left-hand side yields:

$$\int_\Omega f(\mathsf{p},\varphi)d\mathsf{p}d\varphi, \tag{A.16}$$

where f refers to the number of intersections of the line $D(\mathsf{p},\varphi)$ with $\mathcal{C}$. In other words, each line is counted as many times as it intersects $\mathcal{C}$ (if D does not intersect $\mathcal{C}$, $f(\mathsf{p},\varphi) = 0$). □

Note that if $\mathcal{C}$ is convex, one has:

$$f(\mathsf{p},\varphi) = \begin{cases} 2 & \text{if } D \text{ intersects } \mathcal{C}, \\ 0 & \text{otherwise.} \end{cases} \tag{A.17}$$

Therefore, $\int_{D\cap\mathcal{C}} f(\mathsf{p},\varphi)dD$ becomes:

$$\begin{aligned} \int_{D\cap\mathcal{C}} 2dD &= 2L \\ \text{i.e., } \int_{D\cap\mathcal{C}} dD &= L. \end{aligned} \tag{A.18}$$

In other words, the measure of the set of lines that intersect a convex curve is its length.

□

Appendix B

Thermodynamics of plane curves

In this appendix, the problem:

$$\begin{aligned} &\text{maximise } \mathsf{H}(\mathcal{L}) = -\sum_{k=1}^{\infty} p_k(\mathcal{L}) \log\, p_k(\mathcal{L}) \\ &\text{s.t. } \sum_{k=1}^{\infty} p_k(\mathcal{L}) = 1 \text{ and } \sum_{k=1}^{\infty} k p_k(\mathcal{L}) = {}^{2L}/_{\mathsf{P}(\Omega)} \end{aligned} \tag{B.1}$$

is solved, where $\mathsf{H}(\mathcal{L})$ is the "Boltzmann entropy" of a level line, $\mathcal{L}$ of length L, and $p_k(\mathcal{L})$ is the probability that a straight line intersects $\mathcal{L}$ in k points.

It is shown hereafter that this yields the Gibbs distribution: $p_k = (e^{\beta} - 1)e^{-\beta k}$, with $\beta = \log\left(\frac{{}^{2L}/_{\mathsf{P}(\Omega)}}{{}^{2L}/_{\mathsf{P}(\Omega)} - 1}\right)$, as introduced in (5.8).

To begin with, it is recalled:

$$\text{(A.16)} \sum_{k=1}^{\infty} k m_k = 2L,$$

$$\text{and (A.18)} \sum_{k=1}^{\infty} m_k = \mathsf{P}(\Omega),$$

where m_k is the measure of the set of straight lines that intersect the rectifiable curve $\mathcal{L}$ in exactly k points, and $\mathsf{P}(\Omega)$ is the perimeter of the convex hull Ω of $\mathcal{L}$. Note that the second equality constraint in (B.1) is obtained by defining $p_k = {}^{m_k}/_{\sum_{j=1}^{\infty} m_j}$. This result, which relates the average number (i.e. the expectation) of intersections between a random line and a plane curve, to the length of that curve is also known as the Cauchy-Crofton theorem.

Proof. Maximising H is done by use of the Lagrangian function, $\mathscr{L}$:

$$\mathscr{L}(p_1, p_2, p_3, \ldots, \lambda_1, \lambda_2) = -\sum_{k=1}^{\infty} p_k \log\, p_k - \lambda_1 \Big(\sum_{k=1}^{\infty} p_k - 1 \Big) - \lambda_2 \Big(\sum_{k=1}^{\infty} k p_k - {}^{2L}/_{\mathsf{P}(\Omega)} \Big) \tag{B.2}$$

with the Lagrangian multipliers λ_1 and λ_2.

Differentiating (B.2) w.r.t. p_k and equating to zero yields:

$$-(\log\, p_k + 1) - \lambda_1 - k\lambda_2 = 0. \tag{B.3}$$

Thus,

$$p_k = c e^{-k\lambda_2}, \tag{B.4}$$

where c is a constant.

The first equality constraint in (B.1) finally yields:

$$\begin{aligned} & c \sum_{k=1}^{\infty} e^{-k\lambda_2} = c \frac{1}{e^{\lambda_2} - 1} = 1, \\ & \text{i.e., } c = e^{\lambda_2} - 1, \end{aligned} \tag{B.5}$$

And the second gives:

$$\begin{aligned} & c \sum_{k=1}^{\infty} k e^{-k\lambda_2} = c \frac{e^{\lambda_2}}{(e^{\lambda_2} - 1)^2} = {}^{2L}/_{\mathsf{P}(\Omega)}, \\ & \text{i.e., } \lambda_2 = -\log\Big(1 - \frac{\mathsf{P}(\Omega)}{2L}\Big). \end{aligned}$$

□

Bibliography

[1] Grégoire Malandain, Éric Bardinet, Koen Nelissen, and Wim Vanduffel. Fusion of autoradiographs with an mr volume using 2-d and 3-d linear transformations. *NeuroImage*, 23(1):111–127, 2004.

[2] Charles Frederick Albert Culling. *Handbook of histopathological and histochemical techniques: including museum techniques*. Butterworth-Heinemann, 2013.

[3] Anant Madabhushi and George Lee. Image analysis and machine learning in digital pathology: challenges and opportunities, 2016.

[4] Metin N Gurcan, Laura E Boucheron, Ali Can, Anant Madabhushi, Nasir M Rajpoot, and Bulent Yener. Histopathological image analysis: a review. *Biomedical Engineering, IEEE Reviews in*, 2:147–171, 2009.

[5] Kristin M Gagnier and Thomas F Shipley. Completion in the wild: Perception of 3d forms from cross-sections. In *Proceedings of the 35th Annual Meeting of the Cognitive Science Society, Austin, TX*, volume 31, pages 2350–2355, 2013.

[6] Kinnari Atit, Thomas F Shipley, and Basil Tikoff. Twisting space: are rigid and non-rigid mental transformations separate spatial skills? *Cognitive processing*, 14(2):163–173, 2013.

[7] Andrea Frick, Wenke Möhring, and Nora S Newcombe. Development of mental transformation abilities. *Trends in cognitive sciences*, 18(10):536–542, 2014.

[8] Nick Hopwood. "giving body" to embryos: Modeling, mechanism, and the microtome in late nineteenth-century anatomy. *Isis*, pages 462–496, 1999.

[9] Bruce Fischl. Estimating the location of brodmann areas from cortical folding patterns using histology and ex vivo mri. In *Microstructural Parcellation of the Human Cerebral Cortex*, pages 129–156. Springer, 2013.

[10] John C. Gore. Biomedical imaging: current and future trends. *Physics World*. `http://medicalphysicsweb.org/cws/article/opinion/60791`, 2015.

[11] Massimo Filippi, Maria A Rocca, Frederik Barkhof, Wolfgang Brück, Jacqueline T Chen, Giancarlo Comi, Gabriele DeLuca, Nicola De Stefano, Bradley J Erickson, Nikos Evangelou, et al. Association between pathological and mri findings in multiple sclerosis. *The Lancet Neurology*, 11(4):349–360, 2012.

[12] A Seewann, E-J Kooi, SD Roosendaal, PJW Pouwels, MP Wattjes, P Van der Valk, F Barkhof, CH Polman, and JJG Geurts. Postmortem verification of ms cortical

lesion detection with 3d dir. *Neurology*, 78(5):302–308, 2012.

[13] Jacopo Annese. The importance of combining mri and large-scale digital histology in neuroimaging studies of brain connectivity. *Mapping the connectome: Multi-level analysis of brain connectivity*, 2012.

[14] Kensaku Mori. From macro-scale to micro-scale computational anatomy: a perspective on the next 20 years, 2016.

[15] Song-Lin Ding, Joshua J Royall, Susan M Sunkin, Lydia Ng, Benjamin AC Facer, Phil Lesnar, Angie Guillozet-Bongaarts, Bergen McMurray, Aaron Szafer, Tim A Dolbeare, et al. Comprehensive cellular-resolution atlas of the adult human brain. *Journal of Comparative Neurology*, 524(16):3127–3481, 2016.

[16] Seung Wook Oh, Julie A Harris, Lydia Ng, Brent Winslow, Nicholas Cain, Stefan Mihalas, Quanxin Wang, Chris Lau, Leonard Kuan, Alex M Henry, et al. A mesoscale connectome of the mouse brain. *Nature*, 508(7495):207–214, 2014.

[17] Katrin Amunts, Claude Lepage, Louis Borgeat, Hartmut Mohlberg, Timo Dickscheid, Marc-Étienne Rousseau, Sebastian Bludau, Pierre-Louis Bazin, Lindsay B Lewis, Ana-Maria Oros-Peusquens, et al. Bigbrain: an ultrahigh-resolution 3d human brain model. *Science*, 340(6139):1472–1475, 2013.

[18] Michael J Hawrylycz, Ed S Lein, Angela L Guillozet-Bongaarts, Elaine H Shen, Lydia Ng, Jeremy A Miller, Louie N Van De Lagemaat, Kimberly A Smith, Amanda Ebbert, Zackery L Riley, et al. An anatomically comprehensive atlas of the adult human brain transcriptome. *Nature*, 489(7416):391–399, 2012.

[19] Paul A Yushkevich, Brian B Avants, John Pluta, Sandhitsu Das, David Minkoff, Dawn Mechanic-Hamilton, Simon Glynn, Stephen Pickup, Weixia Liu, James C Gee, et al. A high-resolution computational atlas of the human hippocampus from postmortem magnetic resonance imaging at 9.4 t. *Neuroimage*, 44(2):385–398, 2009.

[20] Katrin Amunts and Karl Zilles. Architectonic mapping of the human brain beyond brodmann. *Neuron*, 88(6):1086–1107, 2015.

[21] Alan Priester, Shyam Natarajan, Pooria Khoshnoodi, Daniel J Margolis, Steven S Raman, Robert E Reiter, Jiaoti Huang, Warren Grundfest, and Leonard S Marks. Mri underestimation of prostate cancer geometry: Use of patient-specific molds to correlate images with whole-mount pathology. *The Journal of Urology*, 2016.

[22] John C Mazziotta, Arthur W Toga, Alan Evans, Peter Fox, and Jack Lancaster. A probabilistic atlas of the human brain: theory and rationale for its development the international consortium for brain mapping (icbm). *Neuroimage*, 2(2PA):89–101, 1995.

[23] Paul A Yushkevich, Brian B Avants, Lydia Ng, Michael Hawrylycz, Pablo D Burstein, Hui Zhang, and James C Gee. 3d mouse brain reconstruction from histology using a coarse-to-fine approach. In *Biomedical Image Registration*, pages 230–237. Springer, 2006.

[24] Amalia Cifor, Li Bai, and Alain Pitiot. Smoothness-guided 3-d reconstruction of 2-d histological images. *Neuroimage*, 56(1):197–211, 2011.

[25] Vicent Caselles, Bartomeu Coll, and Jean-Michel Morel. Topographic maps and local contrast changes in natural images. *International Journal of Computer Vision*, 33(1):5–27, 1999.

[26] Pascal Monasse and Frederic Guichard. Fast computation of a contrast-invariant image representation. *IEEE Transactions on Image Processing*, 9(5):860–872, 2000.

[27] Agnès Desolneux, Lionel Moisan, and Jean-Michel Morel. Edge detection by helmholtz principle. *Journal of Mathematical Imaging and Vision*, 14(3):271–284, 2001.

[28] Bruno Latour. *We have never been modern*. Harvard University Press, 2012.

[29] Martin Chalfie. Gfp: lighting up life (nobel lecture). *Angewandte Chemie International Edition*, 48(31):5603–5611, 2009.

[30] Soraya De Chadarevian and Nick Hopwood. *Models: the third dimension of science*. Stanford University Press, 2004.

[31] James Henry Breasted. *The Edwin Smith surgical papyrus: Hieroglyphic transliteration, translation and commentary*. Kessinger Publishing, 2006.

[32] Papyrus Ebers, Georg Ebers, and Ludwig Christian Stern. *Papyros Ebers: das hermetische Buch über die Arzeneimittel der alten Ägypter in hieratischer Schrift*. Biblio Verlag, 1987.

[33] Ch Singer. A short history of anatomy and physiology from the greeks to harvey. 1958.

[34] Heinrich Von Staden. *Herophilus: the art of medicine in early Alexandria: edition, translation and essays*. Cambridge University Press, 1989.

[35] Lynn Thorndike. A history of magic and experimental science. *The Journal of Nervous and Mental Disease*, 95(4):512–513, 1942.

[36] Brian Scott Baigrie. *Picturing knowledge: Historical and philosophical problems concerning the use of art in science*. University of Toronto Press, 1996.

[37] Kenneth D Keele. Leonardo da vinci's influence on renaissance anatomy. *Medical history*, 8(04):360–370, 1964.

[38] Glenn Harcourt. Andreas vesalius and the anatomy of antique sculpture. *Representations*, (17):28–61, 1987.

[39] Arthur W Toga and John C Mazziotta. *Brain Mapping: The Methods*. Academic press, 2002.

[40] Bruno Latour. Visualization and cognition. *Knowledge and society*, 6(1):1–40, 1986.

[41] Samuel Y Edgerton. *The Renaissance artist as quantifier*. Academic Press, 1980.

[42] Richard Hartley and Andrew Zisserman. *Multiple view geometry in computer vision*. Cambridge university press, 2003.

[43] William M Ivins Jr. *On the Rationalization of Sight, with an Examination of Three Renaissance Texts on Perspective*, volume 8. Metropolitan Museum of Art, 1938.

[44] Thomas N Haviland and Lawrence Charles Parish. A brief account of the use of wax models in the study of medicine. *Journal of the history of medicine and allied sciences*, 25(1):52–75, 1970.

[45] Theodor Schwann. Microscopical researches into the accordance in the structure and growth of animals and plants, trans. *Smith. London*, 1839.

[46] Samuel Y Edgerton. *The mirror, the window, and the telescope: how Renaissance linear perspective changed our vision of the universe*. Cornell University Press, 2009.

[47] FS Sjöstrand. Ultrastructure of retinal rod synapses of the guinea pig eye as revealed by three-dimensional reconstructions from serial sections. *Journal of ultrastructure research*, 2(1):122–170, 1958.

[48] Randle W Ware and Vincent LoPresti. Three-dimensional reconstruction from serial sections. *Int. Rev. Cytol*, 40:325–440, 1975.

[49] J Špaček. Three-dimensional reconstructions of astroglia and oligodendroglia cells. *Zeitschrift für Zellforschung und mikroskopische Anatomie*, 112(3):430–442, 1970.

[50] Cyrus Levinthal and Randle Ware. Three dimensional reconstruction from serial sections. 1972.

[51] V Lopresti, ER Macagno, and C Levinthal. Structure and development of neuronal connections in isogenic organisms: cellular interactions in the development of the optic lamina of daphnia. *Proceedings of the National Academy of Sciences*, 70(2):433–437, 1973.

[52] JF Vibert, F Bertrand, M Denavit-Saubie, and A Hugelin. Three dimensional representation of bulbo-pontine respiratory networks architecture from unit density maps. *Brain research*, 114(2):227–244, 1976.

[53] Walter Bradford Cannon. The movements of the intestines studied by means of the roentgen rays. *American Journal of Physiology–Legacy Content*, 6(5):251–277, 1902.

[54] William G Myers. Georg charles de hevesy: the father of nuclear medicine. *Journal of nuclear medicine: official publication, Society of Nuclear Medicine*, 20(6):590, 1979.

[55] Godfrey N Hounsfield. Computed medical imaging. *Journal of computer assisted tomography*, 4(5):665–674, 1980.

[56] Maggie A Flower. *Webb's physics of medical imaging*. CRC Press, 2012.

[57] Godfrey N Hounsfield. Computerized transverse axial scanning (tomography): Part

1. description of system. *The British journal of radiology*, 46(552):1016–1022, 1973.

[58] Ralph Weissleder and Mikael J Pittet. Imaging in the era of molecular oncology. *Nature*, 452(7187):580–589, 2008.

[59] Michel M Ter-Pogossian, Michael E Phelps, Edward J Hoffman, and Nizar A Mullani. A positron-emission transaxial tomograph for nuclear imaging (pett) 1. *Radiology*, 114(1):89–98, 1975.

[60] David J Brenner and Eric J Hall. Computed tomography—an increasing source of radiation exposure. *New England Journal of Medicine*, 357(22):2277–2284, 2007.

[61] Rebecca Smith-Bindman, Jafi Lipson, Ralph Marcus, Kwang-Pyo Kim, Mahadevappa Mahesh, Robert Gould, Amy Berrington de González, and Diana L Miglioretti. Radiation dose associated with common computed tomography examinations and the associated lifetime attributable risk of cancer. *Archives of internal medicine*, 169(22):2078–2086, 2009.

[62] Albertine Dubois, Julien Dauguet, Anne-Sophie Herard, Laurent Besret, Edouard Duchesnay, Vincent Frouin, Philippe Hantraye, Gilles Bonvento, and Thierry Delzescaux. Automated three-dimensional analysis of histological and autoradiographic rat brain sections: application to an activation study. *Journal of Cerebral Blood Flow & Metabolism*, 27(10):1742–1755, 2007.

[63] John D Bancroft and Marilyn Gamble. *Theory and practice of histological techniques*. Elsevier Health Sciences, 2008.

[64] René J Buesa. Histology safety: now and then. *Annals of diagnostic pathology*, 11(5):334–339, 2007.

[65] Juan Rosai. Why microscopy will remain a cornerstone of surgical pathology. *Laboratory investigation*, 87(5):403–408, 2007.

[66] William B Hardy. On the structure of cell protoplasm: Part i. the structure produced in a cell by fixative and post-mortem change. the structure of colloidal matter and the mechanism of setting and of coagulation. *The Journal of physiology*, 24(2):158, 1899.

[67] Sanjay Kakar, Michael Torbenson, Dhanpat Jain, Tsung-Teh Wu, Matthew Yeh, and Linda D Ferrell. Immunohistochemical pitfalls in the diagnosis of hepatocellular adenomas and focal nodular hyperplasia: accurate understanding of diverse staining patterns is essential for diagnosis and risk assessment. *Modern Pathology*, 28(1):159–160, 2015.

[68] G Rolls. Fixation and fixatives (2)-factors influencing chemical fixation, formaldehyde and glutaraldehyde. *Leica Biosystems. http://www.leicabiosystems.com/pathologyleaders/fixation-and-fixatives-2-factors-influencing-chemical-fixation-formaldehyde-and-glutaraldehyde*, 2012.

[69] Shan Yang, Zhengyi Yang, Karin Fischer, Kai Zhong, Jörg Stadler, Frank Go-

denschweger, Johann Steiner, Hans-Jochen Heinze, Hans-Gert Bernstein, Bernhard Bogerts, et al. Integration of ultra-high field mri and histology for connectome based research of brain disorders. *Front Neuroanat*, 7(31), 2013.

[70] Xue Chen, Zhuming Ai, Mary Rasmussen, Peter Bajcsy, Loretta Auvil, Michael Welge, Lu Leach, Sumalee Vangveeravong, Andrew J Maniotis, and Robert Folberg. Three-dimensional reconstruction of extravascular matrix patterns and blood vessels in human uveal melanoma tissue: techniques and preliminary findings. *Investigative ophthalmology & visual science*, 44(7):2834–2840, 2003.

[71] U Bürgel, T Schormann, A Schleicher, and K Zilles. Mapping of histologically identified long fiber tracts in human cerebral hemispheres to the mri volume of a reference brain: position and spatial variability of the optic radiation. *Neuroimage*, 10(5):489–499, 1999.

[72] Wolfgang J Weninger, Stefan Meng, Johannes Streicher, and Gerd B Müller. A new episcopic method for rapid 3-d reconstruction: applications in anatomy and embryology. *Anatomy and embryology*, 197(5):341–348, 1998.

[73] Thorsten Schormann and Karl Zilles. Three-dimensional linear and nonlinear transformations: an integration of light microscopical and mri data. *Human brain mapping*, 6(5-6):339–347, 1998.

[74] Johannes Streicher, Wolfgang J Weninger, and Gerd B Müller. External marker-based automatic congruencing: a new method of 3d reconstruction from serial sections. *The Anatomical Record*, 248(4):583–602, 1997.

[75] S Baheerathan, F Albregtsen, and HE Danielsen. Registration of serial sections of mouse liver cell nuclei. *Journal of microscopy*, 192(1):37–53, 1998.

[76] Markus Axer, Katrin Amunts, David Grässel, Christoph Palm, Jürgen Dammers, Hubertus Axer, Uwe Pietrzyk, and Karl Zilles. A novel approach to the human connectome: ultra-high resolution mapping of fiber tracts in the brain. *Neuroimage*, 54(2):1091–1101, 2011.

[77] Lejla Alic, Joost C Haeck, Karin Bol, Stefan Klein, Sandra T van Tiel, Piotr A Wielepolski, Marion de Jong, Wiro J Niessen, Monique Bernsen, and Jifke F Veenland. Facilitating tumor functional assessment by spatially relating 3d tumor histology and in vivo mri: image registration approach. *PLoS One*, 6(8):e22835, 2011.

[78] P Bajcsy, S-C LEE, A Lin, and R Folberg. Three-dimensional volume reconstruction of extracellular matrix proteins in uveal melanoma from fluorescent confocal laser scanning microscope images. *Journal of microscopy*, 221(1):30–45, 2006.

[79] Michael S Breen, Roee S Lazebnik, and David L Wilson. Three-dimensional registration of magnetic resonance image data to histological sections with model-based evaluation. *Annals of biomedical engineering*, 33(8):1100–1112, 2005.

[80] Thorsten Schormann, Andreas Dabringhaus, and Karl Zilles. Statistics of deformations in histology and application to improved alignment with mri. *Medical Imaging, IEEE Transactions on*, 14(1):25–35, 1995.

[81] Xia Li, Thomas E Yankeelov, Glenn D Rosen, John C Gore, and Benoit M Dawant. Enhancement of histological volumes through averaging and their use for the analysis of magnetic resonance images. *Magnetic resonance imaging*, 27(3):401–416, 2009.

[82] Smadar Gefen, Nahum Kiryati, and Jonathan Nissanov. Atlas-based indexing of brain sections via 2-d to 3-d image registration. *Biomedical Engineering, IEEE Transactions on*, 55(1):147–156, 2008.

[83] Richard Beare, K Richards, S Murphy, Steven Petrou, and David Reutens. An assessment of methods for aligning two-dimensional microscope sections to create image volumes. *Journal of neuroscience methods*, 170(2):332–344, 2008.

[84] Navid Samavati, Deirdre M McGrath, Jenny Lee, Theodorus van der Kwast, Michael Jewett, Cynthia Ménard, Kristy K Brock, et al. Biomechanical model-based deformable registration of mri and histopathology for clinical prostatectomy. *Journal of pathology informatics*, 2(2):10, 2011.

[85] Yiqiang Zhan, Yangming Ou, Michael Feldman, John Tomaszeweski, Christos Davatzikos, and Dinggang Shen. Registering histologic and mr images of prostate for image-based cancer detection. *Academic radiology*, 14(11):1367–1381, 2007.

[86] Rebecca AB Burton, Gernot Plank, Jürgen E Schneider, Vicente Grau, Helmut Ahammer, Stephen L Keeling, Jack Lee, Nicolas P Smith, David Gavaghan, Natalia Trayanova, et al. Three-dimensional models of individual cardiac histoanatomy: Tools and challenges. *Annals of the New York Academy of Sciences*, 1080(1):301–319, 2006.

[87] Lu Jiang, Tiffany R Greenwood, Erika R Amstalden Hove, Kamila Chughtai, Venu Raman, Paul T Winnard, Ron Heeren, Dmitri Artemov, and Kristine Glunde. Combined mr, fluorescence and histology imaging strategy in a human breast tumor xenograft model. *NMR in Biomedicine*, 26(3):285–298, 2013.

[88] Sergey Osechinskiy and Frithjof Kruggel. Slice-to-volume nonrigid registration of histological sections to mr images of the human brain. *Anatomy Research International*, 2011, 2010.

[89] Yousef Mazaheri, Louisa Bokacheva, Dirk-Jan Kroon, Oguz Akin, Hedvig Hricak, Daniel Chamudot, Samson Fine, and Jason A Koutcher. Semi-automatic deformable registration of prostate mr images to pathological slices. *Journal of Magnetic Resonance Imaging*, 32(5):1149–1157, 2010.

[90] Manbir Singh, Amrita Rajagopalan, Tae-Seong Kim, Darryl Hwang, Helena Chui, Xiao-Ling Zhang, Ae-Young Lee, and Chris Zarow. Co-registration of in vivo human mri brain images to postmortem histological microscopic images. *International journal of imaging systems and technology*, 18(5-6):325–335, 2008.

[91] Julien Le Nobin, Andrew B Rosenkrantz, Arnauld Villers, Clément Orczyk, Fang-Ming Deng, Jonathan Melamed, Artem Mikheev, Henry Rusinek, and Samir S Taneja. Image guided focal therapy for magnetic resonance imaging visible prostate cancer: defining a 3-dimensional treatment margin based on magnetic resonance imaging histology co-registration analysis. *The Journal of urology*, 194(2):364–370,

2015.

[92] Guy Nir, Ramin S Sahebjavaher, Piotr Kozlowski, Silvia D Chang, Erick C Jones, S Larry Goldenberg, and Septimiu E Salcudean. Registration of whole-mount histology and volumetric imaging of the prostate using particle filtering. *Medical Imaging, IEEE Transactions on*, 33(8):1601–1613, 2014.

[93] Eli Gibson, Cathie Crukley, Mena Gaed, José A Gómez, Madeleine Moussa, Joseph L Chin, Glenn S Bauman, Aaron Fenster, and Aaron D Ward. Registration of prostate histology images to ex vivo mr images via strand-shaped fiducials. *Journal of Magnetic Resonance Imaging*, 36(6):1402–1412, 2012.

[94] Aaron D Ward, Cathie Crukley, Charles A McKenzie, Jacques Montreuil, Eli Gibson, Cesare Romagnoli, Jose A Gomez, Madeleine Moussa, Joseph Chin, Glenn Bauman, et al. Prostate: registration of digital histopathologic images to in vivo mr images acquired by using endorectal receive coil. *Radiology*, 263(3):856–864, 2012.

[95] Ignacio Arganda-Carreras, Rodrigo Fernández-González, Arrate Muñoz-Barrutia, and Carlos Ortiz-De-Solorzano. 3d reconstruction of histological sections: Application to mammary gland tissue. *Microscopy research and technique*, 73(11):1019–1029, 2010.

[96] Yangming Ou and Christos Davatzikos. Dramms: deformable registration via attribute matching and mutual-saliency weighting. In *Information Processing in Medical Imaging*, pages 50–62. Springer, 2009.

[97] Charles R Meyer, Bradford A Moffat, K Kuszpit, Peyton L Bland, TL Chenevert, A Rehemtulla, and BD Ross. A methodology for registration of a histological slide and in vivo mri volume based on optimizing mutual information. *Molecular imaging*, 5(1):16, 2006.

[98] Daniel H Adler, John Pluta, Salmon Kadivar, Caryne Craige, James C Gee, Brian B Avants, and Paul A Yushkevich. Histology-derived volumetric annotation of the human hippocampal subfields in postmortem mri. *Neuroimage*, 84:505–523, 2014.

[99] Zhengyi Yang, Kay Richards, Nyoman D Kurniawan, Steven Petrou, and David C Reutens. Mri-guided volume reconstruction of mouse brain from histological sections. *Journal of neuroscience methods*, 211(2):210–217, 2012.

[100] Philippe Mailly, Suzanne N Haber, Henk J Groenewegen, and Jean-Michel Deniau. A 3d multi-modal and multi-dimensional digital brain model as a framework for data sharing. *Journal of neuroscience methods*, 194(1):56–63, 2010.

[101] G Allan Johnson, Alexandra Badea, Jeffrey Brandenburg, Gary Cofer, Boma Fubara, Song Liu, and Jonathan Nissanov. Waxholm space: an image-based reference for coordinating mouse brain research. *Neuroimage*, 53(2):365–372, 2010.

[102] M Mallar Chakravarty, Gilles Bertrand, Charles P Hodge, Abbas F Sadikot, and D Louis Collins. The creation of a brain atlas for image guided neurosurgery using serial histological data. *Neuroimage*, 30(2):359–376, 2006.

[103] Walid S Ibrahim Ali and Fernand S Cohen. Registering coronal histological 2-d sections of a rat brain with coronal sections of a 3-d brain atlas using geometric curve invariants and b-spline representation. *IEEE Transactions on Medical Imaging*, 17(6):957–966, 1998.

[104] J Annese, DM Sforza, M Dubach, D Bowden, and AW Toga. Postmortem high-resolution 3-dimensional imaging of the primate brain: blockface imaging of perfusion stained tissue. *Neuroimage*, 30(1):61–69, 2006.

[105] Stephan Handschuh, Thomas Schwaha, and Brian D Metscher. Showing their true colors: a practical approach to volume rendering from serial sections. *BMC developmental biology*, 10(1):41, 2010.

[106] Yi Song, Darren Treanor, Andrew J Bulpitt, Derek R Magee, et al. 3d reconstruction of multiple stained histology images. *Journal of pathology informatics*, 4(2):7, 2013.

[107] Derek Magee, Yi Song, Stephen Gilbert, Nicholas Roberts, Nagitha Wijayathunga, Ruth Wilcox, Andrew Bulpitt, and Darren Treanor. Histopathology in 3d: From three-dimensional reconstruction to multi-stain and multi-modal analysis. *Journal of pathology informatics*, 6, 2015.

[108] Shan-Rong Shi, MARC E Key, and KRISHAN L Kalra. Antigen retrieval in formalin-fixed, paraffin-embedded tissues: an enhancement method for immunohistochemical staining based on microwave oven heating of tissue sections. *Journal of Histochemistry & Cytochemistry*, 39(6):741–748, 1991.

[109] Martin Capek, Petr Bruza, Jiri Janacek, Petr Karen, Lucie Kubinova, and Radomira Vagnerova. Volume reconstruction of large tissue specimens from serial physical sections using confocal microscopy and correction of cutting deformations by elastic registration. *Microscopy research and technique*, 72(2):110–119, 2009.

[110] Harald C Groen, Theo Van Walsum, Sietske Rozie, Stefan Klein, Kim Van Gaalen, Frank JH Gijsen, Piotr A Wielopolski, Heleen MM Van Beusekom, Rini De Crom, Hence JM Verhagen, et al. Three-dimensional registration of histology of human atherosclerotic carotid plaques to in-vivo imaging. *Journal of biomechanics*, 43(11):2087–2092, 2010.

[111] Stephen R Peters. The art of embedding tissue for frozen section. part i: a system for precision face down cryoembedding of tissues using freezing temperature-embedding wells. *Journal of histotechnology*, 26(1):11–19, 2003.

[112] Jacopo Annese, Natalie M Schenker-Ahmed, Hauke Bartsch, Paul Maechler, Colleen Sheh, Natasha Thomas, Junya Kayano, Alexander Ghatan, Noah Bresler, Matthew P Frosch, et al. Postmortem examination of patient hm's brain based on histological sectioning and digital 3d reconstruction. *Nature communications*, 5, 2014.

[113] Maik Stille, Edward J Smith, William R Crum, and Michel Modo. 3d reconstruction of 2d fluorescence histology images and registration with in vivo mr images: Application in a rodent stroke model. *Journal of neuroscience methods*, 219(1):27–40, 2013.

[114] Ann S Choe, Yurui Gao, Xia Li, Keegan B Compton, Iwona Stepniewska, and Adam W Anderson. Accuracy of image registration between mri and light microscopy in the ex vivo brain. *Magnetic resonance imaging*, 29(5):683–692, 2011.

[115] Christoph Palm, Markus Axer, David Gräßel, Jürgen Dammers, Johannes Lindemeyer, Karl Zilles, Uwe Pietrzyk, and Katrin Amunts. Towards ultra-high resolution fibre tract mapping of the human brain-registration of polarised light images and reorientation of fibre vectors. *Frontiers in human neuroscience*, 4:9, 2010.

[116] Christoph Palm, Graeme P Penney, William R Crum, Julia A Schnabel, Uwe Pietrzyk, and David J Hawkes. Fusion of rat brain histology and mri using weighted multi-image mutual information. In *Medical Imaging*, pages 69140M–69140M. International Society for Optics and Photonics, 2008.

[117] Julien Dauguet, Sharon Peled, Vladimir Berezovskii, Thierry Delzescaux, Simon K Warfield, Richard Born, and Carl-Fredrik Westin. Comparison of fiber tracts derived from in-vivo dti tractography with 3d histological neural tract tracer reconstruction on a macaque brain. *Neuroimage*, 37(2):530–538, 2007.

[118] LINDA K Barthel and PAMELA A Raymond. Improved method for obtaining 3-microns cryosections for immunocytochemistry. *Journal of Histochemistry & Cytochemistry*, 38(9):1383–1388, 1990.

[119] Stephen R Peters. *A practical guide to frozen section technique*. Springer, 2010.

[120] Jerome B Taxy. Frozen section and the surgical pathologist: a point of view. *Archives of pathology & laboratory medicine*, 133(7):1135–1138, 2009.

[121] JL Humm, D Ballon, YC Hu, S Ruan, C Chui, PK Tulipano, A Erdi, J Koutcher, K Zakian, M Urano, et al. A stereotactic method for the three-dimensional registration of multi-modality biologic images in animals: Nmr, pet, histology, and autoradiography. *Medical physics*, 30(9):2303–2314, 2003.

[122] Jérôme Yelnik, Eric Bardinet, Didier Dormont, Grégoire Malandain, Sébastien Ourselin, Dominique Tandé, Carine Karachi, Nicholas Ayache, Philippe Cornu, and Yves Agid. A three-dimensional, histological and deformable atlas of the human basal ganglia. i. atlas construction based on immunohistochemical and mri data. *Neuroimage*, 34(2):618–638, 2007.

[123] Erin H Seeley, Kevin J Wilson, Thomas E Yankeelov, Rachelle W Johnson, John C Gore, Richard M Caprioli, Lynn M Matrisian, and Julie A Sterling. Co-registration of multi-modality imaging allows for comprehensive analysis of tumor-induced bone disease. *Bone*, 61:208–216, 2014.

[124] Georgia Lockwood-Estrin, Maria Thom, Niels K Focke, Mark R Symms, Lillian Martinian, Sanjay M Sisodiya, John S Duncan, and Sofia H Eriksson. Correlating 3t mri and histopathology in patients undergoing epilepsy surgery. *Journal of neuroscience methods*, 205(1):182–189, 2012.

[125] Jessica Lebenberg, A-S Hérard, Albertine Dubois, Julien Dauguet, Vincent Frouin, Marc Dhenain, Philippe Hantraye, and Thierry Delzescaux. Validation of mri-based

3d digital atlas registration with histological and autoradiographic volumes: an anatomofunctional transgenic mouse brain imaging study. *Neuroimage*, 51(3):1037–1046, 2010.

[126] Ching-Wei Wang, Shuk-Man Ka, and Ann Chen. Robust image registration of biological microscopic images. *Scientific reports*, 4, 2014.

[127] Ching-Wei Wang, Eric Budiman Gosno, and Yen-Sheng Li. Fully automatic and robust 3d registration of serial-section microscopic images. *Scientific reports*, 5, 2015.

[128] Julien Dauguet, Davi Bock, R Clay Reid, and Simon K Warfield. Alignment of large image series using cubic b-splines tessellation: Application to transmission electron microscopy data. In *International Conference on Medical Image Computing and Computer-Assisted Intervention*, pages 710–717. Springer, 2007.

[129] Shawn Mikula and Winfried Denk. High-resolution whole-brain staining for electron microscopic circuit reconstruction. *Nature methods*, 12(6):541–546, 2015.

[130] Winfried Denk and Heinz Horstmann. Serial block-face scanning electron microscopy to reconstruct three-dimensional tissue nanostructure. *PLoS Biol*, 2(11):e329, 2004.

[131] Lesley Graham and Jan Marc Orenstein. Processing tissue and cells for transmission electron microscopy in diagnostic pathology and research. *Nature protocols*, 2(10):2439–2450, 2007.

[132] Leonard F Belanger and Charles P LeBlond. A method for locating radioactive elements in tissues by covering histological sections with a photographic emulsion. *Endocrinology*, 39(1):8–13, 1946.

[133] Nicole Schubert, Markus Axer, Martin Schober, Anh-Minh Huynh, Marcel Huysegoms, Nicola Palomero-Gallagher, Jan G Bjaalie, Trygve B Leergaard, Mehmet E Kirlangic, Katrin Amunts, et al. 3d reconstructed cyto-, muscarinic m2 receptor, and fiber architecture of the rat brain registered to the waxholm space atlas. *Frontiers in neuroanatomy*, 10, 2016.

[134] Farzad Ghaznavi, Andrew Evans, Anant Madabhushi, and Michael Feldman. Digital imaging in pathology: whole-slide imaging and beyond. *Annual Review of Pathology: Mechanisms of Disease*, 8:331–359, 2013.

[135] Ronald S Weinstein, Anna R Graham, Lynne C Richter, Gail P Barker, Elizabeth A Krupinski, Ana Maria Lopez, Kristine A Erps, Achyut K Bhattacharyya, Yukako Yagi, and John R Gilbertson. Overview of telepathology, virtual microscopy, and whole slide imaging: prospects for the future. *Human pathology*, 40(8):1057–1069, 2009.

[136] G Rolls et al. 101 steps to better histology. *Melbourne: Leica Microsystems*, 2008.

[137] Xavier Moles Lopez, Etienne D'Andrea, Paul Barbot, Anne-Sophie Bridoux, Sandrine Rorive, Isabelle Salmon, Olivier Debeir, and Christine Decaestecker. An

automated blur detection method for histological whole slide imaging. *PloS one*, 8(12):e82710, 2013.

[138] Yukako Yagi and John R Gilbertson. Digital imaging in pathology: the case for standardization. *Journal of telemedicine and telecare*, 11(3):109–116, 2005.

[139] Aldo Badano, Craig Revie, Andrew Casertano, Wei-Chung Cheng, Phil Green, Tom Kimpe, Elizabeth Krupinski, Christye Sisson, Stein Skrøvseth, Darren Treanor, et al. Consistency and standardization of color in medical imaging: a consensus report. *Journal of digital imaging*, 28(1):41–52, 2015.

[140] Rafael C Gonzalez and Richard E Woods. Digital image processing. 2002.

[141] Maryana Alegro, Edson Amaro-Jr, Burlen Loring, Helmut Heinsen, Eduardo Alho, Lilla Zollei, Daniela Ushizima, and Lea T Grinberg. Multimodal whole brain registration: Mri and high resolution histology. In *Proceedings of the IEEE Conference on Computer Vision and Pattern Recognition Workshops*, pages 194–202, 2016.

[142] Grégoire Malandain and Eric Bardinet. Intensity compensation within series of images. In *International Conference on Medical Image Computing and Computer-Assisted Intervention*, pages 41–49. Springer, 2003.

[143] Can Ceritoglu, Lei Wang, Lynn D Selemon, John G Csernansky, Michael I Miller, and J Tilak Ratnanather. Large deformation diffeomorphic metric mapping registration of reconstructed 3d histological section images and in vivo mr images. *Frontiers in human neuroscience*, 4:43, 2010.

[144] Ramón Casero, Urszula Siedlecka, Elizabeth S Jones, Lena Gruscheski, Matthew Gibb, Jürgen E Schneider, Peter Kohl, and Vicente Grau. Transformation diffusion reconstruction of three-dimensional histology volumes from two-dimensional image stacks. *Medical image analysis*, 38:184–204, 2017.

[145] Simone Gaffling, Florian Jäger, Volker Daum, Miyuki Tauchi, and Elke Lütjen-Drecoll. Interpolation of histological slices by means of non-rigid registration. In *Bildverarbeitung für die Medizin 2009*, pages 267–271. Springer, 2009.

[146] M Mallar Chakravarty, Gilles Bertrand, Maxime Descouteaux, Abbas F Sadikot, and D Louis Collins. The creation of a brain atlas for image guided neurosurgery using serial histological data. In *International Conference on Medical Image Computing and Computer-Assisted Intervention*, pages 343–350. Springer, 2003.

[147] Laszlo G Nyul and Jayaram K Udupa. On standardizing the mr image intensity scale. *image*, 1081, 1999.

[148] Ulaş Bagci and Li Bai. Automatic best reference slice selection for smooth volume reconstruction of a mouse brain from histological images. *IEEE Transactions on Medical imaging*, 29(9):1688–1696, 2010.

[149] Julien Dauguet, Jean-François Mangin, Thierry Delzescaux, and Vincent Frouin. Robust inter-slice intensity normalization using histogram scale-space analysis. In *International Conference on Medical Image Computing and Computer-Assisted Inter-*

vention, pages 242–249. Springer, 2004.

[150] Peter Shirley. Color transfer between images. *IEEE Corn*, 21:34–41, 2001.

[151] Yi-Ying Wang, Shao-Chien Chang, Li-Wha Wu, Sen-Tien Tsai, and Yung-Nien Sun. A color-based approach for automated segmentation in tumor tissue classification. In *2007 29th Annual International Conference of the IEEE Engineering in Medicine and Biology Society*, pages 6576–6579. IEEE, 2007.

[152] Pinky A Bautista, Noriaki Hashimoto, Yukako Yagi, et al. Color standardization in whole slide imaging using a color calibration slide. *Journal of pathology informatics*, 5(1):4, 2014.

[153] Pinky A Bautista and Yukako Yagi. Staining correction in digital pathology by utilizing a dye amount table. *Journal of digital imaging*, 28(3):283–294, 2015.

[154] Ulf-Dietrich Braumann, Jens-Peer Kuska, Jens Einenkel, Lars-Christian Horn, Markus Löffler, and Michael Höckel. Three-dimensional reconstruction and quantification of cervical carcinoma invasion fronts from histological serial sections. *Medical Imaging, IEEE Transactions on*, 24(10):1286–1307, 2005.

[155] Marc Macenko, Marc Niethammer, James Stephen Marron, David Borland, John T Woosley, Xiaojun Guan, Charles Schmitt, and Nancy E Thomas. A method for normalizing histology slides for quantitative analysis. In *ISBI*, volume 9, pages 1107–1110, 2009.

[156] Derek Magee, Darren Treanor, Doreen Crellin, Mike Shires, Katherine Smith, Kevin Mohee, and Philip Quirke. Colour normalisation in digital histopathology images. In *Proc Optical Tissue Image analysis in Microscopy, Histopathology and Endoscopy (MICCAI Workshop)*, volume 100. Citeseer, 2009.

[157] Adnan Mujahid Khan, Nasir Rajpoot, Darren Treanor, and Derek Magee. A nonlinear mapping approach to stain normalization in digital histopathology images using image-specific color deconvolution. *IEEE Transactions on Biomedical Engineering*, 61(6):1729–1738, 2014.

[158] Jared Vicory, Heather D Couture, Nancy E Thomas, David Borland, James Stephen Marron, John Woosley, and Marc Niethammer. Appearance normalization of histology slides. *Computerized Medical Imaging and Graphics*, 43:89–98, 2015.

[159] Abhishek Vahadane, Tingying Peng, Amit Sethi, Shadi Albarqouni, Lichao Wang, Maximilian Baust, Katja Steiger, Anna Melissa Schlitter, Irene Esposito, and Nassir Navab. Structure-preserving color normalization and sparse stain separation for histological images. 2016.

[160] Babak Ehteshami Bejnordi, Geert Litjens, Nadya Timofeeva, Irene Otte-Höller, André Homeyer, Nico Karssemeijer, and Jeroen AWM van der Laak. Stain specific standardization of whole-slide histopathological images. *IEEE transactions on medical imaging*, 35(2):404–415, 2016.

[161] Sonal Kothari, John H Phan, May D Wang, et al. Eliminating tissue-fold artifacts in

histopathological whole-slide images for improved image-based prediction of cancer grade. *Journal of pathology informatics*, 4(1):22, 2013.

[162] Pinky A Bautista, Yukako Yagi, et al. Improving the visualization and detection of tissue folds in whole slide images through color enhancement. *Journal of pathology informatics*, 1(1):25, 2010.

[163] Sakari Palokangas, Jyrki Selinummi, and Olli Yli-Harja. Segmentation of folds in tissue section images. In *2007 29th Annual International Conference of the IEEE Engineering in Medicine and Biology Society*, pages 5641–5644. IEEE, 2007.

[164] Justin Solomon, Etienne Vouga, Max Wardetzky, and Eitan Grinspun. Flexible developable surfaces. In *Computer Graphics Forum*, volume 31, pages 1567–1576. Wiley Online Library, 2012.

[165] X Qiu, T Pridmore, and A Pitiot. Correcting distorted histology slices for 3d reconstruction. *Med Image Underst Anal*, 2009.

[166] LM Kindle, IA Kakadiaris, T Ju, and JP Carson. A semiautomated approach for artefact removal in serial tissue cryosections. *Journal of microscopy*, 241(2):200–206, 2011.

[167] Michael S Breen, Tanya L Lancaster, and David L Wilson. Correcting spatial distortion in histological images. *Computerized Medical Imaging and Graphics*, 29(6):405–417, 2005.

[168] Fred L. Bookstein. Principal warps: Thin-plate splines and the decomposition of deformations. *IEEE Transactions on Pattern Analysis & Machine Intelligence*, (6):567–585, 1989.

[169] Alexandre X Falcão, Jayaram K Udupa, Supun Samarasekera, Shoba Sharma, Bruce Elliot Hirsch, and Roberto de A Lotufo. User-steered image segmentation paradigms: Live wire and live lane. *Graphical models and image processing*, 60(4):233–260, 1998.

[170] Eric Mortensen, Bryan Morse, William Barrett, and Jayaram Udupa. *Adaptive boundary detection using 'live-wire' two-dimensional dynamic programming*. IEEE, 1992.

[171] Weixin Kong and Benjamin B Kimia. On solving 2d and 3d puzzles using curve matching. In *Computer Vision and Pattern Recognition, 2001. CVPR 2001. Proceedings of the 2001 IEEE Computer Society Conference on*, volume 2, pages II–583. IEEE, 2001.

[172] Genady Paikin and Ayellet Tal. Solving multiple square jigsaw puzzles with missing pieces. In *2015 IEEE Conference on Computer Vision and Pattern Recognition (CVPR)*, pages 4832–4839. IEEE, 2015.

[173] Mehmet Yigitsoy and Nassir Navab. Structure propagation for image registration. *IEEE transactions on medical imaging*, 32(9):1657–1670, 2013.

[174] Douglas P Holmes and Alfred J Crosby. Draping films: A wrinkle to fold transition.

Physical review letters, 105(3):038303, 2010.

[175] Tobias Pfaff, Rahul Narain, Juan Miguel de Joya, and James F O'Brien. Adaptive tearing and cracking of thin sheets. *ACM Transactions on Graphics (TOG)*, 33(4):110, 2014.

[176] Christophoros Nikou, Fabrice Heitz, Astrid Nehlig, Izzie Jacques Namer, and Jean-Paul Armspach. A robust statistics-based global energy function for the alignment of serially acquired autoradiographic sections. *Journal of neuroscience methods*, 124(1):93–102, 2003.

[177] Jae Sung Lee, Soon-Hyun Ahn, Dong Soo Lee, Seung Ha Oh, Chong Sun Kim, Jae Min Jeong, Kwang Suk Park, June-Key Chung, and Myung Chul Lee. Voxel-based statistical analysis of cerebral glucose metabolism in the rat cortical deafness model by 3d reconstruction of brain from autoradiographic images. *European journal of nuclear medicine and molecular imaging*, 32(6):696–701, 2005.

[178] Julien Dauguet, Thierry Delzescaux, Françoise Condé, Jean-François Mangin, Nicholas Ayache, Philippe Hantraye, and Vincent Frouin. Three-dimensional reconstruction of stained histological slices and 3d non-linear registration with in-vivo mri for whole baboon brain. *Journal of neuroscience methods*, 164(1):191–204, 2007.

[179] Maged Goubran, Cathie Crukley, Sandrine de Ribaupierre, Terence M Peters, and Ali R Khan. Image registration of ex-vivo mri to sparsely sectioned histology of hippocampal and neocortical temporal lobe specimens. *Neuroimage*, 83:770–781, 2013.

[180] J-F Mangin, Olivier Coulon, and Vincent Frouin. Robust brain segmentation using histogram scale-space analysis and mathematical morphology. In *International Conference on Medical Image Computing and Computer-Assisted Intervention*, pages 1230–1241. Springer, 1998.

[181] Song Chun Zhu and Alan Yuille. Region competition: Unifying snakes, region growing, and bayes/mdl for multiband image segmentation. *IEEE transactions on pattern analysis and machine intelligence*, 18(9):884–900, 1996.

[182] Mariano Uberti, Yutong Liu, Huanyu Dou, R Lee Mosley, Howard E Gendelman, and Michael Boska. Registration of in vivo mr to histology of rodent brains using blockface imaging. In *SPIE Medical Imaging*, pages 726213–726213. International Society for Optics and Photonics, 2009.

[183] Chunming Li, Chenyang Xu, Changfeng Gui, and Martin D Fox. Level set evolution without re-initialization: a new variational formulation. In *2005 IEEE Computer Society Conference on Computer Vision and Pattern Recognition (CVPR'05)*, volume 1, pages 430–436. IEEE, 2005.

[184] Brian B Avants, Nicholas J Tustison, Jue Wu, Philip A Cook, and James C Gee. An open source multivariate framework for n-tissue segmentation with evaluation on public data. *Neuroinformatics*, 9(4):381–400, 2011.

[185] FJ WM Leong, M Brady, and J O'D McGee. Correction of uneven illumination

(vignetting) in digital microscopy images. *Journal of clinical pathology*, 56(8):619–621, 2003.

[186] John G Sled, Alex P Zijdenbos, and Alan C Evans. A nonparametric method for automatic correction of intensity nonuniformity in mri data. *IEEE transactions on medical imaging*, 17(1):87–97, 1998.

[187] Uro Vovk, Franjo Pernus, and Botjan Likar. A review of methods for correction of intensity inhomogeneity in mri. *IEEE transactions on medical imaging*, 26(3):405–421, 2007.

[188] Tingying Peng, Lichao Wang, Christine Bayer, Sailesh Conjeti, Maximilian Baust, and Nassir Navab. Shading correction for whole slide image using low rank and sparse decomposition. In *International Conference on Medical Image Computing and Computer-Assisted Intervention*, pages 33–40. Springer, 2014.

[189] Filippo Piccinini, Alessandro Bevilacqua, Kevin Smith, and Peter Horvath. Vignetting and photo-bleaching correction in automated fluorescence microscopy from an array of overlapping images. In *2013 IEEE 10th International Symposium on Biomedical Imaging*, pages 464–467. IEEE, 2013.

[190] Constantino C Reyes-Aldasoro. Retrospective shading correction algorithm based on signal envelope estimation. *Electronics letters*, 45(9):454, 2009.

[191] Wonpil Yu. Practical anti-vignetting methods for digital cameras. *IEEE Transactions on Consumer Electronics*, 50(4):975–983, 2004.

[192] Rafael C Gonzalez. P. wintz digital image processing. *Addision-Wesley Publishing Company*, pages 275–281, 1987.

[193] Rodrigo Fernandez-Gonzalez, Thomas Deschamps, Adam Idica, Ravikanth Malladi, and C Ortiz de Solorzano. Automatic segmentation of histological structures in mammary gland tissue sections. *Journal of biomedical optics*, 9(3):444–453, 2004.

[194] Martin Čapek, Jiří Janáček, and Lucie Kubínová. Methods for compensation of the light attenuation with depth of images captured by a confocal microscope. *Microscopy research and technique*, 69(8):624–635, 2006.

[195] W-Y Hsu, W-F Poon, and Y-N Sun. Automatic seamless mosaicing of microscopic images: enhancing appearance with colour degradation compensation and wavelet-based blending. *Journal of Microscopy*, 231(3):408–418, 2008.

[196] Jonathan Chappelow, John E Tomaszewski, Michael Feldman, Natalie Shih, and Anant Madabhushi. Histostitcher©: An interactive program for accurate and rapid reconstruction of digitized whole histological sections from tissue fragments. *Computerized Medical Imaging and Graphics*, 35(7):557–567, 2011.

[197] Daniel S Gareau, Yongbiao Li, Billy Huang, Zach Eastman, Kishwer S Nehal, and Milind Rajadhyaksha. Confocal mosaicing microscopy in mohs skin excisions: feasibility of rapid surgical pathology. *Journal of biomedical optics*, 13(5):054001–054001, 2008.

[198] A Murat Tekalp. *Digital video processing*. Prentice-Hall, Inc., 1995.

[199] Petr Karen, Marie Jirkovská, Zoltán Tomori, Erna Demjénová, Jiří Janáček, and Lucie Kubinova. Three-dimensional computer reconstruction of large tissue volumes based on composing series of high-resolution confocal images by gluemrc and linkmrc software. *Microscopy research and technique*, 62(5):415–422, 2003.

[200] Stephan Saalfeld, Richard Fetter, Albert Cardona, and Pavel Tomancak. Elastic volume reconstruction from series of ultra-thin microscopy sections. *Nature methods*, 9(7):717–720, 2012.

[201] Stephan Saalfeld, Albert Cardona, Volker Hartenstein, and Pavel Tomančák. As-rigid-as-possible mosaicking and serial section registration of large sstem datasets. *Bioinformatics*, 26(12):i57–i63, 2010.

[202] F Piccinini, A Bevilacqua, and E Lucarelli. Automated image mosaics by non-automated light microscopes: the micromos software tool. *Journal of microscopy*, 252(3):226–250, 2013.

[203] Stephan Preibisch, Stephan Saalfeld, and Pavel Tomancak. Globally optimal stitching of tiled 3d microscopic image acquisitions. *Bioinformatics*, 25(11):1463–1465, 2009.

[204] Matthew Brown and David G Lowe. Automatic panoramic image stitching using invariant features. *International journal of computer vision*, 74(1):59–73, 2007.

[205] Philippe Thévenaz and Michael Unser. User-friendly semiautomated assembly of accurate image mosaics in microscopy. *Microscopy research and technique*, 70(2):135–146, 2007.

[206] Mario Emmenlauer, Olaf Ronneberger, Aaron Ponti, Patrick Schwarb, Alessandra Griffa, Alida Filippi, Roland Nitschke, Wolfgang Driever, and Hans Burkhardt. Xuvtools: free, fast and reliable stitching of large 3d datasets. *Journal of microscopy*, 233(1):42–60, 2009.

[207] Gregory Penzias, Andrew Janowczyk, Asha Singanamalli, Mirabela Rusu, Natalie Shih, Michael Feldman, Phillip D Stricker, Warick Delprado, Sarita Tiwari, Maret Böhm, et al. Autostitcher: An automated program for efficient and robust reconstruction of digitized whole histological sections from tissue fragments. *Scientific Reports*, 6:29906, 2016.

[208] Bin Ma, Timo Zimmermann, Manfred Rohde, Simon Winkelbach, Feng He, Werner Lindenmaier, and Kurt EJ Dittmar. Use of autostitch for automatic stitching of microscope images. *Micron*, 38(5):492–499, 2007.

[209] Sunny K Chow, Hiroyuki Hakozaki, Diana L Price, Natalie AB MacLean, Thomas J Deerinck, James C Bouwer, Maryann E Martone, Steven T Peltier, and Mark H Ellisman. Automated microscopy system for mosaic acquisition and processing. *Journal of Microscopy*, 222(2):76–84, 2006.

[210] Jiaya Jia and Chi-Keung Tang. Image stitching using structure deformation. *IEEE*

Transactions on Pattern Analysis and Machine Intelligence, 30(4):617–631, 2008.

[211] Albert Cardona, Stephan Saalfeld, Johannes Schindelin, Ignacio Arganda-Carreras, Stephan Preibisch, Mark Longair, Pavel Tomancak, Volker Hartenstein, and Rodney J Douglas. Trakem2 software for neural circuit reconstruction. *PloS one*, 7(6):e38011, 2012.

[212] Dmitri B Chklovskii, Shiv Vitaladevuni, and Louis K Scheffer. Semi-automated reconstruction of neural circuits using electron microscopy. *Current opinion in neurobiology*, 20(5):667–675, 2010.

[213] Philippe Thevenaz, Urs E Ruttimann, and Michael Unser. A pyramid approach to subpixel registration based on intensity. *Image Processing, IEEE Transactions on*, 7(1):27–41, 1998.

[214] Kristina D Micheva and Stephen J Smith. Array tomography: a new tool for imaging the molecular architecture and ultrastructure of neural circuits. *Neuron*, 55(1):25–36, 2007.

[215] Frank Friedrich and Rolf G Beutel. The thoracic morphology of nannochorista (nannochoristidae) and its implications for the phylogeny of mecoptera and antliophora. *Journal of Zoological systematics and evolutionary Research*, 48(1):50–74, 2010.

[216] Marco Feuerstein, Hauke Heibel, José Gardiazabal, Nassir Navab, and Martin Groher. Reconstruction of 3-d histology images by simultaneous deformable registration. In *Medical Image Computing and Computer-Assisted Intervention–MICCAI 2011*, pages 582–589. Springer, 2011.

[217] László Fónyad, Kazunobu Shinoda, Evan A Farkash, Martin Groher, Divya P Sebastian, A Marcell Szász, Robert B Colvin, and Yukako Yagi. 3-dimensional digital reconstruction of the murine coronary system for the evaluation of chronic allograft vasculopathy. *Diagnostic pathology*, 10(1):16, 2015.

[218] Klaudia Lohmann, Eckart D Gundelfinger, Henning Scheich, Rita Grimm, Wolfgang Tischmeyer, Karin Richter, and Andreas Hess. Brainview: a computer program for reconstruction and interactive visualization of 3d data sets. *Journal of neuroscience methods*, 84(1):143–154, 1998.

[219] Philippe Andrey and Yves Maurin. Free-d: an integrated environment for three-dimensional reconstruction from serial sections. *Journal of neuroscience methods*, 145(1):233–244, 2005.

[220] MS Bonnet, M Djelloul, V Tillement, C Tardivel, L Mounien, J Trouslard, J-D Troadec, and M Dallaporta. Central nucb2/nesfatin-1-expressing neurones belong to the hypothalamic-brainstem circuitry activated by hypoglycaemia. *Journal of neuroendocrinology*, 25(1):1–13, 2013.

[221] Yann Cointepas, Jean-François Mangin, Line Garnero, Jean-Baptiste Poline, and Habib Benali. Brainvisa: software platform for visualization and analysis of multimodality brain data. *Neuroimage*, 13(6):98, 2001.

[222] Malin Andersson, M Reid Groseclose, Ariel Y Deutch, and Richard M Caprioli. Imaging mass spectrometry of proteins and peptides: 3d volume reconstruction. *Nature Methods*, 5(1):101–108, 2008.

[223] Pieter Cornillie, Wim Van Den Broeck, and Paul Simoens. Three-dimensional reconstruction of the remodeling of the systemic vasculature in early pig embryos. *Microscopy research and technique*, 71(2):105–111, 2008.

[224] Maristela L Onozato, Stephen Hammond, Mark Merren, and Yukako Yagi. Evaluation of a completely automated tissue-sectioning machine for paraffin blocks. *Journal of clinical pathology*, 66(2):151–154, 2013.

[225] Piotr Majka and Daniel K Wójcik. Possum—a framework for three-dimensional reconstruction of brain images from serial sections. *Neuroinformatics*, pages 1–14, 2015.

[226] Katalin Dezső, Veronika Papp, Edina Bugyik, Hargita Hegyesi, Géza Sáfrány, Csaba Bödör, Péter Nagy, and Sándor Paku. Structural analysis of oval-cell–mediated liver regeneration in rats. *Hepatology*, 56(4):1457–1467, 2012.

[227] Paul A Yushkevich, Laura Wisse, Daniel Adler, Ranjit Ittyerah, John B Pluta, John L Robinson, Theresa Schuck, John Q Trojanowski, Murray Grossman, John A Detre, et al. A framework for informing segmentation of in vivo mri with information derived from ex vivo imaging: Application in the medial temporal lobe. In *Engineering in Medicine and Biology Society (EMBC), 2016 IEEE 38th Annual International Conference of the*, pages 6014–6017. IEEE, 2016.

[228] Hanspeter Winkler. 3d reconstruction and processing of volumetric data in cryo-electron tomography. *Journal of structural biology*, 157(1):126–137, 2007.

[229] Rajesh K Singh, Valéria C Barbosa-Lorenzi, Frederik W Lund, Inna Grosheva, Frederick R Maxfield, and Abigail S Haka. Degradation of aggregated ldl occurs in complex extracellular sub-compartments of the lysosomal synapse. *J Cell Sci*, pages jcs–181743, 2016.

[230] John C Fiala. Reconstruct: a free editor for serial section microscopy. *Journal of microscopy*, 218(1):52–61, 2005.

[231] Thomas Misje Mathiisen, Knut Petter Lehre, Niels Christian Danbolt, and Ole Petter Ottersen. The perivascular astroglial sheath provides a complete covering of the brain microvessels: an electron microscopic 3d reconstruction. *Glia*, 58(9):1094–1103, 2010.

[232] James R Kremer, David N Mastronarde, and J Richard McIntosh. Computer visualization of three-dimensional image data using imod. *Journal of structural biology*, 116(1):71–76, 1996.

[233] Yuriy Mishchenko. Automation of 3d reconstruction of neural tissue from large volume of conventional serial section transmission electron micrographs. *Journal of neuroscience methods*, 176(2):276–289, 2009.

[234] Caroline A Schneider, Wayne S Rasband, Kevin W Eliceiri, et al. Nih image to imagej: 25 years of image analysis. *Nat methods*, 9(7):671–675, 2012.

[235] WS Rasband and DS Bright. Nih image-a public domain image-processing program for the macintosh. *Microbeam Analysis*, 4(3):137–149, 1995.

[236] PP Laissue, CH Reiter, PR Hiesinger, S Halter, KF Fischbach, and RF Stocker. Three-dimensional reconstruction of the antennal lobe in drosophila melanogaster. *Journal of Comparative Neurology*, 405(4):543–552, 1999.

[237] Michael T McCann, John A Ozolek, Carlos A Castro, Bahram Parvin, and Jelena Kovacevic. Automated histology analysis: Opportunities for signal processing. *IEEE Signal Processing Magazine*, 32(1):78, 2015.

[238] JB Antoine Maintz and Max A Viergever. A survey of medical image registration. *Medical image analysis*, 2(1):1–36, 1998.

[239] Derek LG Hill, Philipp G Batchelor, Mark Holden, and David J Hawkes. Medical image registration. *Physics in medicine and biology*, 46(3):R1, 2001.

[240] Barbara Zitova and Jan Flusser. Image registration methods: a survey. *Image and vision computing*, 21(11):977–1000, 2003.

[241] Aristeidis Sotiras, Christos Davatzikos, and Nikos Paragios. Deformable medical image registration: A survey. *IEEE transactions on medical imaging*, 32(7):1153–1190, 2013.

[242] Max A Viergever, JB Antoine Maintz, Stefan Klein, Keelin Murphy, Marius Staring, and Josien PW Pluim. A survey of medical image registration–under review. *Medical Image Analysis*, 2016.

[243] Alan Colchester, Sébastien Ourselin, Yonggen Zhu, Eric Bardinet, Yang He, Alexis Roche, Safa Al-Sarraj, Bill Nailon, James Ironside, and Nicholas Ayache. 3-d reconstruction of macroscopic optical brain slice images. In *Medical Image Computing and Computer-Assisted Intervention–MICCAI 2000*, pages 95–105. Springer, 2000.

[244] Stelios Krinidis, Christophoros Nikou, and Ioannis Pitas. A global energy function for the alignment of serially acquired slices. *Information Technology in Biomedicine, IEEE Transactions on*, 7(2):108–113, 2003.

[245] Sébastien Ourselin, Alexis Roche, Gérard Subsol, Xavier Pennec, and Nicholas Ayache. Reconstructing a 3d structure from serial histological sections. *Image and vision computing*, 19(1):25–31, 2001.

[246] Alain Pitiot, Eric Bardinet, Paul M Thompson, and Grégoire Malandain. Piecewise affine registration of biological images for volume reconstruction. *Medical image analysis*, 10(3):465–483, 2006.

[247] Jonas Pichat, Marc Modat, Tarek Yousry, and Sebastien Ourselin. A multi-path approach to histology volume reconstruction. In *Biomedical Imaging (ISBI), 2015 IEEE 12th International Symposium on*, pages 1280–1283. IEEE, 2015.

[248] Thomy Mertzanidou, John H Hipwell, Sara Reis, Babak Ehteshami Bejnordi, Meyke Hermsen, Mehmet Dalmis, Suzan Vreemann, Bram Platel, Jeroen van der Laak, Nico Karssemeijer, et al. Whole mastectomy volume reconstruction from 2d radiographs and its mapping to histology. In *International Workshop on Digital Mammography*, pages 367–374. Springer, 2016.

[249] Mirabela Rusu, Thea Golden, Haibo Wang, Andrew Gow, and Anant Madabhushi. Framework for 3d histologic reconstruction and fusion with in vivo mri: Preliminary results of characterizing pulmonary inflammation in a mouse model. *Medical physics*, 42(8):4822–4832, 2015.

[250] D Louis Collins, Peter Neelin, Terrence M Peters, and Alan C Evans. Automatic 3d intersubject registration of mr volumetric data in standardized talairach space. *Journal of computer assisted tomography*, 18(2):192–205, 1994.

[251] D Louis Collins, Colin J Holmes, Terrence M Peters, and Alan C Evans. Automatic 3-d model-based neuroanatomical segmentation. *Human brain mapping*, 3(3):190–208, 1995.

[252] Art Riddle, Justin Dean, Joshua R Buser, Xi Gong, Jennifer Maire, Kevin Chen, Tahir Ahmad, Victor Cai, Thuan Nguyen, Christopher D Kroenke, et al. Histopathological correlates of magnetic resonance imaging–defined chronic perinatal white matter injury. *Annals of neurology*, 70(3):493–507, 2011.

[253] Carlos Ó S Sorzano, Philippe Thévenaz, and Michael Unser. Elastic registration of biological images using vector-spline regularization. *Biomedical Engineering, IEEE Transactions on*, 52(4):652–663, 2005.

[254] Tobias Boehler, Doerte van Straaten, Stefan Wirtz, and Heinz-Otto Peitgen. A robust and extendible framework for medical image registration focused on rapid clinical application deployment. *Computers in biology and medicine*, 41(6):340–349, 2011.

[255] Michael Schwier, Tobias Böhler, Horst Karl Hahn, Uta Dahmen, Olaf Dirsch, et al. Registration of histological whole slide images guided by vessel structures. *Journal of pathology informatics*, 4(2):10, 2013.

[256] Ignacio Arganda-Carreras, Carlos OS Sorzano, Jan Kybic, and Carlos Ortiz-de Solorzano. bunwarpj: Consistent and elastic registration in imagej, methods and applications. In *Second ImageJ User & Developer Conference*, 2008.

[257] Stefan Klein, Marius Staring, Keelin Murphy, Max A Viergever, and Josien PW Pluim. Elastix: a toolbox for intensity-based medical image registration. *Medical Imaging, IEEE Transactions on*, 29(1):196–205, 2010.

[258] Marc Modat, Gerard R Ridgway, Zeike A Taylor, Manja Lehmann, Josephine Barnes, David J Hawkes, Nick C Fox, and Sébastien Ourselin. Fast free-form deformation using graphics processing units. *Computer methods and programs in biomedicine*, 98(3):278–284, 2010.

[259] Marc Modat, David M Cash, Pankaj Daga, Gavin P Winston, John S Duncan, and Sébastien Ourselin. Global image registration using a symmetric block-matching

approach. *Journal of Medical Imaging*, 1(2):024003–024003, 2014.

[260] Thomas Hartkens, Daniel Rueckert, Julia A Schnabel, David J Hawkes, and Derek LG Hill. Vtk cisg registration toolkit an open source software package for affine and non-rigid registration of single-and multimodal 3d images. In *Bildverarbeitung für die Medizin 2002*, pages 409–412. Springer, 2002.

[261] L Benetazzo, A Bizzego, R De Caro, G Frigo, D Guidolin, and C Stecco. 3d reconstruction of the crural and thoracolumbar fasciae. *Surgical and radiologic anatomy*, 33(10):855–862, 2011.

[262] Roger P Woods, Scott T Grafton, Colin J Holmes, Simon R Cherry, and John C Mazziotta. Automated image registration: I. general methods and intrasubject, intramodality validation. *Journal of computer assisted tomography*, 22(1):139–152, 1998.

[263] Roger P Woods, Scott T Grafton, John DG Watson, Nancy L Sicotte, and John C Mazziotta. Automated image registration: Ii. intersubject validation of linear and nonlinear models. *Journal of computer assisted tomography*, 22(1):153–165, 1998.

[264] Eric M Brey, Timothy W King, Carol Johnston, Larry V McIntire, Gregory P Reece, and Charles W Patrick. A technique for quantitative three-dimensional analysis of microvascular structure. *Microvascular research*, 63(3):279–294, 2002.

[265] Terry S Yoo, Michael J Ackerman, William E Lorensen, Will Schroeder, Vikram Chalana, Stephen Aylward, Dimitris Metaxas, and Ross Whitaker. Engineering and algorithm design for an image processing api: a technical report on itk-the insight toolkit. *Studies in health technology and informatics*, pages 586–592, 2002.

[266] Kishore Mosaliganti, Tony Pan, Richard Sharp, Randall Ridgway, Srivathsan Iyengar, Alexandra Gulacy, Pamela Wenzel, Alain de Bruin, Raghu Machiraju, Kun Huang, et al. Registration and 3d visualization of large microscopy images. In *Medical imaging*, pages 61442V–61442V. International Society for Optics and Photonics, 2006.

[267] Johanna MM Gijtenbeek, Pieter Wesseling, Cathy Maass, Lambert Burgers, and Jeroen AWM van der Laak. Three-dimensional reconstruction of tumor microvasculature: simultaneous visualization of multiple components in paraffin-embedded tissue. *Angiogenesis*, 8(4):297–305, 2006.

[268] Brian B Avants, Nick Tustison, and Gang Song. Advanced normalization tools (ants). *Insight J*, 2:1–35, 2009.

[269] Simone Gaffling, Volker Daum, and Joachim Hornegger. Landmark-constrained 3-d histological imaging: A morphology-preserving approach. In *VMV*, pages 309–316, 2011.

[270] Weizhao Zhao, Tzay Y Young, and Myron D Ginsberg. Registration and three-dimensional reconstruction of autoradiographic images by the disparity analysis method. *Medical Imaging, IEEE Transactions on*, 12(4):782–791, 1993.

[271] Arjan W Simonetti, Vedat A Elezi, Régine Farion, Grégoire Malandain, Christoph Segebarth, Chantal Rémy, and Emmanuel L Barbier. A low temperature embedding and section registration strategy for 3d image reconstruction of the rat brain from autoradiographic sections. *Journal of neuroscience methods*, 158(2):242–250, 2006.

[272] Cecilia Hughes, Olivier Rouvière, Florence Mege-Lechevallier, Rémi Souchon, and Rémy Prost. Robust alignment of prostate histology slices with quantified accuracy. *IEEE Transactions on Biomedical Engineering*, 60(2):281–291, 2013.

[273] Wei-Yen Hsu. Analytic differential approach for robust registration of rat brain histological images. *Microscopy research and technique*, 74(6):523–530, 2011.

[274] Jun-Wei Hsieh, Hong-Yuan Mark Liao, Kuo-Chin Fan, Ming-Tat Ko, and Yi-Ping Hung. Image registration using a new edge-based approach. *Computer Vision and Image Understanding*, 67(2):112–130, 1997.

[275] Yansun Xu, John B Weaver, Dennis M Healy, and Jian Lu. Wavelet transform domain filters: a spatially selective noise filtration technique. *IEEE transactions on image processing*, 3(6):747–758, 1994.

[276] Stephane Mallat and Sifen Zhong. Characterization of signals from multiscale edges. *IEEE Transactions on pattern analysis and machine intelligence*, 14(7):710–732, 1992.

[277] David Casasent and Demetri Psaltis. Position, rotation, and scale invariant optical correlation. *Applied optics*, 15(7):1795–1799, 1976.

[278] Faouzi Ghorbel. A complete invariant description for gray-level images by the harmonic analysis approach. *Pattern recognition letters*, 15(10):1043–1051, 1994.

[279] David G Lowe. Object recognition from local scale-invariant features. In *Computer vision, 1999. The proceedings of the seventh IEEE international conference on*, volume 2, pages 1150–1157. Ieee, 1999.

[280] Matthew Toews and William Wells. Sift-rank: Ordinal description for invariant feature correspondence. In *Computer Vision and Pattern Recognition, 2009. CVPR 2009. IEEE Conference on*, pages 172–177. IEEE, 2009.

[281] Ives Rey Otero and Mauricio Delbracio. Anatomy of the SIFT Method. *Image Processing On Line*, 4:370–396, 2014.

[282] P Koshevoy, Tolga Tasdizen, and R Whitaker. Implementation of an automatic slice-to-slice registration tool. *University of Utah, SCI Institute Technical Report UUSCI-2006-018*, 2006.

[283] Stephan Saalfeld and Pavel Tomancák. Automatic landmark correspondence detection for imagej. In *Proceedings of the ImageJ User and Developer Conference*, pages 128–133, 2008.

[284] Matthew Brown, Richard Szeliski, and Simon Winder. Multi-image matching using multi-scale oriented patches. In *Computer Vision and Pattern Recognition, 2005. CVPR 2005. IEEE Computer Society Conference on*, volume 1, pages 510–517.

IEEE, 2005.

[285] Ching-Wei Wang and Hsiang-Chou Chen. Improved image alignment method in application to x-ray images and biological images. *Bioinformatics*, 29(15):1879–1887, 2013.

[286] Herbert Bay, Tinne Tuytelaars, and Luc Van Gool. Surf: Speeded up robust features. In *European conference on computer vision*, pages 404–417. Springer, 2006.

[287] Oleg Lobachev, Christine Ulrich, Birte S Steiniger, Verena Wilhelmi, Vitus Stachniss, and Michael Guthe. Feature-based multi-resolution registration of immunostained serial sections. *Medical Image Analysis*, 35:288–302, 2017.

[288] Stefan Leutenegger, Margarita Chli, and Roland Y Siegwart. Brisk: Binary robust invariant scalable keypoints. In *2011 International conference on computer vision*, pages 2548–2555. IEEE, 2011.

[289] Christine Ulrich, Oleg Lobachev, Birte Steiniger, and Michael Guthe. Imaging the vascular network of the human spleen from immunostained serial sections. In *VCBM*, pages 69–78. Citeseer, 2014.

[290] Elmar Mair, Gregory D Hager, Darius Burschka, Michael Suppa, and Gerhard Hirzinger. Adaptive and generic corner detection based on the accelerated segment test. In *European conference on Computer vision*, pages 183–196. Springer, 2010.

[291] Jared Heinly, Enrique Dunn, and Jan-Michael Frahm. Comparative evaluation of binary features. In *Computer Vision–ECCV 2012*, pages 759–773. Springer, 2012.

[292] Antonio Ruiz, Manuel Ujaldon, Lee Cooper, and Kun Huang. Non-rigid registration for large sets of microscopic images on graphics processors. *Journal of signal processing systems*, 55(1-3):229–250, 2009.

[293] Jeff Prescott, Matthew Clary, Gregory Wiet, Tony Pan, and Kun Huang. Automatic registration of large set of microscopic images using high-level features. In *3rd IEEE International Symposium on Biomedical Imaging: Nano to Macro, 2006.*, pages 1284–1287. IEEE, 2006.

[294] Lee Cooper, Olcay Sertel, Jun Kong, Gerard Lozanski, Kun Huang, and Metin Gurcan. Feature-based registration of histopathology images with different stains: an application for computerized follicular lymphoma prognosis. *Computer methods and programs in biomedicine*, 96(3):182–192, 2009.

[295] Yiwen Xu, J Geoffrey Pickering, Zengxuan Nong, Eli Gibson, John-Michael Arpino, Hao Yin, and Aaron D Ward. A method for 3d histopathology reconstruction supporting mouse microvasculature analysis. *PloS one*, 10(5):e0126817, 2015.

[296] Ulf-Dietrich Braumann, Jens Einenkel, Lars-Christian Horn, Jens-Peer Kuska, Markus Löffler, Nico Scherf, and Nicolas Wentzensen. Registration of histologic colour images of different staining. In *Bildverarbeitung für die Medizin 2006*, pages 231–235. Springer, 2006.

[297] Y Song, Darren Treanor, Andrew J Bulpitt, N Wijayathunga, N Roberts, R Wilcox,

and Derek R Magee. Unsupervised content classification based nonrigid registration of differently stained histology images. *IEEE Transactions on Biomedical Engineering*, 61(1):96–108, 2014.

[298] Franz Pernkopf and Djamel Bouchaffra. Genetic-based em algorithm for learning gaussian mixture models. *IEEE Transactions on Pattern Analysis and Machine Intelligence*, 27(8):1344–1348, 2005.

[299] Rushin Shojaii, Stephanie Bacopulos, Wenyi Yang, Tigran Karavardanyan, Demetri Spyropoulos, Afshin Raouf, Anne Martel, and Arun Seth. Reconstruction of 3-dimensional histology volume and its application to study mouse mammary glands. *JoVE (Journal of Visualized Experiments)*, (89):e51325–e51325, 2014.

[300] Rushin Shojaii and Anne L Martel. A novel edge point selection method for registration of histology images. In *Optical Tissue Image analysis in Microscopy, Histopathology and Endoscopy.(OPTIMHisE) Workshop, MICCAI*, 2009.

[301] Fernand S Cohen, Zhengwei Yang, Zhaohui Huang, and J Nianov. Automatic matching of homologous histological sections. *IEEE transactions on biomedical engineering*, 45(5):642–649, 1998.

[302] S Cohen Fernand, Huang Zhaohui, and Zheng Wei. Invariant matching and identification of curves using b-splines curve representation. *IEEE Trans. Image Processing*, 4(1):1–10, 1995.

[303] Anand Rangarajan, Haili Chui, Eric Mjolsness, Suguna Pappu, Lila Davachi, Patricia Goldman-Rakic, and James Duncan. A robust point-matching algorithm for autoradiograph alignment. *Medical Image Analysis*, 1(4):379–398, 1997.

[304] John Canny. A computational approach to edge detection. *IEEE Transactions on pattern analysis and machine intelligence*, (6):679–698, 1986.

[305] Yunhao Tan, Jing Hua, and Ming Dong. Feature curve-guided volume reconstruction from 2d images. In *Biomedical Imaging: From Nano to Macro, 2007. ISBI 2007. 4th IEEE International Symposium on*, pages 716–719. IEEE, 2007.

[306] Stelios Krinidis, Chistophoros Nikou, and Ioannis Pitas. Reconstruction of serially acquired slices using physics-based modeling. *IEEE Transactions on Information Technology in Biomedicine*, 7(4):394–403, 2003.

[307] Elizabeth Guest and Richard Baldock. Automatic reconstruction of serial sections using the finite element method. *Bioimaging*, 3(4):154–167, 1995.

[308] Alberto F Goldszal, J Tretiak, Peter J Hand, Sanjay Bhasin, and Donald L McEachron. Three-dimensional reconstruction of activated columns from 2-[14 c] deoxy-d-glucose data. *Neuroimage*, 2(1):9–20, 1995.

[309] JL Humm, Roger M Macklis, XQ Lu, Y Yang, K Bump, B Beresford, and LM Chin. The spatial accuracy of cellular dose estimates obtained from 3d reconstructed serial tissue autoradiographs. *Physics in medicine and biology*, 40(1):163, 1995.

[310] Jorge J Moré. The levenberg-marquardt algorithm: implementation and theory. In

Numerical analysis, pages 105–116. Springer, 1978.

[311] Qin-sheng Chen, Michel Defrise, and Frank Deconinck. Symmetric phase-only matched filtering of fourier-mellin transforms for image registration and recognition. *IEEE Transactions on pattern analysis and machine intelligence*, 16(12):1156–1168, 1994.

[312] Martin A Fischler and Robert C Bolles. Random sample consensus: a paradigm for model fitting with applications to image analysis and automated cartography. *Communications of the ACM*, 24(6):381–395, 1981.

[313] Jeffrey S Beis and David G Lowe. Shape indexing using approximate nearest-neighbour search in high-dimensional spaces. In *Computer Vision and Pattern Recognition, 1997. Proceedings., 1997 IEEE Computer Society Conference on*, pages 1000–1006. IEEE, 1997.

[314] Jan Modersitzki. *Numerical methods for image registration*. Oxford University Press on Demand, 2004.

[315] Josien PW Pluim, JB Antoine Maintz, and Max A Viergever. Image registration by maximization of combined mutual information and gradient information. In *International Conference on Medical Image Computing and Computer-Assisted Intervention*, pages 452–461. Springer, 2000.

[316] Nicolas Wentzensen, Ulf-Dietrich Braumann, Jens Einenkel, Lars-Christian Horn, Magnus von Knebel Doeberitz, Markus Löffler, and Jens-Peer Kuska. Combined serial section-based 3d reconstruction of cervical carcinoma invasion using h&e/p16ink4a/cd3 alternate staining. *Cytometry Part A*, 71(5):327–333, 2007.

[317] Richard S Millman and George D Parker. *Elements of differential geometry*. 1977.

[318] Nicholas Trahearn, David Epstein, David Snead, Ian Cree, and Nasir Rajpoot. A fast method for approximate registration of whole-slide images of serial sections using local curvature. In *SPIE Medical Imaging*, pages 90410E–90410E. International Society for Optics and Photonics, 2014.

[319] Farzin Mokhtarian and Alan Mackworth. Scale-based description and recognition of planar curves and two-dimensional shapes. *IEEE transactions on pattern analysis and machine intelligence*, (1):34–43, 1986.

[320] Paul J Besl and Neil D McKay. Method for registration of 3-d shapes. In *Robotics-DL tentative*, pages 586–606. International Society for Optics and Photonics, 1992.

[321] Bernd Fischer and Jan Modersitzki. Curvature based image registration. *Journal of Mathematical Imaging and Vision*, 18(1):81–85, 2003.

[322] A Andreasen, AM Drewes, JE Assentoft, and NE Larsen. Computer-assisted alignment of standard serial sections without use of artificial landmarks. a practical approach to the utilization of incomplete information in 3-d reconstruction of the hippocampal region. *Journal of neuroscience methods*, 45(3):199–207, 1992.

[323] Sébastien Ourselin, Alexis Roche, Sylvain Prima, and Nicholas Ayache. Block

matching: A general framework to improve robustness of rigid registration of medical images. In *International Conference on Medical Image Computing And Computer-Assisted Intervention*, pages 557–566. Springer, 2000.

[324] Peter J Rousseeuw. Least median of squares regression. *Journal of the American statistical association*, 79(388):871–880, 1984.

[325] Smadar Gefen, Oleh Tretiak, and Jonathan Nissanov. Elastic 3-d alignment of rat brain histological images. *IEEE transactions on medical imaging*, 22(11):1480–1489, 2003.

[326] Amalia Cifor, Tony Pridmore, and Alain Pitiot. Smooth 3-d reconstruction for 2-d histological images. In *Information Processing in Medical Imaging*, pages 350–361. Springer, 2009.

[327] Simone Gaffling, Volker Daum, Stefan Steidl, Andreas Maier, Harald Köstler, and Joachim Hornegger. A gauss-seidel iteration scheme for reference-free 3-d histological image reconstruction. *IEEE transactions on medical imaging*, 34(2):514–530, 2015.

[328] Julian Besag. On the statistical analysis of dirty pictures. *Journal of the Royal Statistical Society. Series B (Methodological)*, pages 259–302, 1986.

[329] Tao Ju, Joe Warren, James Carson, Musodiq Bello, Ioannis Kakadiaris, Wah Chiu, Christina Thaller, and Gregor Eichele. 3d volume reconstruction of a mouse brain from histological sections using warp filtering. *Journal of Neuroscience Methods*, 156(1):84–100, 2006.

[330] Hiroaki Sakoe and Seibi Chiba. Dynamic programming algorithm optimization for spoken word recognition. *Acoustics, Speech and Signal Processing, IEEE Transactions on*, 26(1):43–49, 1978.

[331] Stefan Wirtz, Bernd Fischer, Jan Modersitzki, and Oliver Schmitt. Superfast elastic registration of histologic images of a whole rat brain for 3d reconstruction. In *Medical Imaging 2004*, pages 328–334. International Society for Optics and Photonics, 2004.

[332] Stefan Wirtz, Nils Papenberg, Bernd Fischer, and Oliver Schmitt. Robust and staining-invariant elastic registration of a series of images from histologic slices. In *Medical imaging*, pages 1256–1262. International Society for Optics and Photonics, 2005.

[333] Markus Müller, Mehmet Yigitsoy, Hauke Heibel, and Nassir Navab. Deformable reconstruction of histology sections using structural probability maps. In *Medical Image Computing and Computer-Assisted Intervention–MICCAI 2014*, pages 122–129. Springer, 2014.

[334] Robert Brandt, Torsten Rohlfing, Jürgen Rybak, Sabine Krofczik, Alexander Maye, Malte Westerhoff, Hans-Christian Hege, and Randolf Menzel. Three-dimensional average-shape atlas of the honeybee brain and its applications. *Journal of Comparative Neurology*, 492(1):1–19, 2005.

[335] Thomas W Sederberg and Scott R Parry. Free-form deformation of solid geometric models. *ACM SIGGRAPH computer graphics*, 20(4):151–160, 1986.

[336] Oliver Schmitt, Jan Modersitzki, Stefan Heldmann, Stefan Wirtz, and Bernd Fischer. Image registration of sectioned brains. *International Journal of Computer Vision*, 73(1):5–39, 2007.

[337] NM Alpert, JF Bradshaw, D Kennedy, and JA Correia. The principal axes transformation-a method for image registration. *J Nucl Med*, 31:1717–1723, 1990.

[338] L Cooper, K Huang, A Sharma, K Mosaliganti, and T Pan. Registration vs. reconstruction: Building 3-d models from 2-d microscopy images. In *Proceedings of the workshop on multiscale biological imaging, data mining and informatics*, pages 57–58, 2006.

[339] Jan Modersitzki. *Numerical methods for image registration*. Oxford university press, 2003.

[340] Martin Auer, Peter Regitnig, and Gerhard A Holzapfel. An automatic nonrigid registration for stained histological sections. *IEEE Transactions on Image Processing*, 14(4):475–486, 2005.

[341] Gordon Sze, Stephan J De Armond, Michael Brant-Zawadzki, Richard L Davis, David Norman, and T Hans Newton. Foci of mri signal (pseudo lesions) anterior to the frontal horns: histologic correlations of a normal finding. *American journal of neuroradiology*, 7(3):381–387, 1986.

[342] Gary M Nesbit, Glenn S Forbes, Bernd W Scheithauer, Haruo Okazaki, and Moses Rodriguez. Multiple sclerosis: histopathologic and mr and/or ct correlation in 37 cases at biopsy and three cases at autopsy. *Radiology*, 180(2):467–474, 1991.

[343] Isabelle Bloch. Information combination operators for data fusion: a comparative review with classification. *Systems, Man and Cybernetics, Part A: Systems and Humans, IEEE Transactions on*, 26(1):52–67, 1996.

[344] Alex Pappachen James and Belur V Dasarathy. Medical image fusion: A survey of the state of the art. *Information Fusion*, 19:4–19, 2014.

[345] Mihika Gangolli, Laurena Holleran, Joong Hee Kim, Thor D Stein, Victor Alvarez, Ann C McKee, and David L Brody. Quantitative validation of a nonlinear histology-mri coregistration method using generalized q-sampling imaging in complex human cortical white matter. *NeuroImage*, 153:152–167, 2017.

[346] Jonathan Chappelow, B Nicolas Bloch, Neil Rofsky, Elizabeth Genega, Robert Lenkinski, William DeWolf, and Anant Madabhushi. Elastic registration of multimodal prostate mri and histology via multiattribute combined mutual information. *Medical Physics*, 38(4):2005–2018, 2011.

[347] Daniel Rueckert, Luke I Sonoda, Carmel Hayes, Derek LG Hill, Martin O Leach, and David J Hawkes. Nonrigid registration using free-form deformations: application to breast mr images. *Medical Imaging, IEEE Transactions on*, 18(8):712–721, 1999.

[348] Guokuan Li, Simona Nikolova, and Robert Bartha. Registration of in vivo magnetic resonance t 1-weighted brain images to triphenyltetrazolium chloride stained sections in small animals. *Journal of neuroscience methods*, 156(1):368–375, 2006.

[349] Ardeshir Goshtasby. Image registration by local approximation methods. *Image and Vision Computing*, 6(4):255–261, 1988.

[350] Gaoyu Xiao, B Nicolas Bloch, Jonathan Chappelow, Elizabeth M Genega, Neil M Rofsky, Robert E Lenkinski, John Tomaszewski, Michael D Feldman, Mark Rosen, and Anant Madabhushi. Determining histology-mri slice correspondences for defining mri-based disease signatures of prostate cancer. *Computerized Medical Imaging and Graphics*, 35(7):568–578, 2011.

[351] Kevin D Harkins, Junzhong Xu, Adrienne N Dula, Ke Li, William M Valentine, Daniel F Gochberg, John C Gore, and Mark D Does. The microstructural correlates of t1 in white matter. *Magnetic resonance in medicine*, 2015.

[352] Iris D Kilsdonk, Laura E Jonkman, Roel Klaver, Susanne J van Veluw, Jaco JM Zwanenburg, Joost PA Kuijer, Petra JW Pouwels, Jos WR Twisk, Mike P Wattjes, Peter R Luijten, et al. Increased cortical grey matter lesion detection in multiple sclerosis with 7 t mri: a post-mortem verification study. *Brain*, 139(5):1472–1481, 2016.

[353] Luam Hammelrath, Siniša Škokić, Artem Khmelinskii, Andreas Hess, Noortje van der Knaap, Marius Staring, Boudewijn PF Lelieveldt, Dirk Wiedermann, and Mathias Hoehn. Morphological maturation of the mouse brain: An in vivo mri and histology investigation. *NeuroImage*, 125:144–152, 2016.

[354] MR Lopez Gonzalez, SY Foo, WM Holmes, W Stewart, KW Muir, B Condon, G Welch, and KP Forbes. Atherosclerotic carotid plaque composition: A 3t and 7t mri-histology correlation study. *Journal of Neuroimaging*, 2016.

[355] AA Harteveld, NP Denswil, JCW Siero, JJM Zwanenburg, A Vink, B Pouran, WGM Spliet, DWJ Klomp, PR Luijten, MJ Daemen, et al. Quantitative intracranial atherosclerotic plaque characterization at 7t mri: an ex vivo study with histologic validation. *American Journal of Neuroradiology*, 37(5):802–810, 2016.

[356] AG Van Der Kolk, JJM Zwanenburg, NP Denswil, A Vink, WGM Spliet, MJAP Daemen, F Visser, DWJ Klomp, PR Luijten, and J Hendrikse. Imaging the intracranial atherosclerotic vessel wall using 7t mri: initial comparison with histopathology. *American Journal of Neuroradiology*, 36(4):694–701, 2015.

[357] Yusuke Nakagawa, Ichiro Sekiya, Shimpei Kondo, Takashi Tabuchi, Shizuko Ichinose, Hideyuki Koga, Kunikazu Tsuji, and Takeshi Muneta. Relationship between mri t1rho value and histological findings of intact and radially incised menisci in microminipigs. *Journal of Magnetic Resonance Imaging*, 43(2):434–445, 2016.

[358] Jieun Koh, Yong Eun Chung, Ji Hae Nahm, Ha Yan Kim, Kyung-Sik Kim, Young Nyun Park, Myeong-Jin Kim, and Jin-Young Choi. Intrahepatic mass-forming cholangiocarcinoma: prognostic value of preoperative gadoxetic acid-enhanced mri. *European radiology*, 26(2):407–416, 2016.

[359] Bryn Drew, Edward C Jones, Stefan Reinsberg, Andrew C Yung, S Larry Goldenberg, and Piotr Kozlowski. Device for sectioning prostatectomy specimens to facilitate comparison between histology and in vivo mri. *Journal of Magnetic Resonance Imaging*, 32(4):992–996, 2010.

[360] Hari Trivedi, Baris Turkbey, Ardeshir R Rastinehad, Compton J Benjamin, Marcelino Bernardo, Thomas Pohida, Vijay Shah, Maria J Merino, Bradford J Wood, W Marston Linehan, et al. Use of patient-specific mri-based prostate mold for validation of multiparametric mri in localization of prostate cancer. *Urology*, 79(1):233–239, 2012.

[361] Martina Absinta, Govind Nair, Massimo Filippi, Abhik Ray-Chaudhury, Maria I Reyes-Mantilla, Carlos A Pardo, and Daniel S Reich. Postmortem magnetic resonance imaging to guide the pathologic cut: individualized, 3-dimensionally printed cutting boxes for fixed brains. *Journal of Neuropathology & Experimental Neurology*, 73(8):780–788, 2014.

[362] Joseph R Guy, Pascal Sati, Emily Leibovitch, Steven Jacobson, Afonso C Silva, and Daniel S Reich. Custom fit 3d-printed brain holders for comparison of histology with mri in marmosets. *Journal of Neuroscience Methods*, 257:55–63, 2016.

[363] Peter Steenbergen, Karin Haustermans, Evelyne Lerut, Raymond Oyen, Liesbeth De Wever, Laura Van den Bergh, Linda GW Kerkmeijer, Frank A Pameijer, Wouter B Veldhuis, Floris J Pos, et al. Prostate tumor delineation using multiparametric magnetic resonance imaging: Inter-observer variability and pathology validation. *Radiotherapy and Oncology*, 115(2):186–190, 2015.

[364] Gabrielle Martel, Sabrina Kiss, Guillaume Gilbert, Nicolas Anne-Archard, Hélène Richard, Thomas Moser, and Sheila Laverty. Differences in the vascular tree of the femoral trochlear growth cartilage at osteochondrosis-susceptible sites in foals revealed by swi 3t mri. *Journal of Orthopaedic Research*, 2016.

[365] Charles Meyer, Bing Ma, Lakshmi P Kunju, Matthew Davenport, and Morand Piert. Challenges in accurate registration of 3-d medical imaging and histopathology in primary prostate cancer. *European journal of nuclear medicine and molecular imaging*, 40(1):72–78, 2013.

[366] Primoz Markelj, Dejan Tomaževič, Bostjan Likar, and Franjo Pernuš. A review of 3d/2d registration methods for image-guided interventions. *Medical image analysis*, 16(3):642–661, 2012.

[367] Enzo Ferrante and Nikos Paragios. Slice-to-volume medical image registration: A survey. *Medical Image Analysis*, 39:101–123, 2017.

[368] Anna Khimchenko, Hans Deyhle, Georg Schulz, Gabriel Schweighauser, Jürgen Hench, Natalia Chicherova, Christos Bikis, Simone E Hieber, and Bert Müller. Extending two-dimensional histology into the third dimension through conventional micro computed tomography. *NeuroImage*, 139:26–36, 2016.

[369] Natalia Chicherova, Ketut Fundana, Bert Müller, and Philippe C Cattin. Histology to μct data matching using landmarks and a density biased ransac. In *International Con-*

ference on Medical Image Computing and Computer-Assisted Intervention, pages 243–250. Springer, 2014.

[370] Dirk-Jan Kroon and Cornelis H Slump. Mri modalitiy transformation in demon registration. In *Biomedical Imaging: From Nano to Macro, 2009. ISBI'09. IEEE International Symposium on*, pages 963–966. IEEE, 2009.

[371] T-S Kim, M Singh, W Sungkara, C Zarow, and H Chui. Automatic registration of postmortem brain slices to mri reference volume. *Nuclear Science, IEEE Transactions on*, 47(4):1607–1613, 2000.

[372] C Zarow, T-S Kim, M Singh, and HC Chui. A standardized method for brain-cutting suitable for both stereology and mri-brain co-registration. *Journal of neuroscience methods*, 139(2):209–215, 2004.

[373] Thierry Delzescaux, Julien Dauguet, Françoise Condé, Renaud Maroy, and Vincent Frouin. Using 3d non rigid ffd-based method to register post mortem 3d histological data and in vivo mri of a baboon brain. In *Medical Image Computing and Computer-Assisted Intervention-MICCAI 2003*, pages 965–966. Springer, 2003.

[374] Daniel H Adler, Ranjit Ittyerah, John Pluta, Stephen Pickup, Weixia Liu, David A Wolk, and Paul A Yushkevich. Probabilistic atlas of the human hippocampus combining ex vivo mri and histology. In *International Conference on Medical Image Computing and Computer-Assisted Intervention*, pages 63–71. Springer, 2016.

[375] Jiang H. Li, X. and S. Mori. Diffeomap. *Kennedy Krieger Insitute & Johns Hopkins University,* `https://www.mristudio.org/`, 2001.

[376] D. Louis Collins and Alan C. Evans. Animal: validation and applications of nonlinear registration-based segmentation. *International journal of pattern recognition and artificial intelligence*, 11(08):1271–1294, 1997.

[377] William M Wells, Paul Viola, Hideki Atsumi, Shin Nakajima, and Ron Kikinis. Multi-modal volume registration by maximization of mutual information. *Medical image analysis*, 1(1):35–51, 1996.

[378] Gustavo K Rohde, Akram Aldroubi, and Benoit M Dawant. The adaptive bases algorithm for intensity-based nonrigid image registration. *Medical Imaging, IEEE Transactions on*, 22(11):1470–1479, 2003.

[379] Maged Goubran, Sandrine de Ribaupierre, Robert R Hammond, Catherine Currie, Jorge G Burneo, Andrew G Parrent, Terry M Peters, and Ali R Khan. Registration of in-vivo to ex-vivo mri of surgically resected specimens: A pipeline for histology to in-vivo registration. *Journal of neuroscience methods*, 241:53–65, 2015.

[380] Björn Eiben, Christoph Palm, Uwe Pietrzyk, Katrin Amunts, and C Davatzikos. Perspective error correction using registration for blockface volume reconstruction of serial histological sections of the human brain. In *Bildverarbeitung für die Medizin*, pages 301–305. Citeseer, 2010.

[381] David Mattes, David R Haynor, Hubert Vesselle, Thomas K Lewellen, and William

Eubank. Pet-ct image registration in the chest using free-form deformations. *IEEE transactions on medical imaging*, 22(1):120–128, 2003.

[382] G Allan Johnson, Evan Calabrese, Alexandra Badea, George Paxinos, and Charles Watson. A multidimensional magnetic resonance histology atlas of the wistar rat brain. *Neuroimage*, 62(3):1848–1856, 2012.

[383] Brian B Avants, Charles L Epstein, Murray Grossman, and James C Gee. Symmetric diffeomorphic image registration with cross-correlation: evaluating automated labeling of elderly and neurodegenerative brain. *Medical image analysis*, 12(1):26–41, 2008.

[384] Klaus Stüben and Ulrich Trottenberg. *Multigrid methods: Fundamental algorithms, model problem analysis and applications*. Springer, 1982.

[385] Karl Rohr, H Siegfried Stiehl, Rainer Sprengel, Wolfgang Beil, Thorsten M Buzug, Jürgen Weese, and MH Kuhn. Point-based elastic registration of medical image data using approximating thin-plate splines. In *Visualization in Biomedical Computing*, pages 297–306. Springer, 1996.

[386] Thorsten Schormann, Marcel von Matthey, Andreas Dabringhaus, and Karl Zilles. Alignment of 3-d brain data sets originating from mr and histology. *Bioimaging*, 1(2):119–128, 1993.

[387] Michel E Vandenberghe, Anne-Sophie Hérard, Nicolas Souedet, Elmahdi Sadouni, Mathieu D Santin, Dominique Briet, Denis Carré, Jocelyne Schulz, Philippe Hantraye, Pierre-Etienne Chabrier, et al. High-throughput 3d whole-brain quantitative histopathology in rodents. *Scientific reports*, 6, 2016.

[388] Hervé Delingette, Eric Bardinet, David Rey, JD Lemarechal, Johan Montagnat, Sébastien Ourselin, Alexis Roche, Didier Dormont, Jérôme Yelnik, and Nicholas Ayache. Yav++: a software platform for medical image processing and visualization. In *Workshop on Interactive Medical Image Visualization and Analysis satellite symposia of MICCAI, IMIVA'01*, 2001.

[389] Morand Piert, Hyunjin Park, Asra Khan, Javed Siddiqui, Hero Hussain, Thomas Chenevert, David Wood, Timothy Johnson, Rajal B Shah, and Charles Meyer. Detection of aggressive primary prostate cancer with 11c-choline pet/ct using multimodality fusion techniques. *Journal of Nuclear Medicine*, 50(10):1585–1593, 2009.

[390] Hyunjin Park, Morand R Piert, Asra Khan, Rajal Shah, Hero Hussain, Javed Siddiqui, Thomas L Chenevert, and Charles R Meyer. Registration methodology for histological sections and in vivo imaging of human prostate. *Academic radiology*, 15(8):1027–1039, 2008.

[391] Paul Viola and William M Wells III. Alignment by maximization of mutual information. *International journal of computer vision*, 24(2):137–154, 1997.

[392] Sylvain Prima, Sébastien Ourselin, and Nicholas Ayache. Computation of the mid-sagittal plane in 3-d brain images. *Medical Imaging, IEEE Transactions on*, 21(2):122–138, 2002.

[393] Roee S Lazebnik, Tanya L Lancaster, Michael S Breen, Jonathan S Lewin, and David L Wilson. Volume registration using needle paths and point landmarks for evaluation of interventional mri treatments. *IEEE transactions on medical imaging*, 22(5):653–660, 2003.

[394] George Paxinos, Xu-Feng Huang, and Arthur W Toga. The rhesus monkey brain in stereotaxic coordinates. 2000.

[395] Rachid Deriche. Using canny's criteria to derive a recursively implemented optimal edge detector. *International journal of computer vision*, 1(2):167–187, 1987.

[396] Yutong Liu, Balasrinivasa R Sajja, Mariano G Uberti, Howard E Gendelman, Tammy Kielian, and Michael D Boska. Landmark optimization using local curvature for point-based nonlinear rodent brain image registration. *Journal of Biomedical Imaging*, 2012:1, 2012.

[397] Michael S Breen, Tanya L Lancaster, Roee S Lazebnik, Sherif G Nour, Jonathan S Lewin, and David L Wilson. Three-dimensional method for comparing in vivo interventional mr images of thermally ablated tissue with tissue response. *Journal of Magnetic Resonance Imaging*, 18(1):90–102, 2003.

[398] Gabriele Lohmann. Extracting line representations of sulcal and gyral patterns in mr images of the human brain. *IEEE Transactions on Medical Imaging*, 17(6):1040–1048, 1998.

[399] Andreas Hess, Klaudia Lohmann, Eckart D Gundelfinger, and Henning Scheich. A new method for reliable and efficient reconstruction of 3-dimensional images from autoradiographs of brain sections. *Journal of neuroscience methods*, 84(1):77–86, 1998.

[400] Torsten Rohlfing. Image similarity and tissue overlaps as surrogates for image registration accuracy: widely used but unreliable. *IEEE transactions on medical imaging*, 31(2):153–163, 2012.

[401] Robert M Haralick. Statistical and structural approaches to texture. *Proceedings of the IEEE*, 67(5):786–804, 1979.

[402] Nicholas Roberts, Derek Magee, Yi Song, Keeran Brabazon, Mike Shires, Doreen Crellin, Nicolas M Orsi, Richard Quirke, Philip Quirke, and Darren Treanor. Toward routine use of 3d histopathology as a research tool. *The American journal of pathology*, 180(5):1835–1842, 2012.

[403] Tahir Mansoori, Gernot Plank, Rebecca Burton, Jurgen Schneider, Peter Kohl, David Gavaghan, and Vicente Grau. An iterative method for registration of high-resolution cardiac histoanatomical and mri images. In *Biomedical Imaging: From Nano to Macro, 2007. ISBI 2007. 4th IEEE International Symposium on*, pages 572–575. IEEE, 2007.

[404] Lyndon S Hibbard, James S McGlone, Donald W Davis, and Richard A Hawkins. Three-dimensional representation and analysis of brain energy metabolism. *Science*, 236(4809):1641–1646, 1987.

[405] LYNDON S Hibbard and RICHARD A Hawkins. Three-dimensional reconstruction of metabolic data from quantitative autoradiography of rat brain. *American Journal of Physiology-Endocrinology and Metabolism*, 247(3):E412–E419, 1984.

[406] Lyndon S Hibbard and Richard A Hawkins. Objective image alignment for three-dimensional reconstruction of digital autoradiograms. *Journal of neuroscience methods*, 26(1):55–74, 1988.

[407] Boklye Kim, Jennifer L Boes, Kirk A Frey, and Charles R Meyer. Mutual information for automated unwarping of rat brain autoradiographs. *Neuroimage*, 5(1):31–40, 1997.

[408] Boklye Kim, Kirk A Frey, Sunil Mukhopadhyay, Brian D Ross, and Charles R Meyer. Co-registration of mri and autoradiography of rat brain in three-dimensions following automatic reconstruction of 2d data set. In *Computer vision, virtual reality and robotics in medicine*, pages 262–266. Springer, 1995.

[409] Gilles Bronchti, Peter Heil, Ronen Sadka, Andreas Hess, Henning Scheich, and Zvi Wollberg. Auditory activation of 'visual'cortical areas in the blind mole rat (spalax ehrenbergi). *European Journal of Neuroscience*, 16(2):311–329, 2002.

[410] Philip J Edwards, Ayman D Nijmeh, Mark McGurk, Edward Odell, Michael R Fenlon, Paul K Marsden, and David J Hawkes. Validation of pet imaging by alignment to histology slices. In *Medical Image Computing and Computer-Assisted Intervention–MICCAI 2005*, pages 968–975. Springer, 2005.

[411] Thomy Mertzanidou, John H Hipwell, Sara Reis, David J Hawkes, Babak Ehteshami Bejnordi, Mehmet Dalmis, Suzan Vreemann, Bram Platel, Jeroen der Laak, Nico Karssemeijer, et al. 3d volume reconstruction from serial breast specimen radiographs for mapping between histology and 3d whole specimen imaging. *Medical Physics*, 2017.

[412] Bernard D Coombs, Joseph H Rapp, Phillip C Ursell, Linda M Reilly, and David Saloner. Structure of plaque at carotid bifurcation high-resolution mri with histological correlation. *Stroke*, 32(11):2516–2521, 2001.

[413] Matthew Brett, Ingrid S Johnsrude, and Adrian M Owen. The problem of functional localization in the human brain. *Nature reviews neuroscience*, 3(3):243–249, 2002.

[414] Paul Aljabar, Rolf A Heckemann, Alexander Hammers, Joseph V Hajnal, and Daniel Rueckert. Multi-atlas based segmentation of brain images: atlas selection and its effect on accuracy. *Neuroimage*, 46(3):726–738, 2009.

[415] Joseph Goerres, Ali Uneri, Tharindu De Silva, Michael Ketcha, Sureerat Reaungamornrat, Matthew Jacobson, Sebastian Vogt, Gerhard Kleinszig, Greg Osgood, Jean-Paul Wolinsky, et al. Spinal pedicle screw planning using deformable atlas registration. *Physics in Medicine and Biology*, 62(7):2871, 2017.

[416] N Kovačević, JT Henderson, E Chan, N Lifshitz, J Bishop, AC Evans, RM Henkelman, and XJ Chen. A three-dimensional mri atlas of the mouse brain with estimates of the average and variability. *Cerebral cortex*, 15(5):639–645, 2005.

[417] AE Dorr, Jason P Lerch, Shoshana Spring, N Kabani, and R Mark Henkelman. High resolution three-dimensional brain atlas using an average magnetic resonance image of 40 adult c57bl/6j mice. *Neuroimage*, 42(1):60–69, 2008.

[418] Y Ma, PR Hof, SC Grant, SJ Blackband, R Bennett, L Slatest, MD McGuigan, and H Benveniste. A three-dimensional digital atlas database of the adult c57bl/6j mouse brain by magnetic resonance microscopy. *Neuroscience*, 135(4):1203–1215, 2005.

[419] Kadharbatcha S Saleem and Nikos K Logothetis. *A combined MRI and histology atlas of the rhesus monkey brain in stereotaxic coordinates*. Academic Press, 2012.

[420] Sébastien Ourselin, Eric Bardinet, Didier Dormont, Grégoire Malandain, Alexis Roche, Nicholas Ayache, D Tande, Karine Parain, and Jérôme Yelnik. Fusion of histological sections and mr images: towards the construction of an atlas of the human basal ganglia. In *Medical Image Computing and Computer-Assisted Intervention–MICCAI 2001*, pages 743–751. Springer, 2001.

[421] Eric Bardinet, Manik Bhattacharjee, Didier Dormont, Bernard Pidoux, Grégoire Malandain, Michael Schüpbach, Nicholas Ayache, Philippe Cornu, Yves Agid, and Jérôme Yelnik. A three-dimensional histological atlas of the human basal ganglia. ii. atlas deformation strategy and evaluation in deep brain stimulation for parkinson disease: Clinical article. *Journal of neurosurgery*, 110(2):208–219, 2009.

[422] G Allan Johnson, Anjum Ali-Sharief, Alexandra Badea, Jeffrey Brandenburg, Gary Cofer, Boma Fubara, Sally Gewalt, Laurence W Hedlund, and Lucy Upchurch. High-throughput morphologic phenotyping of the mouse brain with magnetic resonance histology. *Neuroimage*, 37(1):82–89, 2007.

[423] Andrew C Gallagher. Jigsaw puzzles with pieces of unknown orientation. In *Computer Vision and Pattern Recognition (CVPR), 2012 IEEE Conference on*, pages 382–389. IEEE, 2012.

[424] Mehdi Noroozi and Paolo Favaro. Unsupervised learning of visual representations by solving jigsaw puzzles. In *European Conference on Computer Vision*, pages 69–84. Springer, 2016.

[425] Erik D Demaine and Joseph O'Rourke. A survey of folding and unfolding in computational geometry. *Combinatorial and computational geometry*, 52:167–211, 2005.

[426] Pilnam Kim, Manouk Abkarian, and Howard A Stone. Hierarchical folding of elastic membranes under biaxial compressive stress. *Nature materials*, 10(12):952–957, 2011.

[427] Luka Pocivavsek, Robert Dellsy, Andrew Kern, Sebastián Johnson, Binhua Lin, Ka Yee C Lee, and Enrique Cerda. Stress and fold localization in thin elastic membranes. *Science*, 320(5878):912–916, 2008.

[428] Stephanie Deboeuf, Eytan Katzav, Arezki Boudaoud, Daniel Bonn, and Mokhtar Adda-Bedia. Comparative study of crumpling and folding of thin sheets. *Physical review letters*, 110(10):104301, 2013.

[429] Mokhtar Adda-Bedia, Arezki Boudaoud, Laurent Boué, and Stephanie Deboeuf. Statistical distributions in the folding of elastic structures. *Journal of Statistical Mechanics: Theory and Experiment*, 2010(11):P11027, 2010.

[430] John G Ramsay. Interference patterns produced by the superposition of folds of similar type. *The Journal of Geology*, pages 466–481, 1962.

[431] Wilfrid Taylor Dempster. The mechanics of paraffin sectioning by the microtome. *The Anatomical Record*, 84(3):241–267, 1942.

[432] David Marr. Vision: A computational investigation into the human representation and processing of visual information, henry holt and co. *Inc., New York, NY*, 2:4–2, 1982.

[433] F Guichard, JM Morel, and Robert Ryan. Contrast invariant image analysis and pde's. *preprint*, 2004.

[434] Jean-Michel Morel and Guoshen Yu. Is sift scale invariant? *Inverse Problems and Imaging*, 5(1):115–136, 2011.

[435] Ives Rey-Otero, Jean-Michel Morel, and Mauricio Delbracio. An analysis of the factors affecting keypoint stability in scale-space. *Journal of Mathematical Imaging and Vision*, pages 1–19, 2015.

[436] Ives Rey-Otero and Mauricio Delbracio. Is repeatability an unbiased criterion for ranking feature detectors? *SIAM Journal on Imaging Sciences*, 8(4):2558–2580, 2015.

[437] Matthew Toews, Lilla Zöllei, and William M Wells. Feature-based alignment of volumetric multi-modal images. In *International Conference on Information Processing in Medical Imaging*, pages 25–36. Springer, 2013.

[438] Mattias P Heinrich, Mark Jenkinson, Manav Bhushan, Tahreema Matin, Fergus V Gleeson, Michael Brady, and Julia A Schnabel. Mind: Modality independent neighbourhood descriptor for multi-modal deformable registration. *Medical Image Analysis*, 16(7):1423–1435, 2012.

[439] Fred Attneave. Some informational aspects of visual perception. *Psychological review*, 61(3):183, 1954.

[440] Benjamín Gutiérrez-Becker, Diana Mateus, Loïc Peter, and Nassir Navab. Learning optimization updates for multimodal registration. In *International Conference on Medical Image Computing and Computer-Assisted Intervention*, pages 19–27. Springer, 2016.

[441] Hayit Greenspan, Bram van Ginneken, and Ronald M Summers. Guest editorial deep learning in medical imaging: Overview and future promise of an exciting new technique. *IEEE Transactions on Medical Imaging*, 35(5):1153–1159, 2016.

[442] Shun Miao, Z Jane Wang, and Rui Liao. A cnn regression approach for real-time 2d/3d registration. *IEEE transactions on medical imaging*, 35(5):1352–1363, 2016.

[443] Geert Litjens, Thijs Kooi, Babak Ehteshami Bejnordi, Arnaud Arindra Adiyoso Setio, Francesco Ciompi, Mohsen Ghafoorian, Jeroen AWM van der Laak, Bram van Ginneken, and Clara I Sánchez. A survey on deep learning in medical image analysis. *arXiv preprint arXiv:1702.05747*, 2017.

[444] Raf Van de Plas, Junhai Yang, Jeffrey Spraggins, and Richard M Caprioli. Image fusion of mass spectrometry and microscopy: a multimodality paradigm for molecular tissue mapping. *Nature methods*, 12(4):366–372, 2015.

[445] Sayra Cristancho, Lorelei Lingard, Thomas Forbes, Michael Ott, and Richard Novick. Putting the puzzle together: the role of "problem definition" in complex clinical judgement. *Medical education*, 51(2):207–214, 2017.

[446] Helmut W Fischer, Yves Van Haverbeke, Peter A Rinck, Inge Schmitz-Feuerhake, and Robert N Muller. The effect of aging and storage conditions on excised tissues as monitored by longitudinal relaxation dispersion profiles. *Magnetic resonance in medicine*, 9(3):315–324, 1989.

[447] Elena A Kaye, Sonal Josan, Aiming Lu, Jarrett Rosenberg, Bruce L Daniel, and Kim Butts Pauly. Consistency of signal intensity and t2* in frozen ex vivo heart muscle, kidney, and liver tissue. *Journal of Magnetic Resonance Imaging*, 31(3):719–724, 2010.

[448] Francis A Duck. *Physical properties of tissues: a comprehensive reference book*. Academic press, 2013.

[449] Armin Purea and Andrew G Webb. Reversible and irreversible effects of chemical fixation on the nmr properties of single cells. *Magnetic resonance in medicine*, 56(4):927–931, 2006.

[450] Timothy M Shepherd, Peter E Thelwall, Greg J Stanisz, and Stephen J Blackband. Aldehyde fixative solutions alter the water relaxation and diffusion properties of nervous tissue. *Magnetic resonance in medicine*, 62(1):26–34, 2009.

[451] Fan Lin and Jianhui Shi. Standardization of diagnostic immunohistochemistry. In *Handbook of Practical Immunohistochemistry*, pages 17–30. Springer, 2015.

[452] Xenios Milidonis, Ian Marshall, Malcolm R Macleod, and Emily S Sena. Magnetic resonance imaging in experimental stroke and comparison with histology systematic review and meta-analysis. *Stroke*, 46(3):843–851, 2015.

[453] A Traboulsee, JH Simon, L Stone, E Fisher, DE Jones, A Malhotra, SD Newsome, J Oh, DS Reich, N Richert, et al. Revised recommendations of the consortium of ms centers task force for a standardized mri protocol and clinical guidelines for the diagnosis and follow-up of multiple sclerosis. *American Journal of Neuroradiology*, 37(3):394–401, 2016.

[454] A Melbourne, G Ridgway, and DJ Hawkes. Image similarity metrics in image registration. In *SPIE Medical Imaging*, pages 762335–762335. International Society for Optics and Photonics, 2010.

[455] Edsger W Dijkstra. A note on two problems in connexion with graphs. *Numerische mathematik*, 1(1):269–271, 1959.

[456] Jannick P Rolland, V Vo, B Bloss, and Craig K Abbey. Fast algorithms for histogram matching: Application to texture synthesis. *Journal of Electronic Imaging*, 9(1):39–45, 2000.

[457] Jonas Pichat, Juan Eugenio Iglesias, Tarek Yousry, Sébastien Ourselin, and Marc Modat. Registration of histology and clinical imaging: A survey. In *(under review)*, 2017.

[458] Masaki Fukunaga, Tie-Qiang Li, Peter van Gelderen, Jacco A de Zwart, Karin Shmueli, Bing Yao, Jongho Lee, Dragan Maric, Maria A Aronova, Guofeng Zhang, et al. Layer-specific variation of iron content in cerebral cortex as a source of mri contrast. *Proceedings of the National Academy of Sciences*, 107(8):3834–3839, 2010.

[459] Wen-Chi Christina Lee, Mitchell E Tublin, and Brian E Chapman. Registration of mr and ct images of the liver: comparison of voxel similarity and surface based registration algorithms. *Computer methods and programs in biomedicine*, 78(2):101–114, 2005.

[460] Christos Davatzikos, Jerry L Prince, and R Nick Bryan. Image registration based on boundary mapping. *IEEE Transactions on medical imaging*, 15(1):112–115, 1996.

[461] Vicent Caselles, Bartomeu Coll, and Jean-Michel Morel. A kanisza programme. *Progress in Nonlinear Differential Equations and their Applications*, 25:35–56, 1996.

[462] Yehezkel Lamdan, Jacob Theodore Schwartz, and Haim J Wolfson. Object Recognition by Affine Invariant Matching. In *Computer Vision and Pattern Recognition, 1988. Proceedings CVPR'88., Computer Society Conference on*, pages 335–344. IEEE, 1988.

[463] Jose Luis Lisani, Lionel Moisan, Pascal Monasse, and Jean-Michel Morel. On the theory of planar shape. *Multiscale Modeling & Simulation*, 1(1):1–24, 2003.

[464] Luis Alvarez, Frédéric Guichard, Pierre-Louis Lions, and Jean-Michel Morel. Axioms and fundamental equations of image processing. *Archive for rational mechanics and analysis*, 123(3):199–257, 1993.

[465] Marco Mondelli and Adina Ciomaga. Finite Difference Schemes for MCM and amss. *Image Processing On Line*, 1:127–177, 2011.

[466] Pablo Marquez-Neila, Luis Baumela, and Luis Alvarez. A morphological approach to curvature-based evolution of curves and surfaces. *IEEE Transactions on Pattern Analysis and Machine Intelligence*, 36(1):2–17, 2014.

[467] Benoit M Dawant, Alex P Zijdenbos, and Richard A Margolin. Correction of intensity variations in mr images for computer-aided tissue classification. *IEEE transactions on medical imaging*, 12(4):770–781, 1993.

[468] Yves Dupain, Teturo Kamae, and Michel Mendes. Can one measure the temperature

of a curve? *Archive for Rational Mechanics and Analysis*, 94(2):155–163, 1986.

[469] Hugo Steinhaus. Length, shape and area. In *Colloquium Mathematicae*, volume 3, pages 1–13, 1954.

[470] Luis A Santalo. *Integral geometry and geometric probability*. Cambridge university press, 2004.

[471] Jean-Paul Allouche and Laurence Maillard-Teyssier. Inconstancy of finite and infinite sequences. *Theoretical Computer Science*, 412(22):2268–2281, 2011.

[472] G Th Fechner. *Elemente der psychophysik*, volume 2. ĐăĐÿĐ£Đ¿Đż ĐŽĐżĐřÑĄÑĄĐÿĐž, 2012.

[473] Frédéric Cao, Pablo Musé, and Frédéric Sur. Extracting Meaningful Curves from Images. *Journal of Mathematical Imaging and Vision*, 22(2):159–181, 2005.

[474] Agnès Desolneux, Lionel Moisan, and Jean-Michel Morel. Meaningful alignments. *International Journal of Computer Vision*, 40(1):7–23, 2000.

[475] Mariano Tepper, Pablo Musé, and Andrés Almansa. On the role of contrast and regularity in perceptual boundary saliency. *Journal of mathematical imaging and vision*, 48(3):396–412, 2014.

[476] Vincent Caselles and Pascal Monasse. *Geometric description of images as topographic maps*. Springer, 2009.

[477] Jon Louis Bentley and Thomas A Ottmann. Algorithms for Reporting and Counting Geometric Intersections. *IEEE Transactions on computers*, (9):643–647, 1979.

[478] Campbell Barton. `https://github.com/ideasman42/isect_segments-bentley_ottmann`.

[479] Andrew Fitzgibbon, Maurizio Pilu, and Robert B Fisher. Direct Least Square Fitting of Ellipses. *IEEE Transactions on pattern analysis and machine intelligence*, 21(5):476–480, 1999.

[480] Charles A Rothwell. *Object Recognition Through Invariant Indexing*. Oxford University Press, Inc., 1995.

[481] Radim Halır and Jan Flusser. Numerically Stable Direct Least Squares Fitting of Ellipses. In *Proc. 6th International Conference in Central Europe on Computer Graphics and Visualization. WSCG*, volume 98, pages 125–132, 1998.

[482] Janne Heikkila. Using sparse elimination for solving minimal problems in computer vision. In *Proceedings of the IEEE Conference on Computer Vision and Pattern Recognition*, pages 76–84, 2017.

[483] Zuzana Kúkelová. Algebraic Methods in Computer Vision. 2013.

[484] Luc Habert. Computing Bitangents for Ellipses. In *CCCG*, pages 294–297, 2005.

[485] Richard I Hartley. In Defense of the Eight-Point Algorithm. *IEEE Transactions on*

pattern analysis and machine intelligence, 19(6):580–593, 1997.

[486] CA Rothwell, Andrew Zisserman, David A Forsyth, and Joseph L Mundy. Planar Object Recognition using Projective Shape Representation. *International Journal of Computer Vision*, 16(1):57–99, 1995.

[487] Minghui Xia and Bede Liu. Image registration by" super-curves". *IEEE transactions on image processing*, 13(5):720–732, 2004.

[488] Helmut Alt and Michael Godau. Computing the fréchet distance between two polygonal curves. *International Journal of Computational Geometry & Applications*, 5:75–91, 1995.

[489] Kevin Buchin, Maike Buchin, Rolf Van Leusden, Wouter Meulemans, and Wolfgang Mulzer. Computing the fréchet distance with a retractable leash. *Discrete & Computational Geometry*, 56(2):315–336, 2016.

[490] Thomas Eiter and Heikki Mannila. Computing discrete fréchet distance. Technical report, Tech. Report CD-TR 94/64, Information Systems Department, Technical University of Vienna, 1994.

[491] Kevin Buchin, Maike Buchin, and Yusu Wang. Exact algorithms for partial curve matching via the frechet distance. In *Proceedings of the twentieth Annual ACM-SIAM Symposium on Discrete Algorithms*, pages 645–654. Society for Industrial and Applied Mathematics, 2009.

[492] Pascal Monasse. *Représentation morphologique d'images numériques et application au recalage*. PhD thesis, Paris 9, 2000.

[493] Anne Driemel and Sariel Har-Peled. Jaywalking Your Dog: Computing the Fréchet Distance with Shortcuts. *SIAM Journal on Computing*, 42(5):1830–1866, 2013.

[494] Doug M Boyer, Yaron Lipman, Elizabeth St Clair, Jesus Puente, Biren A Patel, Thomas Funkhouser, Jukka Jernvall, and Ingrid Daubechies. Algorithms to automatically quantify the geometric similarity of anatomical surfaces. *Proceedings of the National Academy of Sciences*, 108(45):18221–18226, 2011.